Mathematical modelling of blood coagulation and thrombus formation under flow in normal and pathological conditions

Anass Bouchnita

Université Mohamed V
Ecole Mohammadia d'Ingénieurs
Centre des Etudes Doctorales: Sciences
et Techniques pour l'Ingenieur

Université de Lyon
Université Claude Bernard Lyon 1
Ecole doctorale: Evolution Ecosystèmes
Microbiologie Modélisation (E2M2)

N° d'ordre NNT : 2017LYSE1300

THÈSE DE DOCTORAT EN COTUTELLE

Pour obtenir le grade de

Docteur en Physiologie et Biologie des Organismes - Populations - Interactions de l'Université Claude Bernard Lyon 1

et

Docteur en Sciences et Techniques de l'Ingénieur de l'Ecole Mohammadia d'Ingénieurs, Université Mohamed V

Soutenue publiquement le 04/12/2017, par :

Anass BOUCHNITA

Mathematical modelling of blood coagulation and thrombus formation under flow in normal and pathological conditions

---

Devant le jury composé de :

Pr. Soumaya BOUJENA,	Professeure, Université Hassan II	Rapporteure
Pr. Rachid ELLAIA,	Professeur, EMI Rabat	Rapporteur
Pr. Adélia SEQUEIRA,	Professeure, CEMAT Portugal	Rapporteure
Pr. Stéphane AVRIL,	Professeur, Mines Saint Etienne	Examinateur
Pr. François GUEYFFIER,	Professeur et praticien hospitalier, UCBL Lyon	Examinateur
Pr. Michel TOD,	Professeur et praticien hospitalier, UCBL Lyon	Examinateur
Pr. Rajae ABOULAICH,	Professeure, EMI Rabat	Directrice de thèse
Dr. Patrice NONY,	Praticien hospitalier, Hospices Civils de Lyon	Directeur de thèse
Pr. Khalid NAJIB,	Professeur, ENSMR Rabat	Invité
Pr. Vitaly VOLPERT,	Directeur de recherche, CNRS,	Invité

Remerciements

Il me sera difficile de remercier tout le monde car c'est à l'aide de nombreuses personnes que j'ai pu mener cette thèse à son terme.

Tout d'abord, je voudrais exprimer ma profonde gratitude envers mes trois directeurs de thèse. Je remercie chaleureusement Professeur Rajae ABOULAICH pour sa gentillesse, sa disponibilité, son aide et soutien sur les plans personnels et professionnels. C'est grâce à elle que j'ai pu découvrir les applications biomédicales de la modélisation mathématique. Je remercie également Docteur Patrice NONY pour de m'avoir proposé un sujet aussi riche et intéressant. Ses conseils biomédicaux m'ont énormément aidé dans mes recherches et sa grande expertise clinique m'a certainement assisté à améliorer la qualité de cette dissertation. Je souhaite aussi exprimer ma reconnaissance envers Professeur Vitaly VOLPERT pour sa confiance, sa gentillesse, sa disponibilité, et son soutien inestimables. J'ai été très heureux de travailler et collaborer avec lui dans différents travaux de modélisation. C'était un grand plaisir pour moi d'apprendre de son savoir-faire.

Je remercie ensuite Professeur Soumaya BOUJENA, Professeur Rachid ELLAIA, et Professeur Adélia SEQUEIRA d'avoir accepté d'être rapporteurs de cette thèse. Je les remercie pour l'attention et le temps qu'ils ont accordés à mon manuscript.

Mes remerciements s'adressent également à Professeur Stéphane AVRIL, Professeur François GUEYFFIER et Professeur Michel TOD de m'avoir fait l'honneur d'accepter de participer jury de cette thèse. Je remerçie également Professeur Khalid NAJIB qui a accepté l'invitation à ma soutenance.

Je remercie également tous les membres de l'équipe EMET du Laboratoire de Biométrie et Biologie Evolutive (LBBE) pour tout l'intérêt et le support qu'ils ont accordé à mes travaux. Je remercie aussi l'Institut Camille Jordan (ICJ) pour m'avoir accueilli dans ses locaux et donné l'accès à ses ressources de calcul.

Il m'est impossible d'oublier les nombreux collaborateurs avec qui j'ai eu la chance de travailler pendant cette thèse. Je remercie en particulier Tatiana GALOCHKINA, et Alen TOSENBERGER pour les collaborations fructueuses sur différentes questions. Mes remerciements vont aussi au Professeur Yuri VASSILEVSKI et son équipe pour m'avoir donné l'opportunité d'effectuer un stage important au sein de l'Institute of Numerical Mathematics (INM) à Moscou.

Finalement, je remercie mes parents et ma famille pour leur soutien tout au long de mes années d'études.

Résumé

Cette thèse est consacrée à la modélisation mathématique de la coagulation sanguine et de la formation de thrombus dans des conditions normales et pathologiques. La coagulation sanguine est un mécanisme défensif qui empêche la perte de sang suite à la rupture des tissus endothéliaux. C'est un processus complexe qui est réglementé par différents mécanismes mécaniques et biochimiques. La formation du caillot sanguin a lieu dans l'écoulement sanguin. Dans ce contexte, l'écoulement à faible taux de cisaillement stimule la croissance du caillot tandis que la circulation sanguine à fort taux de cisaillement la limite. Les désordres qui affectent le système de coagulation du sang peuvent provoquer différentes anomalies telles que la thrombose (coagulation exagérée) ou les saignements (insuffisance de coagulation).

Dans la première partie de la thèse, nous présentons un modèle mathématique de coagulation sanguine. Le modèle capture la dynamique essentielle de la croissance du caillot dans le plasma et le flux sanguin quiescent. Ce modèle peut être réduit à un modèle qui consiste en une équation de génération de thrombine et qui donne approximativement les mêmes résultats. Nous avons utilisé des simulations numériques en plus de l'analyse mathématique pour montrer l'existence de différents régimes de coagulation sanguine. Nous spécifions les conditions pour ces régimes sur différents paramètres pathophysiologiques du modèle. Ensuite, nous quantifions les effets de divers mécanismes sur la croissance du caillot comme le flux sanguin et l'agrégation plaquettaire.

La partie suivante de la thèse étudie certaines des anomalies du système de coagulation sanguine. Nous commençons par étudier le développement de la thrombose chez les patients présentant une carence en antihrombine ou l'une des maladies inflammatoires. Nous déterminons le seuil de l'antithrombine qui provoque la thrombose et nous quantifions l'effet des cytokines inflammatoires sur le processus de coagulation. Puis, nous étudions la compensation de la perte du sang après un saignement en utilisant un modèle multi-échelles qui décrit en particulier l'érythropoïèse et la production de l'hémoglobine. Ensuite, nous évaluons le risque de thrombose chez les patients atteints de cancer (le myélome multiple en particulier) et le VIH en combinant les résultats du modèle de coagulation sanguine avec les produits des modèles hybrides (discret-continues) multi-échelles des systèmes physiologiques correspondants.

Finalement, quelques applications cliniques possibles de la modélisation de la coagulation sanguine sont présentées. En combinant le modèle de formation du caillot avec les modèles pharmacocinétiques-pharmacodynamiques (PK-PD) des médicaments anticoagulants, nous quantifions l'action de ces traitements et nous prédisons leur effet sur des patients individuels.

Mots-clés: Coagulation sanguine, formation de caillots dans l'écoulement sanguin, thrombose, saignement, modélisation mathématique, simulation numérique, modèles multi-échelles hybrides, modélisation PK-PD des médicaments anticoagulants.

Abstract

This thesis is devoted to the mathematical modelling of blood coagulation and clot formation under flow in normal and pathological conditions. Blood coagulation is a defensive mechanism that prevents the loss of blood upon the rupture of endothelial tissues. It is a complex process that is regulated by different mechanical and biochemical mechanisms. The formation of the blood clot takes place in blood flow. In this context, low-shear flow stimulates clot growth while high-shear blood circulation limits it. The disorders that affect the blood clotting system can provoke different abnormalities such thrombosis (exaggerated clotting) or bleeding (insufficient clotting).

In the first part of the thesis, we introduce a mathematical model of blood coagulation. The model captures the essential dynamics of clot growth in quiescent plasma and blood flow. The model can be reduced to a one equation model of thrombin generation that gives approximately the same results. We used both numerical simulations and mathematical investigation to show the existence of different regimes of blood coagulation. We specify the conditions of these regimes on various pathophysiological parameters of the model. Then, we quantify the effects of various mechanisms on clot growth such as blood flow and platelet aggregation.

The next part of the thesis studies some of the abnormalities of the blood clotting system. We begin by investigating the development of thrombosis in patients with antihrombin deficiency and inflammatory diseases. We determine the thrombosis threshold on antithrombin and quantify the effect of inflammatory cytokines on the coagulation process. Next, we study the recovery from blood loss following bleeding using a multiscale model which focuses on erythropoiesis and hemoglobin production. Then, we evaluate the risk of thrombosis in patients with cancer (multiple myeloma in particular) and HIV by combining the blood coagulation model results with the output of hybrid multiscale models of the corresponding physiological system.

Finally, possible clinical applications of the blood coagulation modelling are provided. By combining clot formation model with pharmacokinetics-pharmacodynamics (PK-PD) models of anticoagulant drugs, we quantify the action of these treatments and predict their effect on individual patients.

Keywords: Blood coagulation, clot formation in blood flow, thrombosis, bleeding, mathematical modelling, numerical simulation, hybrid multiscale models, PK-PD modelling of anticoagulant drugs.

Publications

1. Bouchnita, A., Eymard, N., Koury, M., & Volpert, V. (2014). Initiation of erythropoiesis by BFU-E cells. In ITM Web of Conferences (Vol. 4, p. 01002). Workshop on Mathematics for Life Sciences (WMLS 2014), Sidi Bel-abbès, Algeria, EDP Sciences.

2. Bouchnita, A., Kurbatova, P., Tosenberger, A., Nony, P., & Volpert, V. (2015). Numerical simulations of thrombosis development in blood flow, CMBE, Paris, France.

3. Bouchnita, A., Eymard, N., Moyo, T., Koury, M., & Volpert, V. (2015). Normal erythropoiesis and development of multiple myeloma. ITM Web of Conferences. Vol. 5. Workshop on hybrid and multiscale modelling in cell and cell population biology, Paris, France, EDP Sciences.

4. Bouchnita, A., Tosenberger, A., & Volpert, V. (2016). On the regimes of blood coagulation. Applied Mathematics Letters, 51, 74-79.

5. Bouchnita, A., Eymard, N., Moyo, T. K., Koury, M. J., & Volpert, V. (2016). Bone marrow infiltration by multiple myeloma causes anemia by reversible disruption of erythropoiesis. American journal of hematology, 91(4), 371–378.

6. Bouchnita, A., Rocca, A., Fanchon, E., Koury, M. J., Moulis, J. M., & Volpert, V. (2016). Multi-scale Modelling of Erythropoiesis and Hemoglobin Production. Journal of Inorganic and Organometallic Polymers and Materials, 26(6), 1362-1379.

7. Bouchnita, A., Galochkina, T., & Volpert, V. (2016). Influence of Antithrombin on the Regimes of Blood Coagulation: Insights from the Mathematical Model. Acta Biotheoretica, 1-16.

8. Galochkina, T., Ouzzane, H. Bouchnita, A. & Volpert, V. (2016). Traveling wave solutions in the mathematical model of blood coagulation. Applicable Analysis, 1-15.

9. Bouchnita, A., Galochkina, T., Kurbatova, P., Nony, P., & Volpert, V. (2016). Conditions of microvessel occlusion for blood coagulation in flow. International Journal for Numerical Methods in Biomedical Engineering.

10. Bouchnita, A., Bouzaachane, K., Galochkina, T., Kurbatova, P., Nony, P., & Volpert, V. (2016). An individualized blood coagulation model to predict INR therapeutic range during warfarin treatment. Mathematical Modelling of Natural Phenomena, 11(6), 28-44.

11. Bocharov, G., Bouchnita, A., Clairambault, J., & Volpert, V. (2016). Mathematics of Pharmacokinetics and Pharmacodynamics: Diversity of Topics, Models and Methods. Mathematical Modelling of Natural Phenomena, 11(6), 1-8.

12. Bouchnita, A., Bocharov, G., Meyerhans, A., & Volpert, V. (2017). Towards a Multiscale Model of Acute HIV Infection. Computation, 5(1), 6.

13. Bouchnita, A., Belmaati, F. E., Aboulaich, R., Koury, M. J., & Volpert, V. (2017). A Hybrid Computation Model to Describe the Progression of Multiple Myeloma and Its Intra-Clonal Heterogeneity. Computation, 5(1), 16.

14. Galochkina, T., Bouchnita, A., Kurbatova, P., & Volpert, V. (2017). Reaction-diffusion waves of blood coagulation. Mathematical Biosciences, 288, 130-139.

15. Bouchnita, A., Bocharov, G., Meyerhans, A., & Volpert, V. (2017). Hybrid approach to model the spatial regulation of T cell responses. BMC Immunology, 18(1), 29.

16. Bouchnita, A., Miossec, P., Tosenberger, A., & Volpert, V. (2017). Modeling of the effects of IL-17 and TNF-α on endothelial cells and thrombus growth. Comptes rendus biologies, 340(11), 456-473.

Contents

List of acronyms

ADP	Adenosine diphosphate
AHSP	α-hemoglobin stabilizing protein
ALA-S2	Mitochondrial enzyme amino-levulinatesynthetase 2
APC	activated protein C
aPTT	activated partial thromboplastin time
ATIII	antithrombin III
BMP-4	Bone morphogenetic protein 4
CFU-E/Pro-EB	Colony-forming units-erythroid
DVT	deep venous thrombosis
DPD	dissipative particle dynamics
EBI	erythroblastic island
EPO	erythropoietin
HIF	hypoxia-inducible factor
HIV	Human Deficiency Virus
HO-1	heme oxygenase-1
HRI	geme regulated inhibitor
HSC	hematopoietic stem cell
IL	interleukin
IGF	insulin-like growth factor
INR	international normalized ratio
IRP	iron regulatory proteins
KL/SCF	kit ligand/stem cell factor
LPS	lipopolysaccharide
MM	multiple myeloma
ODE	ordinary differential equation
PC	protein C
PDE	partial differential equation
PK-PD	pharmacokinetics-pharmacodynamics
PT	prothrombin time
RBC	red blood cell
TF	tissue factor
TfR	transferrin receptor
TM	thrombomodulin
TNF	tumor necrosis factor
VEGF	vascular endothelial growth factor
VTE	venous thromboembolism

Chapter 1

Introduction

This thesis is devoted to the mathematical modelling of blood coagulation and clot formation in normal and pathological conditions. In this introduction, we begin by presenting the biological concepts and the mathematical models of blood coagulation and its related disorders. We proceed to study the interplay between clot growth and blood flow. Then, we explore some clinical and pharmaceutical applications of the modelling of blood clotting and thrombus formation. We conclude by presenting a summary of the main results of this thesis.

1.1 Blood coagulation

The injury of the endothelial tissue always triggers an appropriate blood clotting response. In the process of hemostasis, tissue factor (TF) is exposed to the bloodstream which initiates a chain of biochemical reactions that ultimately culminates in the production of the fibrin clot. Platelets accelerate the coagulation process and reinforce the clot by adhering to the injury site and forming an aggregate. Under some conditions, the coagulability of blood can be altered resulting in a blood clotting abnormality. In this section, we will describe each of the physiological mechanisms regulating blood coagulation and provide some of the mathematical models that were developed in order to understand it.

1.1.1 The coagulation cascade

Biological background

Blood coagulation is the process by which blood changes from a liquid to a gel, forming a blood clot. The coagulation cascade plays a vital role in this process characterized by the formation of fibrin polymer. This cascade consists of a network of biochemical reactions where blood clotting factors are successively activated resulting in the conversion of fibrinogen into fibrin, a loose mesh of strands that entangles platelets and red blood cells (Fig. 1.1). The concept of the coagulation cascade was first introduced by Davie, Ratnoff and Macfarlane in the 1960's [1]. They described the 'Y'-shaped pathways where the intrinsic and the extrinsic pathways come together into a common pathway leading to the production of thrombin and the subsequent generation of the fibrin mesh. The coagulation cascade consists of the three main phases regulated by different mechanisms [2].

The activation phase. The coagulation process can be initiated by different pathways. The most common one is the extrinsic pathway, also known as the tissue factor pathway, where tissue factor (TF) is exposed to the bloodstream and activates FVII. The active form of the later forms a complex with TF (TF/FVIIa) and generates an initial concentration of the factors FIXa and FXa. These two active factors converts prothrombin into thrombin which triggers the clotting process. Another possible mechanism of the coagulation process activation is the contact pathway. In this mechanism, FXII is activated upon the contact with any foreign material. FXIIa then converts both FIX and FX into their active form resulting in the generation of an initial amount of thrombin (FIIa). The coagulation process can also be activated

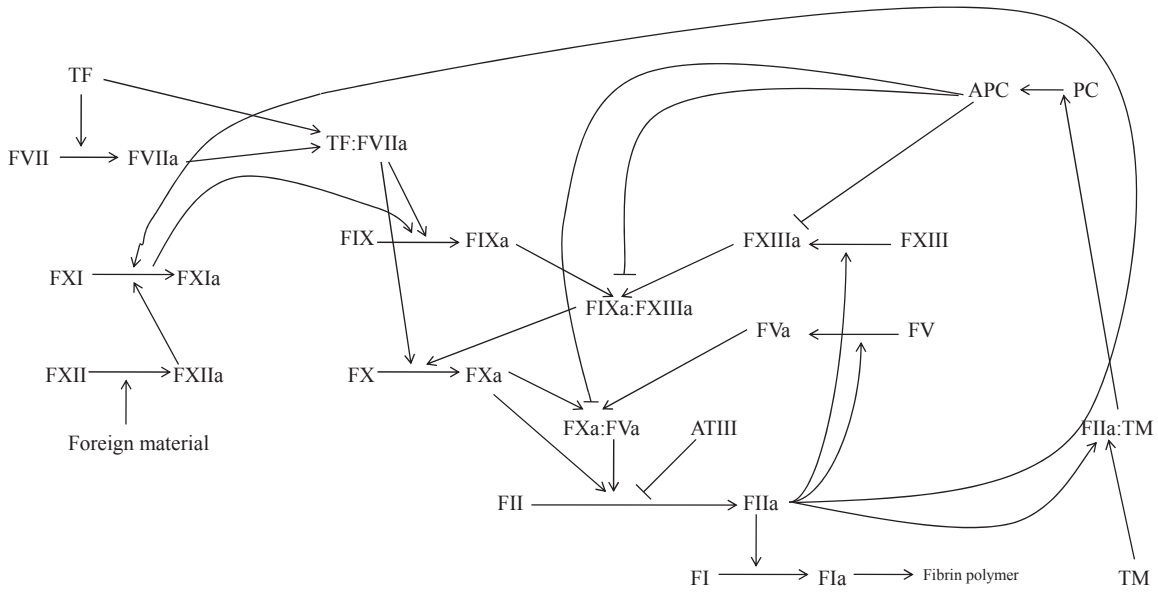

Figure 1.1: Schematic representation of the coagulation cascade.

directly by the thrombin expressed at the surface of platelets. In this mechanism, thrombin directly activates factors of the intrinsic pathway which leads to a further conversion of prothrombin (FII) into thrombin.

The elongation phase. The generated concentration of thrombin activates blood clotting factors such as FV, FVIII, and FXI which further converts more prothrombin into thrombin through a feedback process. This phase is only triggered when a threshold of generated thrombin is reached [3]. The elongation phase is characterised by the amplification of the thrombin generation and the subsequent growth of the clot. In this phase, FIXa and FVIIIa come together to form an intrinsic tenase complex which further activates FX. The active form of the later forms the prothrombinase complex with FVa that converts prothrombin into thrombin.

The termination phase. There exist various mechanisms that prevent excessive blood clotting such as antithrombin, tissue factor pathway inhibitor (TFPI), and activated protein C (APC). Antithrombin is a small protein that inactivates several factors in the coagulation system. It binds to thrombin and FXa which disables their action in the clotting process and ultimately results in blood clotting arrest. TFPI is another protein that plays an anticoagulant role during the coagulation process especially when initiated by the extrinsic pathway. TFPI is considered as a dual inhibitor because it binds to both the TF/FVIIa complex as well as FXa. In this context, FXa exerts a negative feedback on its own production by forming a complex with TFPI (TFPI/FXa) which further inhibits FXa and TF/FVIIa. Another possible mechanism of the clot growth arrest involves protein C (PC) and thrombomodulin (TM). PC is a vitamin-K dependent protein that circulates in the blood plasma. TM is a membrane protein expressed on the surface of intact endothelial cells. It forms a complex with thrombin which activates PC. Subsequently, activated protein C (APC) inactivates clotting factors of the intrinsic pathway such as FVIIa and FXIIIa which inhibits the amplification of thrombin generation.

Mathematical modelling

Different mathematical modelling approaches were used to describe the coagulation cascade. The most widely used technique consists in representing the biochemical reactions of the cascade by a system of ordinary differential equations (ODEs). In such models, the concentration of each blood clotting factor is described by an ODE where the production and the degradation terms depend on the concentrations

of other clotting factors. In this context, Hockin et al. developed an important deterministic model of the coagulation cascade that is able to reproduce clinical data [4]. The model is able to simulate the experimental results in the case of normal, excessive and insufficient thrombin generation. It is considered to be one of the most complete models devoted to the modelling of the extrinsic pathway as it includes 34 ODEs with nonlinear terms. As a result, it was used in other works as a basis to develop more realistic models that study the spatial clot growth dynamics and include blood flow and platelets. However, one of the important limitations of this model is the lack of the intrinsic pathway. This feature was overcome in more recent works [5, 6]. These models also include platelets and many details of the coagulation cascade providing the possibility of studying different blood clotting disorders. There are several other works devoted to the modelling of the coagulation cascade using a deterministic approach [7, 8, 9, 10]. Stability results of a mathematical model of the coagulation cascade were presented in another study [11]

Deterministic models of blood coagulation are usually studied using numerical simulations. However, due to the complexity of such model, it becomes difficult to explore them using mathematical analysis tools. Fortunately, the numerical simulation of such models is usually computationally cheap and requires a short time. As a result, sensitivity analysis becomes an essential tool to test the reliability of the predictions made by these models. In this context, a Monte Carlo study was used by Luan et al. to determine the most sensitive parameters that affect thrombin generations [5]. Ultimately, they show that the concentrations of FX and FII are the most sensitive parameters and this is what makes them a therapeutic target to prevent excessive clotting.

Another possible application of sensitivity analyses consists in determining the appropriate rate constants that reproduce the most accurate results. The difference in the experimental conditions where these constants are measured gives rise to divergent model outputs. Hence, the same mathematical model can have two different results when two parameter sets are used as demonstrated in a recent study [12]. An exhaustive sensitivity analysis devoted to the impact of the parameter uncertainty on thrombin generation was performed in another work [13]. Another possible modelling methodology that is used to describe the coagulation cascade is the stochastic models. One of the most important works in this area of research is the model developed by Lo et al. [14]. In this study, a kinetic Monte Carlo simulation method was used to capture the stochastic variability in the clotting process.

1.1.2 Blood clotting abnormalities

There are many abnormalities that are associated with the blood clotting system. These abnormalities can be divided into two families depending on the blood clotting scenario: excessive clotting (thrombosis) and insufficient clotting (bleeding) (Fig. 1.2). In this section, we present some disorders of blood coagulation and provide the corresponding mathematical models developed to study them.

Pathological conditions associated with thrombosis

Thrombosis occurs when an upregulation in the coagulability of blood results in the formation of a blood clot. These clots, also known as thrombi, can become calcified which results in the complete or partial occlusion of the vessel. Alternatively, they can detach and migrate with the flow causing the occlusion of smaller vessels in the circulatory system. This is a serious medical condition known as embolism and can potentially lead to dangerous complications such as ischemia or a necrosis of some part of the system (e.g. stroke). There are many causes and medical conditions that provoke thrombosis.

Deep venous thrombosis. Deep venous thrombosis (DVT) is a condition characterized by the formation of a blood clot within a deep vein, most commonly located in the legs. DVT has many symptoms such as the swelling, redness, warmness, and engorged superficial veins. It is associated with a dangerous complication where a part of the clot detaches and migrates with the flow to the lungs provoking a pulmonary embolism (PE). The combination of DVT and PE gives birth to a medical condition as the venous thrombo-embolism (VTE). According to Virchow, the interaction between three processes is behind the development of DVTs. These processes include the immobility of flow, the hypercoagulability

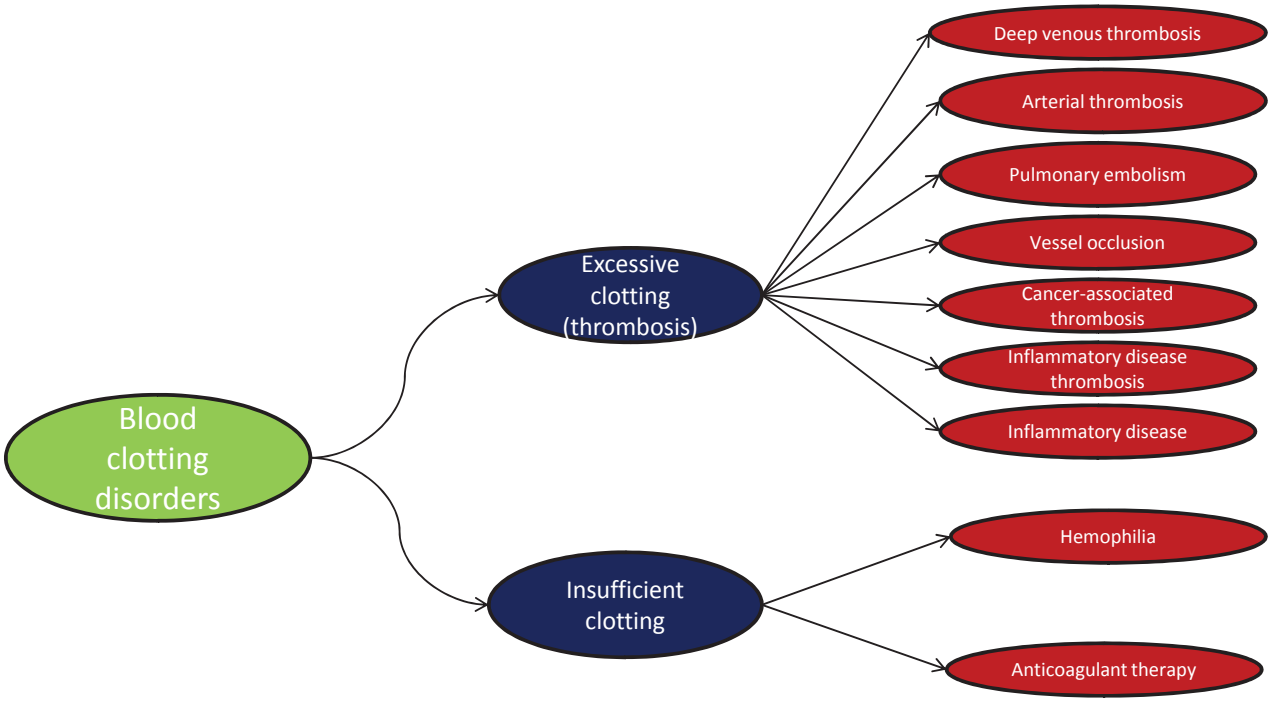

Figure 1.2: Classification of the main blood clotting abnormalities.

of blood, and changes in the vessel wall [15]. Hence, the severity of DVT differs from one individual to another. In order to quantify the coagulability of blood in DVT patients, researchers incorporated the blood characteristics of such patients into existing mathematical models of the coagulation cascade. In this context, Brummel-Ziedins et al. have used the model developed by Hockin et al. [4] in order to compute the thrombin and FXa generation curves belonging to blood samples of DVT patients [16]. A more realistic model of the coagulation cascade was developed by including other details of the coagulation cascade such as protein C [7]. These models show how individual plasma compositions can lead to different results of thrombin generation and quantify the effect of different clotting factors on the blood coagulability. In the future, they can help the clinicians to determine the coagulation cascade components that should be targeted by the new anticoagulant drugs. They can also be used to assess the effectiveness and safety of the existing therapies.

Cancer-associated thrombosis. Cancer is a group of malignancies that involve the excessive growth of a type of cells that invade the neighboring tissues and potentially the other organs. These aggressive cancer cells are usually eliminated using a type of treatments known as chemotherapy. Venous thromboembolism is not only a common complication of cancer, but also a an important side effect of chemotherapy [17]. It is estimated that 20% of cancer patients develop VTE during their treatment period. There are many mechanisms involved in the formation of blood clots due to cancer. First, cancer cells secrete procoagulant cytokines such as interleukin 1β (IL-1β), tumor necrosis factor-α (TNF-α), and vascular endothelial growth factor (VEGF). These factors have different effects on the endothelial cells. For example, they can upregulate the expression of tissue factor on these cells. They can also decrease the expression of thrombomodulin. Furthermore, they also promote the adhesion of leukocytes and platelets to the endothelial tissue which increases the chances of thrombosis formation [18]. Another mechanism by which cancer provokes thrombosis is through the expression of tissue factor by cancer cells themselves. It was reported that many types of cells express tissue factor in various cancers such as breast, colon, pancreas, lung, brain [19]. Circulating tumor cells (CTCs) aggregate platelets and leukocytes to create tissue factor-bearing microparticles that promote thrombi formation in different areas of the circulatory system.

Chemotherapy has also several prothrombotic effects which makes it an independent risk factor of

VTE [20]. A clinical study has shown an incidence rate of VTE in patients undergoing chemotherapy estimated at 10.9% [21]. Chemotherapy induces thrombosis by increasing the expression of TF in endothelial tissues, activating platelets and altering the concentration of clotting factors in the plasma. Both tumor cells and chemotherapy stimulate development of vascular networks which in turns stimulates the formation of blood clots. The modelling of the interaction between vascular networks remodeling and blood flow was conducted using a systems biology method [22]. Another work describes the fields of blood clotting factors generated by mobile CTCs in flow [23].

Thrombosis in inflammatory diseases. Inflammation is a mechanism of innate immunity. It is characterized by the progressive destruction of tissues by harmful stimulus to compromise the survival of the organism. There are many disorders which induce abnormal inflammation such as atherosclerosis, rheumatoid arthritis, HIV, in addition to some types of cancers. There exist complex interactions between blood coagulation and inflammation [24]. These interactions involve the secretion of procoagulant cytokines and chemokines by inflamed tissues, the upregulation of tissue factor expression by endothelial cells, and the activation of platelets and endothelial cells. Atherosclerosis is an inflammatory disease that has an elevated number of prothrombotic complications. In this disease, white blood cells invade an artery wall causing it to become thick. As a result, an atheromatous plaque forms and slowly increases its thickness by cumulating the lipids present in blood which perturbs the flow inside the vessel. The elevation in the shear rate of flow ultimately leads to the rupture of the plaque resulting in the formation of a thrombus overlying the atheroma. Mathematical models were developed in order to investigate the initiation of atherosclerosis and how it spreads in tissues [25, 26]. While the interaction between plaque formation and flow was explored using a fluid-structure interaction formalism [27, 28, 29]. Psoriatic arthritis (PA) and rheumatoid arthritis (RA) are two other inflammatory diseases that provoke thrombosis formation. However, the prothrombotic mechanisms of these two diseases are different from atherosclerosis. In these diseases, inflamed tissues secrete procoagulant cytokines, such as interleukin 17 (IL-17), and tissue necrosis factor α (TNF-α), that upregulates the expression of TF and decreases the concentration of TM on endothelial cells. PA and RA are also known for altering the composition of blood factors in plasma which increases the coagulability of blood. Thrombin generation curves of RA patients were simulated using a coagulation cascade model by Undas et al. [30]. Another inflammatory disease with prothrombotic complications is sepsis. It is a life-threatening condition usually triggered by lipopolysaccharides (LPS), also known as endotoxins. These are molecules present on the outer membrane of the Gram-negative bacteria. They provoke an endothelial inflammatory response chacaterised by the expression of high concentrations of TF which initiates the coagulation cascade. In addition, LPS also increase the number of TF-bearing monocytes that also express pro-inflammatory cytokines on their surface. To our knowledge, there is no mathematical model studying the coagulation cascade dynamics during sepsis. However, several mathematical models were developed to simulate the concentrations of procoagulant and pro-inflammatory cytokines during the progression of the disease [31, 32]. These models can be combined with the models of the coagulation cascade dynamics to estimate the risk of VTE during sepsis.

Thrombosis due to antithrombin deficiency. Antithrombin is a protein that is necessary for clot growth arrest. It is present in blood plasma and binds to several blood clotting factors, such thrombin and FXa, in order to inactivate them. The deficiency of ATIII results in the hypercoagulability of blood which favors the formation of blood clots. There are two types of ATIII deficiencies. The first is inherited and observed in one person out of two to five hundred in the normal population. The second is acquired and involves the decrease of antithrombin following a major surgery, liver dysfunction, or in the proteinuria nephrotic syndrome. Antithrombin deficiency not only reduces the necessary time for blood clotting, but also increases the maximal size reached by the thrombus as shown in a mathematical modelling study [33].

HIV-associated thrombosis. The human immunodeficiency virus (HIV) is considered to be one of the risk factors of thrombosis. HIV infects the vital cells such as $CD4^+$ T-cells, macrophages, and dendritic cells. Once infected, the cell becomes unable to function normally, and represents a target to

$CD8^+$ T-cells. The virus can also induce the death of the infected cell by cytotoxicity. As a result, the immune response system is impaired and the body becomes vulnerable to any infection. HIV has many procoagulant effects on the blood clotting system. First, infected $CD4^+$ T-cells secrete inflammatory cytokines such as IL-6, IL-17, and TNF-α that upregulate the concentration of P-selectin in endothelial cells. It is a protein that is responsible for cell recruitment and adhesion which activates endothelial cells. HIV also increases the number of monocytes and microparticles expressing TF in blood [34]. Then, HIV also causes the deficiency of various anticoagulant factors such as PC and ATIII. The mechanisms by which HIV downregulates these factors are still unknown to this day [35]. To our knowledge, there is no mathematical model that quantifies the effects of HIV on the coagulation process.

Pathological conditions associated with bleeding

Bleeding is the condition where the thrombus does not form properly due to insufficient blood clotting. While excessive clotting can induce dangerous complications such as DVT and strokes, underclotting can provoke equally dangerous conditions such as hemorrhages. Bleeding can lead to other dangerous conditions such as anemia and hematoma. An insufficient blood clotting response can be both inherited and acquired. Below we present some of the most common conditions inducing under-clotting.

Hemophilia. Hemophilia is a rare inherited blood clotting disorder characterized by the lack of a procoagulant factor in blood. There are three types of hemophilia depending on which clotting factor is lacking: FVIII in type A, FIX in type B, and FXI in type C. The deficiency of these factors prevents the generation of thrombin and the subsequent formation of the blood clot. Mathematical modelling can be used to estimate the response of the hemostatic response in patients with hemophilia. In this context, thrombin wave curves of hemophilia B patients were compared with healthy counterparts [36]. As expected, hemophilia B not only reduce the time of clotting but also the size of the clot.

Bleeding incidence during anticoagulant therapy. Anticoagulant drugs are usually prescribed to prevent the incidence of thrombosis. However, when administrated in higher doses, the same drugs can potentially provoke bleeding. Mathematical modelling can be used to assess the safety of these drugs and determine the therapeutic window for every individual patient. We present a review of the main works that attempt to determine the bleeding and thrombosis risk for numerous anticoagulant drugs in Section 1.3.

1.2 Thrombus development under blood flow

Under the real *in vivo* conditions, blood coagulation is usually affected by hemodynamics since it occurs inside blood vessels. Hence, it is particularly important to understand the properties and the dynamics of blood flow before moving to more complex questions such as the interplay between clot growth and the flow. One of the challenges facing the modellers is studying the effect of the different flow conditions on the formation of the clot. After exploring the different conditions of blood flow that can be found in the circulatory system, we will study the dynamics of blood clotting in flow. Then, we will present a state of the art of the computational and mathematical modelling studies devoted to hemodynamics and thrombus development in flow.

1.2.1 Blood flow

Biological background

Blood is a body fluid that is present in humans and other animals. The average volume of blood in a human adult is 5 liters. Its main role consists in transporting oxygen and nutrients to the different organs and tissue and move metabolic waste away from the same cells. It is mainly composed of blood plasma and numerous types of cells. Blood plasma is a Newtonian yellow colored liquid that makes up about 55% of the body blood and consists mostly of water (up to 95% of mass). The rest comprises dissolved

proteins that have different functions. These proteins involve clotting factors, hormones, globulins, glucose, oxygen, and carbon dioxide. Each of these has a fundamental role in the normal functioning of the body. Blood also contains several types of cells that are also known as hematopoietic cells because they are a product of hematopoiesis. It is the process by which hematopoietic stem cells give rise to different types of cells after a series of cell differentiations. Blood cells fall into three basic categories: red blood cells (erythrocytes), platelets (thrombocytes), and white blood cells (leukocytes).

Red blood cells (RBCs) are the cells that carry oxygen (O_2) to the different organs of the body. The process by which these cells are produced in the bone marrow is called erythropoiesis. In this process, colony-forming unit and pro-erythroblast (CFU/ProEB) differentiate into reticulocytes after undergoing a process of enucleation. Late erythroblasts and reticulocytes consume the extracellular iron that is present in the bone marrow to produce intracellular hemoglobin, an oxygen-transporting protein metalloprotein. After losing their nucleus, reticulocytes mature into discoid RBCs and leave the bone marrow to bloodstream. There is approximately 4.2-6.1 10^9 RBCs per millimeter in blood. Each RBC remains in blood for around 120 days and then gets recycled by circulating macrophages. Depending on their hemoglobin concentration, RBCs bind oxygen and carry it to the different cells in the body. RBCs are especially known for their effects on blood rheology. When present in blood flow, RBCs exhibit two physiological features that have an impact on hemorheology. The first one is the erythrocyte aggregation observed under low-shear flow. Under such conditions, RBCs form stacks (rouleaux) due to their discoid shape [37] which increases the overall viscosity of blood. The other mechanical property of RBCs is their deformability, which becomes particularly important under higher shear flows and has an adverse effect on hemorheology than erythrocyte aggregation. Because of these two conflicting mechanical properties, blood behaves as a non-Newtonian flow. RBCs and fibrin are the main components of venous thrombus. For this reason, we refer to these thrombi as red clots due to the red color of erythrocytes. Furthermore, RBCs contribute to thrombosis by marginating platelets toward the endothelium. They also express phosphatidylserine on their surface which promotes thrombin generation [38].

Platelets, also known as thrombocytes, are another type of cells that is present in the bloodstream and play an important role in blood coagulation. These smaller cells are fragments of the large bone marrow cells called megakaryocytes after they get divided. They have a diameter of 2-3 μm and can be found in unactivated and activated forms. While unactivated, platelets have a lens-shaped structure. Once activated, they become round and extend filaments in order to cover the wound region and aggregate other platelets. The aggregation of platelets is an important process in blood coagulation whose main role is to prevent bleeding. In this process, platelets are the first to react to an endothelial injury by attaching to the subendothelium. Next, these platelets become activated and express procoagulant factors on their surfaces such as TF, ADP, and thrombin which initiates the blood clotting system. Due to their round shape and their filaments, activated platelets recruit the neighboring unactivated platelets in flow and progressively form the platelet plug. Platelets can also be activated by other mechanisms such as physical damage, lack of oxygen, or under high-shear flow.

The third type of cells that can be found in blood is the white blood cells or leukocytes. These cells protect the body from the infectious diseases and foreign invaders and participate in the immune response. There are different subtypes of white blood cells, such as neutrophils, basophils, lymphocytes, and monocytes, with a specific role for each one. Most of these cells are not directly involved in the blood clotting process except monocytes. Some of these large cells can express procoagulant factors on their surface when exposed to TF or inflammatory cytokines which results in the formation of microparticles that contribute to the development of blood clots [39].

Blood is also an important component of the circulatory system which is composed of several organs. In this system, blood is transported through vessels known as arteries and veins. When it leaves the heart, blood goes through the aorta, then the arteries until it reaches smaller microvessels called the arterioles, and then the capillaries. It returns to the heart by moving through the venules and then the veins. Blood flow exhibits different velocities and characteristics as it circulates through each of these vessel types. In this context, venous flow is generally low-shear laminar flow, while arterial flow can be unsteady especially in curves and branches [40]. Furthermore, the circulation of flow throughout the vascular network is pressure driven across a branched network of vessels. The arterial flow is pulsatile with an amplitude that decreases as the distance of the artery from the heart increases. It was observed that this flow is affected by flow obstructions in other parts of the circulatory system [41].

Mathematical modelling

Mathematical modelling is used to study several questions that are essential to properly describe the dynamics of blood. These questions involve the rheology of blood, mechanical modelling of erythrocytes, 1D models of flow networks, modelling the distribution of cells in flow among others [42]. To capture the dynamics of blood flow inside blood vessels, researchers typically use continuous models that are based on the Navier-Stokes equations. There exist two subtypes of these models: Newtonian and non-Newtonian viscosity models. The Newtonian approximation of blood viscosity is only valid when shear rate does not exceed a critical value. In this case, we can assume that the viscosity of blood depends on the hematocrit [43]. Each of the Newtonian models suggested a specific formula for the viscosity which depends on various characteristic of the flow such as the interaction between cells and their migration [44, 45, 46]. The second subtype of blood flow continuous models is the non-Newtonian viscosity models. These models include the shear thinning behavior of blood through an equation that defines the relationship between the viscosity and shear rate [47, 48, 49]. These models can be either time independent or time dependent because shear rate changes during the cardiac cycle. They usually use experimental data on viscosity to determine the used constants. These are commonly used in Computational Fluid Dynamics (CFD) studies of blood flow. In this context, viscoeslatic models represent one of the most accurate rheological description of blood flow.

Another approach that is used to model blood flow consists in describing flow using particle methods. These Lagrangian methods involve Smoothed-Particle Hydrodynamics (SPH), Lattice Boltzmann (LBM), Dissipative Particle Dynamics (DPD), Molecular Dynamics (MD), and Cellular Potts Methods (CPM). By suggesting a Boltzmann Bi-viscosity model, Liu was able to develop a validated LBM model of blood flow [50]. In SPH, MD and DPD, the plasma is divided to a set of elements called particles whose dynamics are governed by different forces. Although these methods can be more computationally expensive than the classical CFD methods, they are certainly better adapted to the modelling of complex fluids cases such as blood flow in patient-specific vessels. In this context, SPH was used to computationally describe blood flow in CT-reconstructed arteries [51]. The DPD method was successfully used to provide a realistic representation of blood flow including erythrocytes and platelets [52]. The same model was able to explain the magination of platelets by red blood cells.

1.2.2 The development of the thrombus under flow

Biological background

In thrombosis, the formation of the fibrin clot takes place in a medium of circulating blood. Hence, it is normal for blood flow to affect the dynamics of clot growth. While low-shear flow stimulates clot growth by transporting the platelets and the procoagulant factors to the thrombus, high-shear flow limits clot growth by detaching platelets and washing away the same factors. In this context, experimental studies have shown that for low-shear flow, the rate of clot growth rate increases as the shear rate increases until it reaches a critical value. Then, the rate of clot growth starts decreasing until it reaches a constant value [53]. On one hand, it is important for blood flow to be steady and fast for a normal hemostatic response to take place. On the other hand, alterations in blood flow are considered to be a factor that contributes to the pathogenesis of thrombosi. In this context, the factors leading to the development of venous thrombosis belong to three categories: the hypercoagulability of blood, the endothelial injury, and the stasis of blood flow. These three broad categories form what is called the Virchow's triad of venous thrombosis [54] (Fig. 1.3). Hence, the study of hemodynamic changes is of paramount important for researchers who try to understand the pathophysiology of thrombosis.

There are many conditions that can potentially lead to the stasis and stagnation of venous flow. For instance, prolonged periods of immobility and paralysis of the lower limbs are sufficient to decrease the rate and velocity of blood flow in deep veins and increase the risk of DVT. Varicose veins are another important risk factor of DVT. In this condition, veins become enlarged and twisted due to diseased valves that cannot prevent the flow from going backwards anymore. Reduced flow velocity can also result from the perturbation of flow in other areas of the vascular network. Overall, the stasis of blood flow facilitates the interaction between blood factors, platelets, and the vessel wall. Furthermore, it

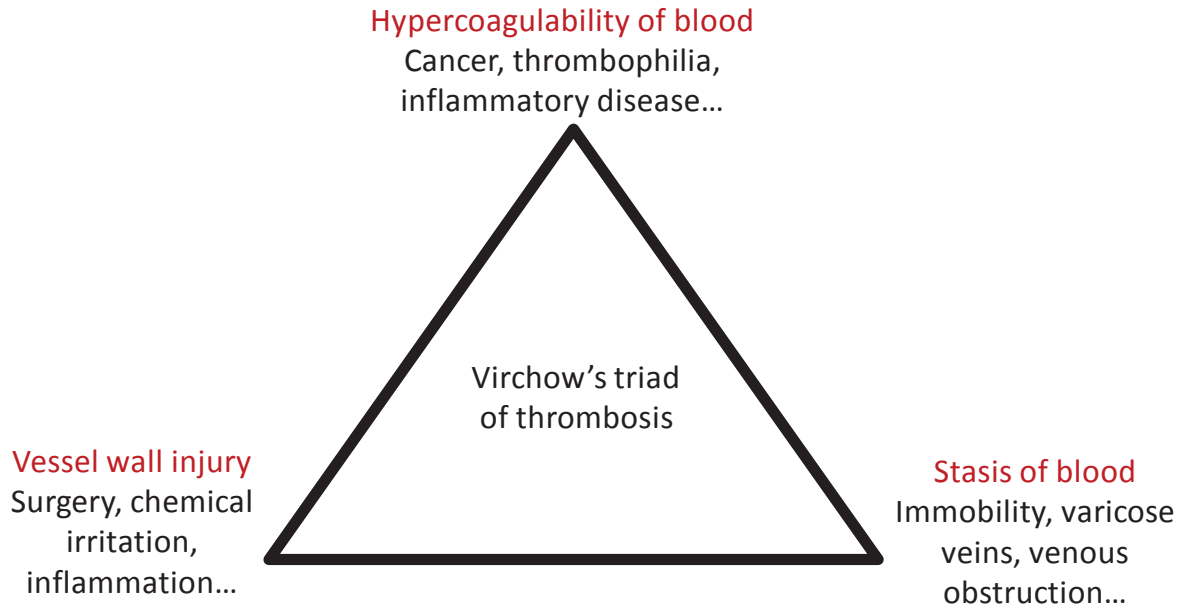

Figure 1.3: The Virchow's triad of risk factors for venous thrombosis.

deprives the endothelial tissues of oxygen resulting in their hypoxia. This results in the expression of TF and P-selectin on the surface of these cells which leads to the activation of the coagulation process [55]. Hence, reduced flow does not only increase the coagulability of blood, but also provoke a change in the endothelial wall which confirms the hypothesis that the categories of the Virchow's triad are interlinked. If the speed at which blood circulates is sufficiently high, then it does not only delay the formation of the clot, but can also completely stop it. For this reason, fast steady blood flow is considered to be a fundamental condition for a healthy hemostatic response.

If blood flow changes the dynamics of thrombosis development, the latter have various effects on the hemodynamical properties of blood. Venous thrombi are composed mainly of fibrin polymer and red blood cells which makes them a dense porous medium. It was shown in *in vitro* experimental studies that the permeability of blood clots depends on the densities of fibrin polymer and platelets [56]. Therefore, exaggerated clot formation can either perturb or completely block the circulation of blood. For this reason, venous thrombosis can be occlusive when the thrombus completely obstructs blood flow. Otherwise, it is considered to be non-occlusive as the clot perturbs blood flow but does not completely stop it. In this case, the rate of blood flow and its velocity can still be reduced because it is driven by a constant pressure difference.

Mathematical modelling

Blood coagulation is a complex process whose complexity further increases when the interaction with blood flow is considered. Hence, mathematical modelling becomes an important tool that can provide new insights into the complex puzzle of clot growth in flow. Before incorporating blood flow, the deterministic ODEs models are extended to PDEs by including the spatial aspect of clot growth such as diffusion and advection in most cases. However, it is possible to include blood flow directly to ODEs by considering a term of removal by flow [57, 58, 59]. While these models use a simple treatment for blood flow and do not consider hemodynamical changes during clot growth, they represent a simple way to introduce flow effects on clot growth.

The rest of the model considers a spatiotemporal representation of clot formation usually inside a blood vessel. These models simulate both flow dynamics and clot growth in the same domain. The first approach that is used in this regard consists in considering a continuous model for both blood flow and the blood coagulation factors. This approach is especially efficient because it allows to couple both models and to solve them in the same numerical mesh. Usually, the Navier-Stokes equations are used

to describe blood flow while advection-diffusion-reaction equations are solved to capture the concentrations of clotting factors and fibrin polymer. As a first approximation, some researchers considered that fibrin polymer does not affect blood flow dynamics [60]. Others preferred using a generalized Newtonian model for blood flow where the viscosity depends on the concentration of fibrin [61, 62]. Another type of continuous models considers blood clot to be solid and use a fluid-structure approach to capture its growth under the flow [63]. More recent models consider the fibrin clot to be a porous medium whose permeability directly affects the flow through a resistance term incorporated into the Navier-Stokes equations [64, 65]. This method is particularly important because we can track the development of the thrombus as well as the hemodynamical changes in the same domain without recomputing the computational mesh at each time step.

Other types of modelling approach of thrombus formation under flow include the hybrid models. These models combine both the continuous and discrete description of blood flow, cells, and clotting factors to achieve a realistic representation of the coagulation process. Some of these models use a continuous approach to describe both blood flow and the clotting factors and a discrete one to track the motion of blood cells [66, 67, 68]. Other researchers opt for a particle representation of blood flow using methods such as DPD coupled with continuous approach to describe the distributions of blood clotting factors [69, 70].

1.3 Clinical applications of blood coagulation modelling

Developing mathematical models of blood coagulation is essential in understanding the pathogenesis of blood clotting abnormalities such as thrombosis, hemophilia, etc. Usually, the developed models are firstly built in order to describe the dynamics of healthy blood coagulation. However, it is sufficient to change some parameters associated with a coagulation disorder to describe pathological blood coagulation. The ultimate goal of these models is to study the action of treatments on the coagulation process. Despite the wide range of mathematical methods used in the development of PK-PD hemostasis models, the modellers are faced with numerous challenges due to the complexity of the blood clotting system. Below, we present a state of the art of the approaches used in the mathematical modelling of blood clotting disorders and their treatment.

1.3.1 The characterization of individual patients

Developing individual profiles of the blood clotting response is important to bridge the clinical data with the outputs of mathematical models. There are several diagnostic tests that are used by clinicians in order to assess the blood coagulability of individual patients. The most commonly used diagnostic test is the prothrombin time (PT) which describes the necessary time for thrombin generation after adding an amount of tissue factor to blood plasma. This test is mainly used to evaluate the functioning of the tissue factor extrinsic pathway based on the composition of the patient's plasma. The International Normalized Ratio (INR), which is obtained by standardizing the PT, is commonly used to estimate the risk of thrombosis and bleeding during the treatment with vitamin K antagonists. In this context, clinicians can adjust the dose of anticoagulant drugs to target a therapeutic INR range of 2-3.5, depending on the underlying disease. A lower value than 2 indicates the predisposition of the patient to thrombosis while a higher INR than 4.5 shows that the patient is exposed to an increased risk of bleeding. Other commonly used test of blood clotting include the partial thromboplastin time (PTT) and the activated partial thromboplastin time (aPTT). These diagnostic tests are used to verify the functioning of the intrinsic pathway by initiating the coagulation cascade through contact with an activator such as silica, celite, and kaolin. The blood coagulation assay that is most compatible with mathematical models is the thrombin generation test. In this assay, the concentration of generated thrombin is captured after the initiation of the coagulation cascade which is exactly the result of the ODEs model of blood clotting.

Developing PK-PD models of blood coagulation pathologies requires an appropriate characterization of individual patientśprofiles. Brummel-Ziedins [71] addressed this point by developing and validating computational approaches which capture the dynamics of thrombin generation in individual patients depending on plasma composition. Such approaches can be used in identifying thrombosis risk during

anticoagulant treatments. Other models study the hemostatic response in individuals with pre-existing health conditions associated with clotting disorders including rheumatoid arthritis [30], cancer [22], and deep venous thrombosis [72].

1.3.2 Pharmacokinetics-pharmacodynamics modelling of anticoagulant treatments.

Venous thrombosis is a blood clotting disorder characterized by the formation of excessive blood clots within a vein resulting in the perturbation of blood flow. Warfarin and heparin are two anticoagulant drugs that are usually prescribed to prevent and/or to treat venous thrombosis [73]. Warfarin is an anti-vitamin K which reduces the coagulability of blood by downregulating the synthesis of several blood clotting factors in the liver. In a recent model [74], the effect of warfarin on clot growth in flow was studied. Its action is monitored by an *in vitro* assay called INR (international normalized ratio) which is based on the necessary time for prothrombin conversion into thrombin. The authors used previously developed models for both *in vivo* clot formation and *in vitro* PT and INR assays, and then compared the action of warfarin on individual patients under these two conditions. They conducted numerical simulation describing clot growth during warfarin treatment under various flow conditions. They concluded that the *in vitro* assays do not represent a reliable tool for monitoring warfarin treatment due to the absence of blood flow in *in vitro* tests. This explains the persistence of thrombosis for some patients even when their INR is in the targeted range.

In addition to warfarin, heparin is one of the commonly used venous thrombosis treatments. Heparin upregulates the activity of antithrombin which reduces blood coagulability. In a recent work [75], Dydek and Chaikof equipped a previously developed model for *in situ* clot growth with the action of heparin. The resulting model is detailed and focuses on the spatio-temporal dynamics of clot growth during heparin treatment. The authors evaluated the effects of different doses and types of heparin under venous and arterial flows and included the effect of circulating tissue factor. In the future, this work can be combined with pharmacokinetics models of heparin treatments to assess the efficacy and safety of various protocols.

A comprehensive model which encompasses both the PK-PD and the *in vitro* assays aspects of venous thrombosis was developed using systems pharmacology [76]. It uses ODEs to describe the concentrations of drugs, proteins, and clotting factors in different time scales which affect each other. In this work, the authors compared the results of different *in vitro* tests and clotting times such as PT and aPTT during anticoagulant treatment. They studied the action of different drugs such as warfarin and heparin and simulated the pathogenesis of blood clotting disorders such as thrombosis, hemophilia A and B. To the best of our knowledge, this is one of the few complex models that were validated by experimental data in the literature. The model can serve as an *in silico* predicting tool in drug development and clinical trials.

Although most of the PK-PD models of thrombosis study the action of warfarin and heparin, some of the recent works are devoted to the action of new oral anticoagulants such as rivaroxaban. It is a direct factor Xa inhibitor which is commonly used to prevent strokes and thrombo-embolic events in adult patients. An important PK-PD model which assesses the efficacy and safety rivaroxaban treatments was developed by Burghaus et al. [77]. This work is of practical interest because it is based on previously validated models [6, 4]. Furthermore, it encompasses both the extrinsic and intrinsic pathways as well as the effects of blood flow on clot growth. All of these factors make the model appropriate for clinical studies. Recently, the model was used in order to study the optimal dosing schedule for switching from warfarin to rivaroxaban treatment (Burghaus et al. 2014). Another systems pharmacology model of rivaroxaban action was developed by Zhou et al. [78]. It contains one of the most complete descriptions of the blood coagulation cascade and accurately predicts clotting times during anticoagulant treatment. Direct thrombin inhibitors are another class of new oral anticoagulant drugs which are used in the prevention of thromboembolic events. Dabigatran etexilate is one of the commonly used direct thrombin inhibitors as it can replace warfarin but does not require monitoring by the INR test. The only *in vitro* assay which can potentially assess the efficacy and safety of such treatments is the thrombin generation test. In a recent study [79], the authors used a calibrated version of this test to assess the efficacy of

dabigatran. Although the study does not directly provide a mathematical model which can be used in *in silico* dabigatran treatments assessment, it presents valuable experimental data which can help the future developments of PK-PD models describing the action of dabigatran on the coagulation process.

1.3.3 Discussion

There are many other systems pharmacology models which describe blood coagulation pathologies and the action of treatments ([80, 81, 82, 83, 84]). While most of these models are more appropriate for an accurate multiscale description of the coagulation process during treatment, they are usually built in complex and sophisticated ways that incorporate many details. As a result, it becomes difficult to interpret the obtained results and to derive simple relations between the parameters of interest. To encourage the use of multiscale models in clinical studies, Gulati et al. showed how to reduce a 62-state model to 5-state model [81]. They also derived mechanistic relationships between coagulation parameters that agree with experimental data.

PK-PD models of thrombosis and other blood coagulation disorders represent a promising tool that can potentially predict individual haemostatic responses. However, for these models to be incorporated in clinical studies, it is crucial to confront them with *in vitro* and *in vivo* blood clotting experimental data. Ultimately, we can expect that accurate computer models of blood coagulation will replace *in vitro* diagnostic assays. Until then, a significant effort should be made in order to develop more accurate and experimentally validated models that capture all the pathophysiological aspects of blood coagulation.

1.4 Main results of the thesis

This thesis is devoted to the mathematical modeling of blood coagulation and clot formation under flow in normal and pathological conditions. Chapters 2 and 3 are devoted to the development and the study of mathematical models of the coagulation cascade and the formation of the thrombus in quiescent plasma and blood flow. These models are used to show the existence of different regimes of clot formation depending on the values of different parameters. Chapter 4 presents a study of the association between thrombosis and two pathological conditions: antithrombin deficiency and inflammation. In Chapter 5, we study the dynamics of the recovery from blood loss due to bleeding. For this reason, we develop a hybrid-discrete continuous multiscale model of erythropoiesis and iron production. The model shows the recovery of the normal levels of hemoglobin after 10-14 days of blood loss. In Chapter 6, we use the previous model of erythropoiesis to study its impairment by multiple myeloma (MM), a malignant cancer that destroys erythroid cells and causes anemia. We study the risk of thrombotic complications during MM chemotherapy. Chapter 7 presents a hybrid model of the immune response and HIV infection. The output of these models is used to quantify the risk of thrombosis during acute HIV progression. Chapter 8 deals with clinical applications of the modeling of blood coagulation. The combination between the blood coagulation models and PK-PD models of anticoagulant treatments explains the incidence of thrombi and bleeding during treatment and predict the risk of VTE in individual patients during anticoagulant therapy. The thesis investigates the interactions between blood coagulation, its treatment, and different physiological systems such as erythropoiesis and diseases such as cancer (multiple myeloma) and HIV. To better explain the structure of the thesis, we present the underlying interactions between these different concepts in Fig. 1.4.

1.4.1 Mathematical modelling of the formation of blood clots and the regimes of clot growth

We present a continuous mathematical model of the coagulation cascade describing the concentration of the blood clotting factors during thrombin generation. We extend the model to include the spatiotemporal aspects of the fibrin clot formation as observed in quiescent plasma. We further extend the model by introducing blood flow and its interaction with the developing thrombus. In this model, the clot is treated as a porous medium whose porosity depends on the concentration of fibrin polymer. The resulting

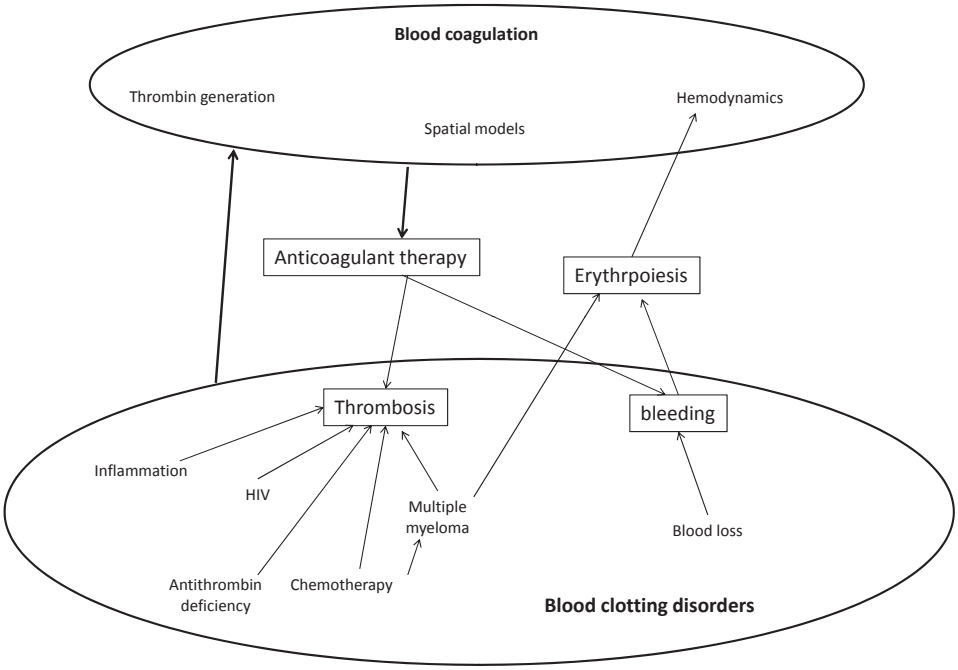

Figure 1.4: A representation of the complex cause and effect relationships between the main topics of the thesis: blood coagulation, erythropoiesis, clotting abnormalities and anticoagulant therapy.

exhaustive model consists of a system advection-reaction-diffusion equations coupled with the Navier-Stokes equations that contain an additional term describing the deceleration of flow as it goes through the clot. For each blood clotting factor F_i, we describe its concentration during clot growth using an equation of the following form:

$$\frac{dF_i}{dt} + \nabla.(vF_i) = D\Delta F_i + R_i, \tag{1.4.1}$$

where v is the blood flow velocity, D is the diffusion coefficient, and R_i is a the reaction term. Similar equations will be used to describe the densities of different subtypes of platelets. To this system of equations, we add the Navier-Stokes equations in order to capture the effect of hemodynamics on the distribution of blood clotting factors:

$$\rho\left(\frac{\partial \vec{u}}{\partial t} + \vec{u}\nabla\vec{u}\right) = -\nabla p + \mu\Delta\vec{u} - \frac{\mu}{K(\vec{x})}\vec{u}, \tag{1.4.2}$$

$$\nabla\vec{u} = 0,$$

where $\vec{u} = (u_x, u_y)$ is the velocity vector, p is the pressure, ρ the density of blood, μ the viscosity. We consider laminar incompressible flow. K is the hydraulic permeability of the thrombus which can be expressed as a function of fibrin polymer concentration and platelets density.

The above model considers the thrombus as a porous medium whose permeability depends on the concentration of fibrin polymer and the density of platelets. One of the computational advantages of this approach is the possibility to describe the development of the thrombus and blood flow on one mesh and without considering two distinct domains. The model will be used to conduct realistic numerical simulations of thrombus development in a rectangular domain representing a section of a blood vessel. The domain includes an injury site where tissue factor is present and initiates blood coagulation (Fig.

1.5). Another advantage of the developed model is that it can be reduced to a one equation model of thrombin distribution (T):

$$\frac{\partial T}{\partial t} = D\frac{\partial^2 T}{\partial y^2} + \Phi(T,y), \tag{1.4.3}$$

where D is the diffusion coefficient, $\Phi(T,y)$ is the reaction term that includes the initiation of thrombin generation, its amplification, and its inhibition due to different mechanisms. The simplified model gives a good approximation of the solution of the complete model. Furthermore, it corresponds to a bistable reaction-diffusion equation that sustains mathematical analysis. Using both the complete and the simplified model, we show the existence of different regimes of blood coagulation and determine their respective conditions. In other words, we specify the range of parameters where a normal, excessive or an insufficient clot formation can be observed. Then, we present another mathematical model of blood coagulation that focuses on the details of the intrinsic pathway. The model is able to accurately estimate the speed of clot propagation. Furthermore, it can be reduced to a one equation model that gives a good approximation. The analytical formula of the clot propagation speed is obtained using the narrow reaction zone method and a piecewise linear approximation.

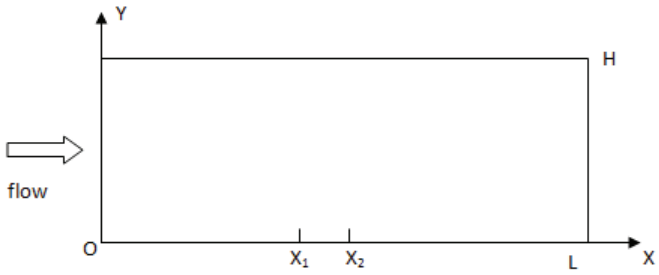

Figure 1.5: A 2D schematic representation of a blood vessel domain where the numerical simulations of the complete model are conducted. The section $[x_1, x_2]$ denotes the injury site.

1.4.2 Mathematical modeling of blood clotting abnormalities

After understanding the regimes of blood coagulation and their corresponding conditions, we then study the pathologies andl mechanisms that contribute to their development. These mechanisms usually results in conditions where the production of tissue factor or of some other blood clotting factors is altered.

Antithrombin deficiency

We begin with the cases of antithrombin deficiency where a hypercoagulable state of blood is acquired due to the lack of antithrombin. We use a mathematical model of blood coagulation to quantify the effects of antithrombin and prothrombin on the formation of the clot using numerical simulations. The model is then reduced to a one equation model in order to obtain the mathematical relation between the concentration of antithrombin and the threshold of thrombosis.

The effects of IL-17 and TNF-α on blood clotting in inflammatory diseases

The same approach is used to investigate the association between thrombosis and inflammatory diseases. In this case, we study the effects of the inflammatory cytokines IL-17 and TNF-α on the coagulation process. These cytokines upregulate the concentration of tissue factor, decrease the expression of thrombomodulin and increase the aggregation of platelets. We study the individual and combined effects of these cytokines on clot growth in order to estimate the risk of thrombosis in patients with inflammatory diseases such as rheumatoid arthritis (RA) and psoriatic arthritis (PsA). We use a continuous model of clot formation in order to study the dynamics of clot growth in patients with inflammatory diseases under venous flow conditions. Then, we use a previously developed DPD-PDE model of clot formation

([69, 70]) in order to investigate the development of arterial thrombosis in chronic inflammation. The two models show that the combined effects of IL-17 and TNF-α significantly increase the incidence risk of both venous and arterial thrombosis. A reduced version of the continuous model is derived in order to determine the exact conditions of thrombosis on the actions of IL-17 and TNF-α.

The role of erythropoiesis in the recovery from anemia due to excessive bleeding

Bleeding, or hemorrhage, is the medical condition characterized by the escaping of blood from the circulatory system. Bleeding is usually observed when the ability of blood to coagulate is impaired. Such deficiency in clot formation can be cause by disorders such as hemophilia or by the excessive use of anticoagulant drugs. One of the main complications of bleeding is the massive loss of blood and erythrocytes in particular. These cells are formed in the bone marrow in a process known as erythropoiesis. It is a cellular system that is regulated by different mechanisms that ultimately control the production of RBCs production. One of these mechanisms is a protein called erythropoietin (EPO). It is a hormone that is released by the kidneys and stimulates the production of RBCs by increasing the survival and differentiation of CFU-E/ProEBs in the bone marrow. In order to study the regulation of RBCs production, we present a hybrid multiscale model of erythropoiesis and hemoglobin production. Erythropoiesis occurs in the bone marrow and is organized in multicellular structures called erythroblastic islands (EBI). These structures are composed by early and late erythroblasts as well as central macrophages. The most important cells in the regulation of erythropoiesis are the early erythroblasts or CFU-E/ProEBs. These cells have the possibility to auto-renew, differentiate into late erythroblasts or die by apoptosis. Hence, the choice of each action is regulated by a network or intracellular proteins whose concentrations depend on cytokines that diffuse in the extracellular matrix (ECM). To investigate the cellular dynamics of erythopoiesis following blood loss, we extend a previously developed hybrid discrete-continuous model of erythropoiesis [85] by including hemoglobin production the regulation of EPO release depending on the concentration of hemoglobin in the circulating RBCs. We also include the regulation of the release of EPO during anemia. It now depends on the difference between the present and needed hemoglobin levels. In this model, cells are considered to be individual agents that move, auto-renew, differentiate, or die by apoptosis. Their fate is determined by the concentration of intracellular and extracellular proteins. We show a screenshot of a model simulation in Fig. 1.6. The relationship between blood clotting and erythropoiesis includes other aspects such as the contribution of erythrocytes to the strength and resistance of the developed fibrin clot and to the viscosity of blood. These questions as well as others will not be investigated in this dissertation.

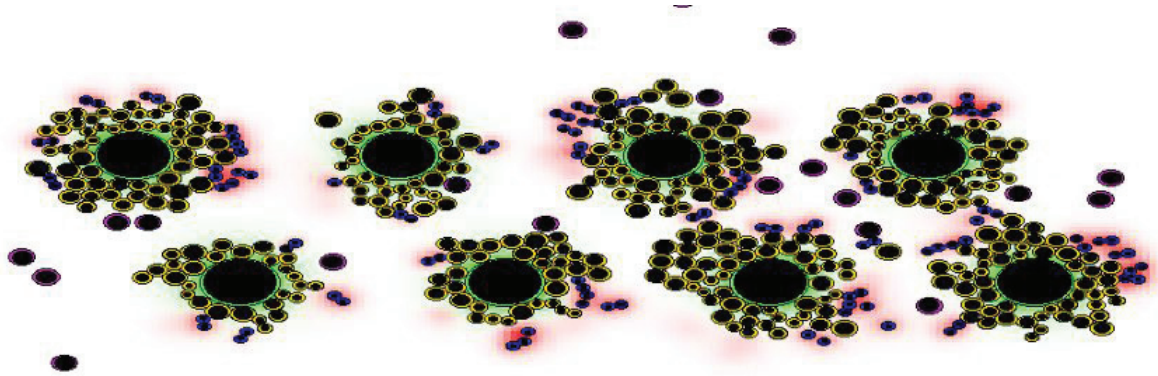

Figure 1.6: A screenshot from a numerical simulation of the erythropoiesis hybrid model showing the normal functioning of eight EBIs.

Multiple myeloma, its treatment, and their impact on erythropoiesis and blood clotting

Multiple myeloma (MM) is genetically complex cancer characterized by the infiltration of malignant plasma cells to the bone marrow. These cells proliferate excessively and perturb the functioning of the bone marrow multicellular systems such as erythropoiesis. MM cells also secrete apoptosis-inducing cytokines which further downregulate the production of red blood cells resulting in chronic anemia. MM is treated using chemotherapeutic agents that eliminate the malignant cells and restore the normal functioning of erythropoiesis and the other perturbed processes. However, these agents have a number of side effects such as increasing the risk of venous thrombosis. In this dissertation, we present a hybrid model of MM that focuses on the development of this disease and the intra-clonal heterogeneity that characterizes it. We also study its impact on erythropoiesis using the previously presented model of erythropoiesis. We introduce the effects of different treatment protocols on cells and reproduce the restoration of erythropoiesis as it was observed in clinical data. Ultimately, we quantify the effect of MM treatment on the risk of the incidence of thrombosis.

Multiscale modelling of HIV and its prothrombotic complications

Human immunodeficiency Virus (HIV) is a lentivirus that targets the human immune response by infecting various cells of the immune system such as $CD4^+$ T-cells, macrophages, and dendritic cells and destroys them. As a result, the production of $CD8^+$ T-cells (killer cells) is downregulated which ultimately results in the spread of the virus in bloodstream and the lymph nodes. To describe the dynamics of acute HIV infection, we first present a hybrid multiscale model of the immune response. The model describes the cell dynamics in the lymph node and the level of infection in blood at the same time. We then introduce the effect of HIV by introducing the virus cell-cell and cell-free infection mechanisms. We also quantify the viral load and number of healthy $CD4^+$ T-cell in blood during the infection. These outputs are then used to estimate the expression of TF by endothelial cells over time and predict the risk of thrombi incidence in HIV-infected patients.

1.4.3 Individualized blood coagulation models for the monitoring of anticoagulant therapy

The blood coagulation models presented in this dissertation contain a certain number of parameters that are different from one patient to another. These parameters include the composition of the blood plasma (concentrations of clotting factors and density of platelets), the levels of TF and TM expression, the type and diameter of the blood vessel, and the pressure of blood. The difference in these parameters from one patient to another can simply be due to the intervariability of patients' characteristics. However, it can also results from one or more of the bleeding and thrombotic risk factors observed in some patients. To assess the coagulability of blood and its predisposition to bleeding or overclotting, clinicians use *in vitro* diagnostic tests such as PT and INR. They also use these tests to monitor the administrated daily dose of these drugs. The advantage of such assays is that they can be used to evaluate the efficacy and safety of anticoagulant drugs during treatment. However, the conditions where these tests take place are different from the *in vivo* conditions where clot formation takes place. As a result, these tests are calibrated in order to correspond to the healthy normal individual patient. However, in patients with abnormal hemodynamics or who went through a major surgery, it is possible for to observe the incidence of thrombosis or bleeding even for patients with an INR in the normal range. To accurately diagnose the underlying mechanisms behind the persistence of thrombosis and bleeding when the INR is in the therapeutic window, we develop an individualized blood coagulation model of anticoagulant therapy. The model includes an individualized submodel of blood coagulation in *in vivo* conditions, coupled with a PK-PD submodel of two anticoagulant treatments that have different actions: warfarin and rivaroxaban, and another submodel describing the *in vitro* INR test. The resulting model provides the individual conditions where the persistence of thrombosis and bleeding can be observed depending on the INR as well as other parameters. It also represents a more reliable way than the INR test to predict the individual response of patients to different anticoagulant treatments.

1.4.4 Modelling methods: hybrid models

The dynamics of cell populations represent complex systems where mechanisms from different levels regulate their normal functioning. These levels include the intracellular, extracellular, and cell-cell regulations. In order to properly capture these different mechanisms and how they affect the global cell population, we use a hybrid discrete-continuous description where cells are represented by individual objects (spheres). Each cell has the possibility to grow, move, divide, and die by apoptosis. The fate of each cell depends on its interaction with the surrounding domain and with other cells. It is regulated by a network of intracellular proteins that depend on the local concentration of cytokines in the extracellular matrix. The motion of each cell i is described using the Newton's second law of mechanics:

$$m\ddot{x}_i + m\mu\dot{x}_i - F_i = 0,$$

where m is the mass of the cell, μ is the friction coefficient, F_i is the sum of the various forces applied on the cell such as chemoattraction, random perturbations, and contact with other cells. The fate of each cell is decided by rules set on the intracellular concentrations of different proteins inside it. In order to describe these concentrations over time, we use a system of ODEs:

$$\frac{dc^i_j}{dt} = \Psi^i_j(t, c^i_j, c^i_k, C_{ex}, ...),$$

where c^i_j is the intracellular concentration of the j-th intracellular protein in the i-th cell. $\Psi^i_j(t, c^i_j, c^i_k, C_{ex}, ...)$ is a reaction term that can depend on the concentration of other intacellular proteins (c^i_k) and extracellular cytokines C_{ex}. These concentrations can be described using PDEs of the form:

$$\frac{\partial C_{ex}}{\partial t} = D\Delta C_e x + K - \sigma C_e x,$$

where D is the diffusion coefficient, K is the production term and σ is the degradation rate. the values of intracellular cytokines determine the fate of each individual cell.

Chapter 2

Mathematical Modelling of the Chemical Kinetics of Blood Clotting and the Dynamics of Clot Growth in Quiescent Plasma

2.1 A mathematical model of the coagulation cascade

2.1.1 Biological background

Blood coagulation is a defensive mechanism that allows the organism to preserve hemostasis. Among various blood factors, thrombin plays a particularly important role in blood coagulation by converting fibrinogen into fibrin polymer in an enzymatic reaction. The generation of thrombin in blood plasma occurs upon the activation of the factors IX and X by tissue factor (TF) located at the outer surface of endothelial cells. In normal situations it interacts with blood plasma in the case of an injury. There are also various pathological situations where it is involved and initiates blood coagulation (thrombosis, inflammation, cancer, etc.). Once activated, the thrombin production can be continued in a self-sustained manner due to a positive feedback but it can also be inhibited by other factors such as antithrombin and activated protein C (APC). In this chapter, we present a mathematical model of blood coagulation describing the kinetics of the blood clotting process using partial differential equations (PDEs). The model captures the essential dynamics of blood coagulation and can be used to model blood clotting in a spatial context. Then, we use the model to study clot growth in quiescent plasma. We observe the existence of three different regimes of clot growth depending on the choice of parameters.

2.1.2 Model formulation

We present the equations for the main blood factors participating in coagulation reactions. Let v be the flow velocity and D the diffusion coefficient:

Prothrombin (P)

We consider a first-order reaction for conversion of prothrombin into thrombin:

$$\frac{\partial P}{\partial t} + \nabla.(vP) = D\Delta P - \Phi(T, B_a, C_a)P, \tag{2.1.1}$$

Since prothrombin is abundantly present in blood plasma under normal conditions, we use the initial condition $P = P_0$. We also prescribe the boundary condition of $P = P_0$ at the left boundary. Zero flux

condition is applied the other boundaries. The coefficient $\Phi(T,B_a,C_a)$ of the reaction rate depends on the concentrations of thrombin T, IXa and Xa (B_a) as well as the activated protein C (C_a) (see below).

Thrombin (T)

Equation for thrombin

$$\frac{\partial T}{\partial t} + \nabla.(vT) = D\Delta T + \Phi(T,B_a,C_a)P - k_4 TA, \tag{2.1.2}$$

contains a similar production term and a degradation term. Thrombin forms a complex with antithrombin A that inhibits the conversion of prothrombin into thrombin. We consider k_a to be the rate of this reaction. We use zero flux conditions at all boundaries, ($\frac{\partial T}{\partial n} = 0$, where n is the outer normal vector).

The function $\Phi(T,B_a,C_a)$ is given by the following expression:

$$\Phi(T,B_a,C_a) = k_2 B_a + \frac{k_3 T^m}{1+k_8 C_a} \tag{2.1.3}$$

The initiation phase corresponds to the first term in the right-hand side of this expression. It describes conversion of prothrombin into thrombin due to factors IXa and Xa. In the initiation phase, active factors IX and X are responsible of the initiation of the blood coagulation cascade.

In the amplification phase, thrombin upregulates the activation of the factors V, VIII and XI and accelerates its own production through these factors [86]. Therefore, the second term in the expression for F is proportional to the T^m where we set $m = 3$ according to the number of upregulating factors.

Activated protein C (APC) donwregulates the production of thrombin through factor V. In order to specify its action, let us consider the reversible reaction $V \rightleftharpoons V_a$. We have:

$$\frac{\partial V_a}{\partial t} = k_V^+ V - k_V^- V_a, \quad \frac{\partial V}{\partial t} = -k_V^+ V + k_V^- V_a, \tag{2.1.4}$$

Hence, $V_a + V = V^0$ where V^0 is the initial concentration of factor V. Under the assumption of the detailed equilibrium:

$$V_a = k_V V = k_V (V^0 - V_a), \tag{2.1.5}$$

where $k_V = k_V^+ / k_V^-$. Then

$$V_a = \frac{k_V V^0}{1+k_V} = \frac{k_V^+ V^0}{k_V^- + k_V^+} \tag{2.1.6}$$

We suppose that the rate of the inverse reaction is proportional to the concentration of activated protein C, $k_V^- = k_V^0 C_a$. Then

$$V_a = \frac{k_V^+ V^0}{k_V^0 C_a + k_V^+} = \frac{V^0}{1+k_5 C_a} \tag{2.1.7}$$

where $k_5 = k_V^0 / k_V^+$. This gives us the expression (2.1.3).

Antithrombin (A)

Antithrombin is a protein that inactivates several enzymes in the coagulation system [87]. We suppose for simplicity that antithrombin inactivates directly thrombin T:

$$\frac{\partial A}{\partial t} + \nabla.(vA) = D\Delta A - k_4 AT - k_5 AB. \tag{2.1.8}$$

Antithrombin is released in blood plasma. Hence, as the initial condition we consider $A = A_0$ in the entire domain.

Factors IX and X and their active forms IXa and Xa

The factors IX and X are activated into IXa and Xa by the complex of tissue factor and factor VIIa ($T_F VIIa$) which is present on damaged endothelial cells [88]. Since both factors act in a similar way, we consider their total concentration and denote by B their inactive and by B_a their activated form:

$$\frac{\partial B}{\partial t} + \nabla.(vB) = D\Delta B, \tag{2.1.9}$$

$$\frac{\partial B_a}{\partial t} + \nabla.(vB_a) = D\Delta B_a - k_5 A B_a. \tag{2.1.10}$$

We use zero flux boundary condition at the intact boundaries (undamaged wall), $\frac{\partial B_a}{\partial n} = 0$. At the damaged endothelial tissue, the boundary condition describes the activation of factors IX and X by the complex of activated tissue factor and VIIa denoted by T_F^*:

$$\frac{\partial B}{\partial n} = -k_f^+ B(T_F^* - [T_F^* B]), \quad \frac{\partial B_a}{\partial n} = k_f^- [T_F^* B], \tag{2.1.11}$$

where $[T_F^* B]$ denotes the surface complex of T_F^* and B. The first equation in (2.1.11) shows that the influx of B from the volume to the wall is proportional to its concentration in the volume and to available sites at the wall. The flux of the activated factor B_a from the wall is proportional to the surface concentration of the complex $[T_F^* B]$.

We have further

$$\frac{\partial [T_F^* B]}{\partial t} = k_f^+ B(T_F^* - [T_F^* B]) - k_f^- [T_F^* B]. \tag{2.1.12}$$

If the constants k_f^+ and k_f^- are large, then we can use the detailed equilibrium:

$$k_f^+ B(T_F^* - [T_F^* B]) = k_f^- [T_F^* B]. \tag{2.1.13}$$

Then

$$[T_F^* B] = \frac{k_f B T_F^*}{1 + k_f B}, \tag{2.1.14}$$

where $k_f = k_7^+ / k_f^-$. From (2.1.12), (2.1.13) and the last equation we obtain:

$$\frac{\partial B}{\partial n} = -k_f^- \frac{k_f B T_F^*}{1 + k_7 B}, \quad \frac{\partial B_a}{\partial n} = k_f^- \frac{k_f B T_F^*}{1 + k_f B}, \tag{2.1.15}$$

We consider a variable $B^0 = B + B_a$. From equations (8.3.31) and (2.1.10) and the boundary conditions given in the last equation we have:

$$\frac{\partial B^0}{\partial t} + \nabla.(vB^0) = D\Delta B^0, \quad \frac{\partial B^0}{\partial n} = 0. \tag{2.1.16}$$

Then B^0 is a constant solution that can be determined from the initial concentration of B. Therefore, $B = B^0 - B_a$ and we rewrite the boundary condition in terms of B_a:

$$\frac{\partial B_a}{\partial n} = \frac{\alpha_1 (B^0 - B_a)}{1 + \beta_1 (B^0 - B_a)}, \tag{2.1.17}$$

where $\alpha_1 = k_f^- k_f T_F^*$ and $\beta_1 = k_f$. We prescribe zero flux conditions for B_a at the intact surfaces. The closed problem for B_a consists of both equation (2.1.10) and the boundary condition (2.1.17).

Let us not that if we take into account the deactivation of B_a, then equations (8.3.31), (2.1.10) become as follows:

$$\frac{\partial B}{\partial t} + \nabla.(vB) = D\Delta B + k_b B_a, \quad \frac{\partial B_a}{\partial t} + \nabla.(vB_a) = D\Delta B_a - k_5 A B_a. \tag{2.1.18}$$

The derivation of the boundary condition in this case remains the same as before.

Protein C and its active form C_a

We consider the following equation for the protein C and the activated protein C (APC) whose concentration is denoted by C_a:

$$\frac{\partial C}{\partial t} + \nabla.(vC) = D\Delta C, \tag{2.1.19}$$

$$\frac{\partial C_a}{\partial t} + \nabla.(vC_a) = D\Delta C_a. \tag{2.1.20}$$

The fluxes at the undamaged endothelial surface of both protein C and its active form are given by the following expressions:

$$\frac{\partial C}{\partial n} = -k_c^+ C((TT_m) - (CTT_m)), \quad \frac{\partial C_a}{\partial n} = k_c^-(CTT_m), \tag{2.1.21}$$

where T_m is the concentration of thrombomodulin present on undamaged surfaces [89]. Thrombomodulin forms a complex with thrombin (TT_m) which activates protein C. Protein C arrives next to form the complex (CTT_m). Here k_8^+ is the reaction rate constat of protein C activation by the complex of thrombin and thrombomodulin, while k_c^- is the reaction rate of the inverse reaction. As before, we obtain:

$$\frac{\partial C_a}{\partial n} = \frac{\alpha_2(C^0 - C_a)(TT_m)}{1 + \beta_2(C^0 - C_a)}\,. \tag{2.1.22}$$

where $\alpha_2 = k_8^+/k_8^-$ and $\beta_2 = k_8^- k_9$. In order to determine the value of (TT_m), let us consider the equation for its surface concentration:

$$\frac{\partial (TT_M)}{\partial t} = k_T^+(T_M - (TT_M))T - k_T^-(TT_M). \tag{2.1.23}$$

From the detailed equilibrium, we obtain the expression for the concentration of the complex (TT_m):

$$(TT_m) = k_T \frac{TT_m}{1 + k_T T}, \tag{2.1.24}$$

where k_T is the reaction rate of thrombin binding with thrombomodulin at the intact surfaces. We obtain a closed problem for C_a with equation (2.1.20) and the boundary conditions (2.1.22) and (2.1.24).

Fibrinogen (F_g)

Fibrinogen is a protein produced by the liver. Fibrinogen (F_g) is converted into fibrin (F) by thrombin (T). For simplicity, we suppose that the reaction rate of fibrinogen conversion to fibrin is linear: $k_1(T) = k_1 T$. We use the following equation to describe the fibrinogen concentration:

$$\frac{\partial F_g}{\partial t} + \nabla.(vF_g) = D\Delta F_g - -\frac{k_6 T F_g}{K_6 + F_g}, \tag{2.1.25}$$

The initial conditions are $F_g = F_{g0}$ in the entire domain since fibrinogen is present in blood plasma. We use a similar Dirichlet condition at the entrance of the vessel (left boundary).

Fibrin (F)

Fibrin is a protein that is formed upon the conversion of fibrinogen by thrombin. When polymerized, it forms a hemostatic plug together with platelets. Its concentration is described by the following equation:

$$\frac{\partial F}{\partial t} + \nabla.(vF) = D\Delta F + \frac{k_6 T F_g}{K_6 + F_g} - k_7 F. \tag{2.1.26}$$

Zero flux boundary conditions for fibrin are imposed at all boundaries.

Fibrin polymer (F_p)

Fibrin polymer forms a solid clot, thus its diffusion and convection should be omitted:

$$\frac{\partial F_p}{\partial t} = k_7 F, \tag{2.1.27}$$

2.2 The regimes of blood clotting in quiescent plasma

We consider a two-dimensional rectangular domain corresponding to a section of a blood vessel (Fig. 4.1). Blood flow crosses the domain along the axial direction. A part of the vessel boundary secretes tissue factor (damaged wall) and initiates blood coagulation.

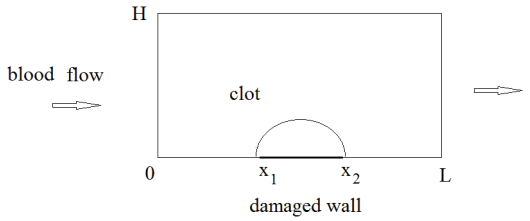

Figure 2.1: A schematic representation of the computational domain. It corresponds to a section of a blood vessel. A part of the lower boundary (damaged wall) initiates the clot growth.

We study the dynamics of clot growth in this domain in absence of blood flow ($v = 0\ mm/s$). The exposed tissue factor at the damaged part of the wall leads to the activation of factors IX and X. They diffuse in the blood plasma and initiate the production of thrombin. Thrombin stimulates the conversion of fibrinogen into fibrin and subsequently to fibrin polymer which forms the fibrin clot. We observe three different regimes of blood clot growth.

2.2.1 Initiation without propagation

The production of thrombin is self-accelerated through a feedback process. In the model considered here we suppose that the rate of thrombin production depends on its own concentration. On the other hand, thrombin production is inhibited by antithrombin. If the concentration of antithrombin is sufficiently high, then the thrombin concentration remains low, and only a small amount of fibrin polymer is produced. As a result we obtain a small clot localized near the vessel wall (not shown). This regime of clot growth corresponds to the initiation without propagation.

2.2.2 Initiation with propagation (thrombosis)

If the concentration of antithrombin is sufficiently low and the concentration of tissue factor at the wall is sufficiently high, then the concentration of thrombin produced near the vessel wall during the initiation stage is large enough to initiate the self-sustained propagation (Fig. 2.2). It propagates in the form of a travelling wave. The initiation without propagation or with an insufficient speed of propagation is observed in the hemophilic plasma [117]. The speed of the reaction diffusion wave of blood coagulation is studied in [90].

Under the normal physiological conditions, the role of antithrombin is to prevent the spontaneous coagulation. However, antithrombin should not stop the propagation stage because it is essential for the clot formation. Therefore, there should exist other mechanisms which limit the clot growth in the regime of its propagation. One such mechanism is based on the activation of protein C which inhibits production of thrombin.

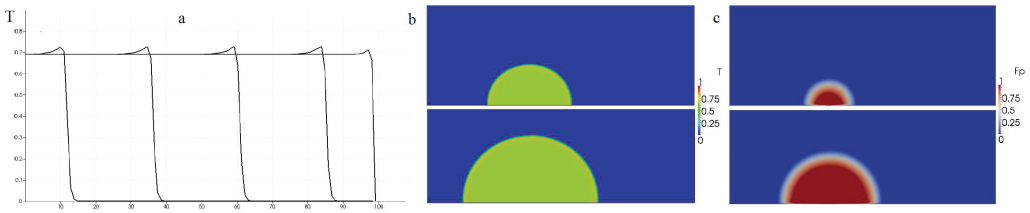

Figure 2.2: The initiation with propagation. Thrombin is produced in a self-sustained way and propagates as a travelling wave. Its concentration in the vertical cross section is shown in the left image. This wave is followed by the production of fibrin polymer. Snapshots of thrombin (middle) and of fibrin polymer (right) at $t = 60$s and $t = 100$s.

2.2.3 Clot growth arrest by activated protein C

If the concentration of antithrombin is sufficiently low and the concentration of tissue factor at the wall is sufficiently high, then the concentration of thrombin produced near the vessel wall during the initiation stage is large enough to initiate the self-sustained propagation (Fig. 2.2). It propagates in the form of a travelling wave. The initiation without propagation or with an insufficient speed of propagation is observed in the hemophilic plasma [117]. The speed of the reaction diffusion wave of blood coagulation is studied in [90].

Under the normal physiological conditions, the role of antithrombin is to prevent the spontaneous coagulation. However, antithrombin should not stop the propagation stage because it is essential for the clot formation. Therefore, there should exist other mechanisms which limit the clot growth in the regime of its propagation. One such mechanism is based on the activation of protein C which inhibits production of thrombin.

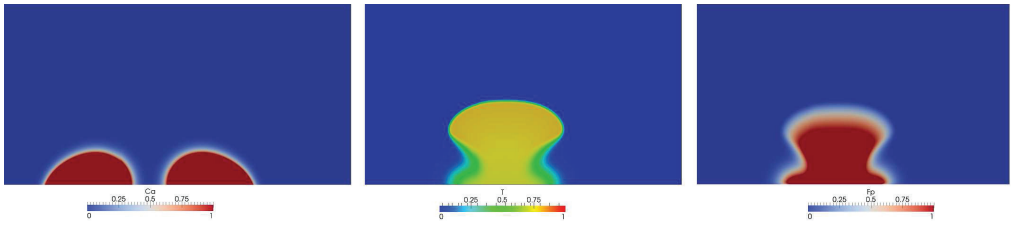

Figure 2.3: The propagation with a partial inhibition by APC. Snapshots of concentration distributions: APC (left), thrombin (middle), fibrin polymer (right).

It is important to note that the activation of protein C occurs at the normal (undamaged) vessel wall. Activated protein C diffuses in the bulk flow from the sides of the injury and limits its growth both in the axial direction and in the direction perpendicular to the wall. However, if the injury (damaged wall) is large enough, then APC will not be able to diffuse far enough inside the region of thrombin production and to stop its propagation (Fig. 2.3). Hence, we can observe a complete or a partial inhibition by APC. In the second case the clot continues to grow (Fig. 2.3, cf. [60]).

2.2.4 Conclusions

Modelling the blood coagulation cascade is complex and requires considering several assumptions. In the model presented in this chapter, we have introduced few simplifications to the complete coagulation cascade to develop a model which captures the important mechanisms of the clotting process. In this context, the effect of some factors such as factor V and VIII is taken implicitly through the term k_3T^3 which represents the amplification phase in the cascade. This is a valid simplification provided that we determine the value of the parameter k_3 which corresponds to the kinetic rate of an unreal reaction. Other simplifications made to the model include neglecting the effects of tissue factor pathway inhibitor

(TFPI), a protein which inhibits factor VII and that can be taken into consideration implicitly through the choice of parameters.

Numerical simulations have shown the existence of three regimes of thrombus formation in quiescent plasma depending on the physical and physiological conditions. While the absence of the clot propagation corresponds to the normal functioning of the clotting mechanism, a thrombin wave that is not stopped results in an exaggerated formation of the thrombus leading to the complete occlusion of the vessel. This corresponds to thrombosis which forms when one or more of the anticoagulant mechanisms is impaired. Until now, we have shown how antithrombin and activated protein C are two important mechanisms that contribute to clot growth arrest.

2.3 The speed of thrombin wave propagation

2.3.1 Biological background

The main function of the coagulation system is terminating bleeding, caused by the vessel wall damage by covering the injury site with a fibrin clot. The reaction of fibrin polymerization appears at the final stage of the proteolytic enzymatic cascade where the activated clotting factors act as catalysts for activation of the others [91, 92].

Formation of thrombin appears due to the prothrombin activation in the coagulation cascade. The process can be launched by the tissue factor expressed to the blood flow in case of the endothelium rupture (extrinsic pathway), or through the activation of factor XII which triggers activation of factor XI in case of the contact with the foreign surface (intrinsic pathway) [92, 93, 94]. Both pathways lead to the activation of factor X that contributes to the prothrombin conversion to thrombin [92]. Once the thrombin concentration reaches the threshold value, further prothrombin activation takes place due to the positive feedback loops of the coagulation cascade [93, 92, 95] (Fig. 2.4).

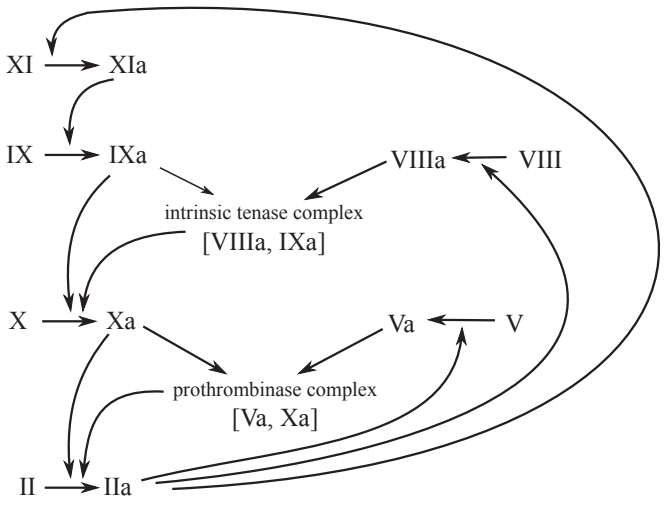

Figure 2.4: The main activation reactions of the intrinsic pathway of the coagulation cascade. Thrombin (IIa) catalyzes activation of factors V, VIII, XI; factors XIa and IXa catalyze activation of factors IX and X respectively; factors VIIIa and Va form active complexes with factors IXa and Xa respectively and further increase thrombin production.

In our work we focus on the detailed theoretical investigation of the mathematical model of the amplification phase of blood coagulation in plasma (Section 2). We derive conditions on the existence and stability of the traveling wave solutions (Section 3) and demonstrate an important property of their speed of propagation (Section 4). The speed of thrombin propagation in mathematical models is usually measured according to the results of the computational simulations [36, 100, 101] or using the combination of analytical and numerical approaches as it was done in [102]. In Section 5 of the current work

we propose an alternative approach and derive theoretical estimates for the speed of the thrombin wave propagation by the reduction of the initial system to the single equation on thrombin concentration. We compare the analytical estimates with computed values of the speed as well as with the experimental data.

2.3.2 Mathematical model

We consider the simplified model of the propagation stage of coagulation cascade. Main reactions of the intrinsic cascade depicted in Fig. 2.4 can be modeled with the following system of the reaction-diffusion equations:

$$\begin{aligned}
\frac{\partial T}{\partial t} &= D\Delta T + \left(k_2 U_{10} + \overline{k_2}\frac{k_{510}}{h_{510}} U_{10}U_5\right)\left(1 - \frac{T}{T_0}\right) - h_2 T,\\
\frac{\partial U_5}{\partial t} &= D\Delta U_5 + k_5 T - h_5 U_5,\\
\frac{\partial U_8}{\partial t} &= D\Delta U_8 + k_8 T - h_8 U_8,\\
\frac{\partial U_9}{\partial t} &= D\Delta U_9 + k_9 U_{11} - h_9 U_9,\\
\frac{\partial U_{10}}{\partial t} &= D\Delta U_{10} + k_{10} U_9 + \overline{k_{10}}\frac{k_{89}}{h_{89}} U_9 U_8 - h_{10} U_{10},\\
\frac{\partial U_{11}}{\partial t} &= D\Delta U_{11} + k_{11} T - h_{11} U_{11}.
\end{aligned} \tag{2.3.28}$$

Here T, U_i denote the concentrations of thrombin and activated forms of the i-th factor respectively, T_0 denotes the initial prothrombin concentration. First term of each equation corresponds to the diffusion of the factors in blood plasma while other terms describe chemical reactions of the coagulation cascade. Since concentrations of precursors are rather high we consider activation reactions as quasi-first order reactions with rate constants $k_i, \overline{k_i}$. Similarly, we assume concentration of plasma inhibitors such as antithrombin to be high enough and take the rates of inhibition reactions to be constant and equal h_i. System 4.1.2 is derived from the previously published model [103] under additional assumptions considered in 7.1.

In the current study we focus on the amplification stage of the coagulation cascade and thus suppose the initial amount of activated factors to be formed in the proximity of the vessel wall. Therefore we use step functions of thrombin and activated factor concentrations as initial conditions for the simulation. In order to take into account the activation of factor XI by factor XIIa we take constant influx boundary condition on the left side of the domain and zero-flux boundary conditions on the right side.

2.3.3 Existence and stability of the traveling wave solutions

Let us set $u = (T, U_5, U_8, U_9, U_{10}, U_{11})$. Then system 4.1.2 can be written in the vector form:

$$\frac{\partial u}{\partial t} = D\Delta u + F(u), \tag{2.3.29}$$

where $F = (F_1, ..., F_6)$ is the vector of reaction rates in equations 4.1.2. It satisfies the following property:

$$\frac{\partial F_i}{\partial u_j} \geq 0, \ \forall i \neq j.$$

This class of systems is called monotone systems and has a number of properties similar to those for one scalar equation including the maximum principle. It allows the proof of existence and stability of the wave solutions for monotone systems as well as the estimation of the wave propagation speed [104]. In order to apply these results to the considered system describing intrinsic pathway functioning we start with the analysis of the existence and stability of the stationary points of system 4.1.2.

Stationary points of the kinetic system

Consider the system of ordinary differential equations:

$$\frac{du}{dt} = F(u). \tag{2.3.30}$$

Its equilibrium points satisfy the following relations:

$$U_5 = \frac{k_5}{h_5}T,\ U_8 = \frac{k_8}{h_8}T,\ U_{11} = \frac{k_{11}}{h_{11}}T,\ U_9 = \frac{k_9 k_{11}}{h_9 h_{11}}T, \tag{2.3.31}$$

$$U_{10} = \frac{k_9 k_{11}}{h_{10}h_9 h_{11}}\left(k_{10}T + \overline{k_{10}}\frac{k_{89}}{h_{89}}T^2\right), \tag{2.3.32}$$

where T is a solution of the equation $P(T) = 0$. Here $P(T) = aT^4 + bT^3 + cT^2 + dT$,

$$a = \frac{\overline{k_{10}}k_{89}k_8\overline{k_2}k_5k_{510}k_9k_{11}}{h_{89}h_8h_5h_{10}h_{510}h_9h_{11}},\quad d = -\frac{k_2k_{10}k_9k_{11}}{h_9h_{11}h_{10}} + h_2T_0,$$

$$b = -\frac{\overline{k_{10}}k_{89}k_8\overline{k_2}k_5k_{510}k_9k_{11}}{h_{89}h_8h_5h_{10}h_{510}h_9h_{11}}T_0 + \frac{k_{10}\overline{k_2}k_5k_{510}k_9k_{11}}{h_5h_{10}h_{510}h_9h_{11}} + \frac{\overline{k_2k_{10}}k_{89}k_8k_9k_{11}}{h_{89}h_8h_9h_{11}},$$

$$c = -\frac{k_{10}\overline{k_2}k_5k_{510}k_9k_{11}}{h_5h_{10}h_{510}h_9h_{11}}T_0 + \frac{k_2k_{10}k_9k_{11}}{h_9h_{11}} - \frac{k_2k_{89}k_8k_9k_{11}}{h_{89}h_8h_9h_{11}h_{10}}T_0.$$

Hence, the stationary points of system 2.3.30 can be found through the stationary points T^* of the equation

$$\frac{dT}{dt} = -P(T), \tag{2.3.33}$$

and equalities 2.3.31, 2.3.32.

Let us determine the number of positive roots of the polynomial $P(T)$. We set $P(T) = TQ(T)$, where $Q(T) = aT^3 + bT^2 + cT + d$. The number of positive roots of $Q(T)$ can be found as follows. First, we consider a function $Q'(T) = 3aT^2 + 2bT + c$. If it has no zeros, then $Q(T)$ is increasing and has one positive root if and only if $Q(0) < 0$. Otherwise, we denote by T_1, T_2 the nonzero solutions of the equation $Q'(T) = 0$: $T_{1,2} = (-b \pm \sqrt{b^2 - 3ac})/(3a)$. Then, the polynomial $Q(T)$ has one positive root in one of the cases:

- $T_1 \le 0,\ Q(0) < 0,$
- $0 \le T_1 < T_2,\ Q(0) < 0$ and $Q(T_1) > 0,\ Q(T_2) > 0$ or $Q(T_1) < 0,$
- $Q(0) > 0,\ Q(T_1) > 0,\ Q(T_2) = 0,$

and it has two positive roots if $0 < T_2,\ Q(0) > 0,\ Q(T_2) < 0$ or $Q(0) < 0,\ Q(T_2) = 0$.

Stability of the stationary points of system 2.3.30 can be determined from stability of the stationary points of equation 2.3.33. The following theorem holds (see Appendix B for the proof).

Theorem 1. *There is one to one correspondence between stationary solutions $u^* = (T^*, U_5^*, U_8^*, U_9^*, U_{10}^*, U_{11}^*)$ of system 4.1.2 and the stationary points T^* of equation 2.3.33 given by 2.3.31, 2.3.32. The principal eigenvalue of the matrix $F'(u^*)$ is positive (negative) if and only if $P'(T^*) < 0$ ($P'(T^*) > 0$).*

Thus, we can make the following conclusions about the existence and stability of stationary points of the kinetic system of equation 2.3.30. It always has a trivial solution $u^* = 0$. It has one (two) positive solution if and only if the polynomial $P(T)$ has one (two) positive root(s). A positive solution u^* is stable if and only if $P'(T^*) > 0$.

Remark. T^* is always less than T^0. Indeed, let us denote by $P^0(T)$ the polynomial $P(T)$ for $h_2 = 0$. It is easy to check that $T = T^0$ is the largest root of $P^0(T)$. Thus, $P^0(T^0) = 0,\ P^{0\prime}(T^0) \le 0$ and for any $T^{**} > T^0$ we get $P^0(T^{**}) < 0$ and subsequently $P(T^{**}) < 0$ for any positive h_2. Thus, largest stable equilibrium point of system 4.1.2 is less than T_0 and starting from initial conditions below this value, first component of system 4.1.2 will remain less than T^0.

Wave existence and stability

We can now formulate a theorem on the existence of the traveling wave solutions in system 4.1.2.

Theorem 2. *Suppose that $P(T^*) = 0$ for some $T^* > 0$ and $P'(0) \neq 0$, $P'(T^*) \neq 0$. Let $u^* = (T^*, U_5^*, U_8^*, U_9^*, U_{10}^*, U_{11}^*)$ be the corresponding stationary solutions of system 2.3.30 determined by relations 2.3.31, 2.3.32.*

- *Monostable case. If there are no other positive roots of the polynomial $P(T)$, then system 4.1.2 has monotonically decreasing traveling wave solutions $u(x,t) = w(x-ct)$ with the limits $u(+\infty) = 0, u(-\infty) = u^*$ for all values of the speed c greater than or equal to the minimal speed c_0,*
- *Bistable case. If there is one more positive root of the polynomial $P(T)$ in the interval $0 < T < T^*$, then system 4.1.2 has a monotonically decreasing traveling wave solutions $u(x,t) = w(x-ct)$ with the limits $u(+\infty) = 0, u(-\infty) = u^*$ for a unique value of c.*

The proof of Theorem 2 follows from the general results on the existence of waves for monotone systems of equation [104, 105]. Let us note that the conditions on the stability of stationary points follow from the assumption of Theorem 2 and Theorem 1. We have $P'(T^*) > 0$ in both cases since it is the largest root of the polynomial increasing at infinity. The sign of $P'(0)$ is negative if there is no other root of $P(T)$ in between of 0 and T^* and the sign is positive if $P(T)$ has one more root.

Monotone traveling wave solutions of monotone systems are asymptotically stable [104, 105] that gives global stability in the bistable case. In the monostable case the wave is globally stable for the minimal speed c_0 and stable with respect to small perturbations in a weighted norm for $c > c_0$ [105].

The unique wave speed in the bistable case and the minimal wave speed in the monostable case admit minimax representations. Below we use such representations for the bistable system since this case is more appropriate for the applications considered in the current work. Indeed, traveling wave solution of system 4.1.2 describes propagation of the thrombin concentration in blood plasma due to the reactions of the coagulation cascade. In this system the convergence to the traveling wave solution takes place only if the initial concentrations of blood factors exceed some critical level, otherwise the clot formation does not start because of the action of plasma inhibitors. This dependency on the initial conditions and stability of zero solution correspond to the bistable case. In the monostable case, on the contrary, any small perturbation would result in the solution converging to the propagating wave. In terms of the coagulation system functioning, monostable case corresponds to the spontaneous disseminated coagulation blocking blood circulation.

Finally, let us note that in Theorem 2 we consider only the case of a single positive root of the polynomial and the case of two positive roots. If $P(T)$ has three positive roots the system would be monostable with a stable intermediate stationary point. While this case is interesting from the point of view of wave existence and stability, it is less relevant for the modeling of blood coagulation, and we will not discuss it here.

2.3.4 Speed of wave propagation

One of the main objectives of this work is to obtain an analytical approximation of the wave speed for the blood coagulation model 4.1.2. We proceed in two steps. First, we reduce system 4.1.2 to a single equation and justify this reduction. Then, we obtain some estimates of the wave speed for one reaction-diffusion equation.

System reduction

In order to simplify the presentation, we describe the method of reduction for the system of two equations:

$$u'' + cu' + f(u,v) = 0, \tag{2.3.34}$$

$$v'' + cv' + \frac{1}{\varepsilon}(au - bv) = 0, \tag{2.3.35}$$

where ε is a small parameter, $\dfrac{\partial f}{\partial v} > 0$ and system 2.3.34–2.3.35 is bistable. If we multiply the second equation by ε and take a formal limit as $\varepsilon \to 0$, then we have $v = \dfrac{a}{b}u$, and the first equation can be rewritten as follows:

$$u'' + cu' + f\left(u, \frac{a}{b}u\right) = 0. \tag{2.3.36}$$

Let us recall that the value of the speed $c = c_\varepsilon$ in system 2.3.34–2.3.35 and $c = c_0$ for the scalar equation 2.3.36 are unknown, and in general they are different from each other. We will demonstrate that $c_\varepsilon \to c_0$ as $\varepsilon \to 0$:

Theorem 3. *The speed of wave propagation for system 2.3.34–2.3.35 converges to the speed of the wave propagation for equation 2.3.36 as* $\varepsilon \to 0$.

Singular perturbations of traveling waves are extensively studied in [104]. Here we present another method of proof based on the estimates of the wave speed. This method is simpler and gives not only the limiting value of the speed for $\varepsilon = 0$ but also the estimates of the speed value for any positive ε. In the following sections we describe the approach in details and construct the wave speed estimates for system 2.3.34–2.3.35.

Wave speed estimate

We get the following estimates from the minimax representation of the wave speed in the bistable case [105] :

$$\min\left(\inf_x S_1(\rho), \inf_x S_2(\rho)\right) \le c \le \max\left(\sup_x S_1(\rho), \sup_x S_2(\rho)\right), \tag{2.3.37}$$

where

$$S_1(\rho) = \frac{\rho_1'' + f(\rho_1, \rho_2)}{-\rho_1'}, \quad S_2(\rho) = \frac{\rho_2'' + (a\rho_1 - b\rho_2)/\varepsilon}{-\rho_2'},$$

$\rho = (\rho_1, \rho_2)$ is an arbitrary test function continuous together with its second derivatives, monotonically decreasing (component-wise) and having the same limits at infinity as the wave solution, $\rho(+\infty) = 0$, $\rho(-\infty) = u^*$.

Let us choose the following test functions:

$$\rho_1 = u_0, \quad \rho_2 = \frac{a}{b}u_0 - \varepsilon f\left(u_0, \frac{a}{b}u_0\right)\frac{a}{b^2}, \tag{2.3.38}$$

where u_0 is the solution of 2.3.36. Neglecting the second-order terms with respect to ε, we get:

$$S_1(\rho) = \left(u_0'' + f\left(u_0, \frac{a}{b}u_0 - \varepsilon\frac{a}{b^2}f\left(u_0, \frac{a}{b}u_0\right)\right)\right)/(-u_0') = \\ \left(u_0'' + f\left(u_0, \frac{a}{b}u_0\right) - \varepsilon\frac{a}{b^2}f_v\left(u_0, \frac{a}{b}u_0\right)f\left(u_0, \frac{a}{b}u_0\right)\right)/(-u_0') = c_0 + \varepsilon\varphi(x), \tag{2.3.39}$$

where

$$\varphi(x) = \frac{a}{b^2u_0'}f_v\left(u_0, \frac{a}{b}u_0\right)f\left(u_0, \frac{a}{b}u_0\right),$$

and c_0 is the value of the speed in 2.3.36. Next,

$$S_2(\rho) = \frac{u_0'' + f\left(u_0, \frac{a}{b}u_0\right) - \frac{\varepsilon}{b}\left(f\left(u_0, \frac{a}{b}u_0\right)\right)''}{-u_0' + \frac{\varepsilon}{b}\left(f\left(u_0, \frac{a}{b}u_0\right)\right)'} = c_0 + \varepsilon\psi(x), \tag{2.3.40}$$

where

$$\psi = \frac{c_0}{bu_0'}\left(f\left(u_0, \frac{a}{b}u_0\right)\right)' + \frac{1}{bu_0'}\left(f\left(u_0, \frac{a}{b}u_0\right)\right)''.$$

Hence, from 2.3.39, 2.3.40 we obtain the estimate

$$c_0 + \varepsilon \max\left\{\min_x \varphi, \min_x \psi\right\} \le c \le c_0 + \varepsilon \min\left\{\max_x \varphi, \max_x \psi\right\}, \tag{2.3.41}$$

where c_0 is the wave propagation speed for 2.3.36, functions $\varphi(x)$, $\psi(x)$ are bounded. The proof of Theorem 3 follows from this estimate.

2.3.5 One equation model

Reduction to the equation on thrombin concentration

If the reaction rate constants in the equations of system 4.1.2 describing dynamics of variables U_9, U_{10}, U_5 and U_8 are sufficiently large, then we can replace these equations by the following algebraic relations (Section 4.1):

$$U_5 = \frac{k_5}{h_5}T,\ U_8 = \frac{k_8}{h_8}T,\ U_9 = \frac{k_9}{h_9}U_{11},\ U_{10} = U_{11}\frac{k_9}{h_9 h_{10}}\left(k_{10} + \frac{\overline{k_{10}}k_{89}}{h_{89}}\frac{k_8}{h_8}T\right).$$

Then, instead of system 4.1.2 we obtain the following system of two equations:

$$\begin{aligned}
\frac{\partial T}{\partial t} &= D\Delta T + U_{11}\frac{k_9}{h_9 h_{10}}\left(k_{10} + \frac{\overline{k_{10}}k_{89}}{h_{89}}\frac{k_8}{h_8}T\right)\left(k_2 + \frac{\overline{k_2}k_{510}}{h_{510}}\frac{k_5}{h_5}T\right)\left(1 - \frac{T}{T_0}\right) - h_2 T,\\
\frac{\partial U_{11}}{\partial t} &= D\Delta U_{11} + k_{11}T - h_{11}U_{11}.
\end{aligned} \tag{2.3.42}$$

Similarly, we can reduce this system to the single equation:

$$\frac{\partial T}{\partial t} = D\Delta T + \frac{k_9 k_{11}}{h_9 h_{10} h_{11}}T\left(k_{10} + \frac{\overline{k_{10}}k_{89}}{h_{89}}\frac{k_8}{h_8}T\right)\left(k_2 + \frac{\overline{k_2}k_{510}}{h_{510}}\frac{k_5}{h_5}T\right)\left(1 - \frac{T}{T_0}\right) - h_2 T. \tag{2.3.43}$$

We realize this reduction in two steps in order to compare the one-equation model to system 4.1.2 as well as to the intermediate model of two equations 2.3.42. Numerical simulations show that for the values of parameters in the physiological range [4, 36], all three models give the wave speed of the same order of magnitude (Fig. 6.3.18). The two equation model 2.3.42 gives a better approximation of model 4.1.2 than the single equation 2.3.43. However, the latter demonstrates the same parameter dependence of the wave speed as other models. Taking into account the complexity of the initial model 4.1.2, the approximation provided by one equation is acceptable. Below we obtain the analytical formulas for the wave speed for the one equation model.

Dimensionless model

Contribution of factor Xa to activation of thrombin during the propagation phase is negligible as compared to the role of the prothrombinase complex [4, 106]. Similarly, activation of factor X is mainly promoted by intrinsic tenase complex and the impact of factor IXa to this process is much less importan [106]. Thus, we can neglect the corresponding activation terms in 2.3.43 and introducing dimensionless variables.

$$T = T_0 u,\ t = \frac{\tilde{t}}{h_2},\ D = \tilde{D}h_2, \tag{2.3.44}$$

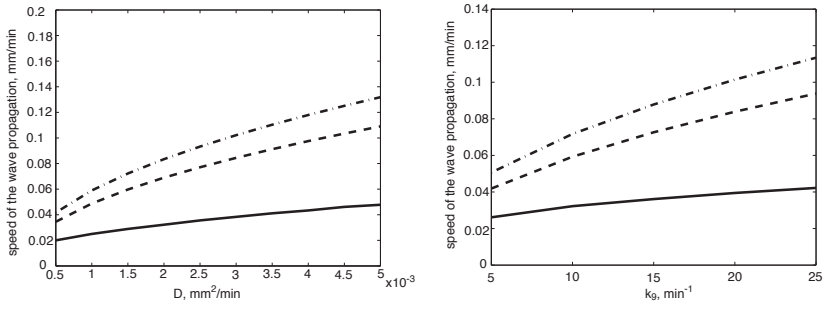

Figure 2.5: Speed of wave propagation (mm/min) as a function of D (left) and k_9 (right). Solid line: reduced model 4.1.2; dashed line: two-equation model 2.3.42; dash-dot line: one equation model 2.3.43. Parameters of the simulations are provided in Appendix B.

we obtain the following equation:

$$\frac{\partial u_1}{\partial \tilde{t}} = \tilde{D}\Delta u_1 + b u_1^3 (1-u_1) - u_1, \tag{2.3.45}$$

where:

$$b = M_1 M_2 M_3,\ M_1 = \frac{k_2 k_9 k_{10} k_{11}}{h_2 h_9 h_{10}},\ M_2 = \frac{k_8 k_{89} \overline{k_{10}}}{h_8 h_{89}} T_0,\ M_3 = \frac{\overline{k_2} k_5 k_{510}}{h_5 h_{510}} T_0. \tag{2.3.46}$$

Wave speed estimate

Equation 2.3.45 can be rewritten in the more general form:

$$\frac{\partial u}{\partial t} = D\Delta u + b u^n (1-u) - \sigma u. \tag{2.3.47}$$

Traveling wave solution of 2.3.47 satisfies the equation:

$$Dw'' + cw' + bw^n(1-w) - \sigma w = 0. \tag{2.3.48}$$

Here we will present two analytical methods to approximate its wave speed.

Narrow reaction zone method. One of the methods to estimate the wave speed for the reaction-diffusion equation is the narrow reaction zone method developed in combustion theory [107]. Let us rewrite equation 2.3.48 in the form:

$$Dw'' + cw' + F(w) - \sigma w = 0,\ F(w) = w^n(1-w). \tag{2.3.49}$$

We assume that the reaction takes place at one point $x = 0$ in the coordinates of the moving front. Then, outside the reaction zone we consider the linear equations:

$$\begin{cases} Dw'' + c_1 w' - \sigma w = 0, & x > 0, \\ Dw'' + c_1 w' = 0, & x < 0. \end{cases} \tag{2.3.50}$$

These equations should be completed with the jump conditions at the reaction zone. In order to derive them, we omit the first derivative w' at the reaction zone since it is small in comparison with two other terms:

$$Dw'' + F(w) = 0. \tag{2.3.51}$$

Multiplying 2.3.51 by w' and integrating through the reaction zone we obtain the following jump conditions:

$$(w'(+0))^2 - (w'(-0))^2 = \frac{2}{D}\int_0^{w^*} F(w)dw, \tag{2.3.52}$$

considered together with the condition of the continuity of solution $w(+0) = w(-0)$.

Solving 2.3.50 we have:

$$w = \begin{cases} w_*, & x < 0, \\ w_* \exp\left(\dfrac{-c_1 - \sqrt{c_1^2 + 4D\sigma}}{2D} x\right), & x > 0. \end{cases} \tag{2.3.53}$$

Then, from 2.3.52 and 2.3.53 we obtain the following equation for the wave speed:

$$c_1{}^2 + c_1\sqrt{c_1{}^2 + 4D\sigma} + 2D\sigma = A, \quad A = \frac{4D}{w_*^2}\int_0^{w^*} F(w)dw. \tag{2.3.54}$$

Hence,

$$c_1 = \frac{A - 2D\sigma}{\sqrt{2A}}, \quad A = 4bD\left(\frac{w_*^{n-1}}{n+1} - \frac{w_*^n}{n+2}\right). \tag{2.3.55}$$

This formula gives a good approximation of the wave speed found numerically for $n \geq 3$ (Fig. 2.6). The approximation improves with increasing values of n. The obtained formula provides an estimation of the speed from below (see Appendix C for the justification of the method).

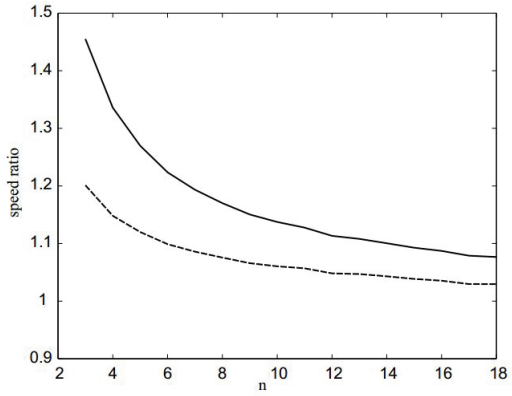

Figure 2.6: Ratio of wave speeds found numerically and analytically for different values of n; $\sigma = 0.01$, $D = 2$, $b = 10$. Solid line: $\dfrac{c}{c_1}$, dashed line $\dfrac{c}{c_2}$. Parameters of the simulations are provided in Tab. **??**.

Piecewise linear approximation. Consider equation 2.3.49 written in the form

$$Dw'' + cw' + f(w) = 0,$$

where $f(w) = w^n(1-w) - \sigma w$ and $f(0) = f(w_*) = 0$. Let us introduce the following approximation of this equation:

$$Dw'' + c_2 w' + f_0(w) = 0, \tag{2.3.56}$$

with

$$f_0(w) = \begin{cases} \alpha w, & 0 < w < w_0, \\ \beta(w - w_*), & w_0 < w < w_*, \end{cases} \tag{2.3.57}$$

where

$$\alpha = f'(0),\ \beta = f'(w_*). \tag{2.3.58}$$

In case of equation 2.3.47 we have:

$$\alpha = -\sigma, \quad \beta = bnw_*^{n-1} - b(n+1)w_*^n - \sigma. \tag{2.3.59}$$

We find the value of w_0 from the additional condition:

$$\int_0^{w_*} f(w)dw = \int_0^{w_*} f_0(w)dw. \tag{2.3.60}$$

Hence we obtain the following equation with respect to w_0:

$$\frac{\alpha-\beta}{2}w_0^2 + \beta w_* w_0 + r = 0, \tag{2.3.61}$$

where

$$r = -\beta w_*^2 - \int_0^{w_*} f(w)dw. \tag{2.3.62}$$

Taking into account the explicit form of function $f(w)$, we obtain:

$$r = bw_*^{n+1}\left(-\frac{n}{2} - \frac{b}{n+1}\right) + bw_*^{n+2}\left(\frac{n+1}{2} + \frac{1}{n+2}\right) + \sigma w_*^2. \tag{2.3.63}$$

From 2.3.61 we get:

$$w_0 = \frac{-\beta w_* + \sqrt{\beta^2 w_*^2 - 2(\alpha-\beta)r}}{\alpha-\beta}. \tag{2.3.64}$$

Thus, instead of 2.3.56 we consider the following equations:

$$\begin{cases} Dw'' + c_2 w' + \beta(w - w_*) = 0, & x < 0, \\ Dw'' + c_2 w' + \alpha w = 0, & x > 0, \end{cases} \tag{2.3.65}$$

with the additional conditions on the continuity of solution and its first derivative:

$$w(0) = w_0,\ w'(-0) = w'(+0).$$

We find the explicit solution:

$$\begin{cases} w = (w_0 - w_*)\exp\left(\dfrac{\sqrt{c_2^2 - 4\beta D} - c_2}{2D}x\right) + w_*, & x < 0, \\ w = w_0 \exp\left(\dfrac{-\sqrt{c_2^2 - 4\alpha D} - c_2}{2D}x\right), & x > 0. \end{cases} \tag{2.3.66}$$

From the condition of continuity of the derivative we obtain the following formula:

$$c_2 = \frac{\sqrt{D}(\alpha\bar{w}^2 - \beta)}{\sqrt{(\bar{w}-1)(\alpha\bar{w}^2 - \beta\bar{w})}}, \quad \bar{w} = \frac{w_0}{w_0 - w_*}. \tag{2.3.67}$$

It gives a good approximation of the wave speed for equation 2.3.49 (Fig. 2.6).

Comparison of the estimated speed of the wave propagation with the complete model and experimental data

Comparison of the estimated speed with the computational speed in system 4.1.2. Considering system 4.1.2 and taking the parameter values for 2.3.55, 2.3.67 according to 2.3.46, we approximate the speed of wave propagation by the following formula obtained by the narrow reaction zone method:

$$c_1 = \sqrt{D}\frac{bT_0^2 - \frac{4}{5}bT_0^3 - 2h_2}{\sqrt{2\left(bT_0^2 - \frac{4}{5}bT_0^3\right)}}, \tag{2.3.68}$$

where

$$b = \frac{k_9 k_{11}\overline{k_{10}}k_8 k_{89}\overline{k_2}k_5 k_{510}T_0^2}{h_9 h_{10} h_{11} h_8 h_{89} h_5 h_{510}}, \tag{2.3.69}$$

and by the piecewise linear approximation:

$$c_2 = \frac{\sqrt{D}\left(-3bT_0{}^2 - h_2\overline{T} + 4bT_0^3 - h_2\right)}{\sqrt{(T_0-1)\,\overline{T}\left(-h_2\overline{T} - 3bT_0^2 + 4bT_0^3 + h_2\right)}}, \tag{2.3.70}$$

where:

$$\overline{T} = \frac{T_*}{T_* - T_0}, \quad T_* = \frac{-3bT_0^2 + 4bT_0^4 + h_2}{4bT_0^2 - 3bT_0} + \frac{\sqrt{\left(3bT_0^2 - 4bT_0^3 - h_2\right)^2 - 2b(4T_0-3)T_0^2\left(-\frac{3}{2}bT_0^2 - \frac{b^2}{4}T_0^2 + \frac{11}{5}bT_0^3 + h_2\right)}}{4bT_0^2 - 3bT_0}. \tag{2.3.71}$$

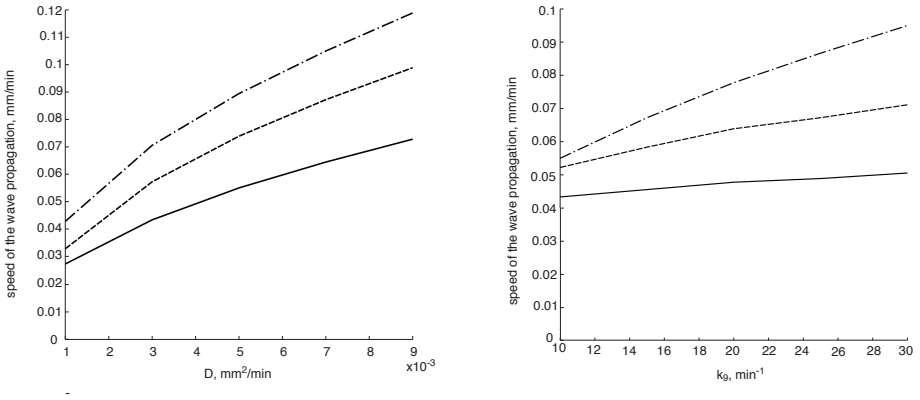

Figure 2.7: Speeds of wave propagation (mm/min) as function of D (left) and k_9 (right). Solid line: model 4.1.2; dashed line: narrow reaction zone approximation; dash-dot line: piecewise linear approximation. Parameters of the simulations are provided in Tab. **??**.

We compare the speed of wave propagation for model 4.1.2 found numerically with the analytical formulas (Fig. 2.7). As it was demonstrated above, the computational speed for the one-equation model is higher than for the complete model (Fig. 6.3.18). The analytical formulas for the speed of the wave propagation for one-equation model in turn provide the estimates from below (Fig. 2.6). As the result, the analytical estimates for one equation give better approximations of the speed in the complete model than

the numerical speed for one equation (Fig. 2.7). If we then compare two different analytical estimates for the wave speed in one-equation model, we can conclude that narrow reaction zone method gives the speed further from the one-equation computational speed than piecewise linear approximation (Fig. 2.6) but at the same time it better approximates the wave speed in the complete model (the narrow reaction zone speed is 1.5 times higher than the computational one).

Comparison with experimental data. The speed of clot formation has crucial influence on the organism physiology. Coagulation disorders such as hemophilia A, B or C are the result of severe deficiency of the clotting factors. The effect of this deficiency on the propagation phase is the most critical for situation *in vivo* [36, 108, 109]. Speed of the thrombin propagation in mathematical model of the intrinsic pathway functioning can provide estimation of the clot growth rate dependence on different factors.

As an example, here we consider the experimental results obtained in [36] on the patients with hemophilia B. Authors examined the effect of factor IX deficiency on the spatial clotting dynamics. Plasma used was obtained from hemophiliacs with different extent of the disease and from severe hemophiliacs treated with factor IX concentrate (Ahemphil B). Clotting process was launched through the intrinsic pathway by contact with plastic material. The obtained results show that the most pronounced changes in clotting kinetics occurred at factor IX activity less than 20% [36].

Experimental data correlate well with the results given by the analytical estimate of the thrombin propagation speed (Fig. 2.8). In the lack of precise kinetic constants we had to fit the approximated speed value at the first point of the plot corresponding to 1% of factor IX activity. While fitting, we varied only the value of the parameter b. In terms of our model, factor IX activity is reflected by the value of the parameter k_9. Thus, analytical estimate provided by 2.3.68 and 2.3.70 are plotted as functions of k_9 and give the values close to the experimental ones for all the considered range.

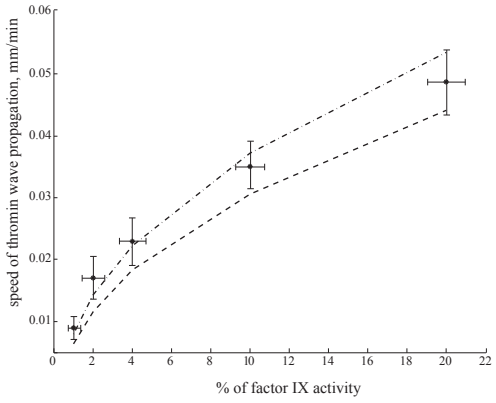

Figure 2.8: Speeds of the thrombin wave propagation (mm/min) as function of percentage of factor IX activity. Dots: experimental data [36]; dashed line: narrow reaction zone approximation; dash-dot line: piecewise linear approximation (Tab. 1)

2.3.6 Discussion and conclusions

Spatio-temporal dynamics of clot growth is of crucial importance for the normal organism functioning. The key stage of the blood coagulation process determining the dynamics of the clot formation is cumulative thrombin production due to the positive feedback reactions of the coagulation cascade. Propagating from the injury site with constant speed during the amplification phase, distribution of thrombin concentration can be modeled as traveling wave solutions in the reaction-diffusion system on plasma factor concentrations [110]. In the current work we derive conditions on the existence and stability of the traveling wave solutions for the mathematical model describing main reactions of the blood coagulation cascade.

Despite the general character of the methods used in this work, the developed approaches imply some limitations. First, the blood coagulation is a very complex process and the considered model describes only one of its stages: amplification phase of thrombin production. We do not take into account neither the initial activation, nor the clot growth inhibition by the activated protein C pathway. In terms of our model, initial thrombin formation appears on the left boundary of the domain. However, since the problem of the existence of the traveling wave solutions is considered on the whole axis, the solutions do not depend on the boundary conditions. The independence of the speed of the thrombin wave propagation during the amplification phase on the nature of the stimuli that launched the clotting process was also demonstrated in multiple experimental studies [92, 93, 36]. Then, inhibition role of the activated protein C appears only in the proximity of the healthy vessel wall due to its activation by thrombin-thrombomodulin complex and thus does not directly impact thrombin propagation on the distance from the vessel wall [33] and we do not incorporate it in our model. Under these assumptions the considered model is monotone, that is equivalent to positive contribution of all factors to the activation reactions. This important feature of the coagulation cascade model allows us to study existence and properties of its traveling wave solutions.

The most important parameter determining the dynamics of clot growth is the speed of the thrombin wave propagation or, in terms of the mathematical model, the speed of propagation of the reaction-diffusion wave. In the current work we obtain analytical estimates for the speed of the wave propagation in the model of blood coagulation. We reduce the system of equations to the single equation on the thrombin concentration and then determine the wave speed for this equation. The method of reduction is based on the minimax representation of the wave speed applicable for monotone reaction-diffusion systems. One-equation model gives the speed of the wave propagation above the wave speed obtained in the initial system. The difference appears due to the assumption on the fast reactions applied for the derivation of the one-equation model. Analytical estimates obtained for the wave speed in the one-equation model in turn provide its approximation from below. Narrow reaction zone method was originally developed for the description of the flame front propagation in the combustion theory with the exponential function in reaction term. In our work thrombin activation is described with the polynomial of the third degree that makes the obtained estimate less precise. Nevertheless, the obtained analytical estimates give good approximation of both computational and experimental speed of the thrombin propagation.

It is important to note that the simplified model of the coagulation cascade considered in the current study does not take into account all the factors that can have impact on clotting process. For example, the speed of clot growth estimated in our model significantly depends on the activity of factor XI. While several studies report increased risk of bleeding in factor XI deficient patients [111, 112], and elevated risk of cardiovascular diseases for patients with increased level of factor XI [113, 114], the correlation between the risk of pathology and the level of factor XI activity is poor [112]. The present mathematical model cannot reflect this phenomena and investigation of the underlying mechanisms requires development of more complex models. At the same time, the described approaches can serve as tools for the analysis of cascade system behavior and for the estimation of the speed of the traveling wave propagation.

Chapter 3

Modelling and Simulation of Clot Formation and Platelet Aggregation Under Flow

3.1 Thrombus development modelling under flow

In this section we formulate the model of blood coagulation and clot growth in a 2D rectangular domain. We use reaction-diffusion equations with convection terms to describe blood factor concentrations in plasma. Navier-Stokes equations are used to simulate blood flow. Clot is considered as a porous medium where flow velocity is described with the Navier-Stokes equations with additional terms depending on the clot porosity. This approach allows us to describe blood flow and clot growth by the same model without tracking the clot geometry. The model is based on several biological assumptions as it is devoted to the study of microvascular thrombosis under specific conditions. The first assumption concerns the blood flow. In order to mimic the *in vivo* condition where a pressure gradient drives the flow through the microvessels, we impose a constant pressure difference between the inlet and the outlet. Next, we only consider *in situ* thrombus formation following the injury of a part of the vessel wall. Other clotting initiation mechanisms such as thrombin activation by ADP are not included in the model. Among the other simplifying assumptions is reducing the study to the fibrin-rich microvascular clots which are known as “red" thrombi. These microvascular thrombi usually develop in microvessels such as arteriols, venules and capillaries. Platelets aggregation is less important in the dynamics of the formation of these clots. Thus, we do not consider platelets, red blood cells and their role in the coagulation process in this model. We will introduce platelets in the future developments of the model. Concerning the role of red blood cells, we note that thrombus growth rates are similar in the normal blood and in the platelet rich plasma [120]. This result suggests that erythrocytes do not affect thrombus growth rates. Their effect is limited to delaying the onset of clot growth through hindering platelets adhesion. Hence, in the absence of platelets, red blood cells have no effect on clot growth dynamics. In continuous models of blood coagulation, red blood cells are taken into account implicitly through hemodynamics (viscosity, rheology of blood flow). The influence of individual erythrocytes can be considered in cell based models where blood flow is modeled as a heterogeneous fluid which consists of plasma and blood cells. Such models become very complex and computationally expensive. They are developed for blood flows with platelets and erythrocytes but without blood coagulation and with platelets and blood coagulation but without erythrocytes. To the best of our knowledge, the works taking into account all three of these factors do not yet exist due to the extreme complexity of such modeling. The Von Willebrand factor and its role in carrying factor VIII in the plasma not included in the model either. To further simplify the study, we restricted the described coagulation cascade to the most important proteins participating in the clotting process. Although a more detailed description of the clotting cascade will improve the model, the resulting complexity will make the interpretation of the obtained results more difficult. Furthermore, we consider the vessel walls to be rigid and not deformed neither by changes in

blood flow nor by thrombus development. Finally, although the model can be used for 3D modelling of thrombosis development, the present work is limited to 2D study case. We expect the main conclusion to be qualitatively similar though they can be different quantitatively in the 3D case.

3.1.1 Exhaustive spatiotemporal model of clot growth

Blood factors concentrations. The clotting cascade is initiated following the activation of factors IX and X by the complex of tissue factor and factor VII. The latter is present along a damaged portion of the vessel wall. The concentration of tissue factor at the damaged wall is considered to be constant. After their activation, factors IX and X convert an initial amount of prothrombin into thrombin. This is known as the initiation phase. When the concentration of the generated thrombin is sufficiently high, it activates some factors of the amplification phase such as factor V, VIII and XI. These factors further convert more prothrombin into its active form. As the result, a positive feedback loop of thrombin generation is sustained. This loop can be inhibited by activated protein C. It is an anticoagulant protein which is activated by the complex of thrombin and thrombomodulin formed at the intact tissues. Another important anticoagulant protein present in the model is antithrombin. It inactivates several factors in the coagulation cascade. In our model, we will restrict the role of antithrombin to the direct inhibition of the thrombin. The part of the clotting cascade described in our model is shown in Fig. 4.1 a.

We consider a two-dimensional rectangular domain that corresponds to a section of blood vessel (Fig. 4.1 b). Blood flow crosses it along the axial direction. The computational domain corresponds to vessels with 50 μm diameters. This allows us to model the conditions observed in the experiments conducted in [122] and [53]. Clot development in microvessels with different heights can be studied with the same model.

We consider the following model of clot formation whose formulation was presented in the previous Chapter:

prothrombin

$$\frac{\partial P}{\partial t} + \nabla.(vP) = D\Delta P - \left(k_1\phi_c + k_2 B_a + \frac{k_3 T^3}{1 + k_8 C_a}\right) P, \tag{3.1.1}$$

thrombin

$$\frac{\partial T}{\partial t} + \nabla.(vT) = D\Delta T + \left(k_1\phi_c + k_2 B_a + \frac{k_3 T^3}{1 + k_{10} C_a}\right) P - k_4 A T, \tag{3.1.2}$$

factors IXa, Xa

$$\frac{\partial B_a}{\partial t} + \nabla.(vB_a) = D\Delta B_a - k_5 A B_a, \tag{3.1.3}$$

APC

$$\frac{\partial C_a}{\partial t} + \nabla.(vC_a) = D\Delta C_a - k_c C_a, \tag{3.1.4}$$

antithrombin

$$\frac{\partial A}{\partial t} + \nabla.(vA) = D\Delta A - k_4 A T - k_5 A B, \tag{3.1.5}$$

fibrinogen

$$\frac{\partial F_g}{\partial t} + \nabla.(vF_g) = D\Delta F_g - \frac{k_6 T F_g}{K_6 + F_g}, \tag{3.1.6}$$

fibrin

$$\frac{\partial F}{\partial t} + \nabla.(vF) = D\Delta F + \frac{k_6 T F_g}{K_6 + F_g} - k_7 F, \tag{3.1.7}$$

fibrin polymer

$$\frac{\partial F_p}{\partial t} = k_7 F. \tag{3.1.8}$$

Boundary conditions. In order to describe the generation of thrombin in the initiation phase at the damaged endothelial wall, we consider the complex T_f^* formed by the tissue factor and factor VII. Factors IX and X interact with this complex due to a surface reaction. They come from the bulk solution being inactive, form a complex $[T_f^* B]$ with T_f^* and return to the solution in the active form. The reaction rate for the surface concentration of this complex can be written as follows:

$$\frac{\partial [T_f^* B]}{\partial n} = k_f^+ B(T_f^* - [T_f^* B]) - k_f^- [T_f^* B],$$

where the first term in the right-hand side of this equation describes the flux of B to the surface, the second term describes the flux from the surface. Assuming that this reaction is fast, we can use the detailed equilibrium

$$k_f^+ B(T_f^* - [T_f^* B]) = k_f^- [T_f^* B].$$

Then

$$[T_f^* B] = \frac{k_f B T_f^*}{1 + k_f B}, \tag{3.1.9}$$

where $k_f = k_f^+ / k_f^-$.

The boundary conditions for the variables B and B_a at the damaged surface are as follows:

$$\frac{\partial B}{\partial n} = -k_f^+ B(T_f^* - [T_f^* B]), \quad \frac{\partial B_a}{\partial n} = k_f^- [T_f^* B],$$

We prescribe the zero flux condition at the intact surface.

In order to simplify the boundary conditions, let us introduce the variable $z = B + B_a$. From equations (3.1.3) and the boundary conditions for B and B_a we get:

$$\frac{\partial z}{\partial t} + \nabla.(vz) = D\Delta z - k_b z, \quad \frac{\partial z}{\partial n} = 0. \tag{3.1.10}$$

Assuming that initially $B + B_a = B^0$, where B^0 is the initial concentration of factors IX and X, we conclude that the solution of problem (3.1.10) is identically constant, $B + B_a = B^0$. Hence we can exclude the variable B from the equations and from the boundary condition:

$$\frac{\partial B_a}{\partial n}\Big|_{\Gamma_d} = \frac{\alpha_1 (B^0 - B_a)}{1 + \beta_1 (B^0 - B_a)}, \tag{3.1.11}$$

where $\alpha_1 = k_f^- k_f T_f^*$ and $\beta_1 = k_f$.

Protein C is activated by the complex of thrombin-thrombomodulin. The fluxes of protein C at the surface in its active and intactive forms are given as follows:

$$\frac{\partial C}{\partial n} = -k_c^+ C((TT_m) - (CTT_m)), \quad \frac{\partial C_a}{\partial n} = k_c^- (CTT_m).$$

Here T_m is the concentration of thrombomodulin present at the undamaged surface. Protein C arrives next to thrombin and thrombomodulin and forms the complex (CTT_m). Here k_8^+ is the reaction rate constant of protein C activation by the complex of thrombin thrombomodulin, k_c^- is the rate of the inverse reaction. Again using the detailed equilibrium, we obtain the condition of APC production on undamaged walls:

$$\frac{\partial C_a}{\partial n}\Big|_{\Gamma_u} = \frac{\alpha_2 (C^0 - C)[TT_m]}{1 + \beta_2 (C^0 - C_a)}, \tag{3.1.12}$$

$$[TT_m] = \frac{k_T TT_m}{1 + k_T TT_m}, \tag{3.1.13}$$

where $\alpha_2 = k_c^- k_c$ and $\beta_2 = k_c$, $[TT_m]$ is the complex thrombin thrombomodulin that activates protein C present in blood plasma. We consider the no-flux boundary conditions for these concentrations at the other parts of the boundary and also for other concentrations. In the case of nonzero flow velocity, the concentrations of prothrombin, fibrinogen and antithrombin at the entrance of the domain ($x = 0$) are kept constant.

Blood flow model. We use the Navier-Stokes equations to describe the blood flow. Non-Newtonian properties of blood are not taken into account. We model clot as a porous medium with the porosity depending on the concentration of fibrin polymer [56]. The flow through the clot is modelled by the Navier-Stokes equations with additional terms which describe the fluid deceleration by the porous medium. The advantage of this approach is that we use the same model in the whole computational domain. We do not need to determine the clot geometry and to solve Navier-Stokes equations in the outer (with respect to the clot) domain. We have the following equations for the incompressible fluid flow:

$$\rho\left(\frac{\partial\vec{u}}{\partial t}+\vec{u}\nabla\vec{u}\right)=-\nabla p+\mu\Delta\vec{u}-\frac{\mu}{K_f(\vec{x})}\vec{u}, \tag{3.1.14}$$

$$\nabla\vec{u}=0,$$

where $\vec{u}=(u_x,u_y)$ is the velocity vector, p is the pressure, ρ the desnity of blood, μ the viscosity, H the height of the vessel. In this work we consider laminar incompressible flow. K_f is the hydraulic permeability of fibrin polymer [56]:

$$\frac{1}{K_f(\vec{x})}=\frac{16}{\alpha^2}F_p(\vec{x})^{1.5}(1+56F_p(\vec{x})^3). \tag{3.1.15}$$

Here α is the fiber radius.

We prescribe the no-slip boundary conditions for the velocity at the upper and lower walls, and periodic boundary conditions in the axial direction. The periodic boundary conditions for the velocity are convenient since they allow us to study steady state flows where the velocity at the entrance and at the exit of the flow are not fixed and can vary in time. Blood flow is driven by the pressure difference. Therefore, we use periodic boundary conditions for velocity coupled with constant pressure difference condition:

$$p_{in}=p_{out}+\Delta p, \tag{3.1.16}$$

where p_{in} is the pressure at the inlet, p_{out} is the outlet pressure and Δp is the pressure difference which is considered as an imposed constant. Contrary to the condition of fixed inlet velocity, this imposed pressure difference condition allows the clot to completely occlude the vessel and obstruct the flow. This condition is verified in experimental settings [122] as well as in some areas of the circulatory system such as capillary networks. It is not verified for large arteries where wall shear rate is high.

Numerical implementation. Reaction-diffusion system of equation is solved numerically with a finite difference method and an upwinding scheme in discretizing convective terms in order to avoid numerical instabilities in the convection dominated cases. A regular 2000×400 mesh is used in the numerical simulations. Accuracy of the results was controlled by decreasing the time and space steps.

Numerical implementation of the Navier-Stokes equations is carried out with the projection method [123], and Successive Over Relaxation (SOR) method is used to solve the pressure Poisson problem. We present the details of the numerical implementation in Appendix A.

3.1.2 Simplified model of thrombin generation

We derive a simplified model from the system (3.1.1) - (3.1.8). The model consists of one reaction-diffusion equation of thrombin distribution in 1D domain corresponding to a vertical section of the 2D computational domain. To the opposite of the exhaustive system, the simplified model admits mathematical analysis of resulting bistable reaction-diffusion equations. We proceed by determining the condition of thrombin wave propagation. We then determine the necessary conditions for clot growth initiation. Finally, we introduce a simplified model of pressure driven Poiseuille flow and describe the exact conditions for blood flow to stop thrombin wave propagation. Thrombin is the most important enzyme of the coagulation cascade. The formation of the fibrin clot is always preceded by the propagation of a thrombin wave. The behavior of this wave depends on the local concentrations of the clotting factors as

well as the perturbations caused by the flow. The propagation of thrombin wave can only occur if the characteristic reaction time is lower than the characteristic convection time. To mathematically capture the dynamics of the thrombin wave propagation, we derive a simplified analytical model of thrombin distribution from the system (3.1.1) - (3.1.8). The model describes the evolution the thrombin wave front and admits mathematical investigation.We replace the concentrations of factors IXa, IXa distribution (B_a) by their steady state values obtained as stationary solutions of equations (3.1.3), (3.1.11). Furthermore, the model does not take into account neither prothrombin nor antithrombin consumption. The concentrations of these two proteins are introduced as constants. Let us consider the 1D model describing the thrombin distribution in the vertical cross section of the 2D model:

$$\frac{\partial T}{\partial t} = D\frac{\partial^2 T}{\partial y^2} + \Phi(T,y), \tag{3.1.17}$$

where

$$\Phi(T,y) = (k_2 B_a(y) + k_3^+ T^3)(P_0 - T) - \sigma(y)T,$$

D is the diffusion coefficient, P_0 is the prothrombin concentration initially present in blood flow, k_1 and k_2 are kinetic coefficients. The function $B_a(y)$ expresses the initiation of thrombin generation by factors IXa and Xa. It corresponds to a stationary solution of the equation (3.1.3), $B_a(y) = \lambda e^{-y/\sigma}$.

The coefficient σ represents inhibition of thrombin production by antithrombin and blood flow. We set $\sigma = k_4 A_0 + av(y)$, where A is the antithrombin concentration supposed to be constant, and $v(y)$ is blood flow velocity in the horizontal direction. Inhibition by APC can be taken into account in the nonlinear reaction term. For simplicity, we do not consider it here.

This equation is obtained as an approximation of the model presented in Section 2 where equations (3.1.1)-(3.1.8) are replaced by the single equation for the thrombin concentration under the assumption of detailed equilibrium (fast reactions). Equations (3.1.6)-(3.1.8) are decoupled, and the corresponding concentrations do not directly influence thrombin production. The flow velocity is replaced by an approximate solution of the Navier-Stokes equations specified below.

If $k_3 = \alpha_2 = 0$, then the function Φ does not depend on y, and (3.2.27) is an autonomous reaction-diffusion equation. It has a traveling wave solution $T(y,t) = W(y - ct)$, where c is the speed of wave propagation [124]. This function satisfies the equation

$$W'' + cW' + \Phi(W) = 0$$

(dependence of the function Φ on y is omitted here) considered on the whole axis with the limits at infinity $W(-\infty) = T^*, W(\infty) = 0$, where T^* is the maximal solution of the equation $\Phi(T) = 0$. Solution of equation (3.2.27) converges to the travelling wave solution if the initial condition is sufficiently large. The speed of the wave is positive if and only if the following condition is satisfied [115]:

$$\int_0^{T^*} \Phi(T,y)dT > 0. \tag{3.1.18}$$

Only positive velocity of thrombin wave propagation corresponds to the regime clot growth. Condition (3.1.18) also implies that thrombin production exceeds its loss due to its inhibition by antithrombin and blood flow.

Let us then consider the case of nonzero coefficients k_3 and k_4 and function Φ depending on y. If we assume that this dependence is weak, that is the derivative $\partial\Phi/\partial y$ is sufficiently small, we can use inequality (3.1.18) for each fixed value of y. Let us take the value of y equal to zero that corresponds to the coordinate of the cell wall and then increase it considering the thrombin concentration on some positive distance from the wall. At some moment the inequality (3.1.18) will be no more satisfied and the critical value of y will give an approximation of the maximal clot height.

We specify the conditions of the thrombin wave propagation (3.1.18) for the exact expression of function Φ . At $y = 0$, we have $B_a(0) = \lambda$ and $v(0) = 0$, hence from (3.1.18) we get:

$$A_0 < \frac{1}{k_4}\left(2k_2\lambda\frac{P_0}{T^*} - k_2\lambda + k_3^+\frac{(T^*)^2 P_0}{2} - 2k_3^+\frac{(T^*)^3}{5}\right). \tag{3.1.19}$$

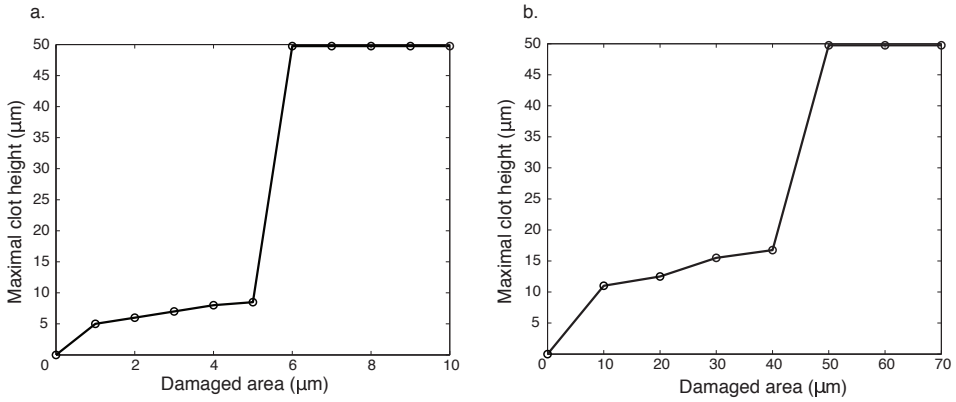

Figure 3.1: The final height of the clot for different damaged area widths. Simulations were run for 10 minutes and the stable clot heights were reached after 2 - 3 minutes of simulations time in agreement with expermental data. : a) in quiescent plasma, b) in pressure driven flow with an initial parabolic flow $v(y)$ where $v(H/2) = v_m = 400\ \mu m/s$ and $A_0 = 0.4$. In both cases there is a sharp transition from the partial occlusion regime to the complete occlusion as the clot width exceeds some critical value. This critical value is much larger for blood coagulation in flow.

If this condition is satisfied, then the initial quantity of thrombin produced near the vessel wall is sufficiently large to initiate clot growth. Otherwise the clot will not form. From the pathophysiological point of view this situation corresponds to bleeding, and it can occur for example in case of hemophilia or treatments with anticoagulant drugs.

3.1.3 The regimes of microvessel occlusion

Blood flow influences clot growth in multiple ways. It brings fibrinogen and inactivated blood factors to the growing clot accelerating chemical reactions. At the same time blood flow removes thrombin and thus prevents thrombin accumulation due to the positive feedback loops of the coagulation cascade and thus slows down clot growth. Finally, blood flow transports APC generated at the intact surface to the wound region thus contributing to the downregulation of the thrombin production.

At the same time, growing clot modifies the blood flow dynamics. In our computational model this influence depends significantly on the conditions imposed on the flow velocity at the boundaries of the considered domain. Let us consider first the case where the fluid velocity at the entrance of the computational domain is time independent. Since fluid velocity decreases inside the clot, then the velocity would increase in the part of the cross section of the vessel without clot according to the mass conservation law. The resulting high fluid velocity prevents clot growth removing thrombin and other blood factors participating in coagulation reactions. If we consider the limiting case where the clot has zero porosity and the fluid velocity inside the clot is zero, then complete vessel occlusion is not possible since fluid should leave the computational domain.

The situation is different in the case of a pressure driven flow where the fluid velocity at the entrance is not fixed and the total flow rate can decrease due to the hydrodynamic resistance exerted by the clot. For a given pressure difference, the fluid velocity can decrease and the total vessel occlusion becomes possible. In this case there are two competing factors determining the blood flow dynamics. Flow velocity increases in the narrow part of the vessel, and the total flow rate decreases because of the clot resistance. It appears that the first factor is more important in the case where the width of the clot is small, while the second one becomes more important in case of large clot.

To better understand the dynamics of clot growth in blood flow, we calculate the dimensionless Damköhler number (D_a). This number represents the degree of conversion that can be achieved by a reaction. It corresponds to the division of the reaction rate by the convection rate. In order to estimate the Damköhler number for prothrombin conversion, we proceed with the nondimensionalization of the

reaction-diffusion system presented in (3.1.1)-(3.1.8). Considering the concentrations to be already nondimensional, we define other nondimensional variables denoted by:

$$x^* = \frac{x}{H}, \quad \nabla = \frac{\nabla^*}{1/H}, \quad \Delta = \frac{\Delta^*}{1/H^2}, \quad v = \frac{v^*}{v_0}, \quad t^* = \frac{t}{H/v_0}.$$

where v_0 and H are the characteristic flow velocity and length which is also the vessel diameter. We also consider transformations for the kinetic rate constants of the system:

$$k_i^* = \frac{k_i}{k^0} \quad i = 1,..,9 \quad k_a^* = \frac{k_a}{k_a^0},$$

where k^0 is the characteristic kinetic rate of the system. With these nondimensional variables, equation (3.1.2) becomes:

$$\frac{\partial T}{\partial t^*} + \nabla^*.(v^* T) = \frac{D}{v_0 H}\Delta^* T + \frac{H}{v_0}\left(\Phi^*(T, B_a, C_a)P - k_4^* A T\right), \tag{3.1.20}$$

where $\Phi^*(T, B_a, C_a) = k_2^* B_a + \frac{k_3^* T^3}{1+k_8^* C_a}$. Under these conditions, we define the Damköhler number at the front where $B_a = 0$ and $C_a = 0$ and considering that for $t >> 0$, thrombin concentration at the bottom boundary equals P_0. We give its expression as follows:

$$D_a = \frac{H}{v_0}\left(k_3^* P_0^4 - k_4^* A_0 P_0\right). \tag{3.1.21}$$

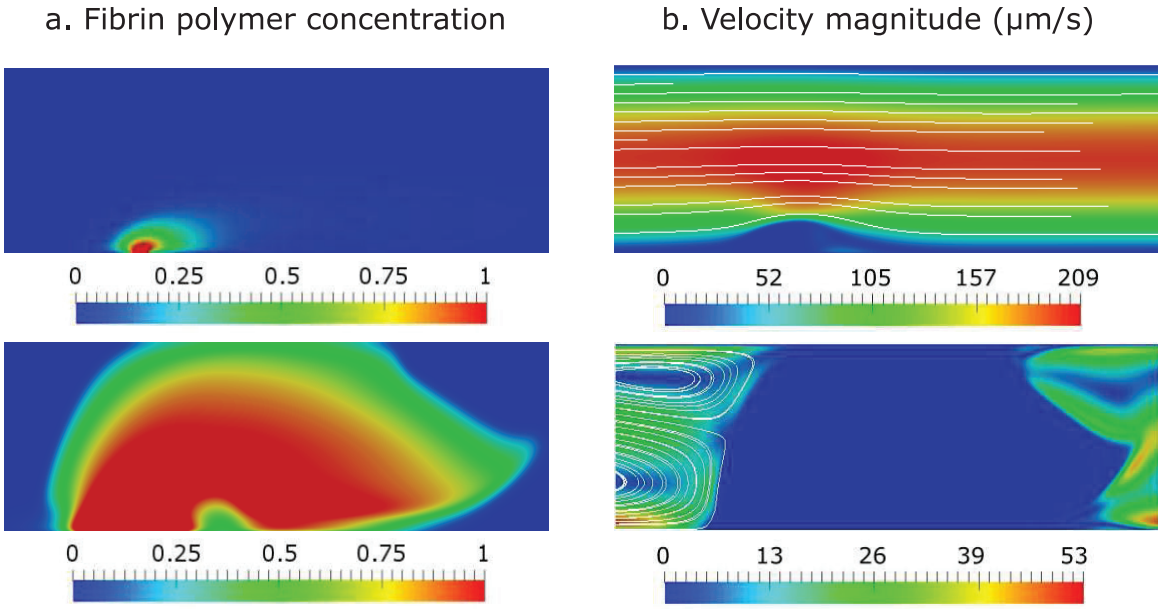

Figure 3.2: Snapshots of simulations for $D_a = 2.24$ at $t = 100\ s$ (top) and $t = 640\ s$ (bottom) of thrombus development resulting in complete occlusion. A microvessel of 250 μm length is considered where the area of the damaged part is equal to 10 μm. Blood flow is not sufficient to stop clot growth (initial velocity is $v = 200\ \mu m/s$). APC does not allow clot growth width but it still grows across the flow. a) Fibrin polymer concentrations are shown at two consecutive moments of time. b) The corresponding flow velocity fields are shown with the velocity value (color scale) and streamlines (white curves).

The described interplay between the dynamics of the clot growth and the distribution of the blood flow velocity is also observed in our computational model. Here we consider the case when the thrombomodulin concentration is large enough to generate a sufficient amount of APC that suppresses clot

expansion in the axial direction. If we take the blood flow velocity rather low, then the thrombin wave still propagates to the top despite the inhibition by APC. As the result, the clot occludes the vessel and completely obstructs blood flow (Fig. 3.2 a). It is important to note that the fast development of the clot can lead to the emergence of vortices (Fig. 3.2 b).

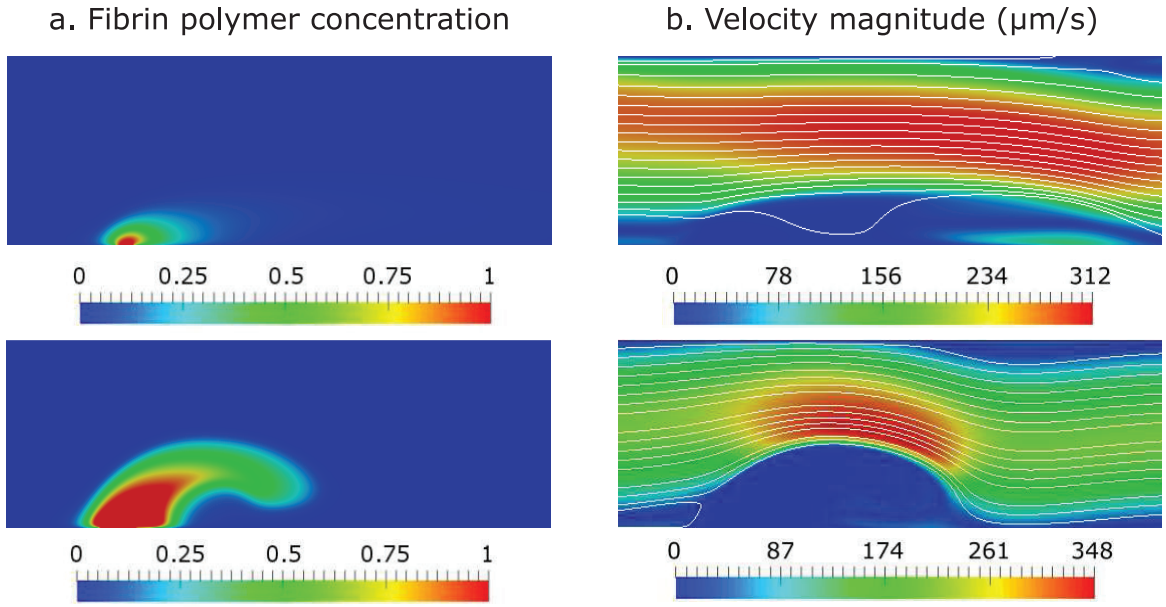

Figure 3.3: Two snapshots at $t = 100\ s$ (top) and $t = 640\ s$ (bottom) of the simulation for $D_a = 1.12$ with partial occlusion. A microvessel of 250 μm length is considered where the area of the damaged part is equal to 10 μm. The initial flow velocity at the entrance of the vessel is $v = 400\ \mu m/s$. a) Fibrin polymer concentrations, b) Blood flow velocity magnitude is shown with a color scale and streamlines as white curves.

If the initial blood flow velocity is sufficiently high, then it stops clot growth (Fig. 3.3). Blood flow transports APC to the wounded area already at the very beginning of the clot formation and thus slows down thrombin production, especially at the part of the damaged area closer to the coming flow (left part of the injury in our computational domain, Fig. 3.3 a). After some time the accumulated concentration of thrombin is sufficient to accelerate its self-sustained production and clot development. Clot growth is stopped by blood flow when clot height approaches to the half of the vessel diameter (Fig. 3.3 b). The observed regime corresponds to the partial vessel occlusion.

The two distinct regimes of microvascular occlusion are seperated by a critical Damköhler number D_{ac}. Its critical value is $D_{ac} \approx 2$. In the fast reaction / slow convection case ($D_a > D_{ac}$), the propagation of the thrombin wave persists resulting in the continuous formation of the fibrin clot. Consequently, the diameter of the vessel is completely covered by the clot and total occlusion of the microvessel is observed. When $D_a < D_{ac}$, the characteristic convection time is smaller than the characteristic reaction time. This means that the chemical reaction is too slow to sustain the perturbations caused by strong convection. The final height of the clot correlates inversely with both the flow velocity and the Damköhler number.

The main parameters that determine the final clot size are the width of damaged area and the initial flow velocity. The dependence of the final clot size on the damaged area width for the model with the flow (Fig. 3.1 b) is qualitatively similar to the case of quiescent plasma (Fig. 3.1 a). If the damaged area width is large enough, then the clot continues growing till it reaches the upper vessel wall. As the result, we observe the regime of complete vessel occlusion. If the width is sufficiently small, the final clot size remains less than the vessel diameter. These two regimes are separated with a narrow transition zone. Let us note that this transition occurs for $40 - 50\ \mu m$ of the wound width in the case of model with the flow while for the model without flow the threshold damaged area width is only about $5 - 6\ \mu m$. Hence

we can conclude that blood flow provides an important additional (with respect to APC) mechanism that can stop clot growth.

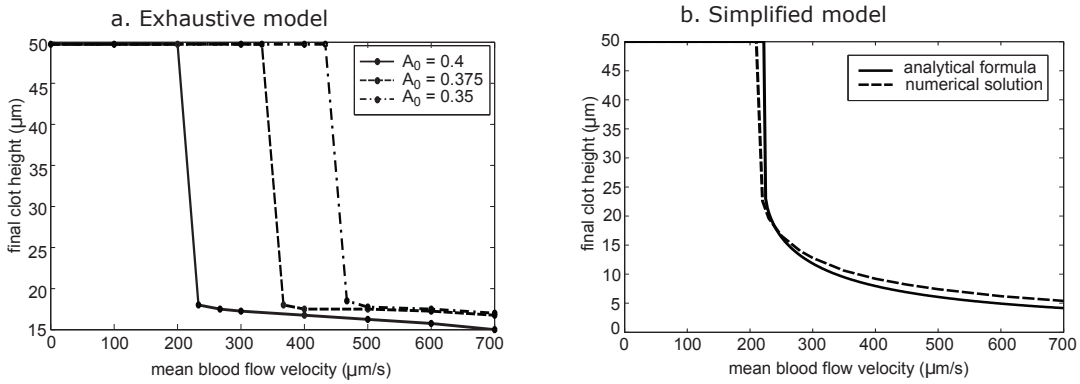

Figure 3.4: The final height of the clot in case of different values of the initial blood flow velocity. a): numerical simulations for three different values of antithrombin concentration in plasma (A_0). b): numerical (solid line) and analytical (dashed line) solutions of the simplified model for $A_0 = 0.4$. For the exhaustive and simplified models we observe complete occlusion for low flow velocities and partial occlusion for high velocities with a sharp transition between these two regimes.

The dependence of the final clot size on the initial flow velocity is shown in Fig. 3.4 a. The complete vessel occlusion occurs only if the flow velocity is small enough. If the flow velocity is sufficiently large, then the size of the clot remains bounded (partial occlusion). We again observe a sharp transition between these two regimes for our model.

Thus, the observed three regimes of clot growth: initiation without propagation, initiation with limited propagation (partial occlusion), and initiation with unlimited propagation (complete occlusion) are qualitatively similar for the clot growth in quiescent plasma and in the blood flow. In the next section we will determine the conditions of the existence of each of these three regimes on the basis of the simplified theoretical model.

3.2 The quantification of the procoagulant effects of platelets on clot growth

3.2.1 Mathematical modelling

We use a previously developed model of clot growth dynamics already presented in Chapters 2 and 3. The model consists of reaction-advection-diffusion equations describing the spatiotemporal distributions of blood coagulation factors during thrombus development:

platelets in flow

$$\frac{\partial \phi_f}{\partial t} + \nabla.(k(\phi_c) v \phi_f) = k(\phi_c) D_p \Delta(\phi_f) - k_9 T \phi_f - k_{10} \phi_f \phi_c, \tag{3.2.22}$$

platelets in clot

$$\frac{\partial \phi_c}{\partial t} + \nabla.(k(\phi_c) v \phi_c) = k(\phi_c) D_p \Delta(\phi_c) + k_9 T \phi_f + k_{10} \phi_f \phi_c, \tag{3.2.23}$$

Here v is the flow velocity, D is the diffusion coefficient that is taken the same for all proteins and $k(\phi_c)D_p$ is the effective diffusion coefficient for platelets, where $k(\phi_c) = \tanh(\pi(1 - \frac{\phi_c+\phi_f}{\phi_{max}}))$ a decreasing function. Fibrin polymer forms a solid clot, it does not diffuse and it is not transported by flow.

To incorporate the action of blood flow on clot growth, we use the Navier-Stokes equations to describe the dynamics of blood flow in the vessel.

$$\rho\left(\frac{\partial\vec{u}}{\partial t}+\vec{u}\nabla\vec{u}\right)=-\nabla p+\mu\Delta\vec{u}-\frac{\mu}{K_f(\vec{x})}\vec{u}, \tag{3.2.24}$$
$$\nabla\vec{u}=0,$$

where $\vec{u}=(u_x,u_y)$ is the velocity vector, p is the pressure, ρ the desnity of blood, ν the kinematic viscosity, H the height of the vessel. In this work we consider laminar incompressible flow. K_f is the hydraulic permeability of fibrin polymer [56]:

$$\frac{1}{K_f(\vec{x})}=\frac{16}{\alpha^2}\bar{F_p}^{1.5}(1+56\bar{F_p}(\vec{x})^3)\left(\frac{1+\bar{\phi_c}(\vec{x})}{1-\bar{\phi_c}(\vec{x})}\right). \tag{3.2.25}$$

Here $\bar{F_p}$ and $\bar{\phi_c}$ are the normalized concentration of fibrin polymer and density of platelets in the clot respectively, α is the fiber radius.

We prescribe the no-slip boundary conditions for the velocity at the upper and lower walls, and periodic boundary conditions in the axial direction. Blood flow is driven by the pressure difference. Therefore, we use periodic boundary conditions for velocity coupled with constant pressure difference condition:

$$p_{in}=p_{out}+\Delta p, \tag{3.2.26}$$

where p_{in} is the pressure at the inlet, p_{out} is the outlet pressure and Δp is the pressure difference which is considered as an imposed constant. Contrary to the condition of fixed inlet velocity, this imposed pressure difference condition allows the clot to completely occlude the vessel and obstruct the flow.

3.2.2 Quantitative study of platelets procoagulant effects on thrombus development

We consider the following reduced thrombin distribution model:

$$\frac{\partial T}{\partial t}=D\frac{\partial^2 T}{\partial y^2}+\Phi(T,y), \tag{3.2.27}$$

where

$$\Phi(T,y)=(k_1\phi_0+k_2B_a(y)+k_3^+T^3)(P_0-T)-\gamma(y)T,$$

D is the diffusion coefficient, P_0 is the prothrombin concentration initially present in blood flow, k_1, k_2, and k_3^+ are kinetic coefficients. The function $\gamma(y)=k_4A_0T+a\gamma T$ shows the influence of antithrombin and of shear rate in the downregulation of thrombin production. Here H is the width of the vessel, v_m is the maximal flow velocity at its axis.

This means that we neglect the boundary effects of clot initiation and the blood flow (quiescent plasma). If $P_0^3<(27k_4A_0)/(4k_3^*)$, then this function has three zeros, $T=0$ and T_1,T_2, where $T_0<T_1<T_2$. The equilibria $T_0=0$ and $T=T_2$ are stable as solutions of the corresponding ODE, while $T=T_1$ is unstable. Thus, we obtain a classical reaction-diffusion equation in the bistable case. If it is considered on the whole axis, it has travelling wave solutions, that is solutions of the form $T(x,t)=W(x-ct)$, where W is a solution of the equation

$$DW''+cW'+\Phi_0(W)=0,\ W(-\infty)=T_2,\ W(\infty)=0,$$

and c is the speed of propagation. In the case of a positive speed c, such solution describes clot growth. It is known that the wave speed is positive if and only if

$$\int_{T_0}^{T_2}\Phi_0(T)dT>0 \tag{3.2.28}$$

Thus, the condition on shear rate for thrombin propagation is as follows:

$$\gamma > \frac{1}{aT_2/2}\left(k_1(\phi_0 P_0 T_2/2 - \phi_0 T_2^2/3) + k_2(B_a P_0 - B_a T_2/2) + k_3^+(P_0 T_2^3/4 - T_2^4/5) - k_4 A_0 T_2/2 - av(y)T_2/2\right). \tag{3.2.29}$$

Let us denote the shear rate threshold by
$\gamma^* = \frac{1}{aT_2/2}\left(k_1(\phi_0 P_0 T_2/2 - \phi_0 T_2^2/3) + k_2(B_a P_0 - B_a T_2/2) + k_3^+(P_0 T_2^3/4 - T_2^4/5) - k_4 A_0 T_2/2 - av(y)T_2/2\right)$,
it correlates linearly with the platelets density as shown in Fig. 3.6.

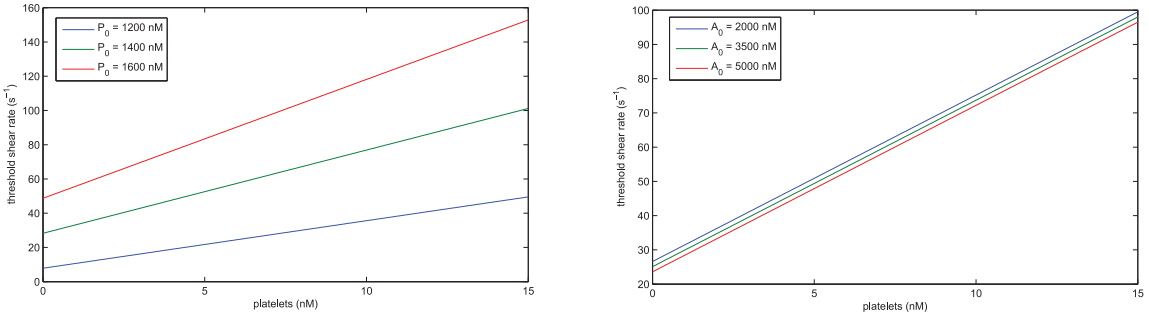

Figure 3.5: The shear rate threshold of clotting initiation as a function of platelets density for different prothrombin (left) and antithrombin concetrations (right).

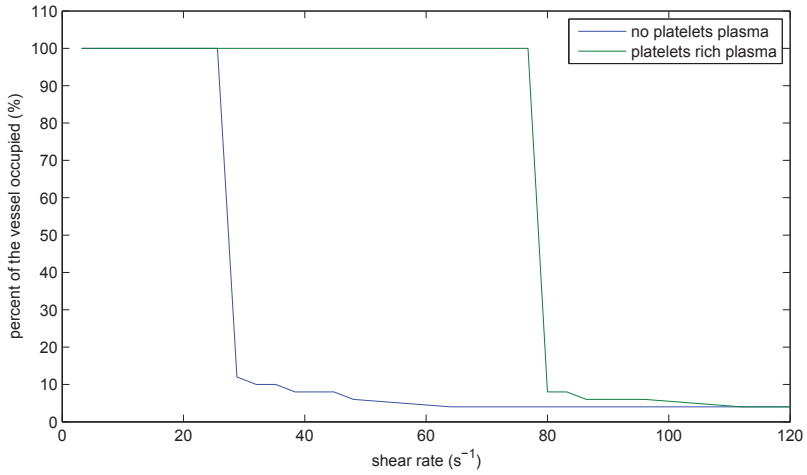

Figure 3.6: The percent of the vessel occupied by the clot at $t = 800\ s$ in the simplified model.

Numerical simulations. In order to reproduce the experiments conducted using *in vitro* microfluidic chambers [153], we compute the necessary time for blood clotting initiation while increasing the shear rate. The latter is given for a newtonian fluid in a pipe by the formula $\gamma = 8v_m/D$. A threshold response is observed in the initiation of blood clotting characterized by a critical value which is higher in platelets rich plasma. These critical values are in good agreement with the ones reported in experiments.

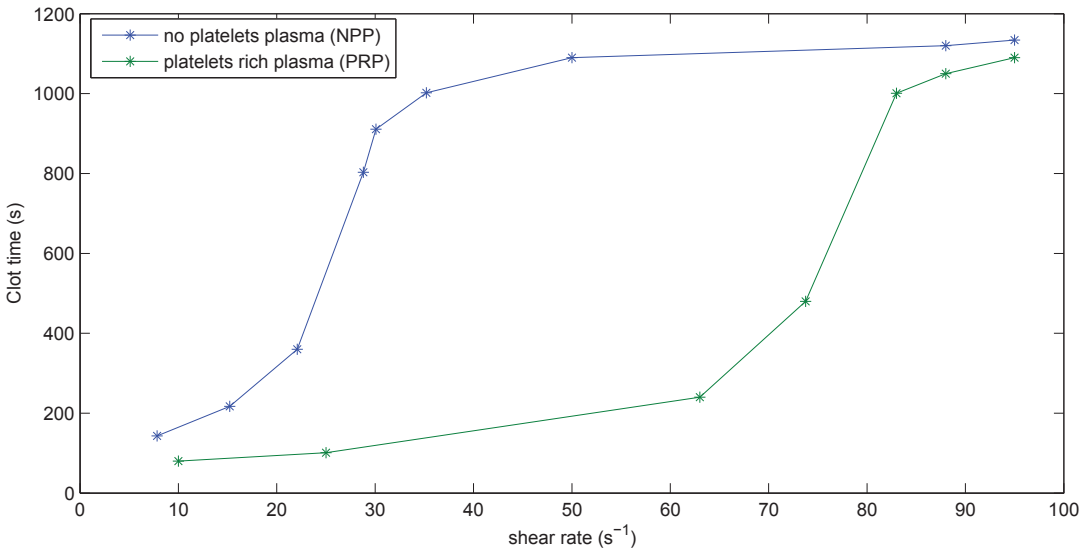

Figure 3.7: The necessary time for blood clotting initiation as a function of shear rate in no platelets plasma (NPP) and platelets rich plasma (PRP).

Chapter 4

Clot Growth Dynamics in Antithrombin Deficiency and Inflammation: insights from mathematical modelling

4.1 The effect of antithrombin deficiency on clot growth

4.1.1 Biological background

Blood coagulation is a complex process whose main function is preventing blood loss in case of the blood vessel damage. As the result, under the normal conditions a fibrin clot is formed on the injury site preventing the vessel from leaking. The reaction of fibrinogen conversion to fibrin is catalyzed by the key enzyme of the coagulation cascade called thrombin. In case of the vessel damage some amount of thrombin is formed near the vessel wall through the tissue factor pathway. If this amount reaches the threshold value, thrombin launches a cascade of activation reactions resulting in the self-sustained bulk production of thrombin whose concentration propagates from the damaged vessel wall to the vascular lumen [110].

Thrombin wave propagation is controlled by the anticoagulant system that incorporates different plasma inhibitors suppressing the activation processes. The most important inhibitor of thrombin is antithrombin that forms a stable complex with thrombin decreasing its activity in the blood flow [131, 132]. Furthermore, antithrombin also binds to other factors participating as activators in the coagulation cascade and thus has a crucial influence on the clotting dynamics [133]. If the thrombin propagation becomes intensive enough the additional anticoagulant mechanisms such as activation of protein C pathway are launched. Nevertheless, the role of antithrombin during the initiation phase of coagulation cascade is predominant and it determines whether the propagation of thrombin wave will take place [132].

4.1.2 Mathematical model of blood clotting initiated by the intrinsec pathway

We consider the following model of the intrinsic pathway of coagulation cascade:

$$
\begin{aligned}
\frac{\partial T}{\partial t} &= D\Delta T + \left(k_2 U_{10} + \overline{k_2}\frac{k_{510}}{h_{510}} U_{10}U_5\right)\frac{P}{P_0} - h_2 T,\\
\frac{\partial P}{\partial t} &= D\Delta P + \left(k_2 U_{10} - \overline{k_2}\frac{k_{510}}{h_{510}} U_{10}U_5\right)\frac{P}{P_0},\\
\frac{\partial U_{11}}{\partial t} &= D\Delta U_{11} + k_{11}T - h_{11}U_{11},\\
\frac{\partial U_{10}}{\partial t} &= D\Delta U_{10} + k_{10}U_9 + \overline{k_{10}}\frac{k_{89}}{h_{89}} U_9U_8 - h_{10}U_{10},\\
\frac{\partial U_9}{\partial t} &= D\Delta U_9 + k_9 U_{11} - h_9 U_9,\\
\frac{\partial U_8}{\partial t} &= D\Delta U_8 + k_8 T - h_8 U_8,
\end{aligned}
\tag{4.1.1}
$$

$$
\begin{aligned}
\frac{\partial U_5}{\partial t} &= D\Delta U_5 + k_5 T - h_5 U_5,\\
\frac{\partial F_g}{\partial t} &= D\Delta F_g - k_1 T F_g,\\
\frac{\partial F}{\partial t} &= D\Delta F + k_1 T F_g - \bar{k}F,\\
\frac{\partial F_p}{\partial t} &= \bar{k}F.
\end{aligned}
$$

Here U_i are the concentrations of the activated forms of i-th factors; P, T, F_g, F, F_p are the concentrations of prothrombin, thrombin, fibrinogen, fibrin and fibrin polymer respectively; D is the diffusion coefficient considered to be the same for all factors; $k_i, \overline{k_i}$ and h_i are the rates of factor i activation and inhibition respectively; k_{ij}, h_{ij} are the rates of formation and inhibition of the complexes of factors i and j. Model 4.1.1 is derived from the model studied in Section 2.3 and is similar to those considered in [103, 134]. As compared to these models, in the current study we take into account the role of blood flow in clot formation. To reflect the mechanical properties of the clot we introduce the variables of fibrinogen, fibrin and fibrin polymer concentrations. Fibrin polymer forms the clot scaffold and is not transported by the blood flow but affects the flow dynamics. Finally, we take the rate of thrombin inhibition to be proportional to antithrombin concentration (A): $h_2 = \alpha^* A$.

We consider a 2D computational domain corresponding to the vessel cross-section with blood flow moving along the x axis (Fig. 4.1). As prothrombin and fibrinogen are abundantly present in blood plasma, we prescribe the Dirichlet conditions $P(x,0,t) = P_0$, $F_g(x,0,t) = F_0$ on the bottom vessel wall (Fig. 4.1) and also use P_0 and F_0 as initial concentrations for prothrombin and fibrinogen respectively. We also prescribe Dirichlet condition $T(x,0,t) = T_0$ and $U_{11}(x,0,t) = U_0$ for $x \in [x_1, x_2]$ supposing that the initial concentration of thrombin is already formed in the proximity of the injury site due to the reactions on the vessel surface. For all the other factors we prescribe zero-flux boundary conditions and zero concentrations as the initial condition.

4.1.3 Simplified model

Model reduction. Let us note that variables F_g, F, F_p do not influence the reactions kinetics of other factors and thus corresponding equations of the system 4.1.1 can be decoupled. Thus, we obtain the following model of thrombin propagation:

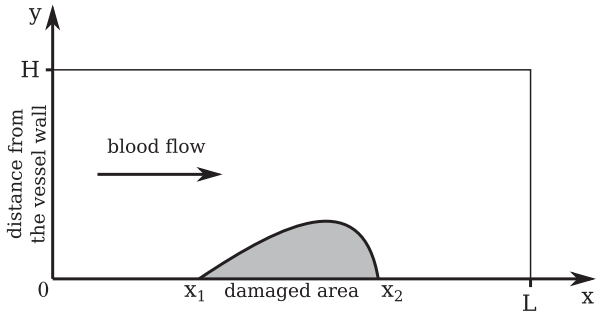

Figure 4.1: Schematic representation of the computational domain corresponding to the vessel cross-section. Here x axis is parallel to the direction of the blood flow, y axis is perpendicular to the vessel wall. The $[x_1, x_2]$ fragment of the vessel wall represent an injury site. H is the vessel diameter and L is the length of the considered vessel fragment.

$$
\begin{aligned}
\frac{\partial T}{\partial t} &= D\Delta T + \left(k_2 U_{10} + \overline{k_2}\frac{k_{510}}{h_{510}} U_{10}U_5\right)\frac{P}{P_0} - h_2 T,\\
\frac{\partial P}{\partial t} &= D\Delta P + \left(k_2 U_{10} - \overline{k_2}\frac{k_{510}}{h_{510}} U_{10}U_5\right)\frac{P}{P_0},\\
\frac{\partial U_{11}}{\partial t} &= D\Delta U_{11} + k_{11}T - h_{11}U_{11},\\
\frac{\partial U_{10}}{\partial t} &= D\Delta U_{10} + k_{10}U_9 + \overline{k_{10}}\frac{k_{89}}{h_{89}} U_9 U_8 - h_{10}U_{10},\\
\frac{\partial U_9}{\partial t} &= D\Delta U_9 + k_9 U_{11} - h_9 U_9,\\
\frac{\partial U_8}{\partial t} &= D\Delta U_8 + k_8 T - h_8 U_8,\\
\frac{\partial U_5}{\partial t} &= D\Delta U_5 + k_5 T - h_5 U_5.
\end{aligned}
\tag{4.1.2}
$$

The system 4.1.2 can be further simplified under the assumption of high rates for the factor activation. Thus, considering the quasi stationary solutions for all factor concentrations except for prothrombin and thrombin, we obtain the following expressions:

$$
U_{11} = \frac{k_{11}}{h_{11}}T,\ U_9 = \frac{k_9 k_{11}}{h_9 h_{11}}T,\ U_8 = \frac{k_8}{h_8}T,\ U_5 = \frac{k_5}{h_5}T,
$$

$$
U_{10} = \frac{k_9 k_{11}}{h_{10}h_9 h_{11}}\left(k_{10}T + \frac{\overline{k_{10}}k_{89}k_8}{h_{89}h_8}T^2\right).
$$

Substituting them to the equation for prothrombin and thrombin we obtain:

$$
\begin{aligned}
\frac{\partial T}{\partial t} &= D\Delta T + \frac{k_9 k_{11}}{h_{10}h_9 h_{11}}\left(k_{10}T + \frac{\overline{k_{10}}k_{89}k_8}{h_{89}h_8}T^2\right)\left(k_2 + \frac{\overline{k_2}k_{510}k_5}{h_{510}h_5}T\right)\frac{P}{P_0} - h_2 T,\\
\frac{\partial P}{\partial t} &= D\Delta P - \frac{k_9 k_{11}}{h_{10}h_9 h_{11}}\left(k_{10}T + \frac{\overline{k_{10}}k_{89}k_8}{h_{89}h_8}T^2\right)\left(k_2 + \frac{\overline{k_2}k_{510}k_5}{h_{510}h_5}T\right)\frac{P}{P_0}.
\end{aligned}
$$

We can neglect the first terms in each expression in brackets as the corresponding coefficients are rather small for the considered rate constants and further reduce the model to the following system of equations:

$$
\frac{\partial T}{\partial t} = D\Delta T + kT^3 P - aT,
$$

$$\frac{\partial P}{\partial t} = D\Delta T - kT^3 P,$$

where:

$$k = \frac{k_9 k_{11} \overline{k_{10}} k_{89} k_8 \overline{k_2} k_{510} k_5}{h_{10} h_9 h_{11} h_{89} h_8 h_{510} h_5 P_0}, \quad a = h_2. \tag{4.1.3}$$

Narrow reaction zone method. Thrombin concentration propagates from the injury site with constant profile and velocity [110]. If we consider thrombin concentration dynamics along the y axis (Fig. 4.1) it would correspond to the traveling wave solution of the model system in 1D case, i.e. to the solutions of 4.1.3-4.1.3 in the form: $P(y,t) = P(z)$, $T(y,t) = T(z)$ where $z = y - ct$. Here c is the speed of the propagation of thrombin concentration in the direction perpendicular to the vessel wall. In 1D case traveling wave solution of 4.1.3-4.1.3 satisfies the equations:

$$DT'' + cT' + f(T)\varphi(P) - aT = 0,$$
$$DP'' + cP' - f(T)\varphi(P) = 0,$$

where c is the speed of wave propagation, the function $f(T)$ shows how the reaction rate of thrombin production depends on its own concentration and $f(T) = kT^3$ in our case; the last term in the left-hand side of the first equation describes thrombin degradation; all the derivatives are taken with respect to z. We set $a = \alpha A + \beta v$ to take into account thrombin binding by antithrombin whose concentration is supposed to be constant (A) and the clot growth inhibition by the blood flow (v). The kinetic function $\varphi(P)$ corresponds to the first-order reaction, $\varphi(P) = P$.

We look for solutions of the system 4.1.3-4.1.3 with the following limits at infinity:

$$T(\pm\infty) = 0, \quad P(-\infty) = 0, \; P(+\infty) = P_0, \tag{4.1.4}$$

where P_0 is the initial prothrombin concentration.

We can estimate the speed of their propagation c for equations 4.1.3-4.1.4 using approximative method of narrow reaction zone. This method was developed by [107] in combustion theory in order to determine the velocity of the propagating flame front. Narrow reaction zone method is based on the approximation where the whole conversion in chemical reaction occurs at a single spatial point, i.e. we neglect the reaction terms in the equations everywhere except for one point. Hence we replace the nonlinear reaction-diffusion equations by an interface problem, which admits an analytical solution. Here we apply the narrow reaction zone method to estimate the speed of thrombin wave propagation. First, we replace the first-order reaction with respect to prothrombin by the zero-order reaction:

$$\varphi(P) = \begin{cases} P_0 & , \quad P > 0, \\ 0 & , \quad P = 0. \end{cases}$$

Then, instead of the nonlinear system 4.1.3-4.1.3 we consider the linear system

$$DT'' + cT' - aT = 0, \quad z \gtrless 0,$$
$$DP'' + cP' = 0, \quad z \gtrless 0,$$

outside of the reaction zone located at $z = 0$ and the jump conditions at the reaction zone. The first condition at the interface implies continuity of both functions:

$$T(-0) = T(+0), \quad P(-0) = P(0). \tag{4.1.5}$$

In order to derive the next jump condition, we take a sum of equations (4.1.3) and (4.1.3) and integrate the resulting equation over the reaction zone. We get

$$P'(+0) - P'(-0) = -(T'(+0) - T'(-0)). \tag{4.1.6}$$

The last condition is obtained multiplying equation (4.1.3) by T' and integrating over the reaction zone:

$$\big(T'(+0)\big)^2 - \big(T'(-0)\big)^2 = \frac{2P_0}{D}\int_0^{T^*} f(T)dT. \tag{4.1.7}$$

Here T^* is the thrombin concentration in the reaction zone. In case if there is no antithrombin and $a = 0$, we have $T^* = P_0$. If $a > 0$, then $T^* < P_0$ due to the thrombin loss.

From 4.1.3-4.1.5 we obtain:

$$P(z) = \begin{cases} 0 & , \quad z < 0 \\ P_0(1 - e^{-cz/D}) & , \quad z > 0 \end{cases}, \quad T(z) = \begin{cases} T^* e^{\lambda_1 z} & , \quad z < 0 \\ T^* e^{\lambda_2 z} & , \quad z > 0 \end{cases},$$

where

$$\lambda_1 = -\frac{c}{2D} + \sqrt{\Big(\frac{c}{2D}\Big)^2 + \frac{a}{D}}, \quad \lambda_2 = -\frac{c}{2D} - \sqrt{\Big(\frac{c}{2D}\Big)^2 + \frac{a}{D}}.$$

We use the remaining two jump conditions to determine T^* and c. From 4.1.6-4.1.7 we get:

$$\frac{c}{D}P_0 = 2T^*\sqrt{\Big(\frac{c}{2D}\Big)^2 + \frac{a}{D}},$$

$$(T^*)^2 c\sqrt{\Big(\frac{c}{2D}\Big)^2 + \frac{a}{D}} = P_0\, I(T^*),$$

where

$$I(T^*) = \int_0^{T^*} f(T)dT.$$

Expressing the square root from 4.1.3 and substituting them into 4.1.3 we obtain the formula for the wave speed:

$$c^2 = \frac{2D}{T^*} I(T^*). \tag{4.1.8}$$

In the particular case where $a = 0$ we have $T^* = P_0$ and formula 4.1.8 gives the wave speed without thrombin loss. Then, if $a \neq 0$ we can substitute 4.1.8 into 4.1.3:

$$\sqrt{\frac{2I(T^*)}{DT^*}}P_0 = 2T^*\sqrt{\frac{I(T^*)}{2DT^*} + \frac{a}{D}},$$

and obtain the following equality:

$$I(T^*) = \frac{2a(T^*)^3}{P_0^2 - (T^*)^2}. \tag{4.1.9}$$

For our case with $f(T) = kT^3$ and from 4.1.8 we have the following approximation of the wave speed:

$$c = T^*\sqrt{\frac{DkT^*}{2}} \tag{4.1.10}$$

and from 4.1.9 we obtain:

$$T^*(P_0^2 - (T^*)^2) = \frac{8a}{k}. \tag{4.1.11}$$

Let us denote $g(T^*) = T^*(P_0^2 - (T^*)^2)$. Then $g'(T^*) = 0$ for $T^* = \pm P_0/\sqrt{3}$ and 4.1.11 has two positive roots if and only if $g(P_0/\sqrt{3}) > 8a/k$ or

$$\frac{12\sqrt{3}a}{kP_0^3} < 1. \tag{4.1.12}$$

If the inequality is opposite, then there are no positive solutions of 4.1.11. Hence, traveling wave solution of the approximated system describing thrombin propagation 4.1.3-4.1.3 exists for sufficiently small antithrombin concentration A and for sufficiently large prothrombin concentration P_0. If condition 4.1.12 is satisfied, then for one of the solutions of 4.1.11 $T^* > P_0/\sqrt{3}$, and for the second solution this inequality is opposite.

4.1.4 Numerical simulations

Thrombin wave propagation

Wave propagation speed for 1D model. Let us consider the thrombin propagation in the direction perpendicular to the vessel wall. Then we can describe it with the system 4.1.2 in 1D case. The speed of the wave propagation depends on multiple parameters and can be approximated by the simplified model 4.1.3-4.1.3 or using the obtained analytical approximation 4.1.10. Both approaches give the result close to the result of numerical simulation of system 4.1.2 (Fig. 4.2)

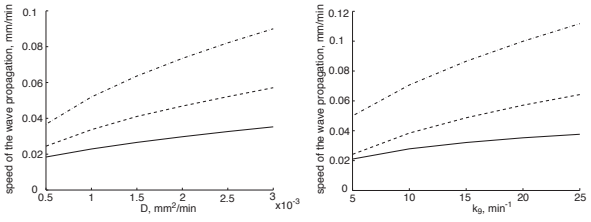

Figure 4.2: Speed of the thrombin wave propagation as function of D (left) and k_9 (right). Solid line: 7 equations model 4.1.2; dashed line: 2 equations model 4.1.3-4.1.3; dash-dotted line: analytical approximation 4.1.10.

The analytical approximation gives values greater than computational speed. This effect is related to the replacement of the first-order reaction by zero-order reaction that we used to apply the narrow reaction zone method.

Role of antithrombin in the model of coagulation in quiescent plasma. The inhibition of thrombin by antithrombin may have crucial effect on the dynamics of clotting process. In terms of our model, sufficient amount of antithrombin leads to the suppression of the thrombin wave propagation that follows both from the analytical estimate 4.1.12, and from the quiescent plasma simulation ($h_2 = \alpha A$, $v = 0$) of 4.1.2 for 1D case (Fig. 4.3) and 2D case (Fig. 4.4). Thus, once the initial amount of thrombin is formed the antithrombin concentration determines whether the thrombin wave propagation will take place (Fig. 4.3a, 4.4a) or the further propagation will be suppressed by thrombin inhibition (Fig. 4.3b, 4.4b).

The thrombin wave propagation in quiescent plasma results in the clot formation. Thus, the concentration of antithrombin determines the dynamics of clotting process. Indeed, according to the results obtained in the simulation of the system 4.1.1, for the concentrations of antithrombin below the threshold value of 963 μg/L we have the thrombin wave propagation and formation of clot (Fig. 4.4a), and for the concentrations above the threshold value the clot formation is stopped because of the thrombin inhibition (Fig. 4.4b).

The critical concentration of antithrombin depends strongly on the initial amount of prothrombin present in plasma (P_0). We can express the antithrombin concentration sufficient to prevent the thrombin wave propagation using the analytical condition 4.1.12 with $a = \alpha A$, $v = 0$:

$$A = \frac{kP_0^3}{12\sqrt{3}\alpha}. \tag{4.1.13}$$

This approximation appears to be rather close to the conditions for the thrombin wave propagation obtained in the numerical simulation of 4.1.2 (Fig. 4.5a).

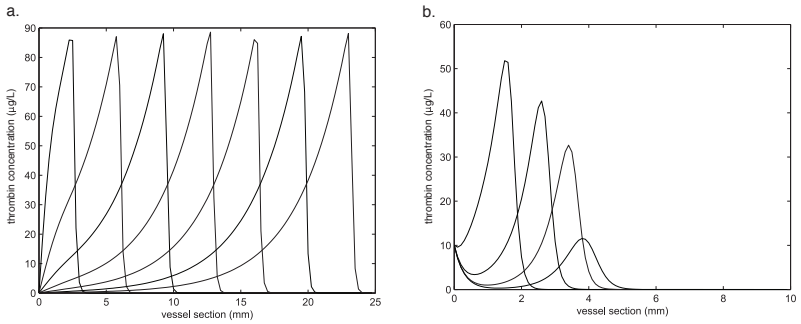

Figure 4.3: Thrombin wave profiles obtained in 1D numerical simulations of 4.1.2 for low (left) and high (right) antithrombin concentration. a) corresponds to the wave propagation and b) to the wave extinction.

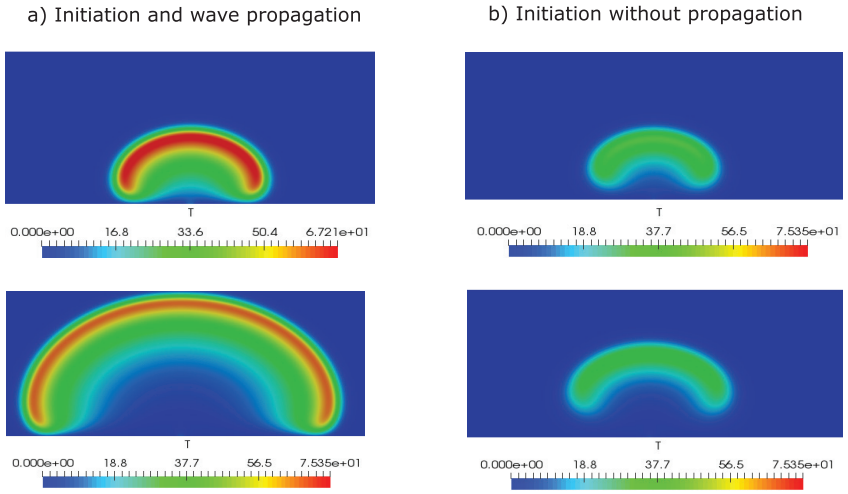

Figure 4.4: Snapshots of thrombin concentration obtained in 2D numerical simulations of 4.1.2 at two consecutive moments for the different regimes of thrombin wave propagation. a) thrombin wave propagates from the injury site; b) the wave propagation stops.

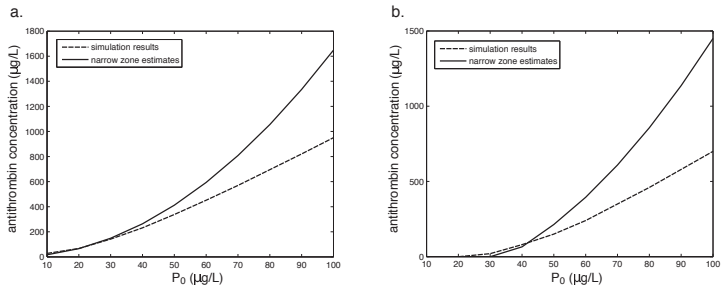

Figure 4.5: Antithrombin concentration sufficient to prevent thrombin wave propagation as function of prothrombin concentration obtained a) in the numerical experiment for the model 4.1.2 in quiescent plasma and using the analytical estimate 4.1.13; b) in the numerical experiment for the model 4.1.2 in blood flow and the analytical estimate 4.1.14 for $v_m = 120$ mm/min.

Role of antithrombin in the model of coagulation in the blood flow. The speed of blood flow influences significantly dynamics of the thrombin wave propagation. We consider the model of blood coagulation in flow for the model 4.1.2 with parabolic speed profile: $v(y) = y(H-y)$, where H is the height of the computational domain (Fig. 4.1), $h_2 = \alpha A + \beta v$. For 4.1.3-4.1.3 we take $a = \alpha A + \beta v_m$,

where v_m is the maximal value of the blood flow velocity corresponding to $y = H/2$. Then, the threshold antithrombin concentration sufficient to prevent thrombin propagation can be estimated from 4.1.12:

$$A = \frac{kP_0^3}{12\sqrt{3}\alpha} - \frac{\beta}{\alpha}v_m, \tag{4.1.14}$$

and gives a good approximation of the simulation results (Fig. 4.5b).

Fibrin clot formation. While distribution of thrombin concentration in the blood flow is a very important factor that determines the dynamics of blood coagulation, final shape and size of the clot are determined by the concentration of fibrin polymer. As fibrin clot is solid, it changes the flow geometry. In order to incorporate this effect we couple the model 4.1.1 with Navier-Stokes equations. The clot is considered as porous medium whose permeability depends on fibrin polymer concentration. Then blood flow dynamics is described by the equations [56]:

$$\rho\left(\frac{\partial\vec{u}}{\partial t} + \vec{u}\nabla\vec{u}\right) = -\nabla p + \mu\Delta\vec{u} - \frac{\mu}{K_f(\vec{x},t)}\vec{u}, \tag{4.1.15}$$

$$\nabla\vec{u} = 0,$$

where $\vec{u}$ is the velocity vector, p is the pressure value, ρ denotes the density of blood and μ denotes its viscosity. In the last term of the right hand side of the last equation, the permeability is given as follows [56]:

$$\frac{1}{K_f(\vec{x},t)} = \frac{16}{\gamma^2}F_p(\vec{x},t)^{1.5}(1 + 56F_p(\vec{x},t)^3). \tag{4.1.16}$$

We prescribe periodic boundary condition on the inlet and the outlet of the flow. The no-slip condition $\vec{u} = \vec{0}$ is used on the top and bottom boundaries. We consider a constant pressure drop between the inlet and outlet $\Delta p = p_{in} - p_{out}$. This condition is verified for experimental settings [122] as well as for some vessels of the circulatory system (capillary networks).

The simulations of the resulting model demonstrate existence of several regimes of clot formation depending on the antithrombin concentration (Fig.4.6,4.7). In case of the low antithrombin concentration we observe complete vessel occlusion (Fig.4.6). Increasing antithrombin concentration leads to smaller sizes of the clot. As compared with thrombin wave dependence on the antithrombin concentration in quiescent plasma, in the model with flow we do not observe such sharp transition in the regimes of clot formation (Fig.4.7). While thrombin wave either propagates for low concentrations of antithrombin or does not propagate at all (Fig.4.7, vertical line), final clot height can reach other intermediate values. This effect takes place due to the presence of the initial amount in thrombin near the vessel wall supposed in our model. While the further propagation of the thrombin can be arrested by its antithrombin inhibition, the diffusion of the initial concentration of thrombin can still lead to the fibrinogen conversion and thus to the clot formation.

The next important phenomena observed in the model concerns the role of blood flow. As we can see from the Fig. 4.7 for the low blood flow rates we have the final clot heights larger than for the quiescent plasma with the same concentration of antithrombin. At the same time, sufficiently high blood flow velocity gives the smaller size of the clot that for the model with no flow. The probable explanation of this effect follows from the details of the transport of the factors participating in the coagulation cascade. While the blood flow velocity is rather low, the flow stimulates clot growth by transporting procoagulant factors to the reaction zone thus contributing to the thrombin wave propagation. For the large blood flow velocities, on the contrary, we have the flow sufficiently strong to remove thrombin from the propagating front that leads to clot growth arrest.

4.1.5 Discussion and conclusions

The role of antithrombin in thrombin inhibition in the regulation of blood coagulation was demonstrated in multiple experiments [132]. Antithrombin deficiency can cause serious aggravations such as thrombosis [**?**, 132]. The anticoagulant action of antithrombin is used not only for treatment of coagulation

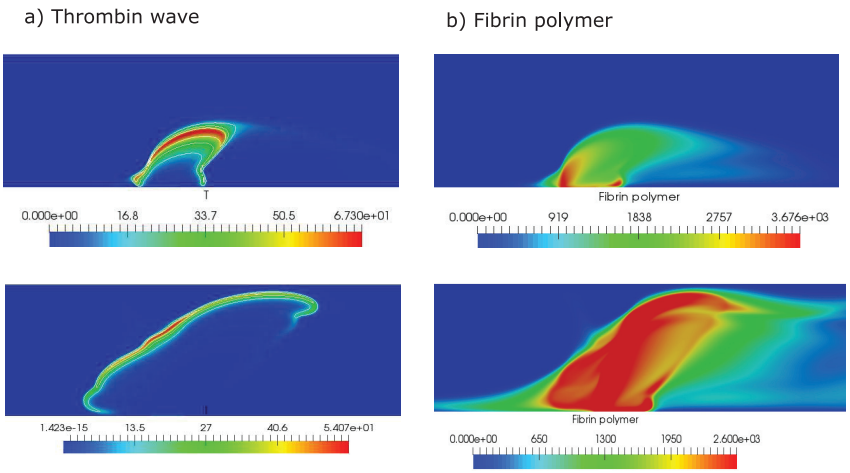

Figure 4.6: Two stages of fibrin clot formation in blood flow: a) thrombin concentration, b) fibrin polymer concentration. First row corresponds to the beginning of clot formation, second row corresponds to the complete vessel occlusion. Simulation parameters are provided in Tab. 8.1, the direction of the blood flow is from left to right parallel to x axis (Fig 4.1).

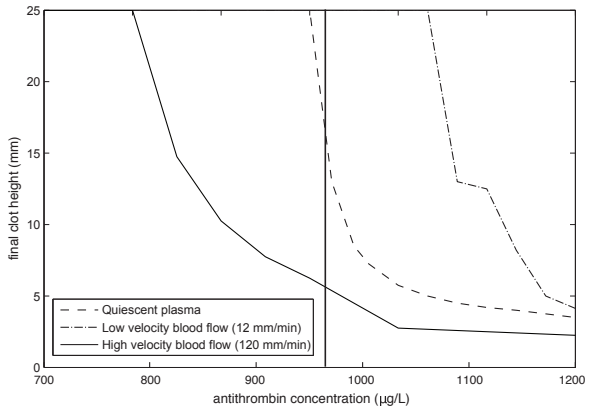

Figure 4.7: The final clot height in quiescent plasma and in the blood flow as function of antithrombin concentration. Dashed line: quiescent plasma; solid line: high velocity flow; dash-dotted line: low velocity flow. The vertical line indicates the threshold concentration of antithrombin preventing thrombin wave propagation in quiescent plasma simulation.

disorders but also in anti-inflammation therapy [135]. In our study we consider a mathematical model of blood coagulation in order to elucidate some details of the antithrombin action in the blood.

The model used in our study is close to the model previously studied by [134]. This model does not take into account the origin of the initial stimuli launching the coagulation cascade but describes the details of the intrinsic pathway functioning. The concentration of thrombin in this model propagates from the injury site on the vessel wall to the vascular lumen as a traveling wave with constant velocity. To determine the conditions under which the propagation of thrombin wave starts, we reduced our model to the bistable system of two equations. For the resulting system we found an analytical condition determining wether the clotting process will take place, using the narrow reaction zone approximation. The narrow reaction zone method and its derivatives provide good estimates of the wave propagation speed for the combustion models with the strongly nonlinear reaction terms [107, 105, 136]. Nevertheless, as it was demonstrated in the current study the approach gives reasonable approximations for the model of thrombin propagation with polynomial reaction term. The obtained estimate of the critical antithrombin concentration appeared to be close to the simulation results for both model of the coagulation in quiescent plasma and in blood flow.

Further study of the model of blood coagulation revealed the importance of considering the fibrin polymer concentration in the model system. While the concentration of thrombin mforly determines the rate of the fibrin formation, the clot growth dynamics appears to differ from the dynamics of the thrombin wave propagation. This effect takes place due to the diffusion process and to the spreading of thrombin concentration with the blood flow. As the result, for the model incorporating blood flow we did not observe the same sharp transition between the regimes of clot formation as for the model of quiescent plasma. Moreover, the blood flow appears to play opposite roles depending on the speed value. While it contributes to the clot growth for low speeds, the high speeds of blood flow lead to the clot growth arrest.

4.2 The effects of IL-17 and TNF-α on clot growth

4.2.1 Biological background

The impact of cardio-vascular (CV) diseases on the society is enormous and any method able to identify early individuals at risk will have a significant effect on morbidity and mortality. Classical CV risk factors related to obesity, hypertension, smoking, etc., have been identified for a long time. More recently chronic inflammation has become an important link between these risk CV factors and the actual CV events. For many years, rheumatoid and psoriatic arthritis (RA, PsA), and similar diseases have been linked to local damage and to function loss. The goal of arthritis care was the control of local inflammation in order to prevent loss of joint function. It is unclear why it took so long to look at patient survival. When compared to control populations, it was obvious that life expectancy was severely affected [137]. Quickly joint destruction and mortality were linked to the level and duration of inflammation [138].

The most common cause of death in RA, PsA, and similar diseases is vascular disease, contributing to 60 % mortality risk in RA patients, comparable to diabetes mellitus as an independent risk factor for CV disease. RA patients have a four-fold increase in CV mortality. Figures are even higher when considering only RA patients who are rheumatoid factor positive or with high CRP levels [138]. In addition, this risk begins very early in the RA disease process [139]. In total, the prevalence of CV disease in RA has been found to be 16.2 %. However, the largest difference in CV between RA patients and controls is seen in those without traditional risk factors - patients who are young, female, and have a low body mass index [140]. With specific regards to cardiac disease, RA patients have a twofold higher risk of myocardial infarction (MI) as compared to controls [139]. The odds ratio of having a MI with RA, as opposed to with osteoarthritis (OA), a less inflammatory joint disease, is 2.14, and the odds ratio of having a MI at some point in life, again as compared to patients with OA, is 1.28 for RA patients (30). RA patients also carry a twofold higher risk of chronic heart failure (CHF) [139]. The odds ratio of having CHF with RA, as opposed to with OA, is 1.43 [141].

Chronic inflammatory diseases are associated with overproduction of cytokines. These factors have a direct effect on the local manifestations that lead to joint destruction. As a consequence, targeting of TNF and more recently of IL-17 has provided an important improvement in care. In addition to the local effects, the same cytokines have also systemic effects. Circulating cytokines can then act on endothelial cells. Our previous research has studied the effects of TNF and IL-17, used alone and combined on human endothelial cells (EC). We recently showed that IL-17, especially when combined with TNF, has procoagulant, pro-aggregation, and pro-thrombotic effects [142], [143]. All these effects are inhibited by the addition of statins [142], [143]. IL-17 may play a significant role in development of endothelial dysfunction and cardiovascular disease [144]. In the apoE deficient mice which have major vessel disease, IL-17A-blocking antibody reduced atherosclerotic lesion development, plaque vulnerability, cellular infiltration, and tissue activation (Smith et al., 2010) [145]. IL-17 deficient mice, when on high fat diet displayed significantly diminished aortic lesion size and macrophage accumulation [162].

Expanding these results to the human situation, a high peak of IL-17 plasma level was found in patients with unstable angina, if followed by myocardial infarction [146]. Thrombosis is the result of platelet aggregation and pro-coagulation activation in EC. To study the role of IL-17 in platelet aggregation, a functional assay with platelet rich plasma (PRP) was performed. Supernatants of EC treated with

IL-17 and TNF were added to PRP and ADP, acting as an agonist of platelet aggregation. Aggregation was monitored by changes in light transmittance in a lumiaggregometer. IL-17 alone enhanced the level of platelet aggregation from 20 % to 45-50 % (p=0.001). Similar effect was seen with TNF combined to IL-17. Regarding the effects on coagulation, IL-17 and TNF induced synergistically a massive expression of tissue factor (F3, 15-fold), a key player to initiate the coagulation cascade. Furthermore, IL-17 and TNF induced plasminogen activator mRNA expression by 6-fold with an additive effect. Conversely, IL-17 in combination with TNF inhibited by 10-fold the expression of thrombomodulin, an inhibitor of coagulation, thus increasing the EC pro-thrombotic phenotype. Microarrays identified CD39, an inhibitor of platelet aggregation, among the genes inhibited by IL-17. The preserved function of CD39/ATPDase is crucial in the inhibition of platelet activation by keeping adenosine nucleotide levels low to inhibit platelet aggregation. After 12h of incubation with IL-17, TNF and their combination, CD39mRNA expression was divided by 3.7. Thus, IL-17A was able to induce an imbalance between a pro-thrombotic and anticoagulant phenotype. These results were the basis for development of the models of interactions between IL-17 and TNF, and genes expressed by activated EC.

4.2.2 Coagulation cascade

Endothelial cells of the vessel wall produce tissue factor (TF, T_f), tissue factor pathway inhibitor (TFPI), thrombomodulin (TM, T_m) and CD39. TF acts as the initiator of the blood clotting process in blood plasma by activating factors IX and X (B). The resulting enzymes activate prothrombin (P) which is produced in liver and circulates in the bloodstream, and creates thrombin (T). A low amount of thrombin is able to rapidly generate more thrombin in a self-accelerated reaction. Thrombin then acts as an enzyme in activation of fibrinogen (F_g) to fibrin (F). Through a polymerisation process fibrin monomers create a net of fibrin polymers (F_p) which solidifies blood plasma. This mechanism ensures a quite rapid closure of possible vessel wall injuries and reduces a potential blood loss. We have shown the part of the coagulation cascade considered in this work in Fig. 4.8. Blood coagulation needs to be triggered only in situations when it is necessary, while otherwise it needs to be prevented. Blood haemostasis hangs on a delicate balance of the involved blood factors, and as such it needs to be quite robust.

There are multiple fail-safe mechanisms which prevent spontaneous blood coagulation and limit the clot growth in a case of an injury (preventing vessel occlusion). The first one is the production of TFPI by EC which acts as an inhibitor of TF and prevents the initiation of the coagulation process. CD39 prevents adhesion of platelets to the vessel wall. Protein C is activated in presence of thrombin and inhibits slowly the thrombin generation. However, in presence of thrombomodulin, which is also produced by EC, the activation of protein C is increased by a factor of thousand-fold, hence increasing the inhibition of the thrombin production. Another mechanism is the direct inhibition of thrombin by antithrombin (AT, A).

In the case of the vessel wall inflammation due to presence of IL-17 and TNF-α in the blood stream, the EC are affected and their production of blood factors is altered. The production of procoagulation factors is increased, while the production of anticoagulation factors is severely decreased. Additionally, the production of TFPI and CD39 is reduced, allowing the platelets to more easily adhere to the vessel wall and disabling the haemostatic system in preventing spontaneous coagulation.

4.2.3 Modelling, using the *in vitro* results

In this work we develop a model and carry out numerical simulations of clot growth taking into account the influence of IL-17 and TNF-α. We show that they promote blood coagulation and clot growth and they can lead to partial or complete vessel occlusion. We develop a simplified analytical model which allows us to obtain explicit conditions of thrombosis. We have previously used the same approach to determine the conditions on prothrombin and antithrombin which potentially results in an exagerrated or insufficient thrombus development. Various approaches are employed to study clot growth. Equations of chemical kinetics are used to describe reactions between the coagulation factors [4], [147], platelet activation and formation of platelets plug [148]. Reaction-diffusion equations for the concentrations of

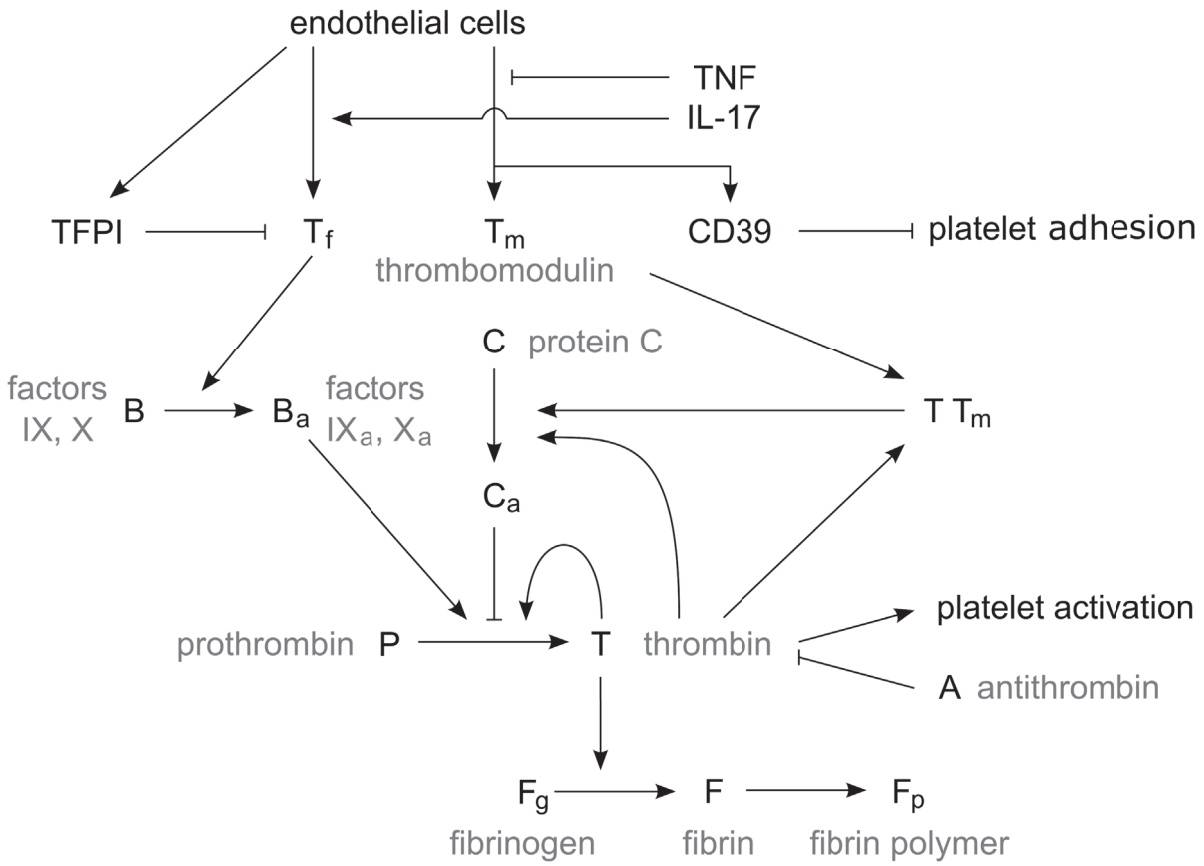

Figure 4.8: Simplified representation of blood coagulation (see the explanation in the text).

blood factors take into account their spatial distribution [149], [150]. These distributions are influenced by hemodynamics. Blood flow can be modelled with partial differential equations or with particle methods. Navier-Stokes equations are used if blood is considered as a Newtonian fluid [152], [101], and various viscoelastic models if non-Newtonian properties of blood are taken into account [152], [42]. Clot growth can be modelled as a free boundary problem where the interface separates blood flow from the clot region [117].

Another approach considers blood flow and clot as a continuous medium where clot is described as a high viscosity or a non-Newtonian fluid [152], [118]. Clot can also be described as a porous medium with an additional resistance term in the Navier-Stokes equations [64] describing fluid velocity deceleration inside the clot. In order to model platelets, both particle and continuous methods were used. Among the particle methods, the immersed boundary method was used in [66], cellular Potts model [67], dissipative particle dynamics in [42], [52], [69], [151], [70]. Advection-diffusion-reaction were also used to model platelet concentration (in their active and non-active forms) [148]. In hybrid models, particle methods are used to describe blood flow and blood cells and PDEs to describe concentrations of blood factors [69], [151].

In this work we begin with the analysis of blood coagulation in quiescent platelet free plasma in order to determine the influence of IL-17 and TNF-α and identify the values of parameters (Section 4.2.4). We continue with numerical simulations of blood coagulation in flow using two different approaches. In the first one, blood flow is described with the Navier-Stokes equations, while the concentrations of blood factors and of platelets with reaction-diffusion equations (Section 4.2.5). In the second approach, blood flow and platelets are modeled with a particle method, while the distribution of blood factors, as before, with reaction-diffusion equations (Section 4.2.6). The first method is more appropriate to study venous thrombosis with relatively low blood flow velocity. The second method is better for arteries and larger flow velocities where platelet aggregation is more important. We describe here platelets interaction (forces, attachment, detachment) in more detail. Numerical simulations are completed by

an approximate analytical approach which allows us to identify different regimes of clot growth and conditions of vessel occlusion (Section 4.2.7).

4.2.4 Modelling blood coagulation and thrombosis

In the mathematical model of blood coagulation we consider a rectangular 2D domain representing a section of a blood vessel. The source of blood factors can be either at the inflow boundary, if they are produced elsewhere and circulate in the blood stream, or at the vessel wall, if they are produced there under normal and pathologic conditions (vessel wall injury, vessel wall inflammation).

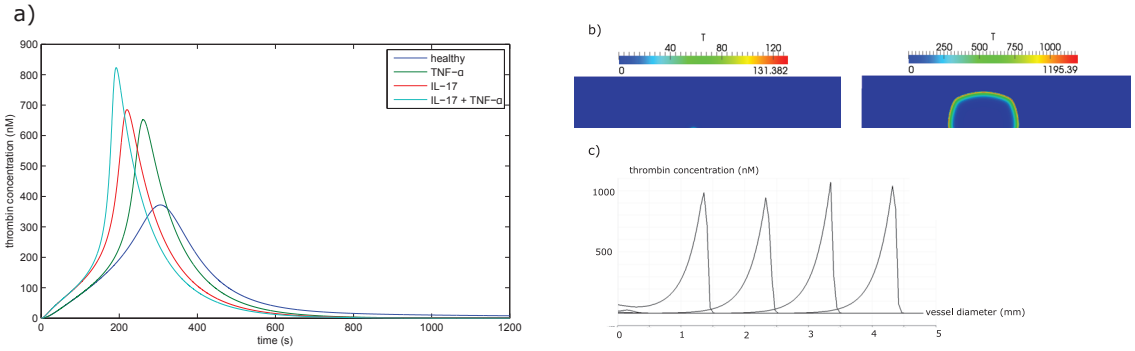

Figure 4.9: a) Thrombin generation curves in the normal case and in the excess of IL-17, TNF-α and their combination. b) Thrombin distribution during clot formation in a quiescent plasma. In the presence of IL-17 only a small clot forms near the wall, while if IL-17 and TNF-α are both present, clot grows up to the opposite wall of the vessel resulting in complete occlusion. c) Thrombin distribution along the middle line of the clot (perpendicular to the vessel wall) in consecutive moments of time.

Clot growth in quiescent plasma

The evolution of thrombin concentration in time (without space distribution) is one of the main characteristics of blood coagulation in plasma. In Fig. 4.9-a, we compare the thrombin generation profile of a healthy patient with those with perturbed tissue factor (T_f) and thrombomodulin (T_m) concentrations due to IL-17 and TNF-α [30]. The results show that in the absence of spatial dynamics, the hypercoagulability is more increased by IL-17 than by TNF-α. The highest thrombosis risk was observed when the effect of the two proteins is combined. Through fitting the thrombin generation curves, we estimated that RA increases the concentration of TF by twofold, while it decreaes the concentration of TM by 20 %.

Next, we consider clot growth in quiescent plasma in a rectangular domain representing a part of blood vessel. There is an inflamed part of the vessel wall where T_f expressed. It is the interval of 0.5 mm length at the center of the lower boundary (Fig. 4.9-b). We compare two cases where the upregulation of TF due to IL-17 is considered. In the first simulation, we neglect the inhibitory action of TNF-α on thrombomodulin. In spite of the excessive level of TF due to IL-17, the thrombin wave does not propagate because of the inhibitory action of activated protein C (APC). It is produced at intact parts of the vessel wall from both sides of the lesion due to the complex of T_m with thrombin. As the result, a small and limited clot forms over the inflamed region (Fig. 4.9-b).

We consider now the case where the action of TNF-α is taken into account. It downregulates the expression of thrombomodulin at the intact neighbouring parts of the wall. As a result, the concentration of TM is reduced, decreasing also the rate of activation of protein C. The generated APC is not sufficient to stop the formation of the clot (Fig. 4.9-b). The distribution of thrombin concentration along the middle line of the clot (perpendicular to the vessel wall) is shown in (Fig. 4.9-c) at successive moments of time. This distribution has a form of localized spike moving from the boundary towards the inside of

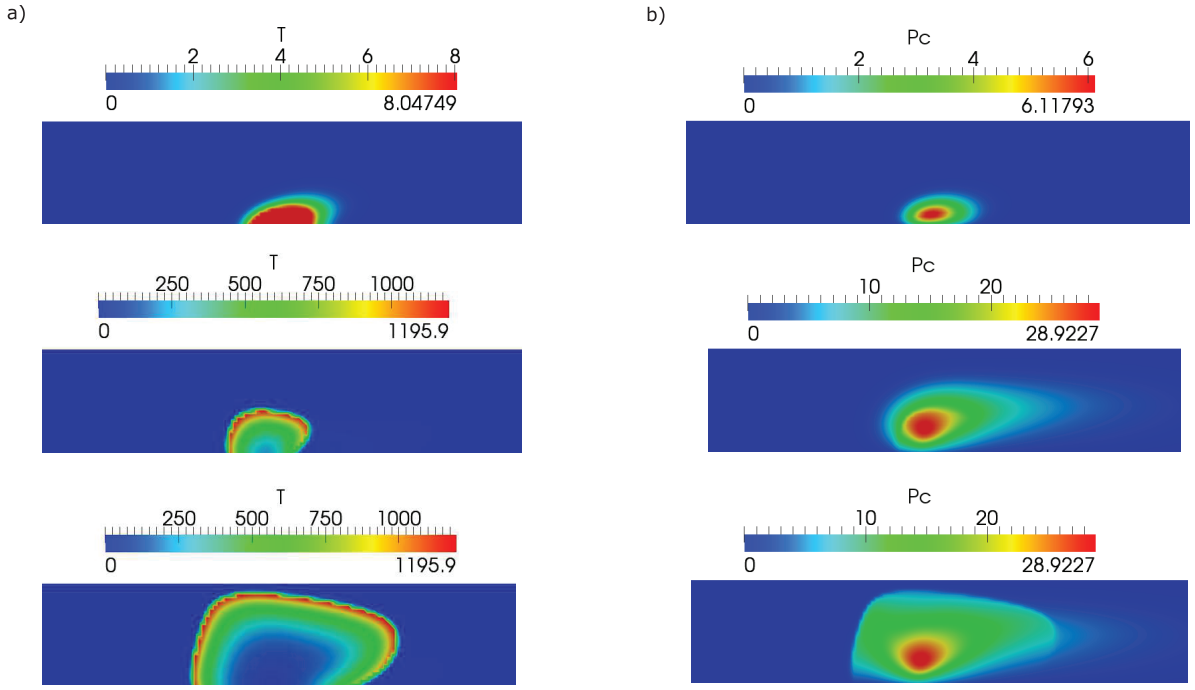

Figure 4.10: Clot growth under the joint action of IL-17 and TNF-α. Thrombin distribution (a) and platelet aggregation (b) are shown at consecutive moments of time. The clot fills the whole vessel cross section leading to a complete vessel occlusion.

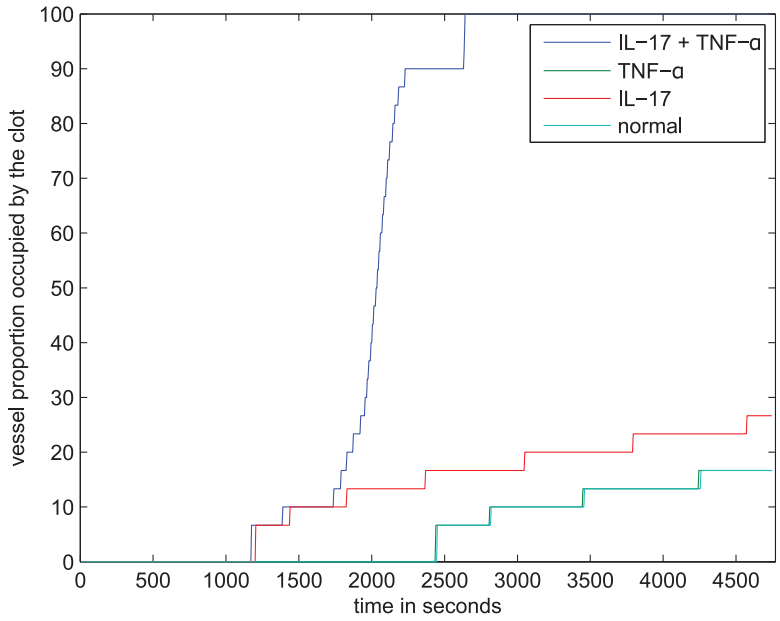

Figure 4.11: Dynamics of clot growth in the case of separate or joint action of IL-17 and TNF-α. TNF-α has no effect on thrombus development in quiescient plasma and when the inflammed tissue is sufficiently wide, the corresponding curve coincides with the normal case.

the vessel. It is a travelling wave solution of the corresponding reaction-diffusion system of equations of blood coagulation. Conversion of fibrinogen into fibrin and clot formation occurs behind the moving zone of thrombin formation.

4.2.5 The influence of blood flow

We describe thrombus formation under a pressure driven blood flow with a low shear rate of 13 s^{-1}. The vessel diameter is set as 1.5 mm. We consider a fixed inflamed region of the blood vessel wall with the length 400 μm. If the inflamed tissue length is relatively small, then the individual actions of IL-17 or TNF-α are not sufficient to trigger the propagation of the clot. Hence, a normal haemostatic response is observed. As a result, a small clot is formed and the flow is not perturbed (not shown).

A joint action of IL-17 and TNF-α initiates clot growth. It results in the complete occlusion of the vessel. Fig. 4.10 shows thrombin distribution (a) and platelets in the clot (b) at three consecutive moments of time. Thrombin distribution resembles that for the case of clot growth in a quiescent plasma, but here the flow breaks the symmetry of thrombin distribution by moving it downstream. The interaction of thrombin and platelets play an important role in clot growth. Thrombin activates platelets and promotes platelet attachment from the flow to the platelets in the clot. Platelet attachment and detachment will be discussed in more detail in the next section. On the other hand, the surface of activated platelets converts prothrombin into thrombin (similar to vessel wall) reinforcing thrombin production. Thus, there is a positive feedback between thrombin generation and platelet aggregation. Hence, TNF-α reinforces platelet adhesion especially when combined with IL-17.

Dynamics of clot growth in normal and inflamed cases are shown in Fig. 4.11. In the normal case (without IL-17, TNF-α) the clot does not grow. Its grows rate is maximal under the joint action of the inflammation factors.

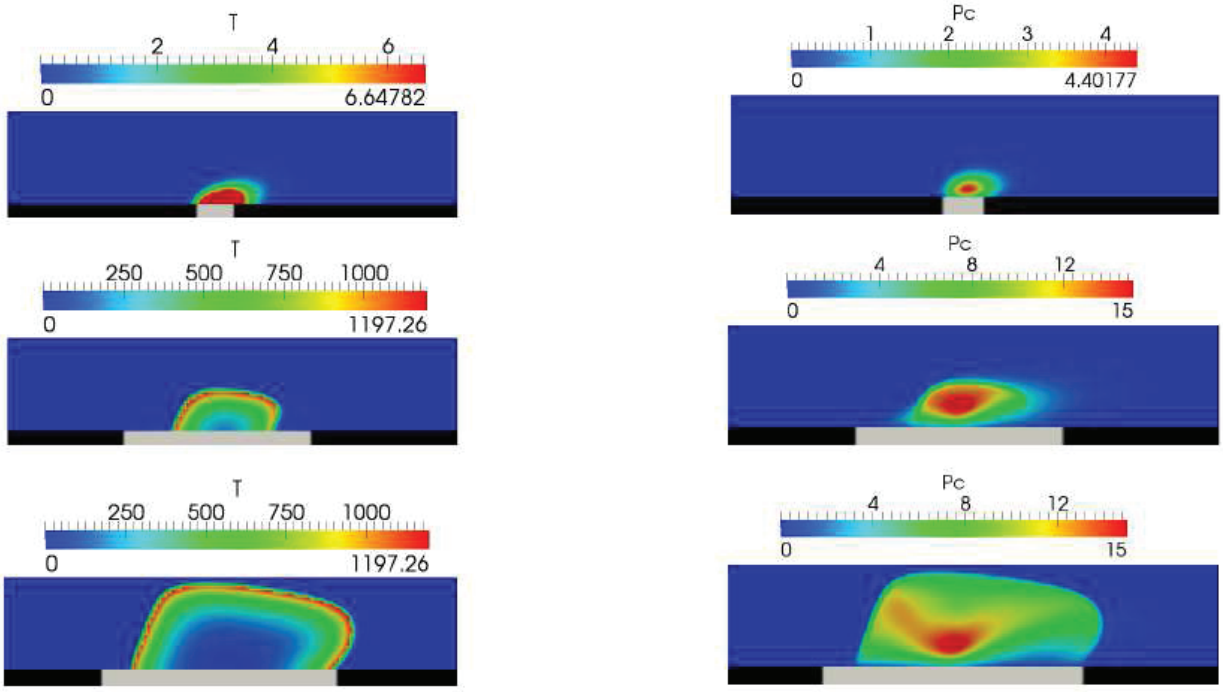

Figure 4.12: Snapshot of thrombin distribution (left column) and platelet aggregation (right column) for different sizes of lesions (grey interval at the vessel wall).

One of the important parameters that determine thrombus formation and growth is the size of the lesion and its evolution in time. There are some experimental data [153] confirmed by modelling [154], (Chapter 3) which show how the risk of vessel occlusion depends on the lesion size. However, it is not known how it grows in time in the case of chronic inflammation. Therefore, we vary this parameter in the model, and we observe its influence on thrombus growth (Fig. 4.12).

4.2.6 Platelet aggregation model

Clot growth consists of two main processes and of their interaction: biochemical reactions in blood plasma resulting in production of fibrin polymer and platelet aggregation. Platelet aggregation is a complex multi-stage process which consists of different mechanisms. These mechanisms include platelet attachment to the clot and its possible detachment, platelet activation, different adhesion forces acting between platelets due to different receptors involved, platelet interaction with fibrin and some other blood factors. In order to study platelet aggregation in more detail, we use a DPD-PDE model developed in [70]-[69]. In this method, dissipative particle dynamics (DPD) is used to describe the motion of blood flow and platelets, while partial differential equations (PDE) are used for the concentration of blood factors in plasma.

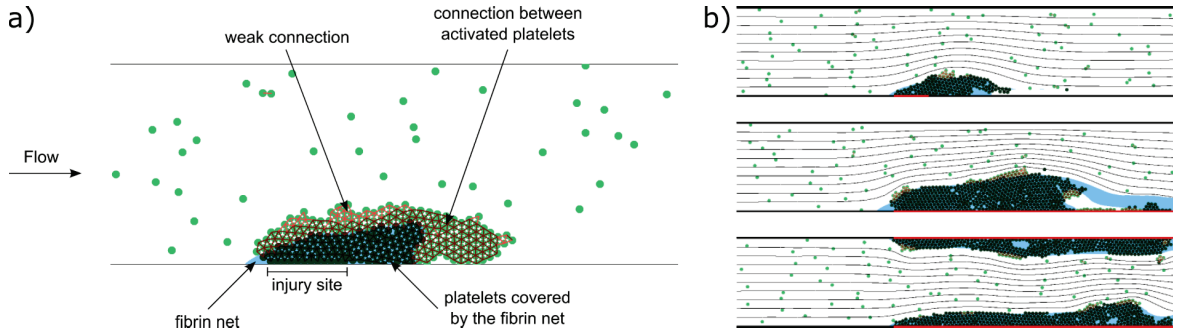

Figure 4.13: a) A scheme of clot structure (snapshot from a simulation). Connections between platelets are shown as red intervals between their centres. Light red lines correspond to weak GPIb connections, dark red to medium connections between activated platelets, and black to strong connections between platelets covered by a fibrin net. Dark green platelets are covered by fibrin net, which is marked by blue color. b) Final stages of clot growth for different sizes of inflamed areas of vessel wall (shown in red). From top to bottom: short inflamed area at the bottom wall, long area at the bottom wall, long area at both walls. The black lines denote flow streamlines.

This approach is more appropriate to study clot growth in arteries where the flow velocity is relatively high, and platelet aggregation becomes a dominant factor. We have shown in the previous works [69], [70] that initial platelet aggregate protects blood factors from the flow allowing the initiation of fibrin production. On the other hand, fibrin clot reinforces platelet aggregate against the action of the flow.

Since platelets are considered as individual objects, their number and, consequently, the vessel diameter becomes a limiting factor for numerical simulations. In all presented simulations the diameter of the vessel was 50 μm, while the mean flow speed in the undisturbed flow was 12.5 mm/s. The diameter of platelets was set to 2 μm. The density and the viscosity of the simulated medium correspond to the density of viscosity of blood plasma [69], [70], [155]. A more complete list of values of model parameters is given in Appendix B.

A typical clot structure is shown in Fig. 4.13-a. There are three types of platelet connections, weak (light red lines between their centres), medium (dark red lines) and strong (black lines). Medium connections appear if platelets are weakly connected during the time period t_c. Hence we model platelet activation and emergence of medium connections as a time delay. Platelets covered by fibrin are shown with dark green color, platelets not covered by fibrin with light green. Weak and medium platelet connection can be disrupted by flow. In this case individual platelets or their aggregates can be detached and roll over the clot or leave the clot completely. Platelets covered by fibrin polymer (strong connection) cannot be detached.

Fig. 4.13-b shows results of simulations for three different cases of coagulation initiated by inflammation. Images show the final stages of clot growth for different sizes of inflamed areas. Inflamed parts of the vessel wall are shown in red. In the first case the inflamed site is short and situated at the bottom wall. In the second and third case the inflamed site is longer, and is situated at the bottom wall and

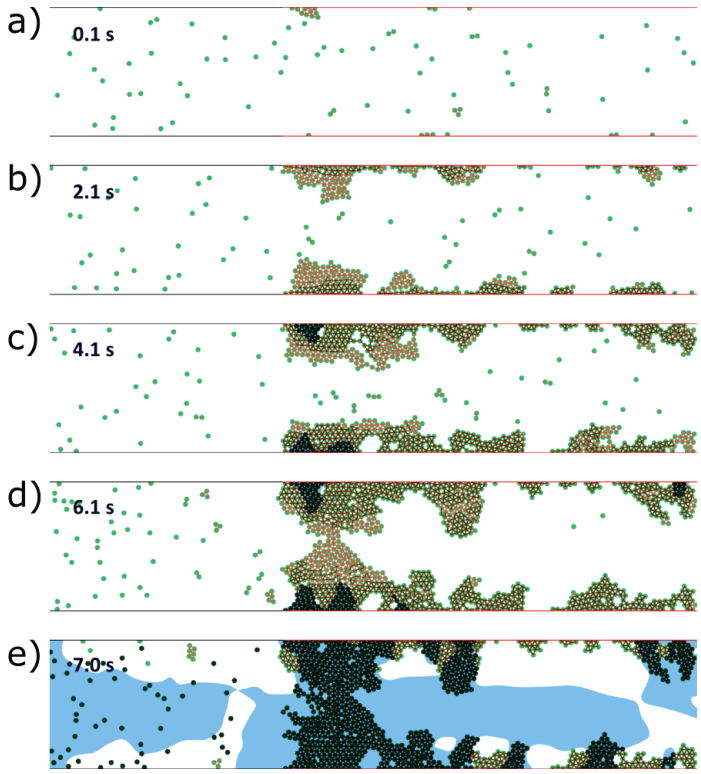

Figure 4.14: Vessel occlusion in the case of inflamed walls on both sides and reduced flow speed. Inactivated platelets begin to aggregate at the inflamed parts of the vessel walls. After a short time delay they activate and reinforce their connections (a and b). Flow velocity decreases inside platelet aggregate stimulating accumulation of thrombin near the wall and production of fibrin polymer (c). The latter makes platelet connection unbreakable by the flow and leads to further growth of platelet clot. The flow speed decreases allowing thrombin production inside the vessel. Finally, fibrin polymer fills the vessel resulting in its complete occlusion (d and e). Green dots are platelets, blue colour shows the region with high concentration of fibrin polymer.

both walls respectively. In the second case the clot was occupying the whole length of the inflamed site, however a part of it has been detached by flow.

In all three cases shown in Fig. 6-b, the coagulation process and the platelet adhesion at the inflamed site are results of presence of IL-17 in blood at the critical concentration. Fig. 4.14 shows an example of evolution of a complete vessel occlusion under condition of reduced flow speed. In the simulation both vessel walls are inflamed, resulting in platelet aggregation on both sides of the vessel as blood clotting occurs at both vessel walls (the formation of the fibrin net).

4.2.7 Conditions of occlusion

In this section we reduce the complete model presented in the appendix to a simplified model which admits an analytical solution and explicit conditions of vessel occlusion:

- the reaction-diffusion system of equations describing the distribution of blood factors is reduced to a single equation for thrombin concentration,

- the blood flow velocity is approximated by the Poiseuille (parabolic) profile,

- the distributions of factors IX and X initiating thrombin production near the vessel wall due to tissue factor are taken in the stationary form to which they converge after a long time.

- Platelets are considered to be exclusively activated by soluble thrombin.

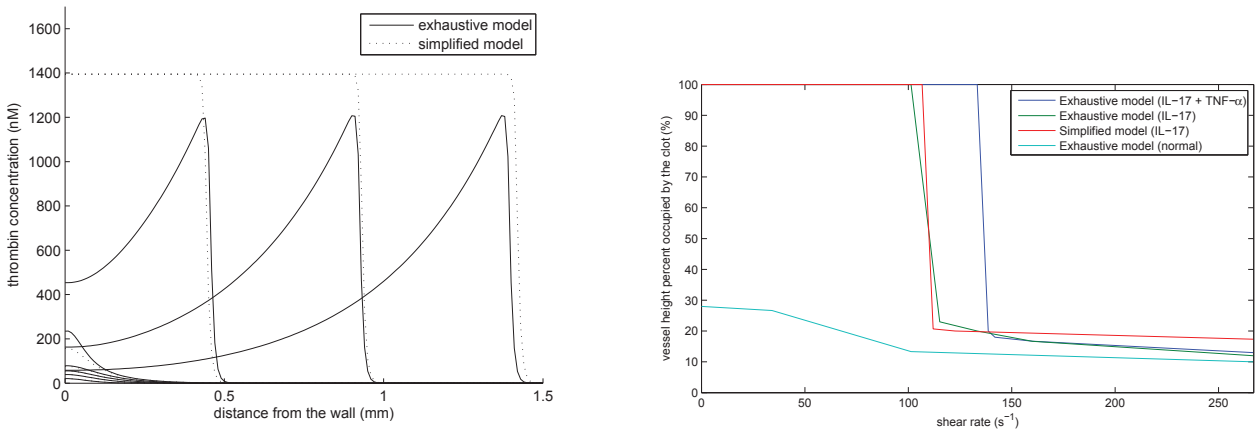

Figure 4.15: Thrombin distribution at successive moments of time in the complete model at the middle line of the clot perpendicular to the vessel wall (solid line) and in the one-dimensional approximate model (dashed line) (left). The final clot size as a function of the maximal flow velocity in the complete model (right).

As a result of these approximations we obtain the following equation for the thrombin concentration:

$$\frac{\partial T}{\partial t} = D\frac{\partial^2 T}{\partial y^2} + \Phi(T,y), \tag{4.2.17}$$

where

$$\Phi(T,y) = (k_1^+ T\phi_0 + k_2 B_a(y) + k_3^+ T^3)(P_0 - T) - \gamma(y)T,$$

D is the diffusion coefficient, P_0 is the prothrombin concentration initially present in blood flow, the first term on the right-hand-side of the equation describes prothrombin activation by platelets, the second denotes its activation by factors IX, X ($B_a(y)$), the third term represents the generation of thrombin the amplification phase. The function $\gamma(y) = k_4 A_0 T + av(y)T$ shows the influence of antithrombin and of flow velocity $v(y) = 4\frac{v_m}{H^2}y(H-y)$ in the downregulation of thrombin production. Here H is the width of the vessel, v_m is the maximal flow velocity at its axis. The function $B_a(y)$ describes the distribution of factors IXa and Xa. It is a solution of the equation:

$$B_a'' - k_7 A_0 B_a = 0, \quad B_a'(0) = \frac{\alpha T_f (B^0 - B_a)}{1 + \beta(B^0 - B_a)} \tag{4.2.18}$$

given in the form $B_a(y) = \lambda e^{-y/\sigma}$, where $\sigma = 1/\sqrt{k_7 A_0}$, and λ can be found from the boundary condition.

Equation (4.2.17) is considered in the interval $0 < y < H$, which corresponds to the cross section of the vessel, with the no-flux boundary conditions

$$y = 0, H: \ \frac{\partial T}{\partial y} = 0. \tag{4.2.19}$$

The simplified model gives a good approximation of the speed of clot growth in a quiescent plasma and of the conditions of vessel occlusion in flow (Chapter 2). In this work we use this approach to study the influence of inflammation on clot growth. To further simplify the study, the activation of prothrombin by plaelets will not be considered in what follows. Fig. 4.15 (left) shows a comparison of the thrombin distributions in the complete model (Chapters 2 and 3) and in the simplified model (4.2.17), (4.2.18). The distribution of thrombin propagates in space due to self-accelerating cascade of coagulation reactions. In the case of the complete model (solid curves) the concentration of thrombin is measured at the center of the clot in the direction perpendicular to the vessel wall. Thrombin distribution has a specific form with a

maximum at the reaction front and with a gradual decay behind it due to its elimination by anthithrombin. The 1D model shows the same dynamics with the same speed of propagation but thrombin profile is monotone in space since the single equation model cannot describe the concentration decay. Except for this difference, it gives a good quantitative approximation of the complete model. Let us note that in the case under consideration, the value of parameter k_3^+ in the simplified model is fitted since it effectively takes into account the joint action of several factors in the complete model.

In order to analyze clot growth described by equation (4.2.17), we begin with a particular case where the function $\Phi(T,y)$ is replaced by the function

$$\Phi_0(T) = k_3^+ T^3(P_0 - T) - k_4 A_0 T.$$

This means that we neglect the boundary effects of clot initiation and the blood flow (quiescent plasma). If $P_0^3 < (27k_4A_0)/(4k_3^*)$, then this function has three zeros, $T = 0$ and T_1, T_2, where $T_0 < T_1 < T_2$. The equilibria $T = 0$ and $T = T_2$ are stable as solutions of the corresponding ODE, while $T = T_1$ is unstable. Thus, we obtain a classical reaction-diffusion equation in the bistable case. If it is considered on the whole axis, it has travelling wave solutions, that are solutions of the form $T(x,t) = W(x - ct)$, where W is a solution of the equation

$$DW'' + cW' + \Phi_0(W) = 0, \;\; W(-\infty) = T_2, \;\; W(\infty) = 0,$$

and c is the speed of propagation. In the case of a positive speed c, such solution describes clot growth. It is known that the wave speed is positive if and only if

$$\int_{T_0}^{T_2} \Phi_0(T)dT > 0. \tag{4.2.20}$$

If we consider the boundary effects and a parabolic velocity distribution, then the function $\Phi(T,y)$ depends on the space variable y, and the problem is considered on the interval $0 < y < H$, which corresponds to the cross section of the vessel in the direction perpendicular to the walls located at $y = 0$ and $y = H$. In this case, travelling wave solution cannot be defined in the strict mathematical sense, and we consider its approximation. We assume that the wave front (thrombin distribution) is sufficiently sharp. This assumption is biologically realistic due to a strong self-acceleration to the thrombin production. Then we consider a quasi-stationary approximation of the wave for each y fixed. This approximation allows us to formulate an explicit condition of clot growth. Instead of condition (5.2.1) we now have the inequality

$$I(y) \equiv \int_{T_0}^{T_2} \Phi(T,y)dT > 0, \tag{4.2.21}$$

where T_0 and T_2 depend, in general, on y. This condition can be satisfied for some values of y and not satisfied for some other values. The clot starts growing if $I(0) > 0$ and stops growing if $I(y_0) \le 0$ for some $y_0 > 0$.

Condition (4.2.21) shows the influence of the boundary and of the flow on clot initiation and propagation. The function $B_a(y)$ describes the distribution of factors IX and X and their contribution to thrombin production. It increases the function $\Phi(T,y)$ near the wall and promotes the initiation of clot growth. However, it decays exponentially and its influence becomes negligible sufficiently far from the vessel wall. On the contrary, the flow velocity $v(y)$ is low near the wall and attains its maximal value at the axis of the vessel. It decreases the function $\Phi(T,y)$ removing thrombin from the reaction zone. Therefore, blood flow acts to stop clot growth. If $I(H/2) \le 0$, then the flow velocity is high enough to stop clot growth. Otherwise, clot overpasses the axis of the flow with the maximal flow velocity and it continues to grow until it reaches the opposite vessel wall. This case corresponds to the complete vessel occlusion.

The explicit form of the condition $I(0) > 0$ allows us to determine the critical concentration of tissue factor at the wall for which clot growth begins:

$$T_f^* = \frac{\lambda^*(e^{-h/\sigma} - 1)}{h\alpha_1(B^0 - \lambda^* e^{-h/\sigma})} \left(1 + \beta_1(B^0 - \lambda^* e^{-h/\sigma})\right). \tag{4.2.22}$$

Here

$$\lambda^* = \frac{1}{k_2(P_0 - T_2/2)} \left(k_1 \phi_0 (P_0 - T_2/2) + k_3^+ T_2^3 (P_0/4 - T_2/5) - k_4 A_0 T_2/2 \right).$$

Since inflammation essentially increases the expression of tissue factor at the vessel wall, it can initiate clot growth.

Next, we express from (4.2.21) the flow speed as a function of the space point y which stops clot growth:

$$v_1(y) = \frac{1}{a} \left(2k_2 B_a(y) \frac{P_0}{T_2} - k_2 B_a(y) + k_3 \frac{T_2^2 P_0}{2} - 2k_3 \frac{T_3^3}{5} - k_4 A_0 \right). \tag{4.2.23}$$

If $v_1(y)$ exceeds $v(y) = v_m y(H - y)$ for some values of y, then blood flow stops clot growth, otherwise complete occlusion occurs. Fig. 4.15 (right) shows a comparison of the numerical simulations of the complete model with the analytical results. The size of the clot (percentage of the vessel cross section) is shown as a function of the maximal flow velocity. For the complete model, the maximal velocity changes in the process of clot growth. So the maximal velocity is taken at the initial moment of time when the velocity profile is the same as in the approximate model. The green line shows the results of numerical simulations of the complete model where only IL-17 is taken into account, and the blue line for the combination of IL-17 and TNF-α. The red line shows the results obtained using the analytical formula. It gives a good approximation of the complete model.

We observe a sharp transition from the complete occlusion to a finite clot size with the increase of flow velocity. Such transition was also observed in *in vitro* experiments [153]. The combined effect of IL-17 and TNF-α acts stronger to promote complete occlusion.

Chapter 5

A Multiscale Model to Describe the Recovery from Acute Blood Loss due to Bleeding

5.1 Biological background

In mammals, hematopoietic stem cells (HSCs) proliferate and differentiate in the bone marrow to form the erythrocytes, platelets and the cells of the immune system of the blood. Within this hematopoietic process, the erythroid lineage begins with committed erythroid progenitor cells that differentiate into morphologically identified erythroblasts, which subsequently differentiate and enucleate to form reticulocytes. Reticulocytes enter the circulation via the marrow venous sinuses. In the blood, the irregularly shaped reticulocytes mature into uniform, biconcave erythrocytes. Normal adult humans produce $3 \cdot 10^9$ reticulocytes per kg of body mass per day [156]. These reticulocytes replace the same number of erythrocytes that are recognized as senescent and removed daily from the circulation. Blood loss or excess erythrocyte destruction (hemolysis) decreases the numbers of circulating erythrocytes resulting in acute anemia. Acute anemia causes tissue hypoxia that, in turn, induces stress erythropoiesis, a process in which erythrocyte production is increased until the numbers of circulating erythrocytes are restored to normal. Under both normal and stress conditions, erythropoiesis is tightly regulated, and its dysregulation results in various disorders including anemia, polycythemia, and leukemia.

5.1.1 Erythroid cells

Bone marrow is the site of normal erythropoiesis in both mice and humans. However, during hypoxic stress accompanying severe anemia, mice greatly expand erythropoiesis in the spleen, whereas humans expand erythropoiesis in the bone marrow. The structural unit of mammalian erythropoiesis is the erythroblastic island (EBI), which consists of a central macrophage surrounded by as many as several dozen erythroid cells, beginning at colony-forming units-erythroid (CFU-Es) and extending through the reticulocyte stage [157]. CFU-Es, which are operationally defined by their growth in tissue culture [158], and their immediate progeny, the proerythroblasts (Pro-EBs), which are defined by their morphological appearance, are considered erythroid progenitor cells. However, purified CFU-Es have the morphological appearance of Pro-EBs [159, 160] and, as CFU-Es and Pro-EBs have become recognized by expression of specific surface proteins [161, 162, 163], an overlap in these two stages is likely. Therefore, we have used the term CFU-E/Pro-EB to describe the erythroid progenitor stage at which the fate decisions are made.

CFU-E/Pro-EBs may have three possible fates: programmed cell death by apoptosis, proliferation without further differentiation (self-renewal), and terminal differentiation into reticulocytes. CFU-E/Pro-EB fate is determined by a complex interaction of intracellular proteins that has not been completely elucidated and that appears to vary in different biological models. CFU-E/Pro-EBs apoptosis is mainly

regulated by FAS, a membrane protein of the TNF receptor family that is activated by Fas ligand. Among all erythroid cells, CFU-E/Pro-EB display the most Fas on their surface membranes [164, 165]. Fas ligand is produced by both erythroid cells and non-erythroid cells in the hematopoietic organs. An important difference between humans and mice is that, among erythroid cells in the EBI, mature late-stage erythroblasts are the main source of FAS-ligand in humans [164], whereas CFU-E/Pro-EB and immature erythroblasts produce most FAS-ligand of hematopoietic origin in mice [165].

Differentiation from HSCs through the CFU-E/Pro-EB stage requires the hematopoietic growth factor Kit ligand/stem cell factor (KL/SCF) [166]. The CFU-E/Pro-EBs lose their KL/SCF requirement and become dependent upon the hormone erythropoietin (EPO) to prevent apoptosis [167, 168]. This EPO dependency persists throughout the period when the CFU-E/Pro-EBs make their fate decisions. EPO is produced by the kidneys in quantities that are inversely and exponentially proportional to the number of erythrocytes in blood [169]. Through specific receptors (EPO-R) on erythroid progenitors, EPO prevents apoptosis via down-regulation of FAS and up-regulation of Bcl-xL, an anti-apoptotic protein [164, 165, 170]. Thus, EPO is the major regulator of erythropoiesis that directly links tissue hypoxia caused by decreased circulating erythrocytes to rates of new erythrocyte production.

Enhanced murine splenic erythropoiesis during hypoxic stress is mediated by bone morphogenetic protein 4 (BMP4), a protein produced by other hematopoietic and non-hematopoietic cells [171]. BMP4 expression in the mouse spleen increases self-renewal of erythropoietic progenitors including the CFU-E/Pro-EBs. Differentiation of erythroid progenitors and erythroblasts depends upon multiple transcription factors including, most prominently, GATA1, the zinc finger-containing component of transcription factor complexes that binds to the DNA sequence (A/T)GATA(A/G). GATA1 is required for both the differentiation of HSCs to the erythroid-committed progenitor stages and terminal differentiation of the CFU-E/Pro-EBs to reticulocytes [172]. These complexities of erythroid differentiation related to species, organ, and stress conditions limit the current understanding of erythropoiesis, and mathematical modeling of this fundamental biological process may contribute to overcome these difficulties.

5.1.2 Erythropoietin regulation

EPO is mainly regulated by the amount of oxygen delivered to the EPO-producing cells in the kidney. EPO levels are low during normal, non-anemic conditions, but during anemia RBCs are decreased, the delivery of oxygen to the tissues is decreased, and EPO production increases exponentially. Tissue hypoxia in the kidneys leads to increased EPO production by increasing the intracellular amount of hypoxia-inducible factor 2-alpha (HIF2-α), the transcription factor that promotes EPO gene transcription, in the EPO-producing cells. When oxygen supply is normal, hydroxylation of two specific prolines in the HIF2-α protein leads to its rapid degradation by the ubiquitin-proteasome pathway. The increase in HIF2-α in the EPO-producing cells during anemia is due to less oxygen being available for the hydroxylation of the two specific prolines in HIF2-α [173].

Erythroid cells require large amounts of iron to make the heme, the oxygen-carrying part of hemoglobin. The erythroid cells accumulate iron from the plasma by endocytosis of diferric transferrin that binds to the transferrin receptor 1 (TfR1) on the cell surface membrane [174]. When the availability of iron is insufficient to maintain erythropoiesis, anemia results. Iron deficiency affects EPO regulation of erythropoiesis by limiting the production of EPO, relative to other anemias of similar severity, by restricting HIF2-α mRNA translation [175]. However, iron deficiency enhances EPO receptor responsiveness through the expression of another transferrin receptor, transferrin receptor 2 (TfR2) [178]. Thus, plasma EPO levels may be partially restricted during iron deficiency, but responsiveness to EPO in erythroid progenitor cells may be increased. When iron levels increase in the body with the administration of iron supplements, the EPO values decrease as the anemia resolves and oxygen delivery improves, thereby decreasing the stability of HIF2-α as hydroxylation of its prolines increases. Also, as iron levels increase, the EPO-R responsiveness decreases. In the model, these effects of iron on EPO concern the erythroid cells at the CFU-E/Pro-EB stages during which decisions about survival/differentiation/apoptosis are made. The CFU-E/Pro-EB stages precede the hemoglobin production stages of differentiating erythroblasts (Fig. 5.1).

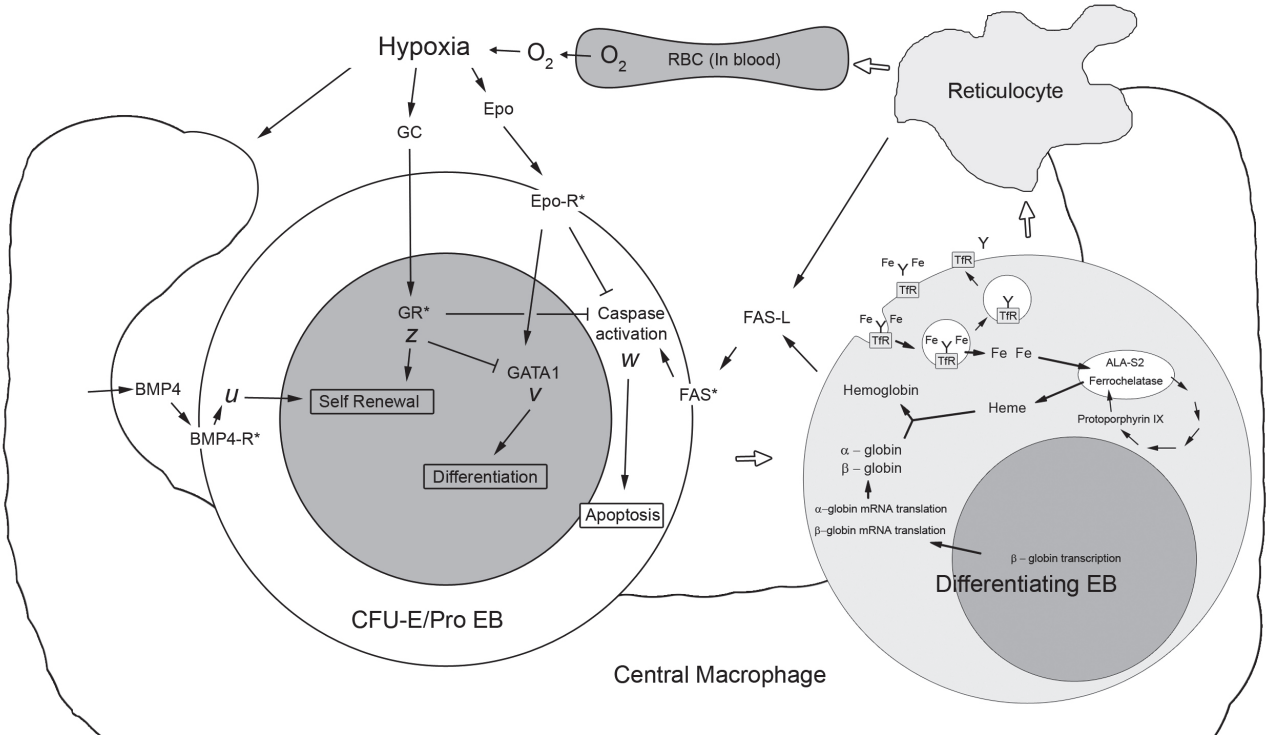

Figure 5.1 : Model of an erythroblastic island showing a central macrophage with adherent sequential erythroid cell differentiation stages. The stages, which are separated by open arrows, are the colony forming units-erythroid/ proerythroblast (CFU-E/ProEB), the differentiating erythroblast, and the reticulocyte. Also shown is the mature red blood cell (RBC),which is formed after the reticulocyte enters the circulating blood and completes maturation. RBCs circulate in the blood, and their major cytoplasmic protein, hemoglobin, delivers oxygen (O_2) from the lungs to the other tissues. Under normal conditions, about 1% of circulating RBCs turnover daily, as senescent RBCs are removed from bloodand replaced by reticulocytes that enter the blood from the marrow. When the number of circulating RBCs decreases due to increased rates of blood loss or RBC destruction, the resulting tissue hypoxiaincreases RBC production until the number of blood RBCs recovers to the normal range. In CFU-E/Pro-EBs, decisions about their fate depend upon the respective concentrations of: 1) activated glucocorticosteroid receptor(z), which determines the rate of self-renewal in normal, steady-state erythropoiesis and in limited hypoxic states in which adjustments of only EPO concentrations maintain a stable number of circulating erythrocytes, 2) activated BMP4 receptor (u), which determines the rate of expansion of CFU-E/Pro-EBs during hypoxic stress, 3) GATA1 (v),which determines the rate of terminal erythroid differentiation, and 4) activated caspases (w), which determine the rate of apoptosis when elevated and the rate of terminal erythroid differentiation when reduced.

Major extracellular mediators that affect the intracellular variables include respective concentrations of: 1) glucocorticosteroid hormone (GC), which is produced by the adrenal glands and varies with the degree of hypoxic stress, 2) BMP4, which is produced by central macrophages and increases with hypoxic stress, 3) EPO, which is produced by the kidneys and varies inversely with the degree of hypoxic stress, 4) FAS, which is expressed on CFU-E/Pro-EB and varies inversely with the EPO concentration, and 5) FAS-ligand, which is produced by other erythroid cells in the erythroblastic island, CFU-E/ProEBs in mice and late stage erythroblasts and reticulocytes in humans. In differentiating erythroblasts, intracellular iron concentration regulates heme synthesis, heme concentration regulates globin synthesis, and heme and globin concentrations determine the rate of hemoglobin accumulation. Iron is imported by endocytosis of diferric transferrin that binds transferrin receptors (TfRs), which recycle after releasing iron. Intracellular iron controls heme synthesis by two mechanisms: 1) increasing the concentrations of the first enzyme in the heme synthesis pathway, erythroid-specific, mitochondrial enzyme amino-levulinatesynthetase 2 (ALA-S2) and 2) acting as a substrate of the last enzyme in the pathway, ferrochelatase, which regulates iron incorporation into protoporphyrin IX to form heme. Intracellular heme increases β-globin transcription by derepression of the inhibitory transcription factor Bach1 and stimulates translation of α-globin and β-globin mRNAs by allosteric derepression of the heme regulated inhibitor (HRI) of translation. Reticulocytes, which are formed by erythroblast enucleation, continue heme synthesis until they lose internal organelles during their maturation to the RBC stage, which is completed after entry into the blood.

5.1.3 Hemoglobin production

With stable extracellular concentrations of transferrin-bound iron, the rate of iron transport into erythroid cells during the differentiating stages in the EBIs is stable until the reticulocyte stage. Iron transport rate declines in reticulocytes as transferrin receptors, ribosomes and mitochondria are degraded in this final stage of differentiation. In erythroid cells, the intracellular iron pool or "in transit" fraction is stable and small in size with iron that is not used in heme synthesis being exported from the cell via ferroportin.

In erythroid cells undergoing terminal differentiation, imported iron is inserted into protoporphyrin IX forming heme, the oxygen-carrying part of hemoglobin. This incorporation of iron into heme occurs in mitochondria and is controlled by ferrochelatase, an enzyme that itself contains iron-sulfur clusters (see Fig. 5.1). Iron controls heme synthesis by regulating an early step in porphyrin synthesis that occurs in the mitochondria, the production of amino-levulinate (ALA), which is mediated by the erythroid-specific enzyme amino-levulinate synthetase 2 (ALA-S2). Iron regulates the translation of ALA-S2 mRNAs into protein via the binding of iron regulatory proteins (IRPs) to an iron responsive element in the 5' untranslated region of ALA-S2 mRNAs [174, 179]. When intracellular iron is low, increased IRP activity decreases ALA-S2 concentrations and, conversely, as intracellular iron increases, ALA-S2 concentrations increase (Fig. 5.1).

Heme regulates globin production by allosteric derepression of β-globin transcription and of α-globin and β-globin mRNA translation by binding to the Bach1 transcription factor [180] and heme-regulated inhibitor (HRI) [181], respectively (Fig. 5.1). However, heme is not consumed in the production of globin. The degradation of heme is regulated by heme oxygenase-1 (HO-1), and intracellular heme can be decreased by its export from erythroid cells via FLVCR1a [182, 183] Heme also regulates iron import into the erythroid cell through its effects on transferrin receptor expression and the acquisition of iron from transferrin [174].

For the globin chains, in addition to the Bach1 and HRI control of synthesis, the newly made α-globin chains are stabilized by binding to α-hemoglobin stabilizing protein (AHSP), and β-globin chains can form stabilizing tetramers of the β-hemoglobin chains that prevent denaturation and precipitation that lead to their removals from the erythroid cell [184].

Intracellular concentration of the normal complete hemoglobin tetramers (2 α chains and 2 β chains) increases until the completion of the reticulocyte maturation. In the erythroid cells in the EBIs of the marrow and in circulating reticulocytes and mature RBCs, denatured hemoglobin accumulates slowly, and it is removed from the cell by formation of small vesicles enriched in the denatured hemoglobin that are shed from the membrane [185, 186].

5.2 multiscale model

The multiscale model of erythropoiesis consists of the following submodels: intracellular regulation of erythroid cell fate in the bone marrow, extracellular regulation of erythroid progenitors in the bone marrow, intracellular hemoglobin production by erythroid progenitors, erythropoietin production in the kidney. The model developed in this work is based on the previous studies in [85].

5.2.1 Erythroid cells dynamics

In EBIs, erythroid cells can divide with or without differentiation and die by apoptosis. Their fate is determined by the intracellular regulation which is determined by the concentrations of some proteins (Section 5.2.2) and it is influenced by the extracellular regulation (Section 5.2.3).

Because erythroid cells divide and increase their number, they can push each other resulting in cell displacement relative to the central macrophage. In order to describe mechanical interaction between cells, we restrict ourselves to the simplest model in which cells are presented as elastic spheres. We consider two elastic spheres with centers at the points x_1 and x_2 and with the radii, respectively, r_1 and r_2. If the distance h_{12} between the centers is less than the sum of the radii, r_1+r_2, then there is a repulsive force between them, f_{12}, which depends on the difference between (r_1+r_2) and h_{12}. If a particle with center at x_i is surrounded by several other particles with centers at the points $x_j, j = 1,...k$, then we consider the pairwise forces f_{ij} assuming that they are independent of each other. This assumption corresponds to small deformation of the particles. Hence, we find the total force F_i acting on the i-th particle from other particles, $F_i = \sum_i f_{ij}$. The motion of the particles can now be described as the motion of their centers by Newton's second law

$$m\ddot{x}_i + m\mu\dot{x}_i - \sum_{j\neq i} f_{ij} = 0,$$

where m is the mass of the particle, the second term in the left-hand side describes the friction by the surrounding medium, and the third term is the potential force between cells. We consider the force between particles in the following form

$$f_{ij} = \begin{cases} K\frac{h_0-h_{ij}}{h_{ij}-(h_0-h_1)} & , \quad h_0-h_i < h_{ij} < h_0 \\ 0 & , \quad h_{ij} \geq h_0 \end{cases},$$

where h_{ij} is the distance between the particles i and j, h_0 is the sum of cell radii, K is a positive parameter, and h_1 accounts for the incompressible part of each cell. This means that the internal part of the cell is incompressible. It allows us to control compressibility of the medium. The force between the particles tends to infinity when h_{ij} decreases to h_0-h_1.

Before division, cells increase their size. When two daughter cells appear, the direction of the axis connecting their centers is chosen randomly from 0 to 2π. Cell cycle duration is taken to be 18 hours with a random perturbation uniformly distributed between -3 and 3 hours [192]. Intracellular and extracellular regulations and equations of motion represent the main features of the hybrid model of erythropoiesis. More detailed description of the hybrid model is given in [191]. The two-dimensional model considered in this work is appropriate to describe the experiments in cell cultures where the third dimension can be neglected.

We consider that the time spent by erythroblasts in the bone marrow after their decision to differentiate is $72 \pm \varepsilon$ hours, where ε is a random value that follows a random distribution with a standard deviation of 11 hours. Reticulocytes leave the bone marrow into the blood flow where they terminate

their maturation and become erythrocytes. In humans, studies of ferrokinetics and reticulocyte maturation patterns in the blood showed that release of reticulocytes into the blood was much more rapid during erythropoietic stress than under normal steady-stage conditions [194, 195]. Based on these studies, a moderately severe phlebotomy-induced anemia induced by a one-time loss of 25% blood volume should result in about two days of marrow erythroblast differentiation followed by decreased reticulocyte retention in the marrow of only a few hours compared to the normal steady-state marrow reticulocyte retention period of one day or slightly longer. The life span of erythrocytes in blood is 120 days (for humans). In the model, we count the number of cells leaving the bone marrow and the number of cells accumulating in blood. Therefore, we get the total amount of hemoglobin in blood. The latter determines EPO production by the kidney (Section 5.2.4).

5.2.2 CFU-E/Pro-EBs regulation

We consider a simplified model of intracellular regulation of erythroid cell fate based on the following differential equations

$$\frac{dz}{dt} = a_0, \quad \frac{du}{dt} = a_1 + b_1 z, \quad \frac{dv}{dt} = a_2 - b_2 z v, \quad \frac{dw}{dt} = a_3 - b_3 z w \tag{5.2.1}$$

for the concentration z of glucocorticoid receptors, u of the BMP4 receptors, v of GATA1 and w of caspase (the concentrations z, u, v and w are nondimensional). They determine the choice of erythroid progenitors between self-renewal, differentiation and apoptosis (Fig. 5.1).

Here z is the concentration of activated glucocorticosteroid receptor (GR). The value of a_0 depends on the extracellular concentration of GC. For a fixed concentration, it is a constant. Next, u is the combined concentrations of activated KIT and activated BMP4-R, which determines cell self-renewal and depends on the concentrations of KL/SCL and BMP4. Hence, a_1 depends on these combined concentrations. The second summand in the right-hand side of the second equation takes into account that self-renewal can be up-regulated by GR. Cell differentiation is determined by a relatively complex sub-scheme based on the transcription factor GATA1. In order to simplify this regulation and to avoid introduction of additional parameters, we will keep only one variable v, which describes the concentration of GATA1. The value of a_2 depends on the extracellular EPO concentration. Finally, w denotes the activated caspase concentration which determines cell apoptosis and depends on the intracellular FAS concentration which, in turn, depends upon the extracellular FAS-ligand concentration. Apoptosis is down-regulated by EPO (through a_3) and by GR taken into account through the last term in the right-hand side of last equation. These are the main features of the regulatory mechanism. Some others are not taken into account in the simplified model because they are less essential, but they can be easily introduced. We give the values of the parameters a_1, a_2, a_3 as follows:

$$a_0 = a_0^0 + a_0^1 GC, \quad a_1 = a_1^0 + a_1^1 S, \quad a_2 = a_2^0 + a_2^1 E, \quad a_3 = a_3^0 + a_3^1 F,$$

where GC describes the concentration of GC, S is the sum of the concentrations of BMP4 and KL/SCF, E is the EPO concentration, F denotes the level of FAS-ligand.

We suppose that cell fate is determined by the values of the variables u, v, w. Namely, if at some moment of time w (caspase) reaches its critical value w_{cr}, then the cell dies by apoptosis. The variables u (KIT + BMP4-R) and v (GATA1) are compared at the end of the cell cycle. If $u > v$, then the cell divides and self-renews, otherwise it divides and differentiates.

5.2.3 Extracellular regulation in the bone marrow

Erythroid cells produce FAS-ligand, F, which influences the surrounding cells by increasing intracellular FAS activity. The FAS-ligand-producing erythroid cells are mainly immature erythroblasts in murine erythropoiesis [165] and mainly the mature erythroblasts in human erythropoiesis [164]. The production of FAS-ligand by reticulocytes decreases exponentially as they mature due to the degradation of their internal organelles. We describe the FAS-ligand production rate in each reticulocyte by

$$W_1(t) = \exp(-\gamma_W (t - \tau)),$$

where τ is the time of their enucleation and γ_W is a positive paramter. On the other hand, macrophages produce a growth factor S, which stimulates erythroid cell proliferation. In mice, S is KL/SCF in normal erythropoiesis and BMP4 in stress erythropoiesis. We denote the sum of the concentrations of both these proteins by S. The concentrations of FAS-ligand and S in the extracellular matrix are described by the reaction-diffusion equations :

$$\frac{\partial F}{\partial t} = D_1 \Delta F + W_1 - \sigma_1 F, \tag{5.2.2}$$

$$\frac{\partial S}{\partial t} = D_2 \Delta S + W_2 - \sigma_2 S. \tag{5.2.3}$$

Here D_1, D_2 are diffusion coefficients and W1, W2 are the rates of production of the corresponding factors. These functions are proportional to the concentrations of the corresponding cells. In numerical simulations, where cells have a finite size, they are considered as distributed source terms in the equations (5.2.2) and (5.2.3). The last terms in the right-hand sides of these equations describe their degradation. The concentrations F and S are adimensionalized such that their values change between 0 and 1. The computations are carried out in dimensionless length units in such a way that the initial cell diameter corresponds to one unit. The computation domain is a square with the side equal 100 length units. In dimensional variables we consider cell diameters to be 10 microns.

5.2.4 EPO regulation

In the present multiscale model, we characterize each RBC by its age and the concentrations of iron (Fe) and hemoglobin that it accumulated being in the bone marrow. The accumulated hemoglobin constitutes the hemoglobin concentration contained in the RBCs in the reference blood volume. During its maturation, the reticulocyte loses its adherence to the central macrophage, and remains in the marrow for a variable length of time before entering the blood via a venous sinus in the marrow. The reticulocyte completes its maturation in the blood. After entering the blood, the reticulocyte disappears from the computational domain, and the population of RBCs in blood increases by one. As a result, the hemoglobin level in blood also increases. After 120 days of its lifetime, the RBC dies, and it is removed by erythrophagocytosis. Consequently, the hemoglobin level in blood decreases by the amount contained in the RBC. Most of the iron contained in the RBC is recycled back to the bone marrow by macrophages, and it is added to the extracellular iron. Under normal steady-state conditions, the number of reticulocytes entering the blood and the number of senescent RBCs removed from the blood are regulated so that the hemoglobin content and attendant tissue oxygen delivery by the circulating blood are maintained.

EPO release depends on the level of hemoglobin with respect to the normal level. EPO regulates the survival of CFU-E in the marrow through the threshold above which activated caspase triggers apoptosis. Furthermore, it upregulates the differentiation of CFU-Es by increasing GATA1. The concentration E of EPO is then given by the relation:

$$E(t) = \begin{cases} E_0 + \gamma_1 \exp\left(\widehat{Hb}^0 - \widehat{Hb}(t)\right) & \text{if } \widehat{Hb}^0 \geq \widehat{Hb}(t) \\ E_0 - \gamma_1 \exp\left(\widehat{Hb}(t)\right) - \widehat{Hb}^0) & \text{if } \widehat{Hb}^0 < \widehat{Hb}(t) \end{cases},$$

where E_0 is a basic EPO level, $\widehat{Hb}^0$ is the normal hemoglobin level in blood and $\widehat{Hb}(t)$ is its current level, γ_1 is a positive parameter. The critical level of caspase is considered in the form

$$w_{cr}(t) = w_{cr}^0 + \gamma_2 E, \tag{5.2.4}$$

where w_{cr}^0 is the basic level and γ_2 is a positive parameter.

5.2.5 Hemoglobin production

We will consider the following equations for the intracellular concentrations of iron Fe, heme H, globin G, hemoglobin Hb:

$$\frac{dFe}{dt} = k_1 Fe_{ex} - k_2 Fe - k_3 Fe, \tag{5.2.5}$$

$$\frac{dH}{dt} = k_3 Fe - k_4 H - 4k_5 HG, \tag{5.2.6}$$

$$\frac{dG}{dt} = k_6 H - 4k_5 HG - k_7 G, \tag{5.2.7}$$

$$\frac{dHb}{dt} = k_5 HG - k_8 Hb. \tag{5.2.8}$$

The first term in the right-hand side of equation (5.2.5) describes iron influx from the extracellular space, the second term its efflux from the cell, the third term is consumption for the production of heme. In equation (5.2.6), the terms in the right-hand side are heme production $k_3 Fe$, heme degradation and transport from the cell $k_4 H$, heme consumption for the production of hemoglobin $k_5 HG$. In the third equation, there is a globin production regulated by heme $k_6 H$, its consumption for the production of hemoglobin $k_5 HG$, and its degradation $k_7 G$. Finally, in the last equation, the two terms are hemoglobin production and degradation.

The system 5.2.5-5.2.8 is used in two different contexts. In the first, it is used as an independent model to describe hemoglobin production in cultured mouse erythroid cells. In Section 5.3.1, we describe how the data obtained from mouse erythroid cell cultures are exploited to estimate the value of parameters occurring in 5.2.5-5.2.8. In Section 5.3.2, this system is then used as part of the multiscale model in order to describe hemoglobin production in differentiating erythroid cells in the context of the bone marrow. We assume here that the parameter values determined with mice data can be transposed to human, at least in a first approach. Exceptions are for k_1 and k_3 which decrease in reticulocytes due to the degradation of TfRs and internal organelles. We mimic the results obtained in *in vitro* experiments by adjusting these two parameters for a constant iron influx. We approximate these results by decreasing the parameter k_1 by 4/5 and the parameter k_3 by 6/7 after erythroblast enucleation.

5.2.6 Iron concentration in the bone marrow

Differentiating erythroid cells import large amount of iron. In our model, we assume that the cells have an average (constant) volume V_{cell}, each cell takes up $k_1 Fe_{ex} V_{cell}$ over dt. Now we consider a small volume V^{BM} of human bone marrow containing 8 EBIs and $N_{diff}(t)$ differentiating cells. We estimate V^{BM} to be about 0.3 nL. The variation of extracellular iron concentration over dt due to uptake is $N_{diff}(t)\ k_1 Fe_{ex} V_{cell}/V^{BM}$.

In the model, we also consider that each differentiated erythroid cell maintains the iron and hemoglobin that it accumulated during its maturation in the bone marrow. The RBCs released into the blood remain in the bloodstream for 120 days, when they are recognized as senescent by macrophages, which remove them from the circulating blood by phagocytosis. The hemoglobin of the phagocytosed RBCs is degraded, and the iron removed from the hemoglobin is recycled by macrophages and returned to the bone marrow bound to plasma transferrin. Considering these three processes, the concentration of extracellular iron in the bone marrow is described by the following equation:

$$\frac{dFe_{ex}}{dt} = \alpha + \beta I(t) - N_{diff}(t)\ k_1^{BM} Fe_{ex}, \tag{5.2.9}$$

where α is the rate of bone marrow iron influx from intestinal absorption or mobilized non-RBC sources including liver storage, $\beta I(t)$ denotes the part of iron contained in phagocytosed RBCs and recycled by macrophages, and $k_1^{BM} = k_1 V_{cell}/V^{BM}$.

Modelling the dynamics of erythroblastic islands and hemoglobin production by differentiated cells provides two essential outputs: the number of reticulocytes leaving the bone marrow at each time step, and the quantity of hemoglobin each RBC accumulated during its differentiation and maturation.

5.3 Results

5.3.1 Intracellular hemoglobin production

In modeling complex biological phenomena the identification of parameter values is always a critical problem due to the paucity of kinetic data. Here the situation is rather favorable. We have been able to use four data sets [196]-[199] to determine the values of the 8 kinetic parameters contained in the model of hemoglobin production presented in Section 5.2.5.

These experiments were performed on cultures of erythroid cells from the spleens of mice during their differentiation from the CFU-E/Pro-EB stage through the time of reticulocyte formation. The general scheme is to add radiolabels (^{59}Fe or ^{3}H-leucine) at different time points, continue the culture for a given time duration and then measure the quantity of ^{59}Fe incorporated in heme or ^{3}H-leucine incorporated in β-major globin. In order to exploit this kind of experiment we wrote two extended systems of equations: the first contains additional equations for the evolution of ^{59}Fe-containing species (intracellular ^{59}Fe itself and radioactive heme and hemoglobin); the second contains additional equations for the evolution of ^{3}H-leucine-containing globin and hemoglobin. In other words each specific type of experiment is simulated by a corresponding system of differential equations.

The first data set (Table 2 in [197]) allowed us to estimate k_1 (see equation 5.2.5). We make the approximation that the flux of iron uptake is approximately constant and equal to 250 atoms/fL/min. In the conditions of this experiment the concentration of ^{59}Fe:Tf in the culture medium is 200 μg/mL. We take the molecular mass of glycosylated, iron-saturated Tf (diferric) as being equal to 80 kDa, and we obtain $k_1 = 1.4 \cdot 10^{-3} s^{-1}$.

For the other 7 kinetic parameters (and 3 initial concentrations) we have to resort to a systematic search. It is known [200] that the IRP concentration decreases down as differentiation proceeds. Because IRP activity represses the biosynthesis of protoporphyrin IX (Fig. 1), which is inversely related to internal Fe concentration, the rate of heme production increases with time. To take this into account we consider that parameter k_3 is time dependent, defined as follows: $k_3(t) = a_{k3} + (b_{k3}t)^4$. With this function, the increase is slow during the first hours and becomes steeper in the later stages of differentiation. A linear time dependence was tried, but, it did not provide a good adjustment to the experimental data. We thus have 8 parameters related to kinetics in total.

Briefly, the method is the following. For each unknown quantity we define a search interval (spanning several orders of magnitudes). The cartesian product of these intervals defines a multidimensional search box in parameter space. We draw a large number of random points in that box, and for each parameter point we perform simulations and compare with experimental data. The simulations we perform mimic the experimental protocol of each particular data set. In order to sample equally all the orders of magnitude, the sampling is done on a logarithmic scale. We use the quasi-Monte Carlo method [201] with the Sobol sequence. For each data set we quantify the agreement between simulated (x_{calc}) and measured (x_{meas}) quantities by computing the following residual:

$$R_q = \frac{\sum_i abs(x_{calc}(i) - x_{meas}(i))}{\sum_i x_{meas}(i)} ,$$

where q identifies one of the three remaining data sets and the sum index i includes the measurements belonging to that data set. A further complication come from the fact we only have access to relative experimental concentrations, we thus have to determine a scale factor for each data set. More details are given in the appendix.

Each data set is associated with a threshold, and we keep as potential solutions all parameter points which satisfy $R_q \leq M_q$, where M_k is the threshold of the kth data set. Since we have 3 data sets, we have 3 constraints of this type. It is, in general, not possible to minimize all 3 residuals simultaneously. In order

Parameters	Min	Max	p_1	p_2	p_3	p_{mean}	Units
k_2	$1.0e^{-10}$	$5.81e^{-9}$	$1.61e^{-10}$	$1.22e^{-10}$	$6.0e^{-10}$	$3.78e^{-10}$	s^{-1}
a_{k3}	$3.43e^{-9}$	$1.47e^{-8}$	$1.42e^{-8}$	$7.70e^{-9}$	$9.25e^{-9}$	$7.4e^{-9}$	s^{-1}
b_{k3}	$6.89e^{-7}$	$7.36e^{-7}$	$7.2e^{-7}$	$7.13e^{-7}$	$7.15e^{-7}$	$7.2e^{-7}$	$s^{-\frac{5}{4}}$
k_4	$3.82e^{-4}$	$5.16e^{-4}$	$3.95e^{-4}$	$4.63e^{-4}$	$4.30e^{-4}$	$4.47e^{-4}$	s^{-1}
k_5	$2.87e^{-6}$	$1.01e^{-5}$	$5.59e^{-6}$	$6.48e^{-6}$	$5.71e^{-6}$	$7.27e^{-6}$	fL.molecules^{-1}.s^{-1}
k_6	$3.94e^{-4}$	$5.68e^{-4}$	$4.74e^{-4}$	$5.10e^{-4}$	$4.31e^{-4}$	$4.47e^{-4}$	s^{-1}
k_7	$2.48e^{-10}$	$5.08e^{-7}$	$4.46e^{-8}$	$2.88e^{-10}$	$3.01e^{-7}$	$4.97e^{-10}$	s^{-1}
k_8	$1.01e^{-5}$	$1.49e^{-5}$	$1.3e^{-5}$	$1.243e^{-5}$	$1.17e^{-5}$	$1.14e^{-5}$	s^{-1}
Fe_0	$2.99e^{+2}$	$6.07e^{+2}$	$3.10e^{+2}$	$3.46e^{+2}$	$3.27e^{+2}$	$3.21e^{+2}$	atoms/fL
ε_1			0.220	0.235	0.239	0.238	NU
ε_2			0.239	0.228	0.238	0.238	NU
ε_3			0.225	0.238	0.199	0.200	NU
ε_{mean}			0.228	0.234	0.226	0.226	NU

Table 5.1: Results of the search procedure. Columns 2 and 3 define the box enclosing the set of valid points in parameter space. The following columns define the values for 4 particular solutions. Columns 4, 5 and 6 provide solutions corresponding to the minimum (within the set of found solutions) of R_1, R_2, and R_3, respectively. The following column is the one with the lowest average residual $(R_1+R_2+R_3)/3$. Fe_0 is the initial concentration of internal iron (not labelled). The concentration of external labelled iron (^{59}Fe) is 3000 atoms/fL, while the concentration of external iron Fe (not labelled) is 4 atoms/fL. NU denotes dimensionless units.

to retain only physiologically relevant solutions we also add constraints bearing on the concentrations reached at the end of the differentiation process.

Since there is no unique way to combine several experimental data sets and additional constraints, we present the results as a set of solutions (a cloud of points in parameter space). The 3 thresholds M_k are chosen equal to 0.25. The box enclosing the cloud of valid points is given in Table 5.1. This gives an idea of the spread of the set of solutions. It can be seen that most parameters are rather well defined, except k_2, and k_7. A scatter plot of the cloud of valid points on the plane $k_4 - k_5$ is displayed in Fig. 5.2 in order to visualize the shape of the cloud on that projection. The ratio between the volume of the region containing the cloud of valid points and the volume of the explored region (in logarithmic scale) is about $1.36e^{-19}$, as estimated with the Monte Carlo method. Table 5.1 shows 4 solutions we have selected in this set: the solutions p_1 ,p_2 , p_3 and p_{mean} which minimize R_1 , R_2, R_3 or $(R_1 + R_2 + R_3)/3$, respectively. Fig. 5.3 displays the evolution of the system with the p_{mean} values. This last solution is the one which has the lowest average residual $(R_1+R_2+R_3)/3$ within the solution set. It can be observed that internal iron concentration goes through a maximum and then decreases to low values. Hemoglobin concentration increases steadily to a value of about 10^2 molecules/fL.

5.3.2 multiscale model

Previously developed models of EBIs [85] are now extended to take into account hemoglobin production by erythroid cells. In this model, each differentiated cell accumulates the available extracellular iron in the marrow and produces hemoglobin according to the model presented in the previous section. In periods of hypoxia, differentiating erythroblasts differentiate into reticulocytes that leave the marrow at about 52 h by entering bloodstream where they become mature erythrocytes. The hemoglobin level in the body corresponds to the total concentration of hemoglobin in the RBCs contained in the bloodstream. If the level of hemoglobin is not sufficient to provide enough oxygen for the normal functioning of the organism, then the feedback by EPO regulates the differentiation and apoptosis of CFU-E/Pro-EBs. It

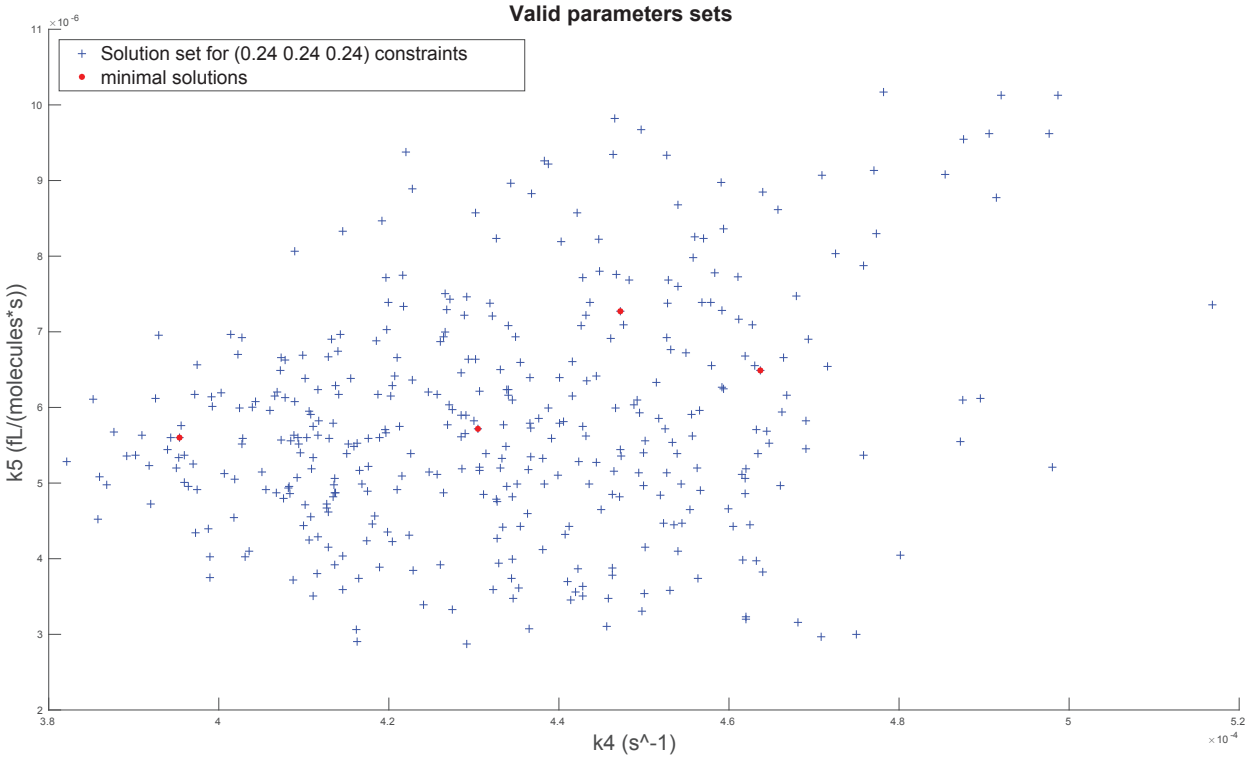

Figure 5.2: Projection of the cloud of valid points on the plane $k_4 - k_5$. The solutions p_1, p_2, p_3, p_{mean} are indicated in red.

adjusts production of erythrocytes and their release in blood. Hence, EPO regulates erythropoiesis to maintain hemoglobin at normal level through feedback control.

The blood reference volume conventionally used for hemoglobin measurement and RBCs count is one deciliter (dL). However, due to limitations in numerical simulations, we model a small section of the bone marrow with eight erythroblastic islands (EBIs). The ranges of RBCs in blood are normally 4.5 - 5.4 million RBCs/μL in men and 3.6 - 5.0 million RBCs/μL in women. Then in the simulations a section of the bone marrow producing 14000 - 15000 RBCs for a woman with 4 million RBCs per μL of blood corresponds to a blood reference volume $V^* = 3.75$ nL.

The acute loss of blood results in a sudden decrease of hemoglobin level. Because the hemoglobin is below the normal range, this corresponds to anemia, which produces tissue hypoxia. With this hypoxia, an additional quantity of EPO is produced in the kidney that stimulates an increased production of RBCs. The recovery from anemia takes about 10-14 days for humans, and the normal ranges of hemoglobin and RBCs are restored. To investigate the underlying mechanisms of anemia recovery, we carry out two simulations of erythropoiesis and hemoglobin production corresponding to two different persons (females). One of them loses 25% of her RBCs on the first day of the simulation. The second simulation corresponds to erythropoiesis under normal conditions. At the beginning of both simulations, EBIs have reached their steady state, which required about 120 days after the beginning of erythrocyte production (Fig.s 5.4a, 5.5). After the sudden blood loss, feedback control mediated by EPO leads to the increase of erythroid cells in EBIs. The number of erythroblasts reaches about 80 cells per EBI 3-5 days after blood loss (Fig.s 5.4b, 5.5a).

The number of cells undergoes stochastic variations since the duration of cell cycle is random. However, we can observe an increase in the overall number of both CFU-E and differentiated cells during 14 days of recovery period (Fig. 5.5). Hence in anemia, EPO increases both the differentiation and survival of CFU-E resulting in an increase of RBCs production. EPO level depends on the difference between the current and the normal levels of hemoglobin. Due to blood loss, the hemoglobin concentration drops

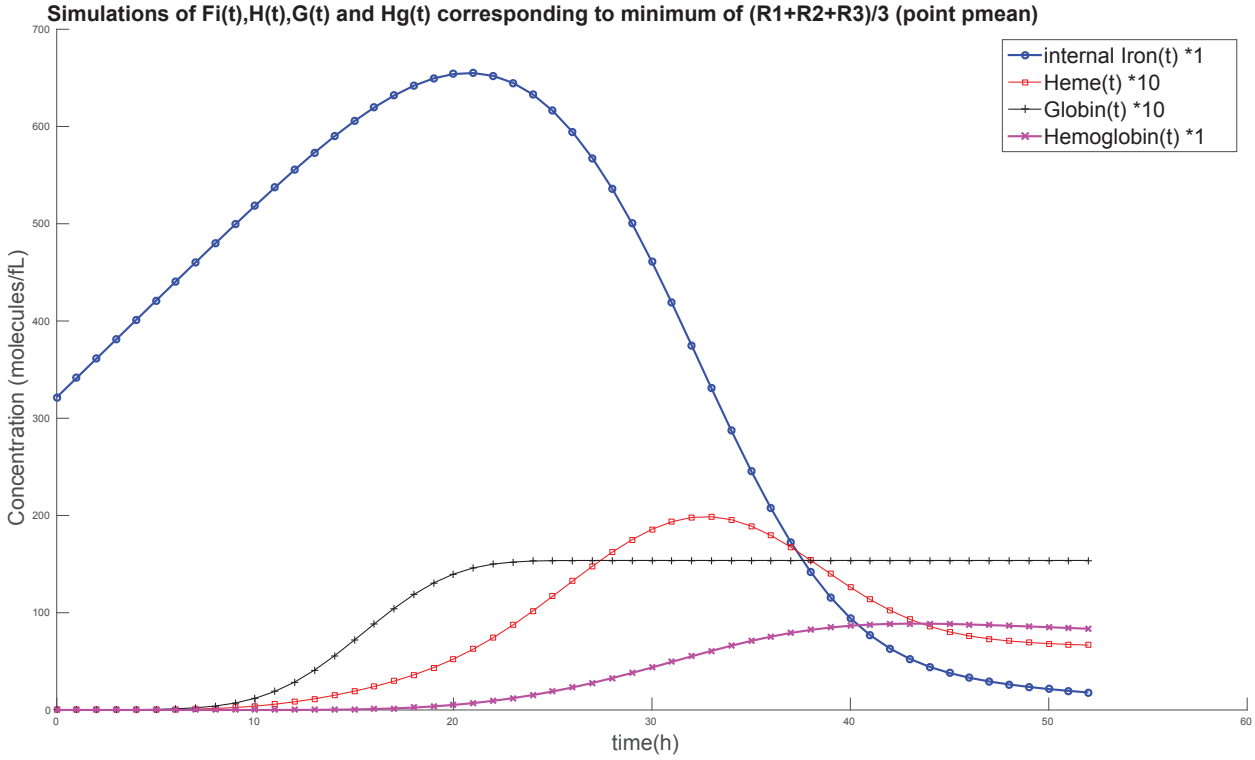

Figure 5.3: Evolution of the 4 concentrations computed with the parameter values identified as p_{mean} in Table 5.1.

below the normal level.

We show the level of EPO and the apoptosis threshold over time in Fig. 5.6. The production of RBCs increases during several days after blood loss. It takes about 14 days for the hemoglobin level to reach the minimal normal level, 12 g/dL for women. Then the hemoglobin level increases slowly and oscillates in the normal range. Since hemoglobin level increases at the same time with the increase of RBCs production, we impose an upper limit of $1.4e5$ mg/dL h on iron consumption by differentiated cells in the bone marrow. The number of RBCs and hemoglobin level are given in Fig. 5.7.

5.4 Discussion

The modeling effort presented herein clearly shows that complex biological phenomena such as erythropoiesis can be readily reproduced *in silico* as long as available knowledge can be synthesized in basic equations describing the main behavioral trends of the system under study. In the present case, the erythroblastic islands are multi-cellular hubs which integrate the variety of signals determining the cellular fate along the erythroid lineage. The end-points are the number of circulating RBCs and the provision of oxygen to tissues they provide, including to the kidney, the main oxygen-sensing EPO-producing organ.

The mutli-scale model presented in this study reproduces the main features of erythropoiesis and hemoglobin regulation both qualitatively and quantitatively. Modelling the dynamics of erythroblastic islands and hemoglobin production by differentiated cells provides two essential outputs: the number of reticulocytes leaving the bone marrow at each time step and the quantity of hemoglobin they accumulated during their maturation. Although we only considered eight EBIs due to limitations in the computational power, these two outputs are sufficient to simulate the population of RBCs and the concentration of hemoglobin in a reference volume of blood V^*. This volume corresponds to the space occupied by the steady-state number of RBCs produced by a section of the bone marrow containing eight EBIs. Scaling

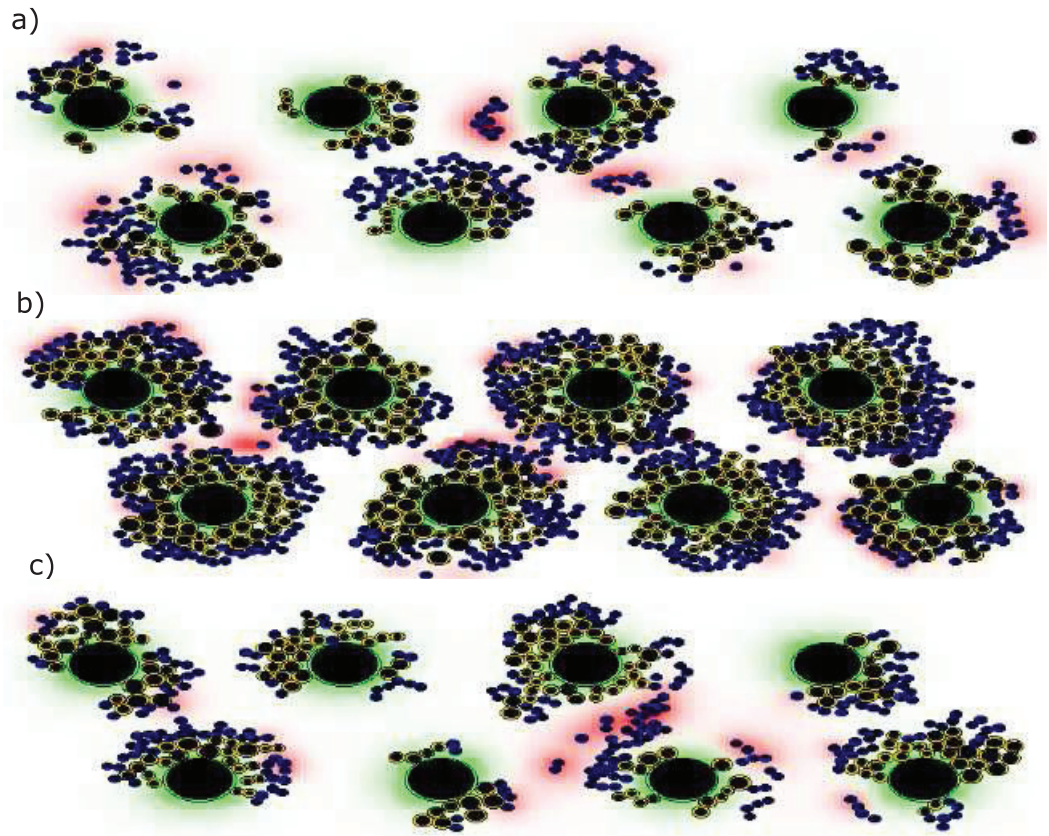

Figure 5.4: Snapshots of erythropoiesis simulation in a section of the bone marrow. a) At the beginning of the simulation, erythropoiesis reaches stability phase and we observe around 50 - 60 cells per EBI, b) about 5-6 days after blood loss, erythropoiesis is maximally stimulated and the number of cells including reticulocytes increases to approximately 110 cells per EBI, c) 50 days after blood loss, normal erythropoiesis is restored and the number of cells returns to 50 - 60 cells per EBI. Here large cells are macrophages, yellow cells around them are erythroid progenitors and blue cells are differentiated cells. Black circle inside the cells show their incompressible part. The concentration of the growth factor produced by the macrophages is shown in green, and the concentration of FAS-ligand in red.

the outputs of our model with this reference volume served for two purposes. Firstly, it allowed us to use physiologically realistic values of parameters of hemoglobin production and of feedback control mediated by EPO obtained from the experimental data. Secondly, it allowed us to interpret the results of our numerical simulations in light of comparison with physiological data. These results are in good agreement with the experimental data validating the model. Indeed, simulations show that the steady-state number of RBCs contained in the reference volume of blood $V^* = 3.75$ nL is 1.4×10^4 RBC. It is known that the total blood volume for an average person of 70 kg (approximately 5.5 L) contains about 2×10^{13} RBCs. Computing the number of RBCs in 5.5L according to the model, we obtain a close number of 2.05×10^{13} RBCs.

By formalizing the main features of this system from the molecular (e.g. hemoglobin synthesis) to the cell population levels, it was possible to reproduce the homeostatic response of erythropoiesis to large decreases in the blood content of red blood cells. In the presented scenario, the functionally important parameters, such as the blood levels of erythroid cells and of hemoglobin, were quickly reset within the normal, non-anemic range in less than 20 days. However, the mediators of the response, such as EPO and the threshold triggering apoptosis, took longer to recover their baseline values. The needed amount of time to recover completely was more than 100 days (not shown), approaching the lifespan of human red blood cells. This suggests that an almost complete turnover of this cell type is required to

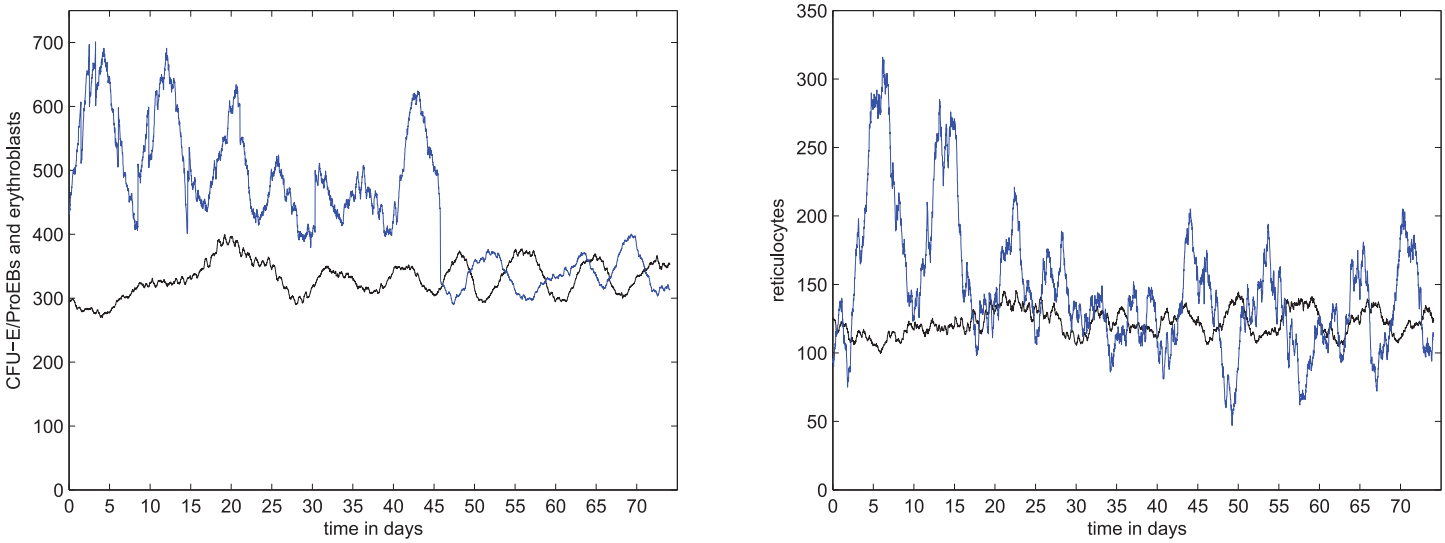

Figure 5.5: The number of CFU-E/ProEbs and erythroblasts (left) and reticulocytes (right) over time. The simulations represent cells counts of eight EBIs belonging to two women, one of them went through acute blood loss at the first day of the simulation (blue curves) and the other without blood loss is considered for comparison (black curves).

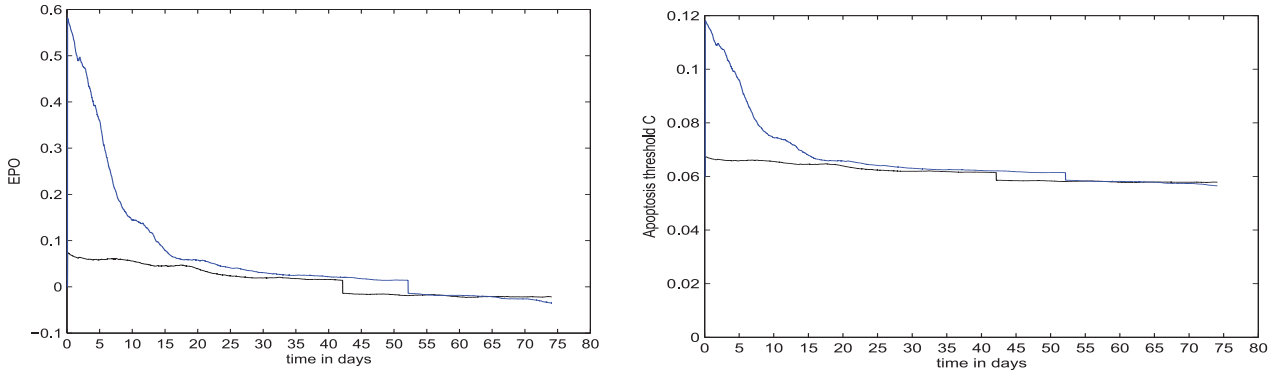

Figure 5.6: The levels of EPO relative to baseline of a woman with blood loss (left) and the corresponding apoptosis threshold of CFU-E cells (right) over time. The simulations represent recovery from anemia after acute blood loss (blue curves) and the normal case (black curves).

recover to the pre-stress situation. Also, even though the number of erythroblasts/island were similar on average for both non-stressed and stressed organisms after 50 days, the amplitude of the variations in islands recovering from a large RBC depletion took nearly twice this time to become similar to those of non-stressed islands again.

The results shown are for an individual with normal iron availability. However, additional factors would need to be considered in an iron-deficient individual. HIF2-α mRNAs have an iron responsive element (IRE) in the 5' region, which binds iron regulatory protein 1 (IRP1). During anemia due to iron deficiency, the baseline rate of HIF2-α production is relatively decreased compared to other anemias because IRP1 activity is increased, and IRP1 binding of the IRE in its 5' region inhibits translation of HIF2-α mRNAs into HIF2 protein [175, 176, 177]. The decreased production of HIF2-α protein means that less is available for the transcription of the EPO gene. This relatively restricted EPO response to anemia in iron deficiency would be expected to resolve as serum iron and transferrin saturation levels rise. However, the decreased HIF2 content is less a factor than the stabilization of HIF2 during the

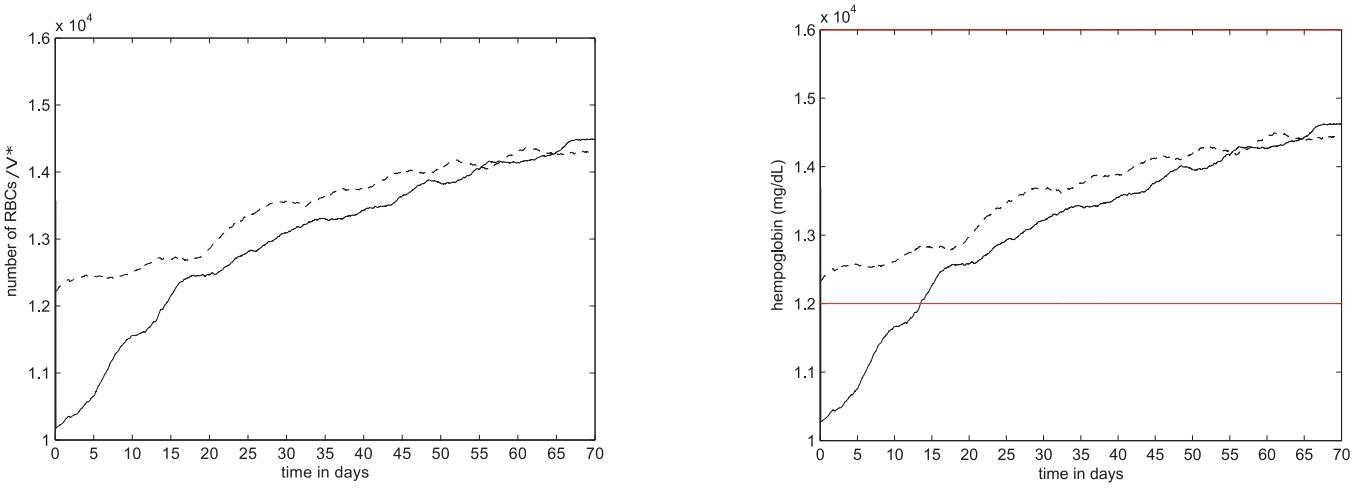

Figure 5.7: The number of simulated RBCs (left) and hemoglobin levels (right) over time.The simulations represent recovery from anemia after acute blood loss (solid lines) and the normal case (dashed lines). The red lines correspond to the limits of the normal range of hemoglobin in women.

anemia of iron deficiency because EPO levels are increased.

The restricted HIF2-α protein production and relatively decreased EPO production during iron deficiency may be counteracted by an increased EPO receptor (EPO-R) responsiveness in iron deficient erythroid cells due to decreased transferrin receptor 2 (TfR2) activity. TfR2 appears to suppress EPO receptor activity, and decreased TfR2 activity in iron deficient erythroid cells has been proposed to enhance their EPO responsiveness [178]. Therefore, EPO values in iron deficiency anemia might not be as increased as in other anemias due to IRP1 restricting HIF2-α production, but the EPO-R response would be increased due to reduced TfR2 activity.

Distinct molecular regulations determine the balance between concentrations of pro- and anti-differentiation mediators of erythropoiesis. They have not all been taken into account in the present work, but, despite its limitations the proposed multiscale modeling recapitulates the main observations previously reported. In particular, experimental data on Hb synthesis are reproduced in a satisfactory way. The results show that the set of kinetic constants associated with the process are fairly homogeneous (Table 1), which can be taken as a sign of the quality of the description. Further, the evolution of the main variable involved in Hb synthesis, iron availability, reveals striking features. Along the maturation of RBC in the bone marrow, the initial sharp increase of intracellular iron is followed by increased heme and globin synthesis, and finally by Hb accumulation. This succession of events points to a kinetically limiting heme concentration for Hb production. As alluded to above, heme synthesis is subjected to various regulatory steps which may be later introduced to refine the model. Lastly, intracellular, non-heme bound, iron and non-globin bound heme decrease in the extended period preceding the release of reticulocytes into the blood stream.

Hematopoietic disorders of the erythropoietic lineage are numerous and they include variations of some parameters considered in the present modeling. A case of hemorrhage was described herein. On the solid conceptual basis used here, it will be now possible to theoretically reproduce other pathological conditions, to include additional biological features that have not been considered in this first approach, and, hopefully, to rationalize some therapeutic interventions in this field.

Chapter 6

Mathematical modelling of the risk of thrombosis during multiple myeloma chemotherapeutic treatment

6.1 A hybrid multiscale model of multiple myeloma progression and its intraclonal heterogeneity

6.1.1 Biological and modelling background

Multiple myeloma (MM) is initiated through the acquisition of genetic changes that transform the plasma cells from normal to malignant. These changes often result in the development of selective advantage leading to the excessive proliferation of myeloma cells. The development of MM leads to several harmful clinical conditions including anemia, renal failure, recurrent infections, hypercalcemia, and osteoporosis with bone fractures. These pathological conditions can frequently result in the death of the patient.

The evolution of myeloma from the clonal premalignant plasma cells termed monoclonal gammopathy of unknown significance (MGUS) through the intermediate stage of smoldering myeloma to the malignant MM stage is mediated by multiple sequential genetic changes, including chromosomal translocations, hyperdiploidy, and mutations, which permit independent growth and spread of MM in the bone marrow [202, 203]. A wide variety of genetic changes involving many different genes have been documented in MM cases. In addition to these sequential genetic changes, MM cells require specific interactions with the non-hematopoietic cells of the bone marrow including the stromal cells (BMSCs), osteoblasts, osteoclasts, and cells associated with vascular supply of the marrow [202, 203]. These marrow microenvironment interactions with the MM cells include direct binding of cell surface adhesion proteins and their binding partners on the other cell types as well as diffusible, soluble molecules that are secreted by one cell type and are bound and internalized by another type cell. These soluble molecules are often chemokines and cytokines produced by other marrow cells, and their receptors are expressed on the MM cells. However, specific molecules produced by MM cells indirectly affect growth of the malignancy by inducing localized resorption of bone, death of hematopoietic cells, and expansion of vessels supplying blood to the MM. The combined effects of sequential genetic changes within the evolving myeloma cells and interactions of the MM cells with the marrow microenvironment affect the migration, proliferation, and survival of the MM cells.

In this work, we develop a hybrid model describing the development and intra-clonal heterogeneity in MM as described in Walker et al. [204]. In this model, malignant cells are represented by elastic spheres that can move, grow, interact, divide and die by apoptosis. Their fate is determined by intracellular and extracellular regulation networks. The growth of the cellular radii between cell divisions and the formation of two daughter cells with each division lead to the expansion of the tumor. To investigate the role of the BM microenvironment in the growth of myeloma tumors, we specifically consider

another population of cells, the bone marrow stromal cells (BMSCs). These cells secrete cytokines such as SDF-1, IGF-1, IL-6 which are necessary to the survival, homing and growth of malignant plasma cells. The concentration of each of these cytokines is modelled by a reaction-diffusion equation. The intracellular regulation of malignant cells is represented by a system of ordinary differential equations which depends on the concentration of extracellular cytokines. We characterize each cell by a specific genotype, and we consider that after its division, daughter cells will either inherit the same genotype or acquire a slightly different one due to random mutations. As the result, aggressive clones emerge during tumor progression in a parallel pattern. Although experiments show the possibility of clones emerging in both linear and branching evolutionary patterns, we restrict this study to the parallel evolutionary case. The MM cells consume cytokines leading to competition between clones for the available resources. We study the dynamics of clonal competition and its role in the progression of MM.

6.1.2 Mathematical model

We develop a hybrid discrete-continuous model of MGUS progression to MM. The discrete aspect of the model is observed at the cellular level: cells are represented as individual objects which move, interact, divide, and die by apoptosis. Each of these actions is regulated by intracellular and extracellular processes described by continuous models. The hybrid model consists of the following submodels: cell motion due to chemotaxis, intracellular regulation of plasma cells, extracellular regulation in the bone marrow, and acquisition of mutations upon cell division. It is an extension of a previously developed simpler model [205]. While the previous model considers the cytokines in the extracellular matrix to be uniformly distributed, the present study provides a more accurate description by considering that these cytokines are produced by the BMSCs and consumed by the myeloma cells. Furthermore, a more detailed description of the intracellular pathways regulating the fate of plasma cells is provided in the present model.

The model is based on the direct effects of sequential genetic changes and marrow microenvironmental chemokine and cytokine activity that influence the chemotaxis, proliferation and survival of MM, but does not include the MM effects on bone resorption, hematopoietic cell loss, or development of specialized vasculature. The complex multiple genetic changes in MM cells and the numerous cell-cell and cytokine-mediated interactions between myeloma cells and their marrow microenviroment are simplified in the model so that four related but evolving clones develop in a process termed intra-clonal heterogeneity [206, 207] (See Fig. 6.1). Competition among these four MM clones is based on differences in cellular growth and survival rates and interactions with the marrow microenvironment. This competition results in predominance of the more fit clones and decline and ultimate extinction of the less fit ones. An early event in the MM model (Fig. 6.1 - a) is a standard risk genetic change, a t(11;14) translocation that involves the immunoglobulin heavy chain switch region on chromosome 14 inducing overexpression of the gene encoding cyclin D1, a regulator of cell cycle progression located on chromosome 11 [208]. This t(11;14) clone has deregulated cell cycle progression due to the translocation, and it undergoes two separate secondary genetic events: mutations involving the oncogenes *N-RAS* and *K-RAS*, which are common secondary events in the development of multiple myeloma [203]. The resultant clone with t(11;14)/mutant *N-RAS* has significantly enhanced proliferation compared to the parent t(11;14) clone, while the t(11;14)/ mutant *K-RAS* clone has much less of an increase in proliferation relative to the t(11;14) parental clone. Thus, the two descendent clones have differing degrees of increased RAS activity resulting in a proliferative advantage for the t(11;14)/mutant *N-RAS* clone compared to both the t(11;14) parental clone and t(11;14)/ mutant *K-RAS* clone. A subsequent genetic event in the t(11;14)/K-RAS clone is, however, a mutation in the gene encoding IRF4. Mutant IRF4 is a protein that can enhance survival and proliferation of MM cells. *IRF4* mutation has been associated with mutations of *N-RAS* or *K-RAS* [207], and it allows the t(11;14)/*K-RAS* mutant/*IRF4* mutant clone in the model to compete more successfully with the t(11;14)/*N-RAS* clone than either the parent t(11;14) clone or the t(11;14)/*K-RAS* mutant clone.

Among the many possible microenvironmental factors that may influence the growth of MM in the marrow, the simplified model includes the chemokine stromal cell-derived factor 1 (SDF-1). It is produced by multiple cell types but mainly by BMSCs. Other extracellular cytokines included in the model are interleukin 6 (IL-6) and insulin-like growth factor 1 (IGF-1), which are also produced others

types of non-hematopoietic cells in the marrow as well as by BMSCs. The marrow stromal cells are considered as sources of SDF-1, IL-6, and IGF-1 in the model (Fig. 6.1 - a). SDF-1 through its receptor CXCR4 mediates the homing of circulating myeloma cells to the marrow and their migration within the marrow space [209, 210]. IL-6 and IGF-1 induce multiple effects after binding to their respective specific surface receptors on the MM cells, but in the model we restrict our study to their effects on the (RAS/ERK) pathway that promotes proliferation and the phosphatidylinositol-3 kinase/protein kinase B/Forkhead in rabdomyosarcoma (Akt/FKHR) pathway that regulates apoptosis [203] (Fig. 6.1 - a).

Cell motion

We represent each cell as an elastic sphere. It contains two parts: an incompressible part and a compressible one. As the cell grows, its radius increases and hence it pushes the neighboring cells. The motion of each cell is determined by Newton's second law. Let us denote the cell number by i. Then we have the following equation for the coordinate x_i of the center of the $i-th$ cell:

$$m\ddot{x}_i + m\mu\dot{x}_i - \sum_{j\neq i} f_{ij} - f_{ch} = 0, \tag{6.1.1}$$

where m is the mass of cell, μ is the friction coefficient, f_{ij} is the interaction force between the cells i and j, f_{ch} is the chemotactic force which depends on the concentration of SDF-1. We consider f_{ij} in the following form:

$$f_{ij} = \begin{cases} K\dfrac{h_0 - hij}{h_{ij} - (h_0 - h_1)}, & h_0 - h_i < h_{ij} < h_0 \\ 0, & h_{ij} \geq h_0 \end{cases}. \tag{6.1.2}$$

Here h_{ij} is the distance between the center of the cells i and j, h_0 is the sum of their radii, K is a positive parameter and h_1 represents the incompressible part of each cell. The chemotactic force represents the motion of the cell in response to SDF-1 stimulus. Let us denote the concentration of SDF-1 by S. Then the expression of f_{ch} is given by:

$$f_{ch} = \kappa\nabla S,$$

where κ is a positive constant and ∇S denotes the SDF-1 gradient.

Extracellular regulation

We consider a square two-dimensional computational domain with the side equal to 1000 microns. The hybrid model contains two types of cells: myeloma cells and BMSCs. The former have a diameter of 10 microns while the latter are considered to have six-fold larger radii as observed in experimental data. Furthermore, they secrete cytokines that are necessary for the survival and proliferation of myeloma cells such as SDF-1, IL-6, IGF-1. Let us denote the total concentration of the last two cytokines by I and the concentration of SDF-1 by S. Assuming that these cytokines have the same diffusion coefficient, production rate, consumption rate, and degradation rate, we describe their concentrations in the extracellular matrix by:

$$\frac{\partial I}{\partial t} = D\Delta I + W - \sum_i \lambda I - \sigma I, \tag{6.1.3}$$

$$\frac{\partial S}{\partial t} = D\Delta S + W - \sum_i \lambda S - \sigma S, \tag{6.1.4}$$

where D is the diffusion coefficient, W the production factor, λ the consumption rate by each myeloma cell, σ the degradation rate. We set the Dirichlet boundary condition $I = 0$ and $S = 0$ at all boundaries. We have prescribed zero Dirichlet boundary condition to represent the local dynamics of tumor growth in a bone marrow site surrounded by adipose tissue.

Intracellular regulation

Although myeloma cells are genetically complex [203], we will restrict the intracellular regulation to two pathways (Fig. 6.1 - a). These pathways are the (RAS/ERK) pathway which is responsible for cell proliferation and the (Akt/FKHR) pathway which regulates its survival. Other pathways such as the (JAK/STAT) are not considered in the model. We have chosen these two pathways in order to study the role of aquired RAS mutations in the progression of MM and how it is affected by the extracellular matrix. Let us denote the concentrations of ERK, Akt, and FKHR by e, a, and f respectively. We describe these concentrations inside each cell as follows:

$$\frac{de}{dt} = \alpha_1(z)(\kappa I) - \beta_1 e, \ \frac{da}{dt} = \alpha_2(\kappa I) - \beta_2 a, \ \frac{df}{dt} = \alpha_3 - \beta_3 af - \gamma_3 f. \tag{6.1.5}$$

where α_i and β_i, $i = 1,2,3$ and γ_3 are positive constants. The coefficient $\alpha_1(z)$ depends on the genotype z, and this coefficient varies depending on the effect of RAS mutations. The cell will die by apoptosis if $f > f^*$ during its lifetime cycle. If the myeloma cell survives, then it will self-renew, if $e > e^*$ by the end of its life cycle. Otherwise, the cell will die by apoptosis. We consider that the proliferation threshold e^* depends on the *IRF4* gene expression.

Myeloma cells division and mutations. In the present study, we investigate the progression of MGUS into MM through RAS mutations [204]. We characterize each cell by an aggressiveness phenotype which represents the cumulative effects of acquired RAS mutations. We introduce an aggressiveness phenotype function $f(z)$ resulting from the RAS genotype for each cell. After its division, the daughter myeloma cell will keep the genome of the mother cell with a probablity of 1/3. Otherwise, it will acquire a mutation and either increases or diminishes its aggressiveness by a positive value ε. We represent the genotype and resultant RAS activation that determine aggressiveness as due to describing the frequency and effects of RAS mutations in the resulting clones in Fig. 6.2 - a. Furthermore, we assume that the ERK threshold for cell division is reduced upon the mutation of the *IRF4* gene as shown in Fig. 6.2 - b. We consider four clones of MM denoted by c_1, c_2, c_3, and, c_4 (Figue 6.1 - b). The clone c_1 is the initial clone which does not harbour any RAS mutations. The clone c_2 is more aggressive than clone c_1. It consists of MM cells that acquired the *N-RAS* gene mutation. The clones c_3 and c_4 belong to a lineage that is independent from the clone c_2. They emerge when the cells of c_1 acquire the *K-RAS* gene mutation for clone c_3 and an additional *IRF4* gene mutation for clone c_4. The latter clone is therefore more aggressive than the former. We show the relationships between these different clones in Fig. 6.1 - b.

6.1.3 Results

Initially, there are 47 myeloma cells in a bone marrow site containing a single BMSC, although the initial number of these cells is not essential for the results of the simulations. All of these malignant cells are considered to be tumor-initiating cells because they belong to the same initial clone. The motion of the malignant cells depends on their distance from the BMSC. Closer cells move faster than farther ones due to the increase in SDF-1 gradient near the BMSC. During their motion, myeloma cells consume the cytokines necessary for their survival such as IL-6 and IGF-1. These cytokines promote survival by activating the (RAS/ERK) pathway, and dowregulating the (Akt/FKHR) pathway. Depending upon its initial distance from the BMSC, the myeloma cell will either survive and get closer to the BMSC or it will die by apoptosis. The surviving myeloma cells will surround the BMSC and form the tumor niche. Initially, this niche consists of cells belonging to the same clone. After some time, other subclones will emerge in the course of tumor growth. We have shown the different steps of myeloma cells homing to a BMSC in Fig. 6.3. The initial condition for the simulation is shown in Fig. 6.3 - a. Due to the low number of myeloma cells in the beginning of the simulation, the BMSC secretes a high concentration of the chemokine SDF-1 which attracts the myeloma cells located close to it (Fig. 6.3 - b). The surviving myeloma cells adhere to the BMSC and surround it while other cells divide and remain farther away (Fig. 6.3 - c). During this process, cells whose aggressiveness phenotype belongs to the intermediate

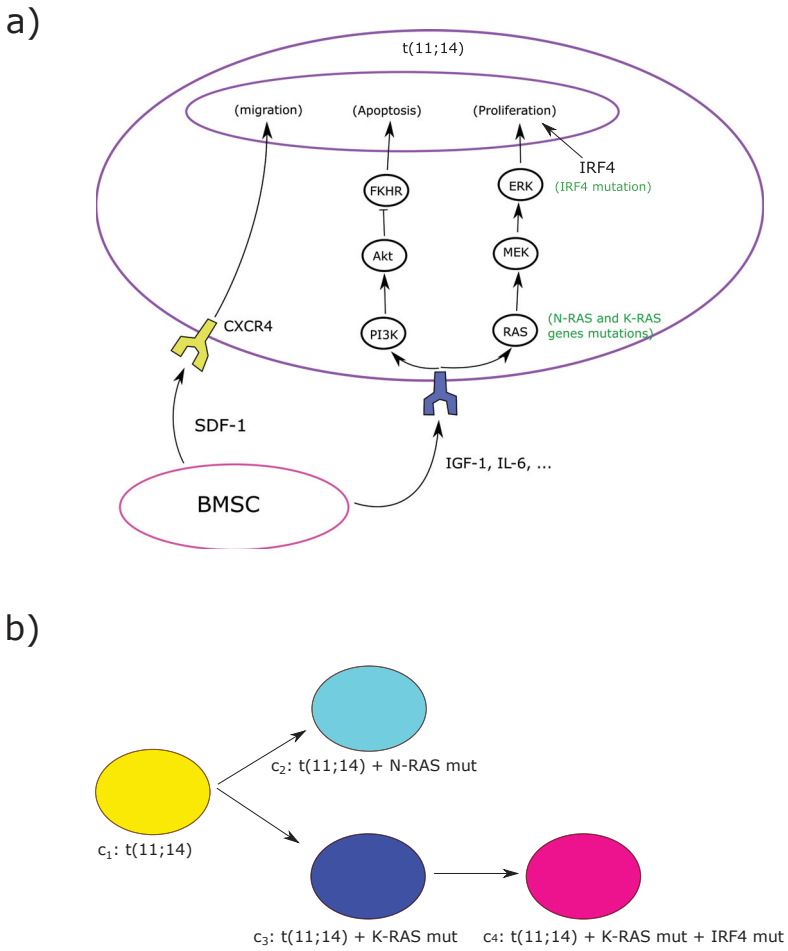

Figure 6.1: a) The regulation of myeloma cells as described in the model. Bone marrow stromal cells (BMSCs) secrete the cytokines IGF-1, IL-6, and SDF-1 which are necessary to the survival, homing and proliferation of myeloma cells. Via their respective receptors, IGF-1 and IL-6 activate the (RAS/ERK) pathway which promotes the cell proliferation. They inhibit apoptosis through the (Akt/FKHR) pathway. The cell migrates and homes to BMSCs through the (SDF-1/CXCR4) axis. IRF4 mutation, which has been associated with concomitant RAS mutations, promotes survival and proliferation. BMSCs, which are much larger cells than the myeloma cells, are shown in reduced in size in this Fig. and we the receptors of both IGF-1 and IL-6. b) The parallel evolution pattern of multiple myeloma clones resulting in intra-clonal heterogeneity. More aggressive clones result from a more aggressive *N-RAS* mutation in clone 2 or the acquisition of IRF4 mutation in addition to the less aggressive *K-RAS* in clone 4. Each clone is shown by its corresponding color in the model.

state between the clones $c_1 - c_2$ and $c_1 - c_3$ emerge (Fig. 6.3 - d) and the global concentration of SDF-1 starts to reach stability due to its consumption by myeloma cells (Fig. 6.4 - a).

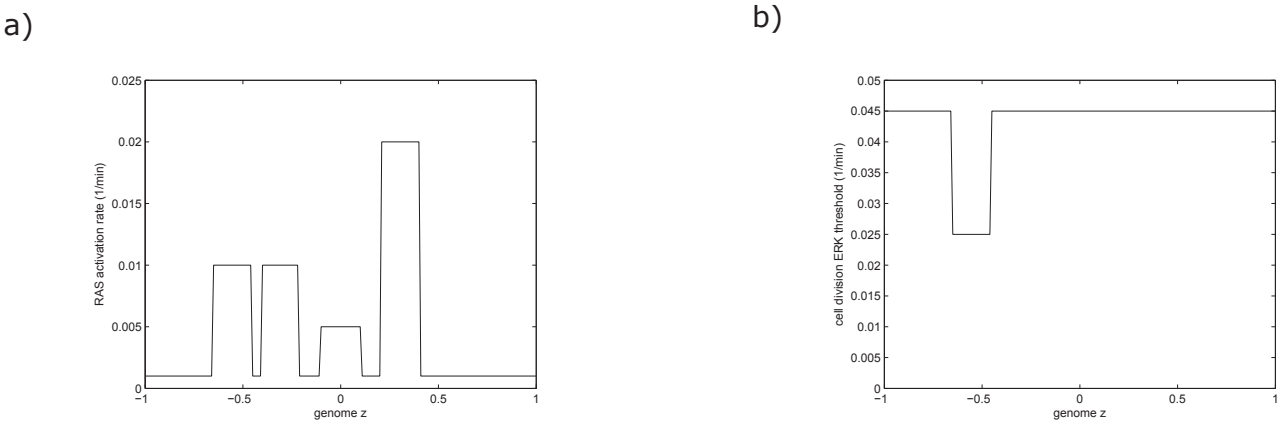

Figure 6.2: a) The activation rate of RAS protein as a function of the genotype function z. b) The ERK threshold for division as a funtion of the genotype function z, it decreases due to the *IRF4* mutation found in the clone c_4.

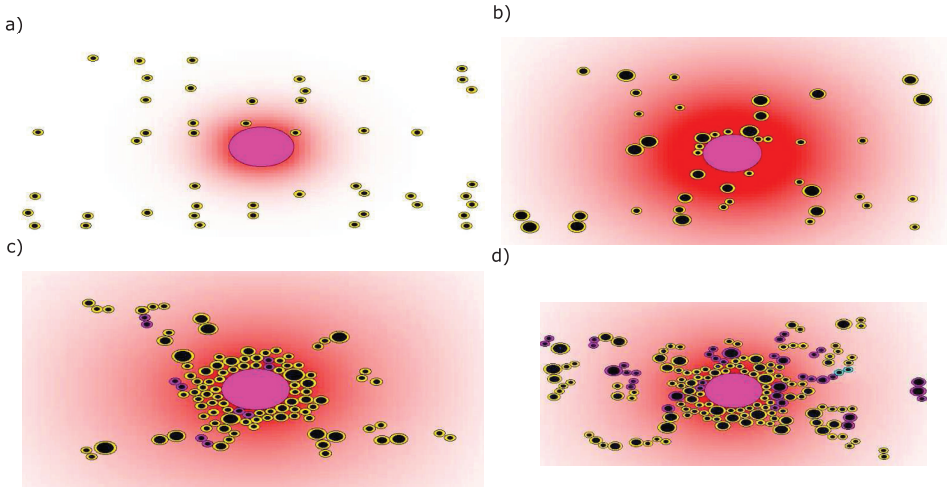

Figure 6.3: The different steps of myeloma cells homing to a BMSC. Myeloma cells are represented by the cells with the smaller radii and the BMSC is the large cell in the middle. Each clone of MM cells is denoted by a specific color. The red color gradient represents the summed concentrations of the cytokines SDF-1, IL-6, and IGF-1 shown with white (0) to red (1).

MGUS progresses to aggressive MM through the acquisition of random mutations by myeloma cells. In this respect, more aggressive subclones emerge in the course of MGUS progression due to the acquisition of RAS-associated mutations. The aggressive subclones need lower concentrations of IL-6 and IGF-1 to survive resulting in the expansion and the persistence of the tumor (Fig. 6.4 - b). Because of their rapid proliferation, they crowd out other clones and consume most of the available resources. Ultimately, these less aggressive subclones remain relatively stable in growth pattern. Still, a few of them manage to survive in proximity to the BMSC where there is a higher concentration of the IL-6 and IGF-1 cytokines, while the more aggressive subclones occupy the outer region of the tumor. The different steps of tumor development and intraclonal competition are shown in Fig. 6.5. As the tumor progresses, the concentrations of IL-6 and IGF-1 become stable due to their consumption by the growing number of myeloma cells. As a result, the aggressive subclones expand to the detriment of the less aggressive ones. By the end of the simulation, we see that the tumor size is stable but the competition between clones is still in progress (Fig. 6.5 - c vs. Fig. 6.5 - d).

The emergence of more aggressive clones not only reduces the populations of the less aggressive ones but also increases the total number of malignant cells. These clones survive in areas farther from the BMSC making the tumor expand. We show the total number of malignant cells over time in Fig.

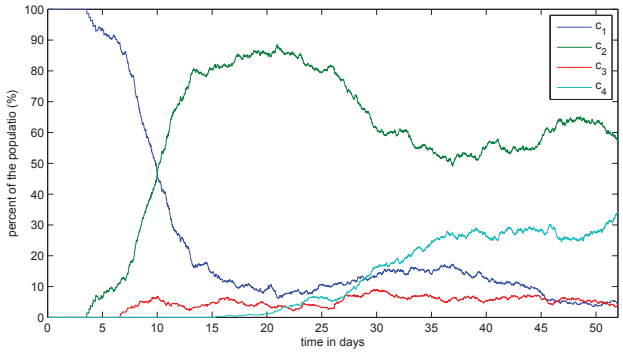

Figure 6.4: a) The total concentration of the IL-6 and IGF-1 cytokines over time in log scale. b) The total number of malignant cells over time.

6.4 - b. The proportions of each clone in the total population show that in the end of the simuation, the clone c_1 only represents $\approx 5\%$ of the total population. The subclone c_2 is predominant with $\approx 60\%$ of cells (Fig. 6.6). Overall, the global population of malignant cells increases with the emergence of more resistant subclones. The emergence of the subclone c_2 leads to an increase in the number of malignant cells because the cells belonging to this subclone can survive far from the BMSC. The subclone c_3 emerges few hours after c_2 but barely manage to survive because of limited resources. It gives rise to the subclone c_4 which is as aggressive as the subclone c_2 due to the additional *IRF4* mutation. As the tumor progresses, these two subclones c_2 and c_4 become predominant because they are better adapted to survive in sites with limited resources. By the end of the simulation, the number of malignant cells oscillates around a stable value as well as the total concentration of cytokines in the domain (Fig. 6.4). We show the percent of the malignant cells population occupied by each clone over time in Fig. 6.6.

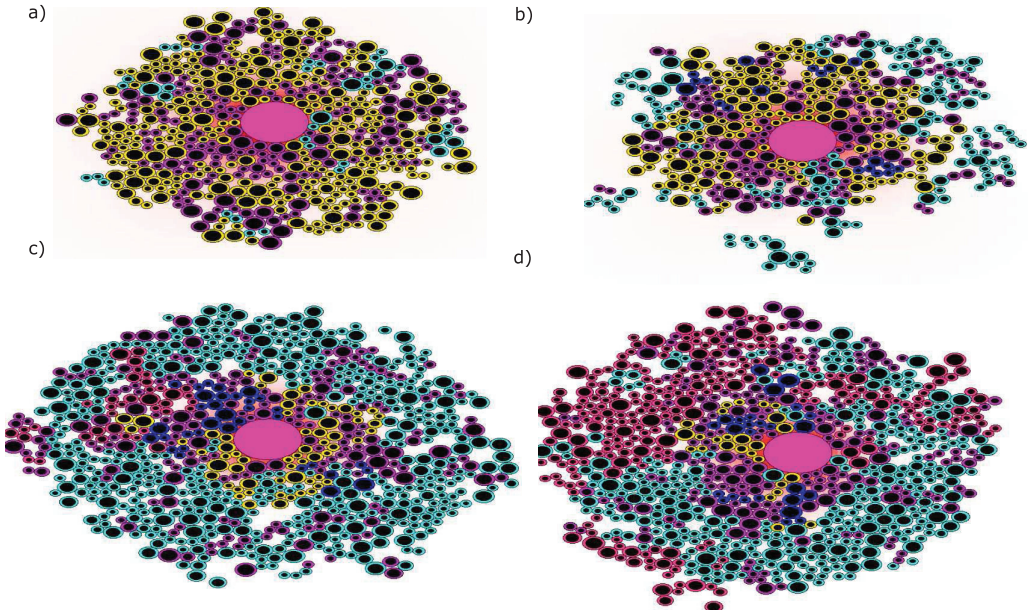

Figure 6.5: Snapshots of a simulation showing the competition between clones. a) The tumor consists mainly of the clone c_1 (shown in yellow) with few cells in the intermediate state (in purple) between clones and the emergence of the clone c_2 (in cyan) in the sides. The size of the tumor remains limited because clone c_1 cells need relatively high concentration of I to survive. b) Compared to the clone c_1, the clone c_2 cells expand and survive in areas with lower concentration of cytokines. c) The clone c_2 cells surround the tumor and crowd out the cells of the clone c_1 leading to the reduction of their population. The clones c_3 (in blue) and c_4 (in magneta). d) The subclone c_4 is as aggressive as the subclone c_2 due to the additional *IRF4* mutation and it manages to coexist with it in the remote areas with fewer cytokines.

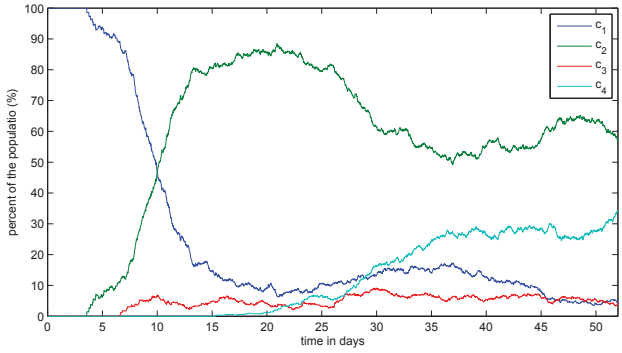

Figure 6.6: The proportion of each clone in the total population over time.

6.1.4 Discussion

Bone marrow stromal cells play an important role in the pathogenesis of MM. After extravasation into the bone marrow, MGUS and myeloma cells migrate and home to the areas surrounding BMSCs. This homing process is mediated by the chemokine SDF-1. It promotes the chemotaxis and homing of myeloma cells upon the interaction with its receptor CXCR4 [211]. However, it is crucial for myeloma cells to be sufficiently close to BMSCs to be attracted by the secreted SDF-1. Otherwise, they will die if they are left without enough resources to survive and divide. The progression of MGUS to MM with t(11;14)

translocation is marked by the emergence of new aggressive subclones which is crucial for the expansion of the tumor because it allows its adaptation to limited resources. As the tumor progresses, the aggressive subclones become predominant because lower concentrations of IL-6 and IGF-1 allow them to survive.

To study the development of MM tumors and its intraclonal heterogeneity, we developed a specific hybrid discrete-continuous model. The model was able to reproduce the experimental results presented in [204]. We have used it to investigate the central role of the BMSCs in myeloma cell homing and the progression of MGUS to MM. BMSCs participate in the homing of myeloma cells and provide them with the necessary cytokines for their survival and proliferation. Numerical simulation results suggest that the initial distance between the BMSC and infiltrating myeloma cells is of paramount importance for the survival of the latter. After their homing, new more aggressive myeloma subclones emerge due to the acquisition of RAS mutations. Other gene mutations such as the one acquired by the *IRF4* gene further increase the aggressiveness of some of these subclones. They compete with each other for the available cytokines resulting in the predominance of the more fit subclones. To better quantify the heterogeneity of clones during MM progression, we show the kernel density plots at different stages of MGUS to MM progression in Fig. 6.7. The x-axis shows the aggressiveness phenotype function scaled from 0 to 1. These results show the predominating subclones at the different stages of tumor progression. Our findings suggest that the total number of malignant cells oscillates around a stable value after a few weeks of MM development in agreement with the *in vivo* experiments conducted in [212]. However, we speculate that MM tumors can further expand due to other mechanisms such as stimulation of IL-6 and IGF-1 production by BMSC, the migration to other BMSCs [213], or the emegence of more resistant clones due to other mutations.

The multiscale model follows a systems biology approach [214] by integrating different interfering biological processes in one model. To understand complex phenomena such as MGUS progression to MM, it is important to properly use available data in describing events at the single cell level where processes such as gene expression and mutations take place as well as the larger tissue level where each cell interacts with its environment. Systems biology approaches focus on the whole system rather than the sum of its components. Similarly, this study is more focused on the behavior of the global model of MM homing and tumor growth than the various individual processes which regulate it.

Although the model presented here was able to reproduce the experiments describing MM intraclonal heterogeneity, it has several limitations. First, the intracellular regulation network was limited to two pathways while in reality MM is more biochemically complex [203]. Furthermore, the number of considered mutations is also reduced compared to those found in MM cases. Interactions of the myeloma cells and BMSCs with other components of the bone marrow such as the osteoblasts and osteoclasts were not included in the present model. Other mechanisms affecting myeloma cells proliferation were introduced implicitly as a random perturbation of the cell cycle in the myeloma cells. The simplification of the myeloma cells transduction pathways and mutations included was due to limitations of computational power and the difficulty of studying complex models. We have limited the model to two pathways of intraecllular regulation because we wanted to study the effect of the cytokines IL-6 and IGF-1 on the fate of the myeloma cells and how that fate is affected by RAS mutations and the IRF4 mutation that is associated with mutant RAS genes. Also, we assumed that IL-6 and IGF-1 play the same role in the activation of the (ERK/RAS) and (Akt/FKHR). This hypothesis was made because it is difficult to distinguish the interfering actions of the different cytokines in the cell culture experiments. Finally, the study was restricted to a site of the bone marrow containing a single BMSC. Other configurations with more BMSCs and other marrow cell types can be considered as well.

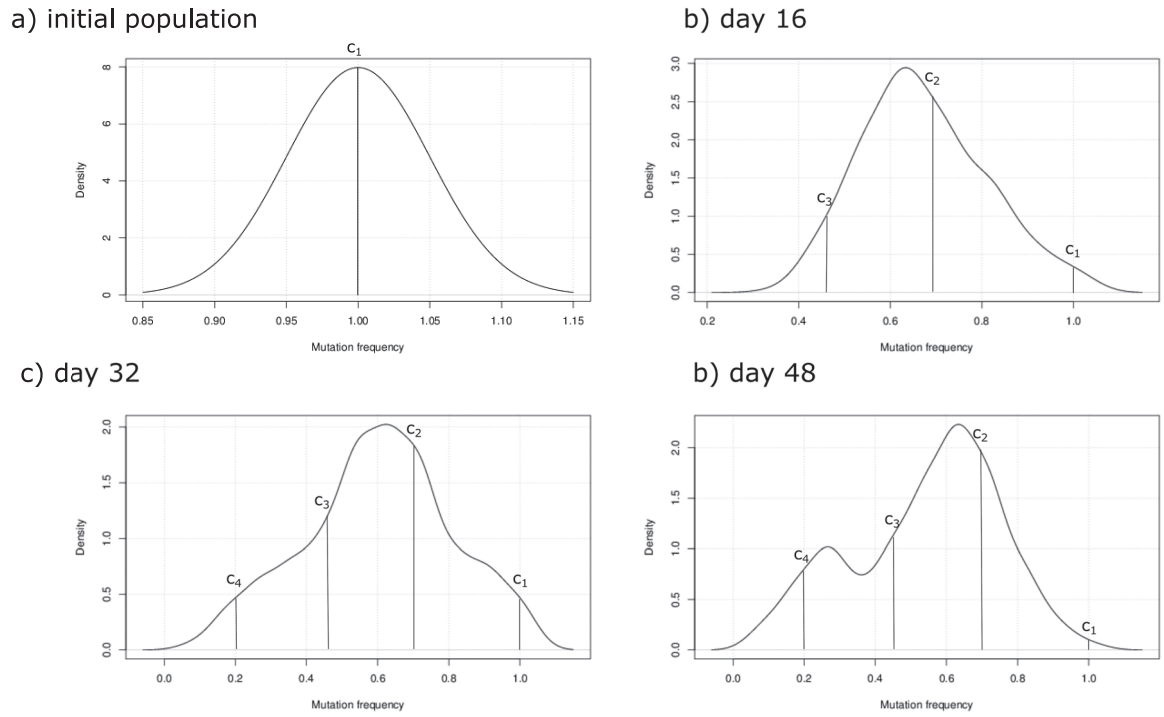

Figure 6.7: Gaussian kernel density plots indicating the frequency of cells acquiring each specific mutation at the different stages of the simuation.

6.2 Multiscale modelling of MM infiltration on erythropoiesis during treatment

6.2.1 Modelling clinical data of MM infiltration

The previously reported hybrid model of normal erythropoiesis based on the spatial arrangement of cells in EBIs (Chapter 5) was expanded to study the effects of myeloma cell infiltration on erythropoiesis. In the EBI model, mechanical interactions based on Newton's second law of motion between erythroid cells, each of which is considered as an elastic sphere with an incompressible inner part, displace the more mature cells peripherally after mitoses [85]. Thus, the more mature erythroid stages are peripherally located in EBIs, consistent with described EBI structure [216]. Nascent reticulocytes remain in or near the EBI for various periods of time before entering the blood through marrow vascular sinuses. In the EBI model, the CFU-E and proerythroblasts can expand by proliferating without differentiation, differentiate with a limited number of cell divisions, or die by apoptosis [85]. These fate decisions of the CFU-E and proerythroblasts are controlled by intracellular regulatory networks that are modeled with ordinary differential equations and extracellular cytokine/hormone concentrations that are modeled with partial differential equations (Chapter 5). Mature erythroblasts and reticulocytes formed by their enucleationsecretethe majority of FL, which induces apoptosis of CFU-E and ProEBs. Counterbalancing this apoptotic loss, central macrophages produce SCF during normal erythropoiesis and BMP4 during anemia,both of which stimulate proliferation of CFU-E and ProEBs. Plasma provides glucocorticoids and EPO,both of which increase during anemia. Glucocorticoids upregulate self-renewal of CFU-Es and ProEBs, while EPO downregulates their apoptosis by decreasing FAS expression and promotes their differentiation by increasing GATA1, anerythroid transcription factor. Because erythroid progenitors die by apoptosis and mature erythroid cells (reticulocytes) exit the bone marrow into the blood, some EBIs can become extinct, with only the central macrophage remaining. Conversely, during severe anemia, EBI size and numberscan increase. New EBIs are assumed to be initiated by burst-forming units-erythroid (BFU-Es), progenitors of CFU-Es which can circulate in blood and lodge in the marrow where they

have some motility. When a BFU-E encounters a potential central macrophage,it divides and givesrise to CFU-Es and Pro-EBs that become physically associatedwith the macrophage generatingan EBI. Fig. 6.8A shows the previously described human EBI model (Chapter 5), and Fig. 6.8B shows a section of normal marrow that contains multiple EBIs. Non-erythropoietic hematopoietic cells,which are not shown in Fig. 6.8B, are situated between the EBIs, and divide or die with a given probability. In the model, these probabilities are chosen such that thenon-erythroid hematopoietic cells do not contract or expand their populations.

MM developsfrom the pre-malignant, marrow-based plasma cell disorder termed monoclonal gammopathy of uncertain significance (MGUS) [217, 218]. Oncogenic events transform MGUS plasma cells into myeloma cells, which have varying rates of proliferation within the marrow space and spread to distant areas of marrow [219, 220, 221]. MM patients most often present with relatively uniform marrow infiltration, the degree of which depends upon the growth rate of myeloma cells and the time elapsed after the transformation to myeloma. To determine the effects of myeloma infiltration on marrow erythropoiesis, a small number of myeloma cells are added to the model of normal erythropoiesis in Fig. 3.1.1B. In early stages of myeloma infiltration, EBIs are only slightly affected, and they continue normal erythropoietic function. The myeloma cells, however, will proliferate at a given rate, producing similar myeloma cells after each division. Infiltrating myeloma cells disrupt EBIs by: 1) producing FL or similar cytokines such as TNF and TRAIL that induce erythroid cell apoptosis, and 2) physical destruction of EBIs. Fig. 6.8C shows both of these processes in a modeled section of bone marrow infiltrated by myeloma cells.

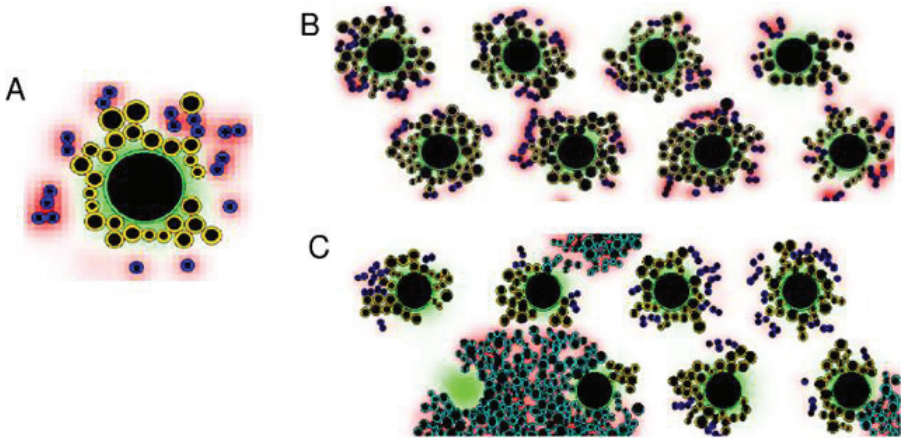

Figure 6.8: Erythroblastic island (EBI) structure in normal marrow and in marrow infiltrated by multiple myeloma (MM). (A) Model of an individual EBI. The central macrophage (large cell in the center) produces growth factor (green) that diffuses and stimulates proliferation of erythroid progenitors (larger yellow cells). All erythroid cells produce FAS ligand (FL), but mature erythroblasts andthe reticulocytes formed by their enucleation (dark blue cells) are the greatest producers in the EBI. FL, which is shown in red around the reticulocytes, stimulates early stage erythroid cells to die by apoptosis at higher concentrations or to differentiate at lower concentrations. Black solid circles inside cells show their incompressible parts. (B) Section of normal bone marrow with eight EBIs.Non-erythroid hematopoietic cells located between EBIs are not shown. (C) Section of marrow with moderateinfiltration by myeloma (light blue cells) atleftof center and in the lower right. Pro-apoptotic cytokines secreted by the myeloma cells including FL, TNF, and TRAIL are shown in red. Lower left EBIs show loss of erythroblasts in both islands and destruction of the central macrophage (complete EBI loss) of the left-most lower island. Other EBIs have reduced erythroid cell populations due to cytokines released from infiltrating myeloma cells.

LBD effectively treated MM, and repeated bone marrow biopsies during the four cycles of chemotherapy were not justified in patients who had progressive decreases in serum monoclonal immunoglobulins

and free light chains. Therefore, monoclonal immunoglobulin and light chain concentrations were used to determinethe relative size of myeloma cell populations in marrow during the course of chemotherapy. In simulations, myeloma cell numbers were determined by differential equations based on changes in paraprotein concentrations at the beginning of each cycle of chemotherapy. Rates of serum paraprotein production per myeloma cell were considered constant and rates of serum paraprotein decay were based on rates reported for each specific protein class. RBC numbers served as measures of erythropoiesis. Like the LBD protocol [222], we modeled four 28-day cycles of treatment, each one consisting of two weeks of drug administration followed by two weeks without any treatment. The drug concentration in the bone marrow was considered as constant during first two weeks of each cycle and zero during the next two weeks. In simulations, achievement of sufficient intracellular drug concentrations that killed myeloma cells was based on concentration and time of drug exposure in the marrow for individual myeloma cells that had constant rates of drug influx and drug degradation. Two variations of the LBD protocol that delivered more or less chemotherapy were also simulated (Fig. 6.9).

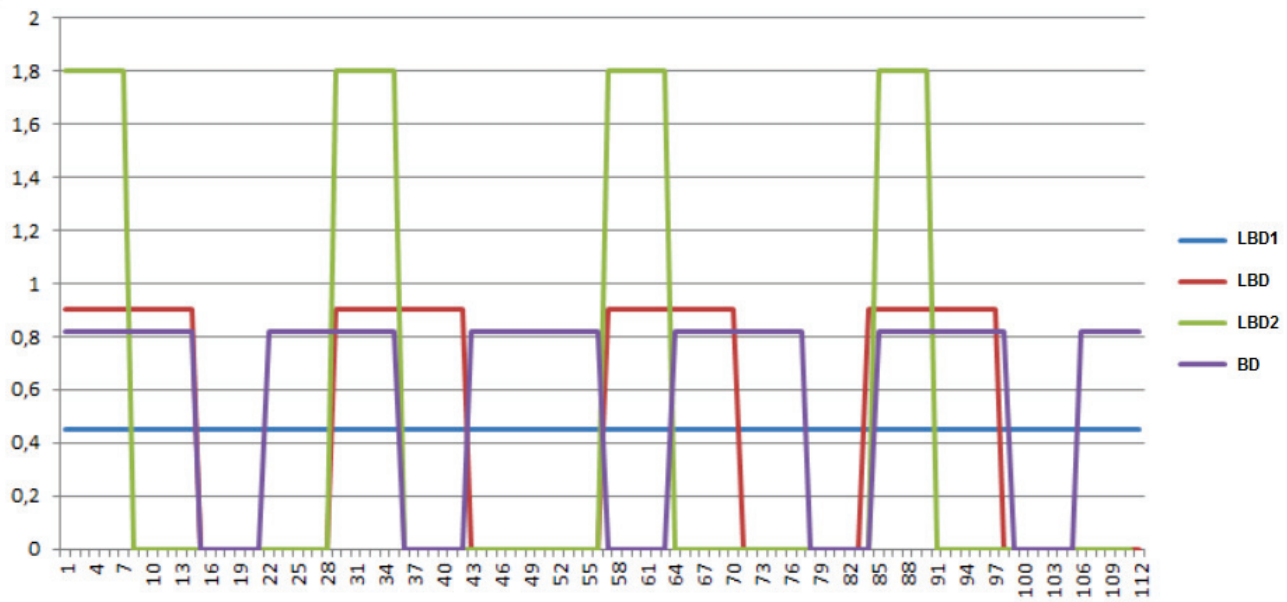

Figure 6.9: The function $p(t)$ corresponding to the four MM treatment protocols over time (in days).

6.2.2 Mathematical model of erythropoiesis and MM

Intracellular regulation. We use a discrete-continuous hybrid models in order to describe erythropoiesis in a part of the bone marrow. In this model, the cells are represented as individual objects that can move in the marrow space, divide, differentiate and die by apoptosis. The fate of these cells is determined by the concentrations of some key cellular proteins $P_1,...,P_k$. The concentrations of these proteins can be described by ordinary differential equations:

$$\frac{dP_j}{dt} = \Phi_j(P), \quad j = 1,...,k, \tag{6.2.6}$$

where $P = (P_1,...,P_k)$ and Φ_j are the rates of production minus the rate of destruction of these proteins. In our model, we consider four key cellular proteins in order to reduce the complexity of the model and reduce the number of unknown parameters. That model was previously used in [**?**]. We consider the regulation of CFU-E/ProEbs cells where each of the possible fate (auto-renewal, differentiation and apoptosis) is determined by the concentrations of four proteins. We present the equation of each of these proteins as follows:

$$\frac{dz}{dt} = a_0, \tag{6.2.7}$$

$$\frac{du}{dt} = a_1 + b_1 z, \tag{6.2.8}$$

$$\frac{dv}{dt} = a_2 - b_2 z v, \tag{6.2.9}$$

$$\frac{dw}{dt} = a_3 - b_3 z w. \tag{6.2.10}$$

The intracellular regulation of CFU-E/ProEbs in our model is described by the concentrations of four major variables: 1) the concentration of activated glucocorticosteroid receptor (z) which determines the rate of self-renewal in normal state erythropoiesis and in limited hypoxia states; 2) the concentration of activated BMP4 receptor (u), a protein that determines the rate of expansion of CFU-E/ProEbs population under hypoxia stress; 3) the concentration of GATA-1 (v) which determines the rate of terminal differentiation; and 4) the concentration of activated caspace (w) that determine the rate of apoptosis when elevated and the rate of terminal differentiation when reduced. These intracellular proteins are affected by major extracellular mediators: 1) the concentration of glucocorticosteroid hormone (GC) which varies with the degree of stress under normal and hypoxic states; 2) the concentration of BMP4 expressed by central macrophages that increases with hypoxic stress; 3) the concentration of EPO which varies inversely with the degree of hypoxia; 4) the expression of Fas-ligand by late-stage erythroblasts and MM cells that also express TRAIL. In (6.2.7), the concentration of (z) depends on the extracellular concentration of GC. Hence, a_0 depends on the extracellular concentration of GC. Next in (6.2.8), (u) depends on the extracellular concentration of BMP4 expressed by the central macrophages. Hence, a_1 depends on this concentration. In the right hand side of the equation (6.2.8), we consider the possibility of up-regulation of self-renewal by GR. Cell differentiation is described by the (v) whose concentration is given in equation (6.2.9). a_2 depends on the concentration of EPO. Finally, (w) depends upon the extracellular concentrations of Fas-ligand and is down-regulated by EPO through a_3 as well as by GR. We do not consider all the features of the regulatory system in order to simplify the interpretation of results. Therefore, we consider that the cell fate is determined the variables u, v, w. When, at some moment of time, the value of w (caspase) reaches a critical value $w_c r$, then the cell dies by apoptosis. If it reaches the end of its cell cycle, then the values of u (BMP4) and v (GATA-1) are compared. If $u \leq v$ then the cell divides and differentiates. Otherwise, it will divide and self-renew.

Extracellular regulation. The regulation of the erythroid progenitors fate is influenced by extracellular substances. Glucocorticosteroids (GC) and soluble growth factors (G) produced by the macrophage stimulate self-renewal. In the model, GC concentration is considered to be constant in the domain and it enters the equation (6.2.7) through the constant a_0. We describe that constant in the first equation of (6.2.11). The growth factor (G), which promote the self-renwal of erythroid progenitors enters the equation (6.2.8) through a_1. EPO, Fas-ligand and Trail influence the differentiation and apoptosis. They are taken into consideration in equations (6.2.9) and (6.2.10) through the coefficients a_2 and a_3. The expressions of these coefficients are given explicitly in the last two equations of (6.2.11):

$$\begin{aligned} a_0 &= a_0^0 + a_0^1 GC, a_1 = a_1^0 + a_1^1 G, a_2 = a_2^0 + a_2^1 E, \\ a_3 &= a_3^0 + a_3^1 F. \end{aligned} \tag{6.2.11}$$

For simplification, the dependancies are considered to be linear which reduces the number of used parameters.

Reticulocytes do not divide, they stay at the bone marrow before they are released into blood. In human, these cell express Fas-ligand that induces CFU-E/ProEbs cells apotosis by activating intracellular caspases. Multiple myeloma cells divide keeps growing until they reach the end of their life cycle, where they either die apoptosis or auto-renew. The rate of their auto-renwal ω is given in accordance with biological considerations.

Late-stage mature erythoid cells produce Fas-ligand. Fas-ligand is also produced by MM cells that also produce another CFU-E/ProEbs apoptosis inducing cytokine known as TRAIL. The effects of Fas-ligand and TRAIL are additive with a combined effect that is slightly less than the sum of their individual effects. We denote the concentration of these two cytokines by F_L. On the other hand, central macrophages produce a growth factor G which stimulates the proliferation of erythroid progenitors. The concentration of G and F_L are expressed using the reaction diffusion equations:

$$\frac{\partial F_L}{\partial t} = D_1 \Delta F_L + W_1 - \sigma_1 F_L, \tag{6.2.12}$$

$$\frac{\partial G}{\partial t} = D_2 \Delta G + W_2 - \sigma_2 G. \tag{6.2.13}$$

where D_1, D_2 are diffusion coefficients and W_1, W_2 are the rates of production of the corresponding factors. In MM cells, the production factor (denoted by W_1^*) is higher 1.8 times the production factor of late-stage erythroid cells. The last terms in the right-hand sides of these equations describe their degradation. The concentrations F_L and G are adimensionalized such that their values change between 0 and 1.

Cells displacement. In the model, cells are represented by individual elastic spheres. They divide and can increase their number which involves pushing each other leading to their displacement in the marrow space. We describe cells displacement by a simple model where cells are represented by elastic sphere. Let us denote the center of two cells by x_1 and x_2 and their radii by r_1 and r_2 respectively. Then, if the distance h_{12} between the two cells is less than the sum of their radii $(r_1 + r_2)$, there will be a repulsive force f_{12} between them. This force should depend on the difference between $(r_1 + r_2)$ and h_{12}. Let us consider the case of one cell interacting with different cells in the marrow space. The total force applied to this cell will be $F_i = \sum_{j \neq i} f_{ij}$. We describe the motion of the particles as the motion of their centers which can be found by the applying Newton's second law:

$$m\ddot{x}_i + m\mu\dot{x}_i - \sum_{j \neq i} f_{ij} = 0,$$

where m is the mass of the particle, μ is the friction factor due to contact with the surrounding medium. The potential force between two cells is given explicitly by:

$$f_{ij} = \begin{cases} K\frac{h_0 - h_{ij}}{h_{ij} - (h_0 - h_1)} & , \quad h_0 - h_i < h_{ij} < h_0 \\ 0 & , \quad h_{ij} \geq h_0 \end{cases},$$

where h_{ij} is the distance between the centers of the two cells i and j, h_0 is the sum of their radii, K is a positive parameter and h_1 is the sum of the incompressible part of each cell. The force between the particles tends to infinity if h_{ij} decreases to $h_0 - h_1$.

When the cell reaches the half of its life cycle, it will increase its size. When it divides, two daughter cells appear, the direction of the axis connecting their centers is chosen randomly from 0 to 2π. The duration of the cell cycle of CFU-E/ProEbs and reticulocytes is of 18 hours with a random perturbation of -3 to 3 hours.

Multiple myeloma treatment protocols. In order to model the intracellular concentration of the drug in MM cells, we use an ordinary differential equation (6.2.14) that depends on the extracellular concentration of the drug. For the protocol BLD, three drugs are used to kill MM cells. Therefore, the extracellular concentration $p_e(t)$ of the thee drugs can be expressed by a time-dependant function which describe the treatment administrated protocol. We denote the intracellular concentration of the drug in the MM cell by p. When p reaches a critical value p^*, it will die by apoptosis. Otherwise, if the cell reaches the end of its life cycle without dying by the drug then it will divide and auto-renew by a given rate ω:

$$\frac{dp}{dt} = k_1 p(t) - k_2 p, \tag{6.2.14}$$

In *in vivo* and *in vitro* experiments, we evaluate multiple myeloma infiltration through a set of immunoglobulins secreted by MM cells. The concentration of immunoglobins is expressed by ordinary differential equations. These immunoglobulins can be M-Protein, a monoclonal antibody, but they can also belong to other classes of immunoglobulins: IgG, IgM, IgD, IgK, IgA. In the ordinary differential equations describing their immunoglobulins concentrations, the first terms of the right hand side depends on the population of MM cells (N). Each immunoglobulin produce a light chain that can be either lambda or kappa. Immunoglobulins have a half life time and their concentrations are degraded over time. We therefore add a degradation term to their respective equations. We denote the each immunoglobulin concentration by a the letter of the class and the light chain of the immunoglobulin. For example, the concentration of the des kappa light chain of the IgG immunoglobulin by G_κ. The equations of each immunoglobulin concentration is given explicitely in (6.2.15) and (6.2.16).

$$\frac{dM}{dt} = k_1^1 N - k_2^1 M, \quad \frac{dG_\kappa}{dt} = k_1^2 N - k_2^2 G_\kappa, \quad \frac{dG_\lambda}{dt} = k_1^3 N - k_2^3 G_\lambda, \tag{6.2.15}$$

$$\frac{dM_\kappa}{dt} = k_1^4 N - k_4^1 M_k, \quad \frac{dD_\kappa}{dt} = k_1^5 N - k_2^5 D_\kappa, \quad \frac{dA_\lambda}{dt} = k_1^6 N - k_2^3 A_\lambda, \tag{6.2.16}$$

6.2.3 Results

Myeloma infiltration of marrow causes a major but reversible cause of anemia. Hemoglobin levels (Figs. 6.10A, 6.10B) and RBCs (Figs. 6.10C, 6.10D) are shown at diagnosis (Dx), Day 1 of cycles 2 to 4 of LBD treatment (C2D1,C3D1, C4D1), and after completing LBD chemotherapy (Post Rx). Patients with greater than 35% myeloma infiltration at diagnosis had lower mean hemoglobin values when compared to patients with less than 30% myeloma infiltration at diagnosis(10.6 $\pm$ 0.4 g/dL vs. 13.6 $\pm$ 0.6 g/dL; $p < 0.001$),and when compared to their own Post Rx values (10.6 $\pm$ 0.4 g/dL vs. 12.1 $\pm$ 0.5 g/dL; $p < 0.05$).Similarly, patients with greater than 35% myeloma infiltration at diagnosis had lower mean RBCs when compared to patients with less than 30% myeloma infiltration at diagnosis (3.37 $\pm$ 0.4 x106/μL vs. 4.52 $\pm$ 0.22 106/μL; $p < 0.001$) and when compared to their own Post Rx values (3.37 $\pm$ 0.4 x106/μL vs. 4.09 $\pm$ 0.20 x 106/μL; $p < 0.05$).Therefore, increased erythropoiesis following LBD treatment in patients with greater than 35% myeloma infiltration at diagnosis increased hemoglobin and RBCs, indicating that myeloma infiltration of marrow played a major role in the development of anemia in these patients, who had no evidence for other common causes of anemia such as bleeding, renal insufficiency, iron deficiency, vitamin B12 deficiency, myelodysplasia, and myelofibrosis.

Serum monoclonal proteins as markers for modelling myeloma marrow infiltration. Serum monoclonal immunoglobulin or free light chain concentrations are shown at Dx, on C2D1,C3D1, C4D1 and Post Rx of LBD chemotherapy for patients with less than 30% myeloma infiltration of the marrow at diagnosis in Figs. 6.11A-C and for patients with greater than 35% myeloma infiltration in Figs. 6.11D-F. As expected with LBD [222], most patients had large decreases in their serum monoclonal immunoglobulin proteins and free light chains after the first cycle of therapy that were followed by further but smaller decreases after subsequent cycles. For mathematical modeling of the patients' responses to LBD chemotherapy, parameters in differential equations were chosen to fit the clinical data in Fig. 6.11. Fig. 6.12 shows results for three virtual patients receiving simulated treatment with the LBD protocol. The three virtual patients different in the proliferation rate of their respective myeloma cells, with patient A having the highest proliferation rate (P=0.617), patient B having an intermediate rate (P=0.616) and patient C having the lowest (P=0.615).Numbers of myeloma cells and concentrations of monoclonal proteins decrease during drug administration (weeks 1 and 2 of each cycle) and, depending upon proliferation rate, they can increase during weeks 3 and 4 of each cycle, which are without treatment. Responses of specific monoclonal proteins and their respective immunoglobulin class are shown

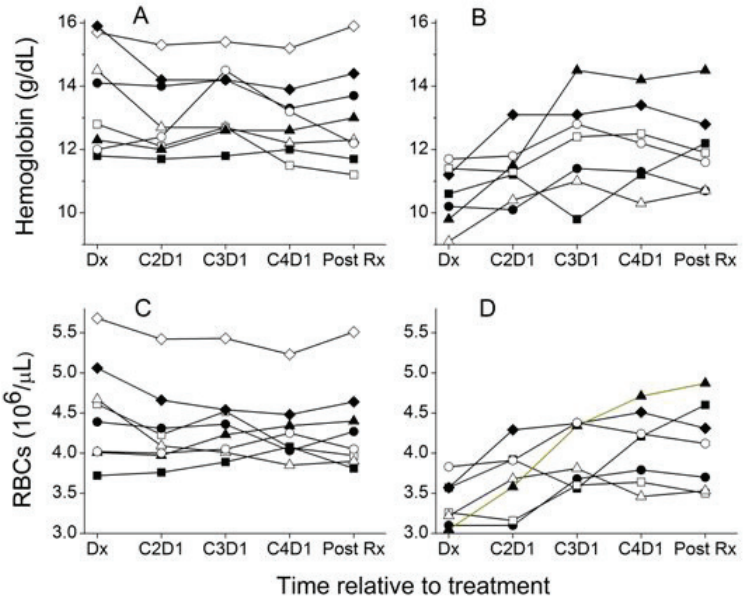

Figure 6.10: Hemoglobin levels and RBC numbers during treatment of MM patients. During treatment with LBD, mean hemoglobin levels did not change in (A) patients with less than 30% myeloma cell infiltration, but increased in (B) patients with greater than 35% myeloma infiltration, who had lower hemoglobin values at diagnosis. Similarly, during treatment with LBD, mean RBC number did not change significantly in (C) patients with less than 30% myeloma cell infiltration, but did increase in (D) patients with greater than 35% myeloma infiltration, who had lower mean RBC numbers at diagnosis. Each curve represents a single patient. Times relative to treatment are: Dx, diagnosis/C1D1; C2D1, cycle 2 day 1; C3D1, cycle 3 day 1; C4D1, cycle 4 day1: Post Rx, after treatment completed.

in Fig. 6.12 .Due to stochasticity in cell division, the concentration of monoclonal protein for some patients can be greater in the beginning of the third cycle when compared to the second cycle (Fig. 6.12A, patient A).

Fig. 6.13 shows application of the mathematical model in simulations comparing the LBD protocol with two variations. LBD2 intensifies therapy by administering in week one of each cycle the total LBD doses normally given over two weeks. BD reduces intensity by using two drugs while increasing the number of cycles from four to five within the similar 112-day period. Based on these simulations, LBD2 would be most effective at clearing myeloma from the marrow. However, in practice it would be highly neurotoxic. Less intensified therapy with BD would be less effective than LBD at clearing myeloma from the marrow.

6.3 The effects of muliple myeloma chemotherapy treatment on the coagulation process

6.3.1 Lenalidomide pharmacokinetics

Lenalidomide is an immunomodulatory agent used to eliminate MM cells by blocking the activation of $NF-\kappa B$, a nuclear factor necessary for their survival, and increasing the number of NK-cells by upregulating the production of interleukin-2 (IL-2). After its administration, the concentration of lenalidomide in the plasma reaches its maximum within 1-2 hours and has a half-life time of 3 hours [223]. Lenalidomide upregulates the concentration of endothelial tissue factor resulting in an increased risk of thrombosis. During a 28 days cycle of MM chemotherapy, lenalidomide 25 mg is administrated on days

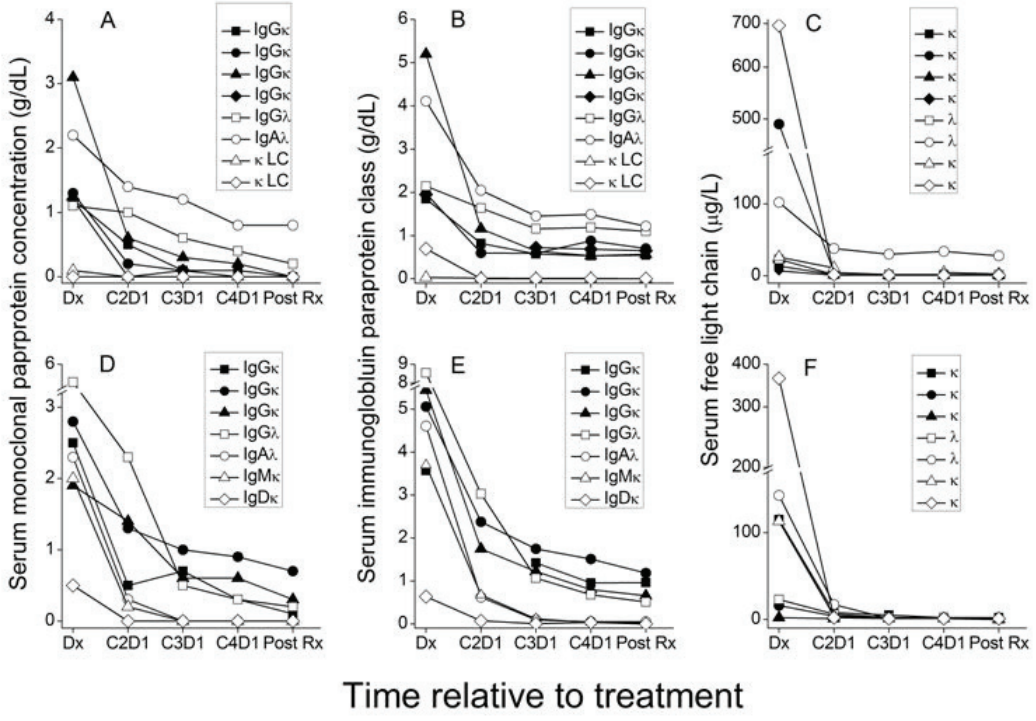

Figure 6.11: Serum levels of monoclonal paraproteins produced by myeloma cells during the LBD treatment of newly diagnosed multiple myeloma patients.(A, B, C) are serum paraprotein values in patients with less than 30% marrow area infiltrated with myeloma at diagnosis and (D, E, F) are values in patients with greater than 35% marrow infiltrated at diagnosis. Serum concentrations of (A, D) monoclonal immunoglobulin paraproteins (M proteins) measured by electrophoresis with immunofixation, (B, E)total immunoglobulin proteins in the class of the respective monoclonal immunoglobulin or light chain, and (C, F) free light chains in newly diagnosed patients with multiple myeloma who were treated with LBD. Each curve represents a single patient. Times are: Dx, diagnosis/C1D1; C2D1, cycle 2 day 1; C3D1, cycle 3 day 1; C4D1, cycle 4 day 1: Post Rx, after treatment completed.

1 to 14. We consider the following equation of lenalidomide concentration in tissues:

$$\frac{dL}{dt} = \kappa_1^1 L(t) - \kappa_2^1 L, \tag{6.3.17}$$

where $L(t)$ takes the value of 25 mg after each oral administration of lenalidomide and 0 elsewhere. κ_1^1 and κ_2^1 are two positive constants. The concentration of lenalidomide is shown in Fig. 6.14.

6.3.2 Dexamethasone pharmacokinetics

Dexamethasone is a corticosteroid commonly used in MM treatments for its anti-inflammatory effects. It has a osnet time of 1-2 hours and a half life time of 190 minutes in blood and 32-45 hours in tissues [225]. Dexamethasone has a procoagulant effect on blood clotting especially when administrated jointly with lenalidomide or thalidomide. It increases the level of tissue factor in monocytic cells through their induction by lipopolysaccharide (LPS) [224]. Dexamethasone 20 mg is administrated the day before and the day after receiving bortezomib. We consider the following equation of lenalidomide concentration in tissues:

$$\frac{dD}{dt} = \kappa_1^2 D(t) - \kappa_2^2 D, \tag{6.3.18}$$

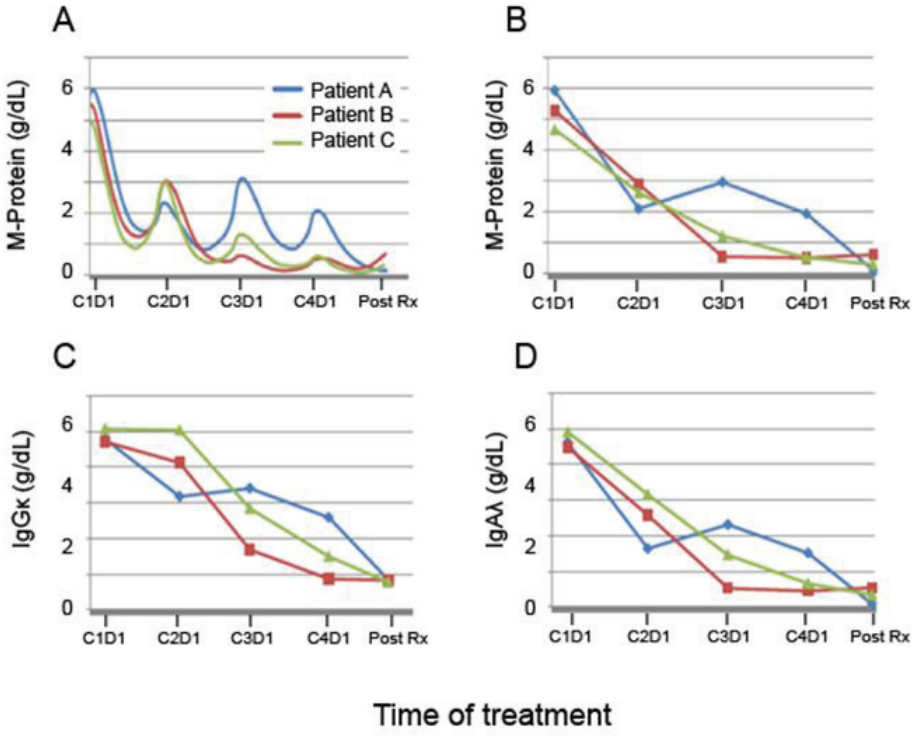

Figure 6.12: Numerical simulations of monoclonal immunoglobulin concentrations in serum. Monoclonal protein concentrationsin three virtual patients as measured (A) daily and (B) on Day 1of each cycle of treatment in numerical simulations of myeloma treatment with protocol LBD (based on data in Fig. 4.12). Serum concentrations of (C) immunoglobulin G_κ and (D) immunoglobulin A_λ in numerical simulations for the same three virtual patients as in (A) and (B).

where $D(t)$ takes the value of 20 mg after each oral administration of lenalidomide and 0 elsewhere. κ_1^2 and κ_2^2 are two positive constants. The concentration of lenalidomide is shown in Fig. 6.15.

6.3.3 The effect of lenalidomide-based regimens on thrombosis risk

Both lenalidomide and dexamethasone increases the concentration of tissue factor in endothelial tissues. Previous studies have shown that lenalidomide increases the TF concentration by 3% when administrated independtly and by 12-24% when given with dexamethasone [226]. Hence, we describe concentration of TF as follows during lenalidomide-based regimens:

$$TF(t) = TF_0 + \Omega_1(\zeta_1 \frac{L(t)}{L_{max}} + \eta_1 \frac{D(t)}{D_{max}}), \tag{6.3.19}$$

where Ω, ζ, and η are positive constants, L_{max}, D_{max} denotes the maximal values that can be taken by lenalidomide and dexamethasone respectively. We use the previously introduced simplified model of thrombin concentration to evaluate the coagulation response in patients during lenalidomide-based regimens:

$$\frac{\partial T}{\partial t} = D\frac{\partial^2 T}{\partial y^2} + \Phi(T,y),$$

where

$$\Phi(T,y) = (k_1^+ T\phi_0 + k_2 B_a(y) + k_3^+ T^3)(P_0 - T) - \gamma(y)T,$$

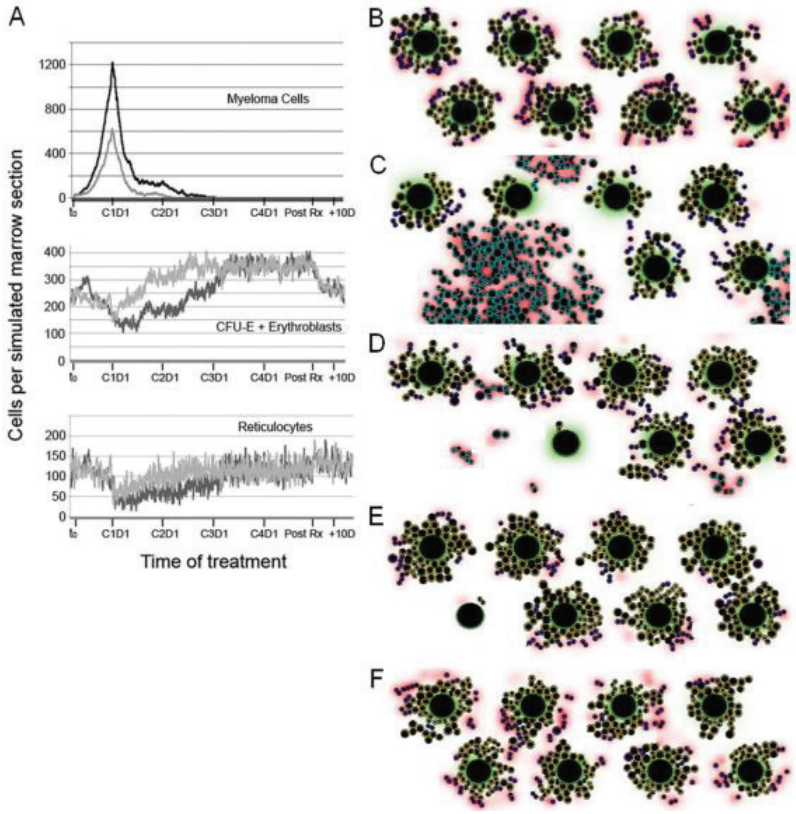

Figure 6.13: Effects on erythropoiesis of simulated marrow infiltration by multiple myeloma with complete remission following LBD therapy. (A) Simulated numbers of myeloma and erythroid cells in a section of marrow that had eight EBIs prior to the introduction of myeloma cells at time zero (t_0). The results are shown for daily numbers of myeloma cells and erythroid cells in the section, with the gray curves representing a simulation initiated with 22 cells and the black curves representing a simulation initiated with 28 cells at t0. Diagnosis and initiation of LBD treatment is on day 23 after t_0, and it is designated as C1D1. Four 28-day cycles of LBD therapy are administered. Time points: t0, C1D1, C2D1, C3D1, C4D1, and day 1 and day 10 after completion of the fourth cycle of therapy (Post Rx and 110D, respectively). Images of the marrow section corresponding to simulation results shown as the gray curves in (A) are shown for the following times: (B) t0, immediately before myeloma cells are introduced, (C) Dx/C1D1, (D) C1D15, (E) C2D1, and (F) C3D1. Central macrophages are the large central cells in the EBIs. CFU-E and erythroblasts are the yellow cells surrounding the central macrophages. Marrow reticulocytes prior to their entry into the blood are dark blue on the periphery of the EBIs. Myeloma cells are light blue. Black solid circles inside cells show their incompressible parts. Secreted proteins shown extracellularly are green for BMP4 and/or SCF produced by central macrophages and red for FAS ligand produced by mature erythroblasts and reticulocytes within EBIs, and FAS ligand and/or TRAIL produced by infiltrating myeloma cells.

The condition of thrombosis on tissue factor was previously given in Section 4.2.7 (Eq. 4.2.22). We use this condition together with the predicted values of TF to asses the thrombosis risk during lenalidomide-based regimens treatments (Fig. 6.16). The results show that the thrombosis risk is high during the two days after the each dexamethasone administration. Anticoagulant therapy is necessary to decrease this risk and prevent thrombo-embolic events. We will study the action of some of these drugs in the next section.

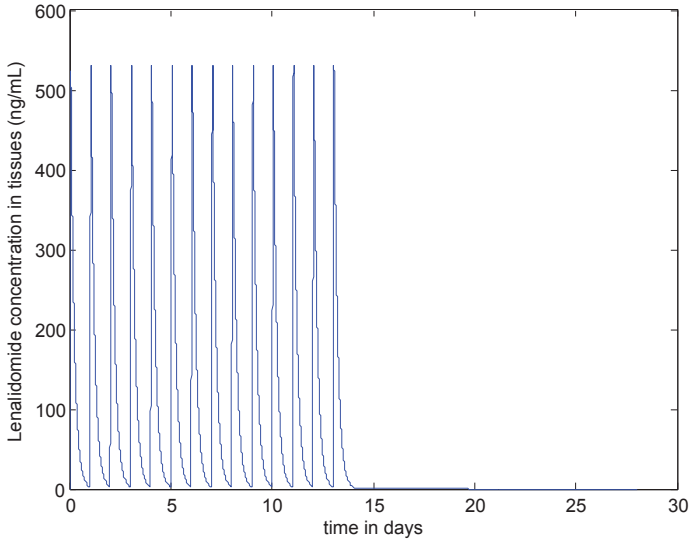

Figure 6.14: The concentration of lenalidomide in plasma during a cycle of MM treatment.

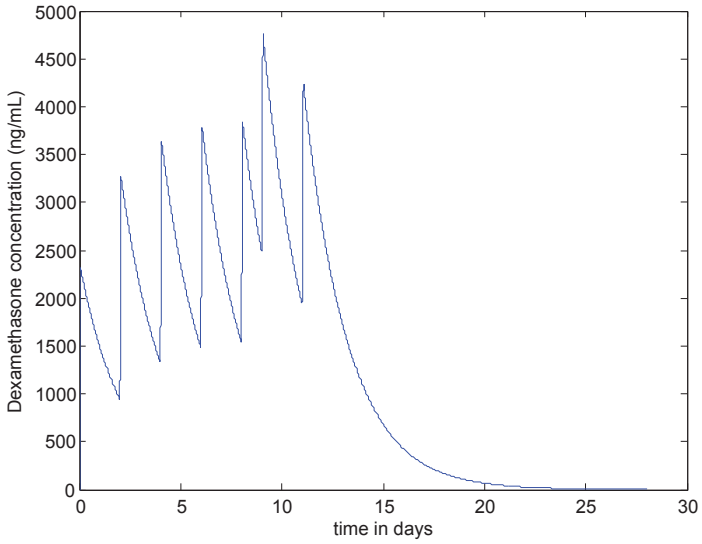

Figure 6.15: The concentration of dexamethasone in plasma during a cycle of MM treatment.

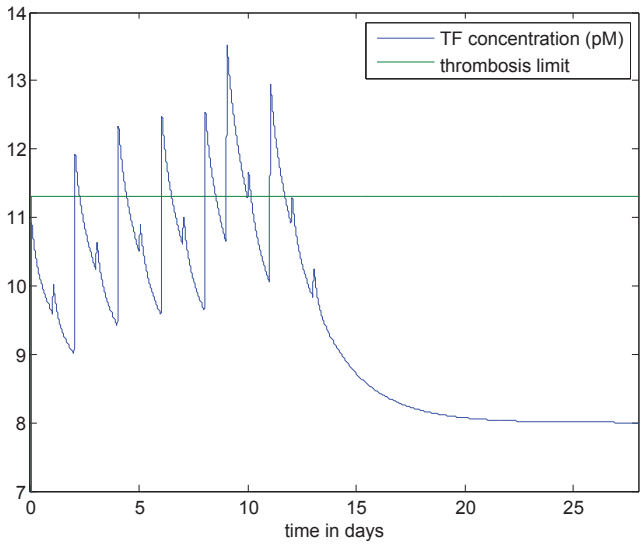

Figure 6.16: Tissue factor concentration during MM chemotherapeutic treatment vs. the threshold of thrombosis.

Chapter 7

Mutiscale Modelling of HIV Infection and the Associated Thrombosis Risk

7.1 A multiscale model of the immune response in the lymph node

7.1.1 Background

The immune system is regulated by multiple processes at various levels of biological organization including the genetic-, cellular-, tissue-, organ- and the whole organism levels. The resulting structural and functional complexity of the immune system called for a major shift towards information-rich, systems-based approaches in immunological research. High throughput technologies generate vast amounts of data that facilitate dissection of the immunological processes at ever finer resolution. The need to embed immune processes into their spatial context both at the molecular- and cellular level is a hallmark of the systems immunology approach. In fact, there are many examples of how the fate decisions in the immune system depend on the spatial-temporal dynamics of cytokines, e.g. the interleukin-2 (IL-2) [286] and type I interferon (IFN) [287, 288].

Moving from the molecular and cellular level to a multiscale systems understanding requires the development of novel modelling methodologies for an iterative integration of data from different biological levels into mechanism-based modular mathematical models red [236, 249, 242]. So far, very few mathematical models have been proposed to describe the multiscale spatial regulation of immune responses in a genuine hybrid manner [247, 241, 248, 244]. The major features of the developed models are summarized in Table 7.1). In contrast to the above studies, our multiscale model considers (1) the spatial cell displacement using a bio-mechanical description, (2) the spatially regulated asymmetry in T lymphocyte division, (3) the intracellular regulation of the T lymphocyte fate depending on the extracellular distribution of the key cytokines IL-2 and type I IFN. Here we present a methodology for an integrative modelling of immunological processes in their spatial context. It uses a hybrid approach to construct multiscale models linking (1) transport phenomena, (2) intra-cellular fate regulation and (3) cellular interactions.

In contrast to the above studies, our hybrid approach to multiscale modelling considers: (1) the transport phenomena by implementing a bio-mechanical description for the spatial cell displacement rather than agent-based or cellular Potts algorithms; (2) the tissue level regulation of T lymphocyte division taking an asymmetry of the process which is affected by the spatial-mechanical characteristics of the cellular interactions; and (3) the intracellular regulation of T cell differentiation pathway by an extracellular distribution of two key cytokines, i.e. IL-2 and type I IFN, with the timing of the respective signalling taken into account.

The spatial part of our approach is based on considering the biophysical properties of cells and mechanical interactions between them according to the Newton's second law. Therefore, we implement the first principle equations in the analysis of the spatial cell dynamics. This is in contrast to other

Table 7.1: Overview of the hybrid and multiscale approaches to model the spatial dynamics of immune responses

Model	Phenomena	Process considered	Types of equations	State variables
Baldazzi *et al.* [247]	Immune response to antigen in lymph node (500 hrs)	Clonal expansion, 3D: transport, reaction-diffusion	Agent-based for cells, PDEs for molecules antigen, chemokines	DCs, B-cells, $CD4^+$ T cells,
Fallahi-Sichani *et al.* [241]	Immune response in Tuberculosis, Granuloma (200 days)	Clonal expansion, 2D: chemotaxis, cell-to-cell interactions single-cell state regulation	Agent-based for cells, ODEs for cytokines, 2D geometry of lung tissue	Macrophages, $CD8^+$ T cells, Treg cells, Tγ cells, M. tuberculosis, TNFα, TNFR
Gong *et al.* [248]	Immune response to antigen in lymph node (550 hours)	Clonal expansion, 3D: trafficking, cell-to-cell interactions	Agent-based for cells, anatomicaly based 3D geometry of lymph node	3 states for: DCs, $CD4^+$ T cells, $CD8^+$ T cells; Locations for HEVs, FRCs
Prokopiou *et al.* [244]	Early $CD8^+$ T-cell response in lymph node (136 hrs)	Clonal expansion, intracellular regulation, 3D: migration, reaction-diffusion	CPM for cells, PDEs for extracellular cytokines, ODEs for intracellular factors	APCs, T-cells, IL-2, IL-2R, Tbet, Caspase, Fas (activated, non-activated)

existing approaches which are phenomenological in their nature such as agent based models or cellular Potts models. The spatial distribution of cytokines is also described by fundamental equations, i.e. the reaction-diffusion PDEs. Finally, the intracellular regulation and infection dynamics are represented by chemical kinetics type ODEs which are widely accepted in mathematical immunology. The proposed approach was validated in modelling other physiological systems such as blood diseases and hematopoiesis as shown in [258]-[263]. Here we present a methodology for an integrative modelling of immunological processes in their spatial context.

Methods

Biophysics of the immune response

To formulate the mathematical model, we consider a part of the lymph node, i.e., the T cell zone, which contains various cell types, mainly the antigen presenting cells (APCs) and subsets of T lymphocytes. Naive T cells and some APCs (such as plasmocytoid Dendritic Cells, pDCs) enter the node with blood flow via the High Endothelial Venules (HEVs) whereas effector and/or memory T cells, and mainly DCs and macrophages home to lymph nodes via afferent lymphatic vessels [289, 290]. Following activation with pathogens, APCs acquire a motile state that allows their translocation to the T cell zone of draining lymph node with the afferent lymph flow [291, 292]. Therefore, we assume that the influx of APCs is

proportional to the level of infection in the organism. Differentiation of naive T cells into $CD4^+$ and $CD8^+$ T cells occurs in the thymus from progenitor T cells [294]. We suppose that they enter lymph nodes already differentiated and that there is a given influx of each cell type.

The APCs bearing foreign antigens activate the clonal expansion of naive T lymphocytes. The activation of T cell division and death is regulated by a set of signals coming from the interactions of the antigen-specific T cell receptors (TCRs) with the MHC class I or class II presented peptides and IL-2 receptors binding IL-2. Naive T cells undergo asymmetric division [295] (Fig. 7.1). Some of the daughter cells continue to proliferate and differentiate. Mature $CD4^+$ T cells produce IL-2 [294, 296, 297] which influences survival and differentiation of both $CD4^+$ and $CD8^+$ T cells. The proliferation of $CD8^+$ T cells is stimulated by IL-2 [296]. They can expand their number many thousand-fold. In addition to IL-2 enhancing the proliferation of T cells, APCs start to secrete type I IFN which has an antiviral- and immunomodulatory function. In fact, the effect of IFNα depends on the temporal sequence of the signals obtained by naïve T cells [287]. It can change from a normal activation of T cells followed by their proliferation and differentiation to an already differentiated state followed by apoptosis as shown schematically in Fig. 7.2. Overall, the regulated death of T cells by apoptosis depends on the availability and the timing of TCR, IL-2 and IFN signalling.

Mature $CD8^+$ T cells (effector cells) leave the lymph node and kill infected cells. Therefore, there is a negative feedback between production of mature $CD8^+$ T cells and the influx of APCs.

In the model, an asymmetric T cell division is considered as shown in Fig. 7.3. Naive T cell entering the draining lymph node is recruited into the immune response after the contact interaction via the T cell receptor (TCR) with APC presenting the foreign antigen. The activation and prolonged contact with APC can results in polarity of the lymphocyte. The position of the contact with the APC determines the direction of cell division and the difference between the daughter cells in terms of their differentiation state. According to [295], the proximal daughter cell will undergo clonal proliferation and differentiation resulting in the generation of terminally differentiated effector cells (mature $CD8^+$ T cells) that leave the lymph node for peripheral tissues to search and kill infected cells. The distal daughter cell becomes a memory cell. The memory cells are capable of self-renewal by slowly dividing symmetrically in the absence of recurrent infection.

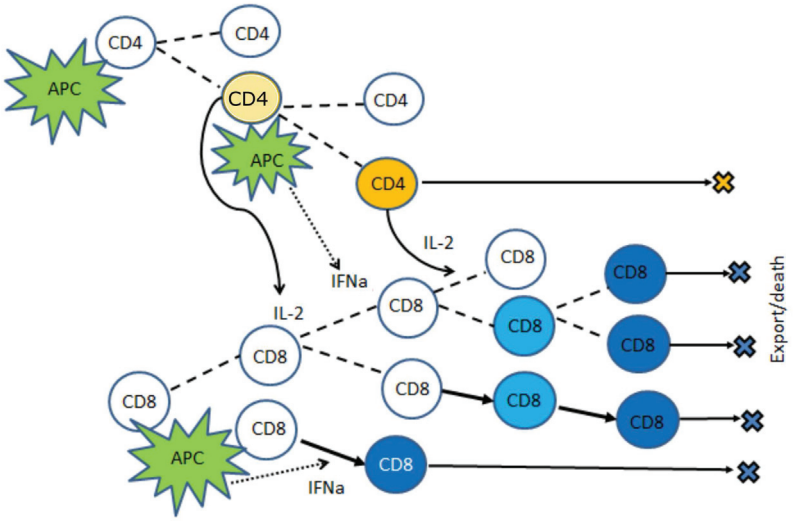

Figure 7.1: Schematic representation of the model. Naive T cells and antigen presenting cells (APC) enter the lymph node. Due to asymmetric cell division, some T cells differentiate. Mature $CD8^+$ T cells leave the lymph node and kill infected cells. Mature $CD4^+$ T cells produce IL-2 that influences cell survival and differentiation. APCs are shown in green, naive T cells are white. Differentiated $CD4^+$ T cells are yellow and $CD8^+$ T cells are blue. Levels of yellow and blue indicate cell maturation.

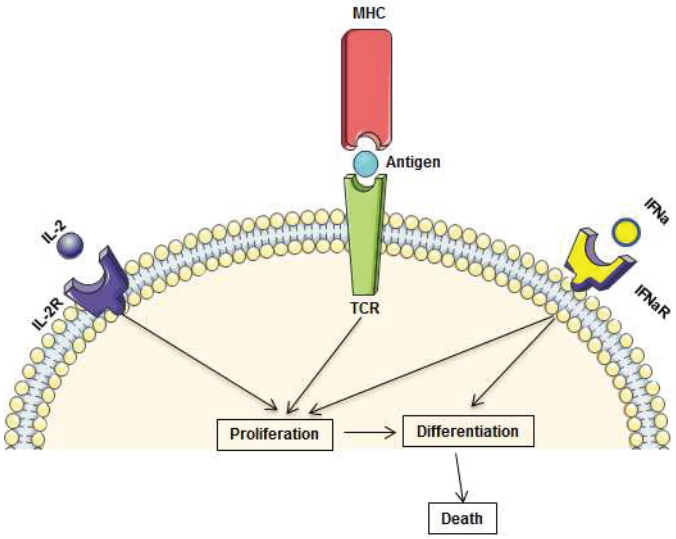

Figure 7.2: Scheme of the integration of TCR-, type I Interferon- and IL-2 signaling sequence by naïve T cells to adaptively program the balance of growth and differentiation

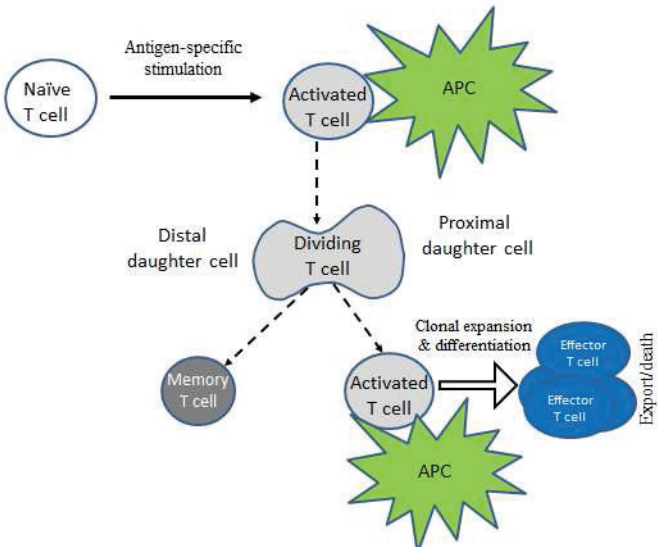

Figure 7.3: Scheme of the spatial regulation of the asymmetric T cell division in lymph nodes (elaborated from [295])

.

Hybrid model of cell dynamics

In our model of cell dynamics, cells are considered as individual objects that can move, divide, differentiate and die. Their behavior is determined by the surrounding cells, by intracellular regulatory networks described by ordinary differential equations and by various substances in the extracellular matrix whose concentrations are described by partial differential equations. This approach was used to model hematopoiesis and blood diseases [**?**]-[152].

Cells and concentrations. Cells in the lymph node:

1. $n_{APC}(\mathbf{x},t)$ - the density of APCs in T cell zone;

2. $n_{CD4}(\mathbf{x},t)$ - the density of CD4$^+$ T cells in T cell zone (with different levels of maturity);

3. $n_{CD8}(\mathbf{x},t)$ - the density of CD8$^+$ T cells in T cell zone (with different levels of maturity);

Extracellular variables:

4. $I_e(\mathbf{x},t)$ - the concentration of IL-2 in T cell zone;

5. $C_e(\mathbf{x},t)$ - the concentration of type I IFN in T cell zone;

Intracellular variables:

6. $I_i(t)$ - the intracellular concentration of IL-2-induced signalling molecules in the ith cell;

7. $C_i(t)$ - the intracellular concentration of type I IFN-induced signalling molecules in the ith cell;

The state variables at the level of the whole organism:

8. $N_{ef}(t)$ - the total number of effector CD8$^+$T cells in the body;

9. $N_{inf}(t)$ - the total number of infected cells in the body;

Cell displacement. In the model, cells are represented by individual elastic spheres. There are two mechanisms of motion of cells in the lymph node. First of all they move in a random way. This motion allows naive T cells to meet APCs which is necessary for their activation, division and differentiation. Second, each two cells, when they meet, they push each other due to a direct mechanical interaction. We consider this interaction as an elastic force acting on cells and influencing their motion. Let us describe it in more detail.

The cells divide and can increase their number which involves pushing each other leading to their displacement in the lymph node. We describe cells displacement by the following model. Let us denote the center of two cells by x_1 and x_2 and their radii by r_1 and r_2 respectively. Then, if the distance h_{12} between the two cells is less than the sum of their radii (r_1+r_2), there will be a repulsive force f_{12} between them. This force should depend on the difference between (r_1+r_2) and h_{12}. Let us consider the case of one cell interacting with different cells in the lymph node. The total force applied to this cell will be $F_i=\sum_{j\neq i} f_{ij}$. We describe the motion of the particles as the motion of their centers which can be found by the applying Newton's second law:

$$m\ddot{x}_i + m\mu\dot{x}_i - \sum_{j\neq i} f_{ij} = 0, \tag{7.1.1}$$

where m is the mass of the particle, μ is the friction factor due to contact with the surrounding medium. The potential force between two cells is given explicitly by:

$$f_{ij} = \begin{cases} K\frac{h_0-h_{ij}}{h_{ij}-(h_0-h_1)} & , \quad h_0-h_i < h_{ij} < h_0 \\ 0 & , \quad h_{ij} \geq h_0 \end{cases},$$

where h_{ij} is the distance between the centers of the two cells i and j, h_0 is the sum of their radii, K is a positive parameter and h_1 is the sum of the incompressible part of each cell. The force between the particles tends to infinity if h_{ij} decreases to h_0-h_1.

Cell division and differentiation. APC and naive T cells enter the computational domain with a given frequency if there is available space. Naive T cells move in the computational domain randomly. If they contact APC, they divide asymmetrically (Fig. 7.3). The distant daughter cell is similar to the mother cell, the proximal daughter cell becomes differentiated.

When the cell reaches the half of its life cycle, it will increase its size. When it divides, two daughter cells appear, the direction of the axis connecting their centers is chosen randomly from 0 to 2π. The duration of the cell cycle is 18 hours with a random perturbation of -3 to 3 hours.

We consider two levels of maturity of CD4$^+$ T cells and three levels of CD8$^+$ T cells. If a differentiated cell has enough IL-2 (see the next paragraph), then it divides and gives two more mature cells. Finally differentiated cells leave the lymph node. In the simulations, this means that they are removed from the computational domain.

Intracellular regulation. The survival and differentiation of activated $CD4^+$- and $CD8^+$ T lymphocytes depends on the amount of signalling via the IL-2 receptor and the type I IFN receptor. It is controlled primarily by the concentration of the above cytokines in the close proximity of the respective receptors. The signalling events lead to the up-regulation of the genes responsible for cell proliferation, differentiation and death. One can use similar type of equation to model qualitatively the accumulation of the respective intracellular signalling molecules linked to IL-2- and type I IFN receptors. The IL-2 dependent regulatory signal dynamics in individual cells can be described by the following equation:

$$\frac{dI_i}{dt} = \frac{\alpha_1}{n_T} I_e(\mathbf{x_i}, t) - d_1 I_i. \tag{7.1.2}$$

Here I_i is the intracellular concentration of signalling molecules accumulated as a consequence of IL-2 signals transmitted through transmembrane receptor IL2R downstream the signaling pathway to control the gene expression in the ith cell. The concentrations inside two different cells are in general different from each other. The first term in the right-hand side of this equation shows the cumulative effect of IL-2 signalling. The extracellular concentration I_e is taken at the coordinate $\mathbf{x_i}$ of the center of the cell. The second term describes the degradation of IL-2-induced signalling molecules inside the cell. Furthermore, n_T is the number of molecules internalized by T cell receptors.

In a similar way, the IFN-dependent regulatory signal dynamics in individual cells can be described by the following equation:

$$\frac{dC_i}{dt} = \frac{\alpha_2}{n_T} C_e(\mathbf{x_i}, t) - d_2 C_i. \tag{7.1.3}$$

Here C_i is the intracellular concentration of signalling molecules accumulated as a consequence of IFN signals transmitted through transmembrane receptor IFNR downstream the signaling pathway to control the gene expression in the i-th cell. The concentrations inside two different cells are in general different from each other. The first term in the right-hand side of this equation shows the cumulative effect of IFN signalling. The extracellular concentration C_e is taken at the coordinate $\mathbf{x_i}$ of the center of the cell. The second term describes the degradation of IFN-induced signalling molecules inside the cell.

To model the fate regulation of growth versus differentiation of the activated cells in relation to the timing of the IL-2 and type I IFN signalling we implement the following decision mechanism.

C1 If the concentration of activation signals induced by type I IFN, C_i, is greater than some critical level C_i^* at the beginning of the cell cycle and that of I_i, is smaller than the critical level I_i^*, then the cell will differentiate resulting in a mature cell.

C2 If the concentration of activation signals induced by IL-2, I_i, is greater than some critical level I_i^* at the end of the cell cycle, then the cell will divide producing two more mature cells.

C3 If $C_i < C_i^*$ at the beginning of cell cycle and $I_i < I_i^*$ at the end of cell cycle, then the cell will die by apoptosis and will be removed from the computational domain.

Stochastic aspects of the model. As it is discussed above, mechanical interaction of cells results in their displacement described by equation (7.1.1) for their centers. In order to describe random motion of cells we add random variables to the cell velocity in the horizontal and vertical directions.

Duration of cell cycle is given as a random variable in the interval $[T-\tau, T+\tau]$.

Extracellular dynamics of cytokines. Proliferation and differentiation of T cells in the lymph node depends on the concentration of IL-2 and type I IFN. These cytokines are produced by mature $CD4^+$ T cells and antigen-presenting cells, respectively. Their spatial distribution is described by a similar reaction-diffusion equation as follows

$$\frac{\partial I_e}{\partial t} = D_{IL} \Delta I_e + W_{IL} - b_1 I_e. \tag{7.1.4}$$

Here I_{ex} is the extracellular concentration of IL-2, D is the diffusion coefficient, W_{IL} is the rate of its production by $CD4^+$ T cells, and the last term in the right-hand side of this equation describes its

consumption and degradation. The production rate W_{IL} is determined by mature CD4$^+$ T cells. We consider each such cell as a source term with a constant production rate ρ_{IL} at the area of the cell. Let us note that we do not take into account explicitly consumption of IL-2 by immature cells in order not to introduce an additional parameter. Implicitly this consumption is taken into account in the degradation term.

For type I IFN, the equation and the terms in it have a similar interpretation:

$$\frac{\partial C_e}{\partial t} = D_{IFN}\Delta C_e + W_{IFN} - b_2 C_e. \tag{7.1.5}$$

Initial and boundary conditions for both concentrations IL-2 and IFN are taken zero. As before, the production rate W_{IFN} equals ρ_{IFN} at the area filled by APC cells and zero otherwise.

Infection. Mature T cells leave the bone marrow. The level of CD8$^+$ T cells (effector cells) N_{ef} in the body is determined by the equation

$$\frac{dN_{ef}}{dt} = k_1 T - k_2 N_{ef}, \tag{7.1.6}$$

where T is their number in the lymph nodes. So the first term in the right-hand side of this equation describes production of effector cells in the lymph nodes and the second term their death in the body.

Denote by N_{inf} the number virus-infected cells. We will describe it by the equation

$$\frac{dN_{inf}}{dt} = f(N_{inf}) - k_3 N_{ef} N_{inf}. \tag{7.1.7}$$

The first term in the right-hand side of this equation describes growth of the number of infected cells and the second term their elimination by the effector cells. The function f will be considered in the form:

$$f(N_{inf}) = \frac{aN_{inf}}{1 + hN_{inf}},$$

where a and h are some positive constants.

Finally, the influx of APC cells into the lymph nodes is proportional to the number of infected cells N_{inf}. This influx is limited by the place available in the lymph node. If there is a free place sufficient to put a cell, the new cells are added. Let us also note that the lymph nodes can increase due to infection in order to produce more effector cells.

Results

We illustrate the model performance by considering two scenarios, reflecting different spatial patterns of IL-2 and type IFN concentration fields. In the first one, both cytokines have the same diffusion coefficient $D_{IL2} = D_{IFN}$, whereas in the second case the diffusion rate of IFN is 10-fold faster. The details of the numerical implementation of the hybrid model and the parameter values used for the simulations are presented in appendix. Cell population densities and cytokine concentrations are scaled with respect to some reference values.

The model presented above contains two compartments, lymph node where effector cells are produced and the body where infection develops. The lymph node is described with the hybrid model while infection development in the organism by ordinary differential equations for infected cells and for effector cells. These two compartments are coupled by means of flux of effector cells from the lymph node to the body and by the flux of APC cells to the lymph node.

The results of the simulations are shown in Fig.s 7.4 - 7.7. Fig. 7.4 represents a snapshot of the lymph node T cell zone with all cells participating in the simulations: APC cells, naive T cells, differentiated CD4$^+$ T and CD8$^+$ T cells. Naive T cells divide when they are close to APC cells. It is an asymmetric division where a proximal daughter cell differentiates while a distant cell remains undifferentiated. Differentiated cells continue their division and maturation in the presence of IL-2 produced by mature CD4$^+$ T cells. If the level of IL-2 is not sufficient, they die by apoptosis. Mature T cells leave

the lymph node. One can see that the cytokine fields are non-uniform and their distribution patterns change essentially if the turnover parameters, e.g. the diffusion coefficient, are varied. Note that the cell distribution is more uniform in the case of large diffusion coefficient of IFN (Fig. 4.12, lower image) compared with the case of small diffusion coefficient (upper image).

The evolution of the total number of $CD4^+$ and $CD8^+$ T cells in the lymph node T cell zone is shown in Fig. 7.5. The dynamics of APC cells in the lymph node T cell zone and the effector cells in the body is shown in Fig. 7.6. The magnitude of the immune response is not sufficient to eradicate completely the infection. Indeed, the number of infected cells decreases but remains positive (Fig. 7.7). As virus infection is not cleared, the cell populations fluctuate around some constant values. Overall, the model reproduces the long-term persistent infection dynamics (e.g., [**?**, **?**, 298]). The primary clonal expansion takes about seven days and is followed by an enhanced long-term T cell response to the persistent infection. The increase in the spread of type I IFN changes the relative distributions pattern of IL-2 and IFN, so that the resulting alteration in the cytokine signalling reduces the clonal expansion and increases the overall level of the virus infection.

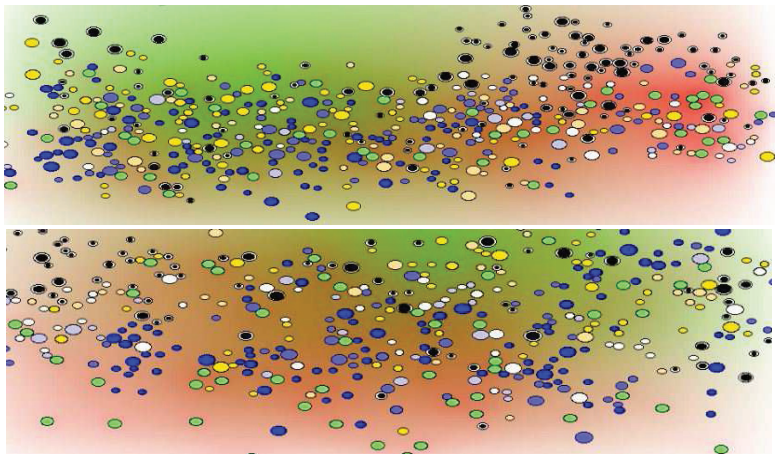

Figure 7.4: Snapshot of numerical simulations of the cells and cytokines distribution in lymph node. Different cells are shown: APC (green), naive $CD4^+$ T cells (black), naive $CD8^+$ T cells (white), three maturity levels of differentiated $CD8^+$ T cells (blue), two maturity levels of $CD4^+$ T cells (yellow). Mature $CD4^+$ T cells produce IL-2 whose concentration in the extracellular matrix is shown by the level of green. APC produce IFN (red). The upper Fig. shows the simulation with equal diffusion coefficients of IL-2 and IFN, in the lower Fig. the diffusion coefficient of IFN is 10 times larger than the diffusion coefficient of IL-2.

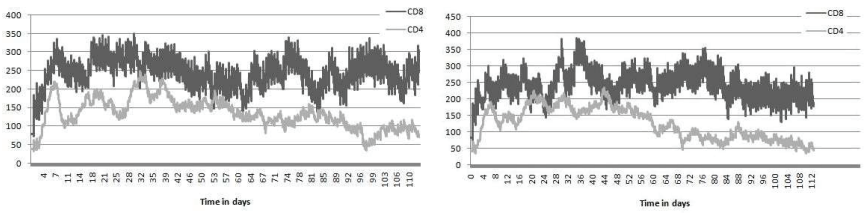

Figure 7.5: The numbers of $CD4^+$ and $CD8^+$ T cells in time in the case of equal diffusion coefficients (left panel) and for the diffusion coefficient of IFN 10 times larger than the diffusion coefficient of IL-2 (right panel).

The cumulative numbers of $CD4^+$ and $CD8^+$ T cells and virus infection load. As single simulation runs of the stochastic model are characterized by a fluctuating and overlapping dynamics, we quantified integrative characteristics of the model behavior. To describe the effect of the diffusion

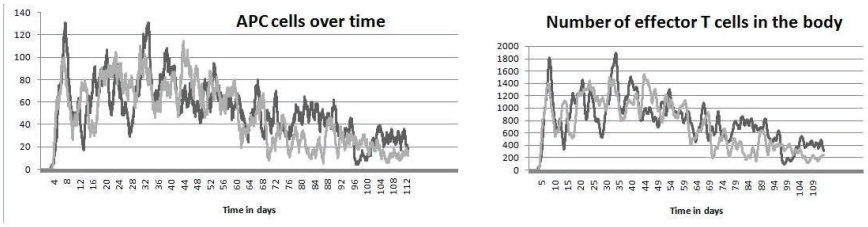

Figure 7.6: The numbers of APC cells (left panel) and effector T cells (right panel) in time in the case of equal diffusion coefficients (black curve) and for the diffusion coefficient of IFN 10 times larger than the diffusion coefficient of IL-2 (grey curve).

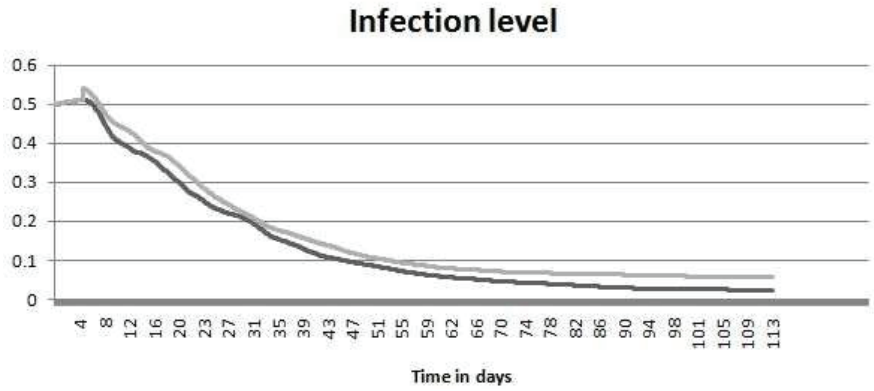

Figure 7.7: The level of virus infection in the body in the case of equal diffusion coefficients (black curve) and for the diffusion coefficient of IFN 10 times larger than the diffusion coefficient of IL-2 (grey curve).

coefficient D_{FN} on the T-cells production, we compared the cumulative numbers of $CD4^+$ and $CD8^+$ T cells as well as the infection load over the overall time of the simulation for the two scenarios. We also show the cumulative numbers of effector T-cells in the body N_{ef}. The results are shown in Table 7.2.

	$D_{FN} = D_{IL-2}$	$D_{FN} = 10D_{IL-2}$
Number of $CD4^+$ T cells	27544	27039.5
Number of $CD8^+$ T cells	15194	14138.7
The infection load	15.98	19.31
Number of N_ef	87848.97	80966.83

Table 7.2: Cumulative numbers of key variables of the model.

The net effect of the increase in the diffusion rate of type I IFN is a reduction in the clonal expansion of the T cells, in particular the effector T cells in the peripheral organs (by $\sim 10\%$) and a rise in the infection level (by $\sim 20\%$). The changes in the clonal T cell expansion are the consequence of the differences in the cytokine concentration fields, which in turn alter the timing and the sequence of the IL-2 and type I IFN signalling.

The types and the relative densities of immune cells present in the simulations correspond to cardinal features clonal APC induced expansion of T cells activated by to virus infections, e.g. [299]. The motility of T cells in lymph nodes which appears to be similar to a correlated random walk [300] is well captured by the modelling the superposition of directed flow and random walk. The spatial distribution of cytokines considered in the model (IL-2 and type I IFN) is poorly understood and this justifies the need of the modelling to explore it. To make the modelling results amenable to experimental data comparison, we show in Fig. 7.8 the spatial distributions of cell and cytokines in a separated manner. One can see

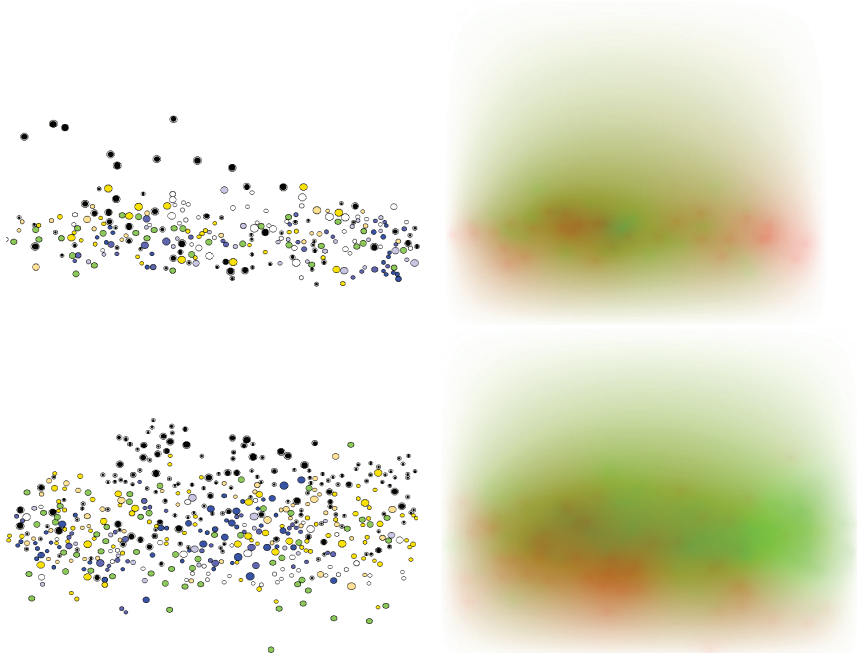

Figure 7.8: Snapshot of numerical simulations of the cells (left panel) and cytokines (right panel) distribution in lymph node. First raw shows the simulation run with equal diffusion coefficients of IL-2 and IFN, and the lower raw represesnt the outcome of the simulation with the diffusion coefficient of IFN is 10 times larger than the diffusion coefficient of IL-2. APC (green), naive $CD4^+$ T cells (black), naive $CD8^+$ T cells (white), three maturity levels of differentiated $CD8^+$ T cells (blue), two maturity levels of $CD4^+$ T cells (yellow).

a clear impact of the differences in the diffusivity of the cytokines on the cytokine fields and the cell distributions.

7.1.2 Discussion

The activation of T cell division and death is regulated by a set of signals coming from the interactions of TCRs with the MHC class I and II presented peptides and IL-2 receptors. However, the effect of type I interferon depends on the temporal sequence of the signals obtained by naïve T cells [287]. It can change from a normal activation of T cells followed by their proliferation and differentiation to an already differentiated state followed by apoptosis. We propose that the altered T cell differentiation and proliferation sequence can result from a spatial separation of the signaling events obtained by T cells, i.e. the TCR versus IFN receptor signaling, due to a generally different location of the APCs and the type I IFN concentration field. The hypothesis is formulated using the results of our study of the spatio-temporal dynamics of the T cell response to infection with the developed hybrid mathematical model integrating intracellular, and systemic levels of the immune response regulation.

Virus persistence in humans is often associated with an exhaustion of T lymphocytes. Many factors can contribute to the development of exhaustion. One of them is associated with a shift from a normal clonal expansion pathway to an altered one characterized by an early terminal differentiation of T cells. The proposed hybrid model allows us to investigate the integrative effects of numerous biophysical and biochemical parameters on the immune regulation that are beyond the scope of the existing experimental techniques.

The need for development of multiscale integrative models in mathematical immunology is well realized [247, 248, 244]. However, implementation of such models embedded into spatial context of immune responses remains a challenge [236, 301]. Our hybrid model has been developed in a modular form to describe a range of specific interactions and regulations of the immune response. This implies that the structure and composition of the model can be adaptively changed to meet the needs of any specific studies. The present study is based upon a simplified description of the virus-target cell interaction. This block of the hybrid model can be easily refined using the existing set of lumped mathematical models. We presented the results of single runs for two different scenarios. Obviously, multiple runs will be used to address the effect of local and global variations in the parameters on the immune response dynamics in future studies.

The presented methodology for developing a hybrid model of immune processes enables integration of data and knowledge across multiple scales. This is essential for understanding the control of the lower level processes by the properties of the higher level processes. We considered here an important example of the regulation of the T cell fate [287] by the spatial structure and material properties of lymphoid organs in which the transport and cell interaction take place [236].

Mathematical modelling of the organism's immune system represents a challenge. Whereas a macroscopic level population dynamics of the immune responses can be followed experimentally and captured with mathematical models under the framework of mono- or two/three compartmental modelling based on ODEs, the embedding of the cell trafficking and interaction processes into the spatial organization of real lymphoid organs represents a fundamental challenge. The effects of spatial heterogeneity of the cytokine fields and cells localization in the lymphoid organs on quantitative and phenotypic features of the T cell responses are poorly understood as these types of parameters are difficult to examine experimentally. Indeed, to describe the cytokine and cellular interactions one need to integrate in a unified manner a range of processes including the lymph flow, constrained diffusion, chemotaxis and haptotaxis in soft tissues. A complementary problem is the assimilation of the data on intracellular regulation of the immune cells' states resulting from a parallel signaling via cell surface receptors to antigens, cytokines, chemokines, hormones, etc. The complexity of the issue is well exemplified in a recent review [281]. Following the presented modelling approach, we hope to be able to examine the sensitivity of the immune responses at the macroscopic level and to parameters of the cell interaction at the microscopic level. This should assist in fine tuning of the offset dynamics of immune responses using a broad spectrum of modern immunomodulatory drugs.

7.1.3 Conclusions

The proposed hybrid mathematical model of the immune response represents a novel analytical tool to examine challenging issues in the spatio-temporal regulation of cell growth and differentiation, in particular the effect of timing and location of activation signals. It allows us to overcome the limitations of reductionist approach to a single factor analysis of the immune regulation and to proceed to the studies of the structure-function relationships in a genuinely systemic manner. As W.E. Paul stated in [302] "...the behavior of immune cells is highly colored by the cellular/molecular environment in which they exist... It is to the quantitative prediction of the outcome of given perturbations in the immune system that we envisage our mathematical/ modeling colleagues will apply themselves." In our view, hybrid modelling approach provides the means for a comprehensive analysis and interpretation of content-rich meta-data obtained by a broad range of scale-specific data acquisition techniques, including imaging, flow cytometry, transcriptome sequencing in an anatomically correct and immunologically meaningful way.

7.2 A multiscale model to describe the immune response during acute HIV infection

7.2.1 Biological and modelling background

Human Immunodeficiency Virus (HIV) type 1 infection represents a complex biological system [227, 229, 228, 230] and a great challenge for cure strategies [231, 232]. Novel approaches for the analysis and prediction of the infection dynamics based on a multiscale integration of virus ontogeny and immune reactions are needed to deal with the systems' complexity [234, 233, 235, 236]. Such approaches have not yet been developed in the HIV modeling field [237, 238, 239].

The term "multiscale models" is used with different meanings in different sciences. In mathematics, it implies the presence of one or several small parameters, homogenization and averaging techniques. In physics, it is understood in the sense of microscopic-macroscopic scales (e.g., molecular dynamics versus continuum mechanics). These questions are exhaustively discussed in particular in [240]. multiscale modeling in biology has been intensively developed during the last decade. It implies that the model includes different biological scales: cells, intracellular regulation, extracellular matrix, the tissue under study and other organs (not necessarily all of them in the same model). It is in this sense that we understand multiscale modeling in this work.

A multiscale framework turned out to be insightful for understanding the mechanisms and identifying potential therapeutic targets for human infection with *Mycobacterium tuberculosis* [241, 242, 243]. Other specific examples of immune system analysis based on multiscale models are the studies of early $CD8^+$ T cell immune responses in Lymph Nodes (LN) [244, 245], the NF-κB signaling pathway [246] and immune processes in lymph nodes [247, 248]. The gained experience led to the formulation of some more general principles for developing and computationally implementing integrative models of immune responses [250, 249, 251]. A recent study integrating the spatial structure of the T cell zone of lymph nodes and the dynamics of T cell responses in HIV infection has quantified the effect of the destruction of the Fibroblastic Reticular Cell (FRC) network on T cell reactivity [252]. The aim of our study is: (1) to formulate a multiscale mathematical model of HIV infection; (2) to implement the model computationally following a hybrid approach; and (3) to calibrate the model by estimating the parameter values enabling one to reproduce the 'standard' dynamics of HIV infection in blood during the acute phase of primary infection.

The major targets of HIV infection are macrophages and $CD4^+$ T cells [230]. Both cell types play a key role in the regulation of immune responses by producing cytokines, such as IL-2 and interferons. The activation state of $CD4^+$ T cells has a strong effect on the replication of the virus [253]. Naive resting $CD4^+$ T cells do not support HIV replication, whereas activated cells are the major source of newly-secreted virus particles. HIV selectively infects and destroys memory $CD4^+$ T cells in lymphoid tissues. After mucosal infection, some period of local replication and amplification takes place, finally resulting in the migration of the infected cells to the draining lymph nodes and, from there, to the rest of the body

[253]. Dendritic cells (DC), which are highly efficient Antigen-Presenting Cells (APC), play a key role in disseminating HIV from mucosal tissues to the draining lymph nodes [254]. Intravenous infection leads to fast direct dissemination of the virus to all lymphoid organs. In these organs, the productive infection is initially observed in the T cell zone. The development of AIDS occurs when the level of mucosal $CD4^+$ T cells drops to 5%–10% of their normal homeostatic level. Although about half of the gut-associated lymphoid tissue $CD4^+$ T cells is depleted after acute infection [255], the prolonged maintenance of $CD4^+$ T cells is explained by an increased turnover of the cells resulting from a chronic immune activation [253].

HIV viremia is controlled primarily by $CD8^+$ T Lymphocytes (CTL) [255]. The infection is characterized by the production of up to 10^{10} new virus particles per day [254]. The viral load drops from $\sim$1–5 $\times$ 10^6 viral copies/mL to a steady state of $\sim 3 \times 10^4$ viral copies/mL [255]. It is remarkable that despite massive HIV-specific CTL responses (up to 19%), a full control of HIV viremia is not achieved. The magnitude and rapidity of the $CD8^+$ T cell response correlate with the viral set point [256]. The set point is a strong predictor of the rate of the progression to AIDS [254]. The failure of HIV-specific CTLs to control HIV infection is attributed to functional defects of these cells associated with apoptosis [257, 256]. The development of CTL responses in lymphoid organs is much less characterized than those in the peripheral blood [255]. Therefore, relating the immune processes in LNs to those in peripheral blood is important for a deeper understanding of the control of HIV infection.

Overall, the failure of the immune system to generate a protective antiviral response to HIV infections is linked to exhaustion of virus-specific immunity, the destruction of lymphoid organs, chronic immune activation and viral escape from the cellular and humoral immunity and is, therefore, multifactorial and multistage [230]. To analyze the regulatory mechanisms causing the chronicity of HIV infections, a multidisciplinary approach is required based on mathematical modeling and animal model systems. In this study, we propose a computational approach for a multiscale integrative modeling of HIV infection. The approach is based on our previous experience in modeling erythropoiesis in blood diseases [85, 259, 260, 261].

7.2.2 Methods

Multiscale Framework

The traditional approaches to model HIV dynamics focus only on one scale [235, 238, 237, 239]. The multiscale and multi-physics approach [240] provides unprecedented opportunities for understanding HIV via linking microscopic (intracellular) regulations in the immune system to the macroscopic environment of the lymphoid organs, resulting in a system level dynamics as observed and monitored in blood. The potential of such a multiscale approach is illustrated by a recent study on HIV spread in an HIV risk population [262]. For a general guideline on the principles of multiscale modeling, we refer to our recent review [263] and a textbook [240]. The model of acute HIV infection developed in this study belongs to the category of coupled-intricate models. It considers two macroscopic compartments, i.e., the blood and lymph nodes, and the cell population dynamics in the T cell zone of the lymph nodes at the mesoscopic level. The individual cell dynamics is regulated by cytokine fields created by APCs and T cells via intracellular signaling cascades linking cellular receptors with gene transcription factors. The conceptual scheme of our modeling approach is summarized in Fig. 7.9.

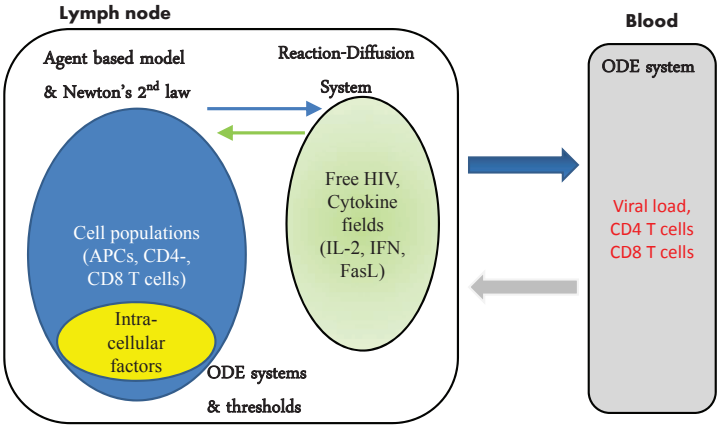

Figure 7.9: General structure of the multiscale model of HIV infection.

Cell Division and Differentiation. Cells enter the computational domain Ω of the LN at some rate if there is free space. Naive T cells move in the computational domain randomly. If they contact APC, they divide (Fig. 7.10). When the cell reaches half of its life cycle, it will increase its size. When it divides, two daughter cells appear; the direction of the axis connecting their centers is chosen randomly from 0–2π. The duration of the cell cycle is 18 h with a random perturbation of −3–3 h. We consider two levels of maturity for $CD4^+$ T cells and three levels for $CD8^+$ T cells. If a differentiated cell has enough IL-2, then it divides and gives two mature daughter cells. Finally, differentiated cells leave the lymph node. In the simulations, this means that they are removed from the computational domain. The overall cell fate regulation is determined by a hierarchy of the gene activation thresholds for signaling coming via TCR, IL-2, IFNa and Fas receptors, as shown in Fig. 7.11. Different activation thresholds uncouple the distinct modes of cellular responses depending on the cytokine levels and intracellular signaling, yielding context-specific functional responses [264].

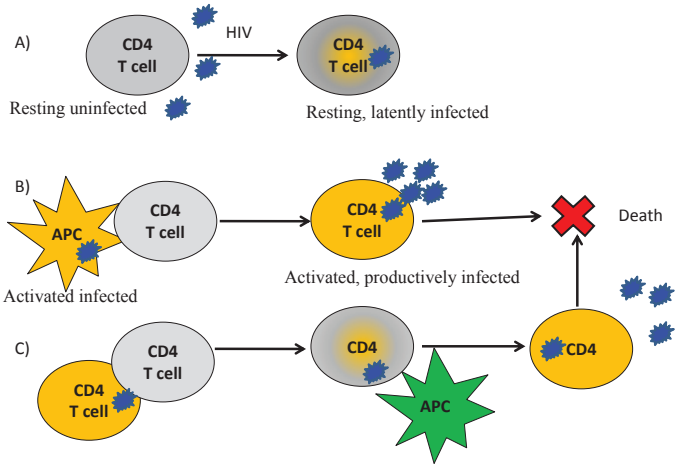

Figure 7.10: Scenarios of virus modes of infection of CD4 T cells. (**A**) Free virus infection of resting CD4 T cells resulting in a latent infection; (**B**) interaction between infected APC and uninfected CD4 T lymphocytes resulting in a productive infection; (**C**) cell-to-cell spread of HIV from infected to uninfected CD4 T lymphocytes resulting in a productive infection upon activation by HIV antigen-presenting APC.

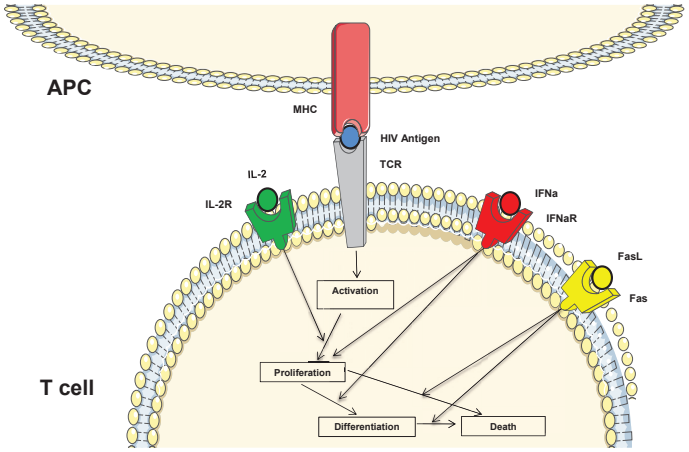

Figure 7.11: Scheme of the cell fate regulation via TCR, IL-2, IFNa and Fas receptor-mediated signaling in naive T cells to adaptively program the balance of growth-differentiation and death.

Biological Assumptions

The model is based on the following assumptions:

- HIV enters the lymph node with infected antigen-presenting cells. These cells secrete HIV and transmit it to uninfected (both HIV-specific and non-specific) $CD4^+$ T cells by cell-cell interaction;
- Each APC or $CD4^+$ T cell is determined by an intracellular viral RNA concentration (H_i). The cell is considered to be infected if H_i reaches some threshold level h_0. HIV upregulates the concentration of caspase, which can result in cell apoptosis;
- The $CD8^+$ T cells produce FasL, as well as other apoptosis-inducing factors. They also activate the caspase cascade through direct cell-cell contact with infected cells resulting in target cell apoptosis. These two mechanisms only affect infected $CD4^+$ T cells and not uninfected cells;
- HIV impairs the immune response by reducing the number of $CD4^+$ T cells in the lymph node. These cells are killed by cytotoxic $CD8^+$ T cells or by the virus itself. As a result, fewer mature helper $CD4^+$ T cells are left, and less IL-2 and type I IFN are produced. This leads to a decrease in the survival and differentiation of $CD8^+$ T cells, which ultimately results in the relapse of the infection.

We will consider three groups of variables characterizing infection development:
Blood:

1. $V_{Blood}(t)$, the viral load in blood;
2. $N_{CD4,inf}(t)$, the abundance of infected $CD4^+$ T cells in blood;
3. $N_{CD4,un}(t)$, the abundance of uninfected $CD4^+$ T cells in blood;
4. $N_{CD8,ef}(t)$, the abundance of HIV-specific effector $CD8^+$ T cells in blood.

Lymph node:

5. $n_{APC}(\mathbf{x},t)$, the density of APCs in the T cell zone of LN, uninfected or infected;
6. $n_{CD4,un}(\mathbf{x},t)$, the density of uninfected $CD4^+$ T cells in the T cell zone of LN; and $n_{CD4,inf}(\mathbf{x},t)$, the density of infected cells;
7. $n_{CD8}(\mathbf{x},t)$, the density of $CD8^+$ T cells in the T cell zone of LN;

8. $H_e(\mathbf{x},t)$, the concentration of free HIV in the T cell zone;

9. $I_e(\mathbf{x},t)$, the concentration of IL-2 in the T cell zone;

10. $C_e(\mathbf{x},t)$, the concentration of type I IFN in the T cell zone;

11. $F_e(\mathbf{x},t)$, the concentration FasL in the T cell zone.

Different cells in the lymph node (APC, CD4, CD8, uninfected, infected) are considered as individual objects. The cell densities represent the number of cells in the unit volume. They are encountered in the model at two levels: locally as sources of IL-2, I IFN and FasL; and globally through their total quantity in the lymph node, which determines cell flux from the lymph node to the blood.

Intracellular factors:

12. $H_i(t)$, the intracellular concentration of viral genomes in the i-th cell;

13. $I_i(t)$, the intracellular concentration of IL-2-induced signaling molecules in the i-th cell;

14. $C_i(t)$, the intracellular concentration of type I IFN-induced signaling molecules in the i-th cell;

15. $w_i(t)$, the intracellular concentration of FasL-induced signaling molecules in the i-th cell.

7.2.3 The Model of Acute HIV Infection

Blood Compartment

In this section, we formulate equations relating the T cell and virus population dynamics in blood (i.e., in an observable compartment) and lymph nodes for which a detailed description of the HIV infection process is given. The HIV-specific $CD8^+$ T cells are generated in the course of the antiviral immune response occurring in LN. The concentration of the cells in blood results from their migration from LN via efferent lymphatic vessels to blood and further to peripheral tissues. A simple description of the above processes is provided by the equation:

$$\frac{dN_{CD8,ef}}{dt} = k_{LN,Blood}T_{CD8,LN} - k_{CD8}N_{CD8,ef}, \tag{7.2.8}$$

where $N_{CD8,ef}$ stands for the concentration of HIV-specific $CD8^+$ T cells in blood and $T_{CD8,LN}$ is the density of HIV-specific $CD8^+$ T cells in LNs,

$$T_{CD8,LN}(t) = \int_\Omega n_{CD8}(\mathbf{x},t)d\mathbf{x}.$$

The first term in the right-hand side of this equation describes the production of effector cells in the lymph nodes and the second term their death in the body.

For the equations of the systemic dynamics of APCs, T cells and infected cell populations, the parameters were specified according to available experimental and clinical data as follows:

1. k_1, rate of T cell production and release into the body: $1.8\ \mathrm{h}^{-1}$;

2. k_2, death rate of T cells in the body: $0.12\ \mathrm{h}^{-1}$;

3. k_3, elimination rate of the infected cells by T cells $1.8\times10^{-6}\ \mathrm{h}^{-1}$;

4. a, a growth rate parameter of infected cells: $0.00024\ \mathrm{h}^{-1}$;

5. h, a parameter in the growth function of infected cells: $0.006\ \mathrm{h}^{-1}$.

For the migration and decay rate constants, the following estimates can be used:

7. $k_{LN,Blood}$, migration rate constant of $CD8^+$ T cells from LN to blood. The fraction of HIV-specific CTLs in acute HIV infection can reach 10% of the total number of $CD8^+$ T cells, i.e., about 100 cell/μL [237]. Therefore, the value of $k_{LN,Blood}$ should be within the range 0.004–0.04 h^{-1};

8. k_{CD8}, the disappearance rate of HIV-specific effector $CD8^+$ T cells from blood [237]: $k_{CD8} = 0.0013\ h^{-1}$.

As the infection process takes place mainly in organized lymphoid tissues, a similar equation applies to the number of HIV-infected $CD4^+$ T cells in blood ($N_{CD4,inf}$). We describe the dynamics of the infected cells in blood by the equation:

$$\begin{aligned}\frac{dN_{CD4,inf}}{dt} = f(N^{LN}_{CD4,inf};a,h) - k_{CD8,CD4}N_{CD8,ef}N_{CD4,inf} \\ +k_{CD4,inf-un}N_{CD4,inf}N_{CD4,un} - k_{CD4,inf}N_{CD4,inf}.\end{aligned} \tag{7.2.9}$$

The first term in the right-hand side of this equation describes the growth of the number of infected cells through the accumulation from the lymph nodes; the second term their elimination by the effector cells; the next term describes contamination of uninfected cells by infected cells; and the last terms the death of the HIV-infected cell due to the cytopathic effect of the virus. The function f is considered in the form:

$$f(N_{inf};a,h) = \frac{aN^{LN}_{inf}}{1+hN^{LN}_{inf}},$$

where a and h are some positive constants and N^{LN}_{inf} is the total number of $CD4^+$ T cells in the lymph node,

$$N^{LN}_{inf}(t) = \int_\Omega n_{CD4,inf}(\mathbf{x},t)d\mathbf{x}.$$

For the migration-accumulation, effector cell- and virus-mediated killing rate constants, the following estimates can be used:

9. a, the accumulation rate constant of HIV-infected $CD4^+$ T cells in blood due to the migration of cells from LNs and other peripheral tissues: the reference value 0.1 h^{-1} suggested in [227] was tuned to 0.35 h^{-1};

10. h, the maximal T cell number in blood that can be infected 1/100 $\text{cell}^{-1}\cdot\ \mu$L;

11. $k_{CD8,CD4}$, the elimination rate of HIV-infected $CD4^+$ T cells by CTL-mediated killing. We used the value estimated in [235] $k_{CD8,CD4} \sim 0.0004\ \mu$L/(cell·h). For a strong $CD8^+$ T cell response, this value reaching 10% of the total CTL population in blood, this value will ensure the elimination rate of the infected cells from blood of about 1 per day;

12. $k_{CD4,inf}$, the death rate of HIV-infected $CD4^+$ T cells in blood due to virus cytopathicity: 0.017–0.17 h^{-1} [238, 237 with the geometric mean estimate 0.05 h^{-1}. We consider a death rate of 0.061 h^{-1}.

We describe the dynamics of the uninfected CD4+ T cells in blood by the commonly-used equation:

$$\frac{dN_{CD4,un}}{dt} = f(N^{LN}_{un};\lambda,h_1) - k_{CD4,inf-un}N_{CD4,inf}N_{CD4,un} - k_{CD4,un}N_{CD4,un}, \tag{7.2.10}$$

The first term in the right-hand side of this equation describes the influx of healthy CD4+ T cells from the lymph node,

$$N^{LN}_{un}(t) = \int_\Omega n_{CD4,un}(\mathbf{x},t)d\mathbf{x}.$$

The second term in the right-hand side of Equation (7.2.10) describes the contamination of uninfected cells by infected cells, and the last term describes the death of uninfected T cells. The following estimates can be used for the parameters adjusted from the values reported in [238, 237]:

13. λ, the influx rate of $CD4^+$ from the lymph nodes: 0.45 $(\mu\text{L}\cdot\text{h})^{-1}$;

14. h_1, the maximal T cell number in blood that can be uninfected: 1/200 cell$^{-1}\cdot\mu$L;

15. $k_{CD4,inf-un}$, the infection rate of the CD4$^+$ T cells in blood: 0.00042 (μL·h)$^{-1}$;

16. $k_{CD4,un}$, the death rate of uninfected CD4$^+$ T cells in blood: 3.3×10^4 h^{-1}.

Finally, an equation for the HIV concentration in blood has to be specified. We utilize a commonly-used description:

$$\frac{dV_{Blood}}{dt} = k_{V,LN-Blood}\int_\Omega H_e(\mathbf{x},t)d\mathbf{x} - d_{V_{Blood}}V. \tag{7.2.11}$$

For the HIV transfer and elimination rate constants, the following estimates are used:

17. k the influx of HIV from LNs to blood was estimated in [265]. Taking into account the volume differences of our computational domain (0.001 μL) and the unit of blood volume μL, we used the following value $k_{V,LN-Blood}\sim 100$ virion/(μL·h);

18. $d_{V_{Blood}}$, the elimination rate of free HIV from blood [238, 237]: 0.5–21 h^{-1}; with the geometric mean taken as an initial guess 3.2 h^{-1} further tuned to 6 h^{-1}.

Population Dynamics of Infection in LN

Free HIV. We describe the concentration of HIV in the extracellular matrix as follows:

$$\frac{\partial H_e}{\partial t} = D_{HIV}\Delta H_e + W_{H_i} - d_{HIV}H_e. \tag{7.2.12}$$

For the diffusion coefficient of the virus, we used the available estimates [266, 267, 268], which provide the following broad range for $D_{HIV} = 3\times10^{-5} - 4$ mm^2/h, with the geometric mean taken to be the baseline value 0.01 mm^2/h.

HIV is secreted by two types of infected cells: APCs and CD4$^+$ T cells. The production depends on the intracellular concentration of HIV DNA in a threshold manner; once the DNA level is above a certain value in the activated cell, the secretion starts to take place. Virus production is presented by the source term W_{H_i},

$$W_{H_i} = \sum_{k=1,K_l}\rho_{HIV}\delta(\mathbf{x}-\mathbf{x}_k)$$

with ρ_{HIV} specifying the per capita secretion rate by activated cells located at some positions $\mathbf{x}_k$. It is a sum of Dirac delta functions, and due to the singularity of the terms, the equation is understood in the weak sense. The maximum secretion rate of HIV by an activated CD4$^+$ T cell is taken to be $\rho_{HIV} = 5\times10^2$ virion/(cell·h) [237]. The clearance rate of free virus is taken to be about $d_{HIV} = 0.5$ 1/h [237].

HIV Infection in Target Cells. The virus is introduced to the lymph node by infected APCs and CD4$^+$ T cells. We suppose that the number of infected APCs CD4$^+$ T cells entering the lymph node and the concentration of proviral HIV DNA inside of them depend on the level of HIV infection. The proportion of the infected APCs and HIV-specific CD4$^+$ entering the lymph node corresponds to the actual level of HIV of infection divided by 20×10^6 virion/μL. The concentration of intracellular HIV DNA is equal to the infection level divided by 5×10^3 virion/μL. HIV infects the CD4$^+$ T cells in the lymph node, resulting potentially in the apoptosis of activated cells. Otherwise, the virus stays latent inside of the cell. Furthermore, infected APCs do not induce the differentiation of CD4$^+$ T cells. To describe the number of the integrated proviral HIV DNA D by (H_i) in each CD4 T cell or APC, we use the equation:

$$\frac{dH_i}{dt} = \underbrace{\beta_1 H_e}_{\text{free HIV infection}} + \overbrace{\frac{\beta_2(t)}{1+\omega_{IFN}C_i}}^{\text{HIV replication inside of the cell}} + \underbrace{\beta_3\left(\sum_{j=1}^{n}H_j - nH_i\right)}_{\text{HIV transmission by cell-cell contact}}. \tag{7.2.13}$$

Here, H_e denotes the concentration of HIV in the extracellular matrix; n is the number of CD4 T cells and APCs in direct contact with infected cell. When in direct contact with uninfected CD4 cells, the virus is transmitted, but remains latent. Hence, the value of the virus inside the previously uninfected cell is set to $H_j = h_0$. Furthermore, $\beta_2(t)$ is equal to zero when the virus is latent. Otherwise, it is equal to a positive constant. Virus multiplication is activated upon a direct contact with an APC (infected or not). We take h_0 equal to 100 virion. The concentration of the integrated DNA in the cell determines if the cell itself is infected or not. To account for this, we consider the cell to be infected if H_i reaches the value h_0. It starts emitting the virus to the extracellular matrix and become susceptible to elimination by CD8 T cells.

For the intracellular HIV replication parameters, we used the following values:

14. β_1, the infection rate constant for susceptible cells by free virus. It can be evaluated using the estimates in [269]: $\beta_1 = 5.6^{-5}$ μL/(virion·h);

15. β_2, specifies the maximal production rate of HIV DNA in the activated cell. We used the following estimate $\beta_2 = 5 \times 10^2$ virion/(cell·h) [237];

16. ω_{IFN}, specifies the protective effect of type I interferon on HIV DNA growth in the activated cell. The following estimate [270] is used to reproduce a 50% reduction in the viral DNA synthesis rate due to the availability of type I IFN: $\omega_{IFN} = 467$ μL/pg;

17. β_3, the probability that a susceptible cell is infected when it contacts infected cells was estimated in [269] to be $\beta_3 = 0.19$.

Cytokine Fields in LN

IL-2. Immature T cells differentiate via direct cell-cell contact with uninfected APCs. Proliferation and differentiation of T cells in the lymph node depend on the concentration of IL-2. It is produced by mature CD4$^+$ T cells. Its spatial distribution is described by the reaction-diffusion equation:

$$\frac{\partial I_e}{\partial t} = D_{IL2}\Delta I_e + W_{IL2} - d_{IL2} I_e. \tag{7.2.14}$$

Here, I_{ex} is the extracellular concentration of IL-2; D is the diffusion coefficient; W_{IL} is the rate of its production by CD4$^+$ T cells; and the last term in the right-hand side of this equation describes its consumption and degradation. The production rate W_{IL} is determined by mature CD4$^+$ T cells. We consider each such cell as a source term with a constant production rate ρ_{IL} at the area of the cell. Let us note that we do not take into account explicitly consumption of IL-2 by immature cells in order not to introduce an additional parameter. Implicitly, this consumption is taken into account in the degradation term. The following estimates of the parameters were used:

3. ρ_{IL2}, the secretion rate of IL-2 by a single CD4$^+$ T cell: 7×10^5 molec/h;

4. d_{IL2}, the degradation rate of extracellular IL-2: 0.5 1/h.

Type I IFN. For type I IFN, the equation and the terms in it have a similar interpretation:

$$\frac{\partial C_e}{\partial t} = D_{IFN}\Delta C_e + W_{IFN} - d_{IFN} C_e. \tag{7.2.15}$$

For the type I IFN-controlled processes, the following parameter values were used, taken from [270]:

5. ρ_{IFN}, the secretion rate of type I IFN by single activated APC (plasmacytoid dendritic cell): 1.6×10^4 molec/h;

6. d_{IFN}, the degradation rate of extracellular type I IFN: 0.012 1/h.

D_{IL}, D_{IFN}, the diffusion coefficients of IL-2 and type I IFN. As the molecular weights of IL-2 and type I IFN are close to that of myoglobin, we used the following estimate of the diffusion coefficient: 0.16 mm^3/h. Initial and boundary conditions for both concentrations IL-2 and IFN are taken to be zero. As before, the production rate W_{IFN} equals ρ_{IFN} at the area filled by APC cells and zero otherwise.

FasL. We also describe the concentration of FasL and other cytokines secreted by $CD8^+$ T cells:

$$\frac{\partial F_e}{\partial t} = D_{F_e}\Delta F_e + W_F - d_{FasL}F_e. \tag{7.2.16}$$

The molecular weight of FasL is estimated to be around 40 kD; therefore, we assumed the diffusion coefficient to be proportionally smaller than that of myoglobin, i.e., $D_{F_e} = 0.07$ mm^2/h. The production rate of FasL by activated T cells can be estimated from the data in [271] to be around $\rho_{FasL} = 2\times 10^3$–$4.5\times 10^4$ (molecules/(cell·h) [271] with the geometric mean value of 9.5 molecules/(cell·h). The degradation rate constant of the soluble FasL is assumed to range from 0.3 h^{-1} (characteristic of the decay rate of Fas receptor [244]) through 0.5 h^{-1} (estimated degradation rate of extracellular IL-2 [272]) to 14 h^{-1} [271], and we used the geometric mean value $d_{FasL} = 2$ h^{-1}.

Intracellular Regulation of Cell Fate

paragraphIL-2 Signaling. The survival and differentiation of both CD4 and CD8 T cells depend on the intracellular concentration of IL-2 (I_i) and interferon (C_i). We describe these two concentrations by the following equations:

$$\frac{dI_i}{dt} = \frac{\alpha_1}{n_T}I_e(\mathbf{x_i},t) - d_1 I_i. \tag{7.2.17}$$

Here, I_i is the intracellular concentration of signaling molecules accumulated as a consequence of IL-2 signals transmitted through transmembrane receptor IL2R downstream of the signaling pathway to control the gene expression in the i-th cell. The concentrations inside two different cells are in general different from each other. The first term in the right-hand side of this equation shows the cumulative effect of IL-2 signaling. The extracellular concentration I_e is taken at the coordinate $\mathbf{x_i}$ of the center of the cell. The second term describes the degradation of IL-2-induced signaling molecules inside the cell. Furthermore, n_T is the number of molecules internalized by T cell receptors. For the IL-2 controlled processes, the following parameter values were used taken from [272]:

1. n_T, the number of IL-2 molecules internalized by T cells via IL-2 receptors: 2000–5000 per T cell;
2. I_i^*, the saturation concentration of IL-2 for T cell division in vitro: 6×10^{10} molec/mL for 5×10^4 cells/mL.

Type 1 IFN Signaling. The IFN-dependent regulatory signal dynamics in individual cells can be described by the following equation:

$$\frac{dC_i}{dt} = \frac{\alpha_2}{n_T}C_e(\mathbf{x_i},t) - d_2 C_i. \tag{7.2.18}$$

Here, C_i is the intracellular concentration of signaling molecules accumulated as a consequence of IFN signals transmitted through transmembrane receptor IFNR downstream of the signaling pathway to control the gene expression in the i-th cell. The concentrations inside two different cells are in general different from each other. The first term in the right-hand side of this equation shows the cumulative effect of IFN signaling. The extracellular concentration C_e is taken at the coordinate $\mathbf{x_i}$ of the center of the cell. The second term describes the degradation of IFN-induced signaling molecules inside the cell.

The quantitative specification of the effect of signaling on gene activation requires a separate study. To illustrate the model performance, it was enough to assume some reference values as follows: $\alpha_1 \sim \alpha_2 \sim 1$ 1/(molec·h) and $d_1 \sim d_2 \sim 0.1$ 1/(h) The proliferation and differentiation thresholds have been arbitrarily set to be $I_i^* = 100$ units (U) and $C_i^* = 2000$ U.

To model the fate regulation of growth versus differentiation of the activated cells in relation to the timing of the IL-2 and type I IFN signaling, we implement the following decision mechanism.

C1 If the concentration of activation signals induced by type I IFN, C_i, is greater than some critical level C_i^* at the beginning of the cell cycle and that of I_i is smaller than the critical level I_i^* at the end of the cell cycle, then the cell will differentiate, resulting in a mature cell.

C2 If the concentration of activation signals induced by IL-2, I_i, is greater than some critical level I_i^* at the end of the cell cycle, then the cell will divide, producing two more mature cells.

C3 If $C_i < C_i^*$ at the beginning of cell cycle and $I_i < I_i^*$ at the end of cell cycle, then the cell will die by apoptosis and will be removed from the computational domain.

FasL Signaling. HIV also upregulates the level of caspase inside the cell. We describe its concentration as follows:

$$\frac{dw_i}{dt} = \underbrace{\gamma_1 H_i}_{\text{upregulation by HIV}} + \overbrace{\gamma_2 F_e}^{\text{upregulation by FasL}} + \underbrace{\gamma_3 n}_{\text{direct activation by contact with CD8s}} - \overbrace{\gamma_4 w_i}^{\text{caspase degradation}} . \quad (7.2.19)$$

Here, F_e denotes the effective concentration of extracellular FasL and other cytokines (e.g., TRAIL, PD1L) secreted by CD8 T cells. n denotes the number of CD8 T cells in direct contact with the cell. The cell dies if $w_i > w^*$.

For the apoptosis-related regulation processes, the following estimates were used:

18. γ_1, the rate of pro-apoptotic signals accumulation because of the viral replication. As the death rate of the infected CD4 T cells is 1.3 h^{-1}, then we used it to quantify the cytopathic effect of the intracellular HIV DNA on the cell. It can be further scaled depending on the choice of the threshold w^*. The latter was estimated in [238], and we set it 2.0 M;

19. γ_2, specifies the FasL-Fas-induced caspase accumulation rate. It was estimated to be $\gamma_4 = 0.24\ h^{-1}$ in [238];

20. γ_3, the killing rate of infected cells by effector CTL. It has been indicated in [271] that once in contact with a target cells, the CTL can program them to undergo apoptosis within 5 min. This value results in the following estimate for the impact of CTL on death likelihood $\gamma_3 = 8.3\ h^{-1}$;

21. γ_4, the caspase degradation rate is taken from [244] $\gamma_4 = 0.23\ h^{-1}$.

Population Dynamics of Immune Response in LN

The influx of APC cells into the lymph nodes is proportional to the number of infected cells N_{inf}. It corresponds to $[N_{inf}/50]$ each 25 h where $[x]$ is the floor function of x. This influx is limited by the place available in the lymph node. If there is a free place sufficient to put a cell, the new cells are added. Let us also note that the lymph nodes can increase due to infection in order to produce more effector cells.

For a hybrid multiscale agent-based model with many parameters, the standards for specifying the model to make it reproducible remain to be developed in immunology. We note that in other fields, such as ecological modeling, the standards for presenting agent-based models in the scientific literature have already been formulated [273, 274].

7.2.4 Numerical Simulation Results

We consider a 2D computational domain in the T cell zone of lymph node of about 100 μm $\times$ 100 μm. The corresponding number of T cells in the computational domain is $\sim 3 \times 10^3$ with the proportions of $CD4^+$ and $CD8^+$ T cells being 2:1 and the number of APCs ranging from 30–300 cells. The maximal number of HIV-specific T cells in the computational domain is assumed to be $\sim 3 \times 10^2$. This corresponds to $\sim$10% of the lymph node space that can be occupied by T cells.

The average CPU time of the acute phase of HIV simulation was around 3 h on a computer with four cores and 6 GB of RAM. The code was written under C++ in the Object Oriented Programming (OOP) style. The characteristic units of the model are the minute for time and the domain length for space. Further details of the numerical methods are described in the Appendix A.

Reaction-diffusion equations were solved using the Alternating Direction Implicit (API) algorithm. We set the initial values for the four fields described by reaction-diffusion equations to zero. Dirichlet conditions were prescribed to the four boundaries of the computational domain. Naive $CD4^+$ and $CD8^+$ T cells are periodically introduced to the middle of the domain when there is available space.

Dynamics of APCs, $CD4^+$ and $CD8^+$ T Cells in LN

The initial spread of infection to lymphoid organs is caused by the migration of a few infected APCs from mucosal compartments. The dynamics of infection in LN described by the model is shown in Fig. 7.12. It characterizes the population dynamics of the total number of HIV-infected APCs and $CD4^+$ T cells over the first 30 days after a few infected APCs appear in LN.

The activation of APCs by HIV induces HIV-specific $CD8^+$ T cell response as reproduced in Fig. 7.13. It is characterized by a sequence of ongoing bursts in the expansion and contraction of CTLs. The strength of the cytotoxic T cell response is enough to limit the spread of infection and to reduced the number of infected APCs and $CD4^+$ T cells from Days 15–20 by four-fold.

The overall comparative dynamics of HIV-specific T cell responses ($CD4^+$ and $CD8^+$) is detailed in Fig. 7.14. The responses are dynamically regulated by the cytokine and HIV distribution in the computational domain.

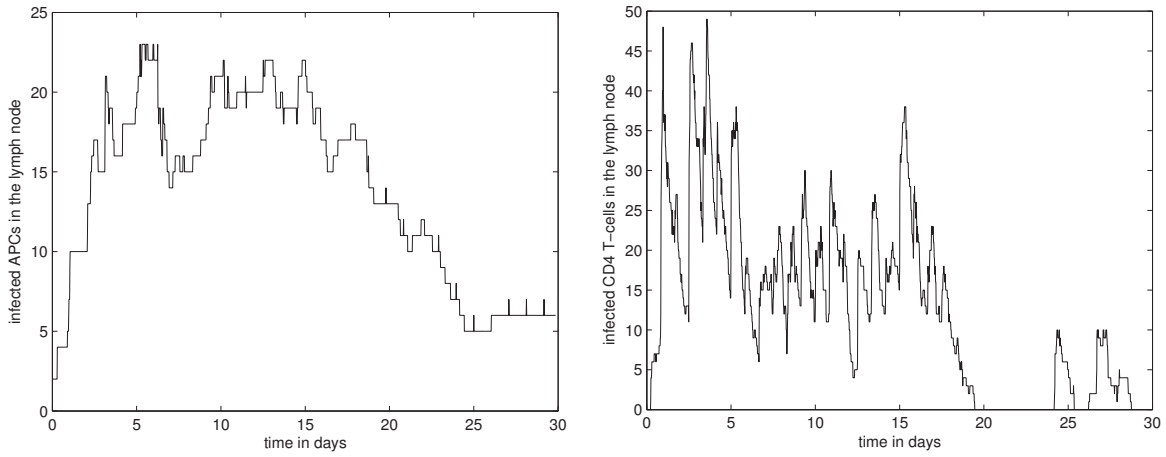

Figure 7.12: (**left**) The dynamics of the population of HIV-infected APCs in the lymph node; (**right**) The dynamics of the population of HIV-infected $CD4^+$ T cells in the lymph node.

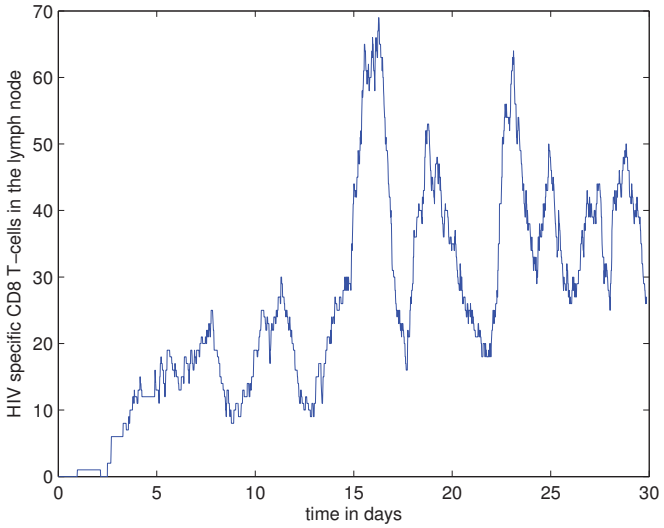

Figure 7.13: The dynamics of HIV-specific effector $CD8^+$ T cell response in the lymph node.

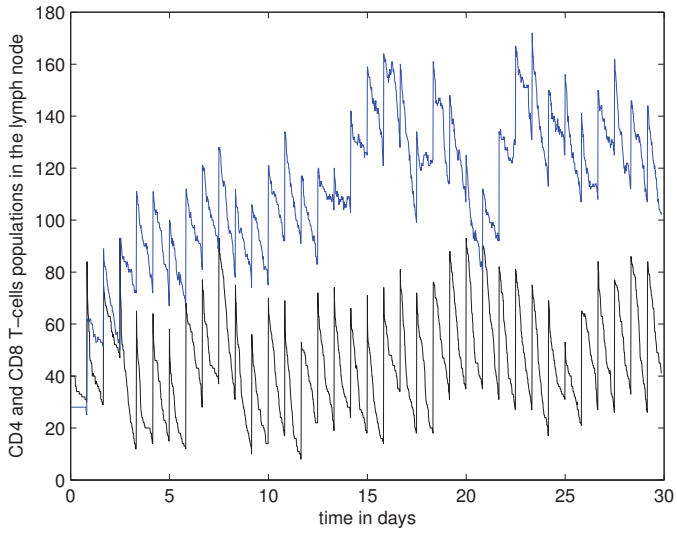

Figure 7.14: The dynamics of populations of naive and mature HIV-specific $CD4^+$ (black curve) and $CD8^+$ (blue curve) T cells in the lymph node.

HIV and Cytokine Fields in LN

The spatial distribution of the virus, IL-2, type I IFN and FasL at Days 3 and 12 post the start of the LN infection is shown in Fig.s 7.15–7.18. In addition to cytokine fields, different cells are shown: uninfected APCs (green), infected APCs (red), naive uninfected $CD4^+$ T cells (black), infected $CD4^+$ T cells (orange), naive $CD8^+$ T cells (white), three maturity levels of differentiated $CD8^+$ T cells (blue) and two maturity levels of uninfected $CD4^+$ T cells (yellow).

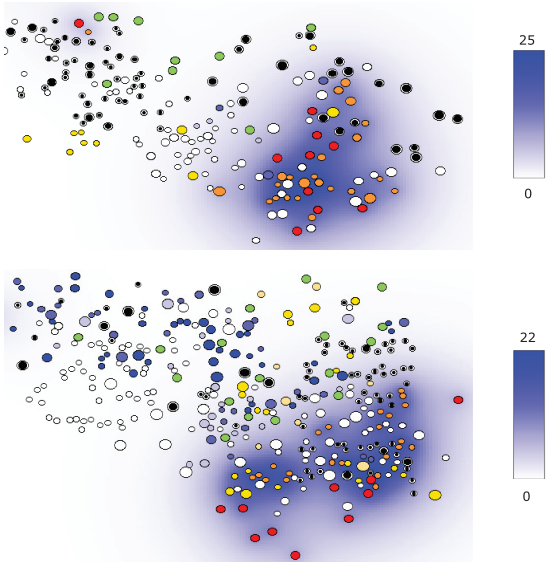

Figure 7.15: Snapshots of the simulation in which the concentration of HIV (in virions/μL) is shown in blue color gradient. Different cell types are represented as follows: uninfected APCs (green), infected APCs (red), naive uninfected $CD4^+$ T cells (black), infected $CD4^+$ T cells (orange), naive $CD8^+$ T cells (white), three maturity levels of differentiated $CD8^+$ T cells (blue) and two maturity levels of uninfected $CD4^+$ T cells (yellow). (**top**) Three days after the virus transmission; (**bottom**) 12 days after virus transmission.

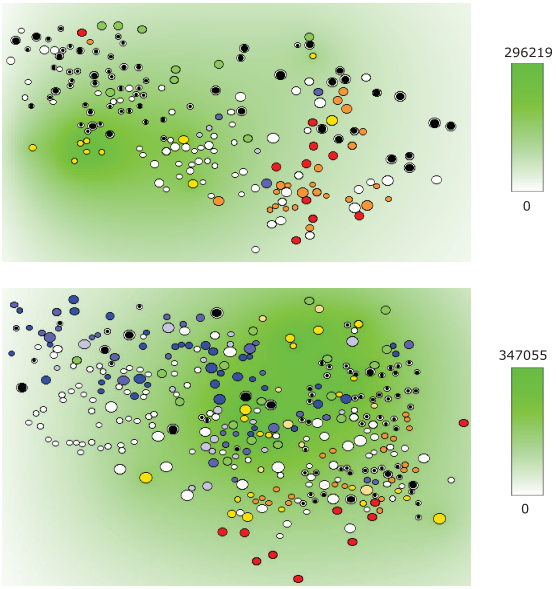

Figure 7.16: Snapshots of the simulation in which the concentration of IL-2 (in molecules/μL) is shown in green gradient. For cell notations, the same color code as in Fig. 7.15 is used. (**top**) Three days after the virus transmission; (**bottom**) 12 days after virus transmission.

Infected APCs and CD4$^+$ T cells secrete HIV as shown in Fig. 7.15 in blue. Mature CD4$^+$ T cells produce IL-2, whose concentration in the extracellular matrix is shown by the level of green; see Fig. 7.16. Activated APCs produce type I IFN shown in red in Fig. 7.17. Finally, the distribution of the apoptosis-inducing ligands is depicted in Fig. 7.18. The simulations clearly indicate that the cytokines and HIV distributions are non-homogeneous and not identical. The relative shifts and differences underlie the existence of compartments differing in the preferential fate of immune cells (division vs. differentiation vs. death) and the niche for infection continuation (domain with a low interferon level).

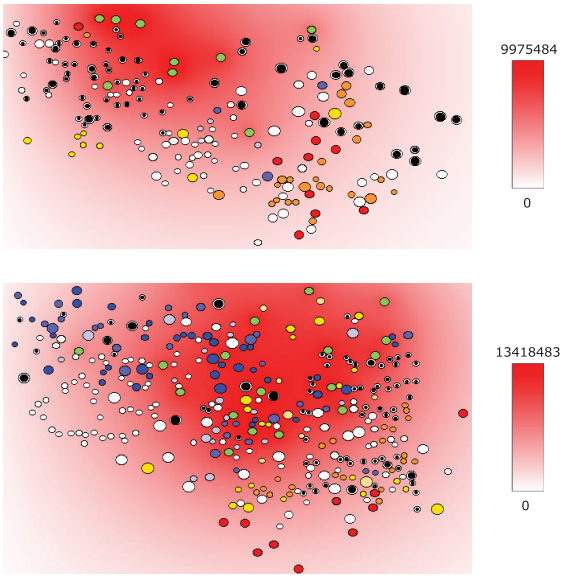

Figure 7.17: Snapshots of the simulation in which the concentration of type I interferon (in molecules/μL) is shown in red color gradient. For cell notations, the same color code as in Fig. 7.15 is used. (**top**) Three days after the virus transmission; (**bottom**) 12 days after virus transmission.

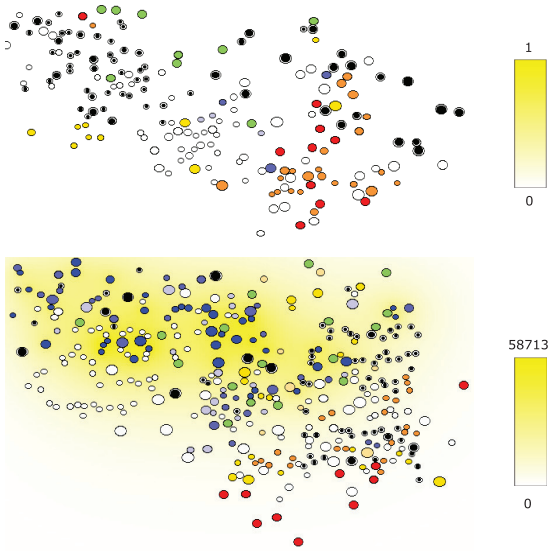

Figure 7.18: Snapshots of the simulation in which the concentration of FasL (in molecules/μL) is shown in yellow color gradient. For cell notations, the same color code as in Fig. 7.15 is used. (**top**) Three days after the virus transmission; (**bottom**) 12 days after virus transmission.

Systemic Dynamics of HIV Infection in Blood

The model offers a unique tool to link the dynamics of the infection and immune responses in blood and the lymph node. The viral load in LN and blood is shown in Fig. 7.19. One can see that their kinetics are pretty similar. The population dynamics of normal $CD4^+$ T cells and infected and $CD4^+$ T cells is presented in Fig. 7.20.

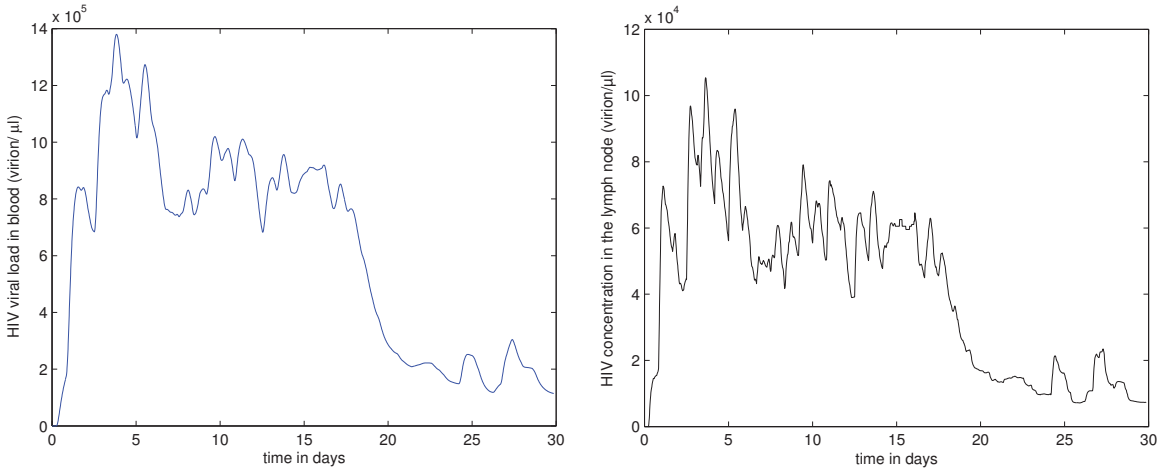

Figure 7.19: (**left**) The viral load in blood (virion/μL); (**right**) The HIV concentration in the lymph node over time.

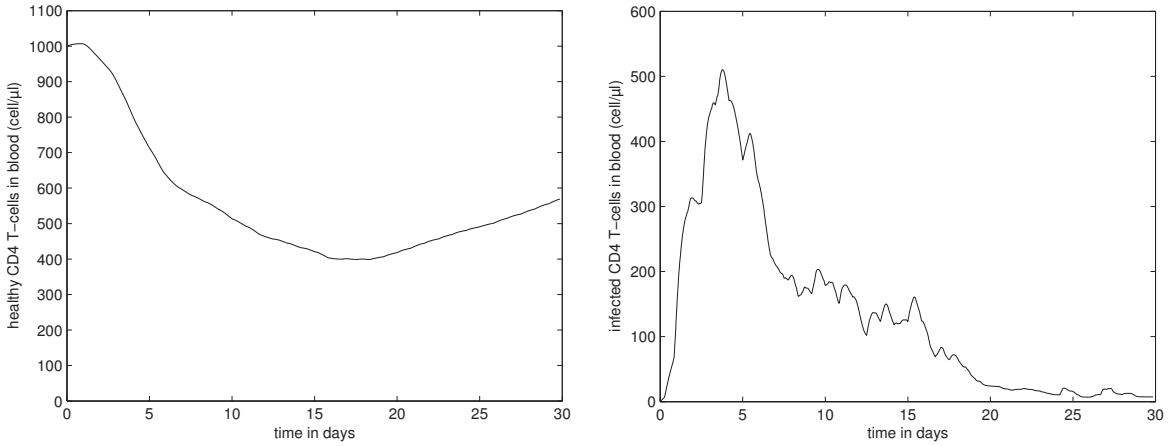

Figure 7.20: Dynamics of infection in blood. (**left**) The population of uninfected $CD4^+$ T cells (cell/μL); (**right**) The population of infected $CD4^+$ T cells (cell/μL).

The elimination of infected T cells is due to the $CD8^+$ T cells' response developing in LN. The HIV-specific $CD8^+$ T cells migrate to blood, as shown in Fig. 7.21. The restoration of naive uninfected $CD4^+$ T cells is only partial and takes longer.

Overall, the simulations indicate that the model consistently reproduces the dynamics of major HIV infection characteristics in blood (viral load and $CD4^+$ T cells during the initial acute phase of infection. These are determined by the specified and calibrated processes of infection spread and immune response development that occur in LN according to the biological schemes implemented in the model equations.

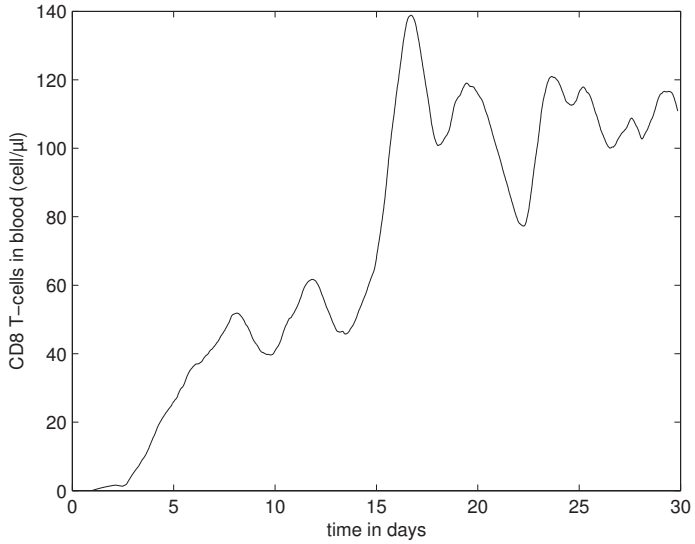

Figure 7.21: Dynamics of immune response in blood. The population of HIV-specific $CD8^+$ T cells over time (cell/μL).

Sensitivity analysis of the model solutions to parameter variations is an important aspect of the assessment of the model performance. A comprehensive analysis of the local and global sensitivity aspects goes beyond the scope of this study. In Fig.s 7.22 and 7.23, we illustrate how the variation in the value of the migration rate of effector $CD8^+$ T cells from lymph node to blood ($k_{LN,Blood}$) affects the dynamics of the observed characteristics of HIV infection. A variation by $\pm 11\%$ of the rate from its reference values has a strong impact on the dynamics of viral load and reduction in the blood number of uninfected $CD4^+$ T cells.

The simulations before represent a single run of the model. To illustrate the variations in individual model realizations due to random effects built into the model, Fig. 7.24 shows an ensemble of three single runs of the model from the same starting conditions.

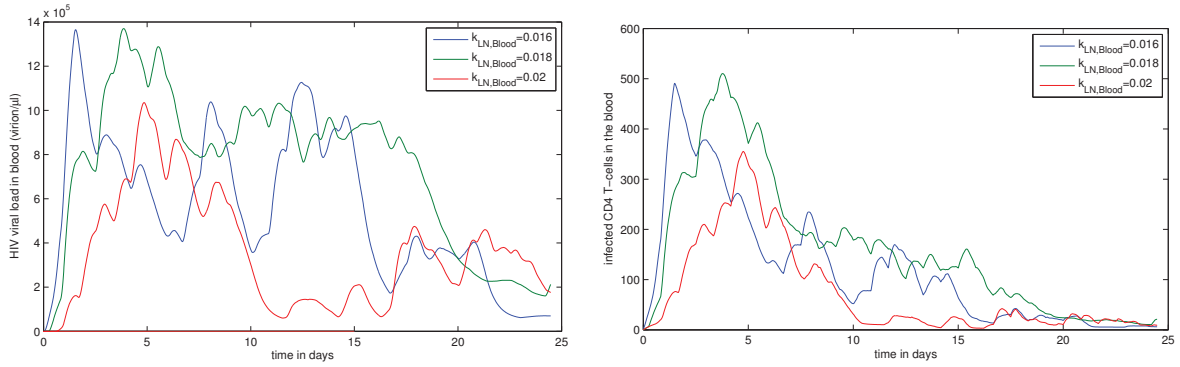

Figure 7.22: Sensitivity analysis for blood. The effect of the variation of the rate of CD8$^+$ T cell migration from lymph node to blood ($k_{LN,Blood}$) by $\pm$ 11%. (**left**) Viral load (virion/μL); (**right**) Infected CD4$^+$ T cells (cell/μL).

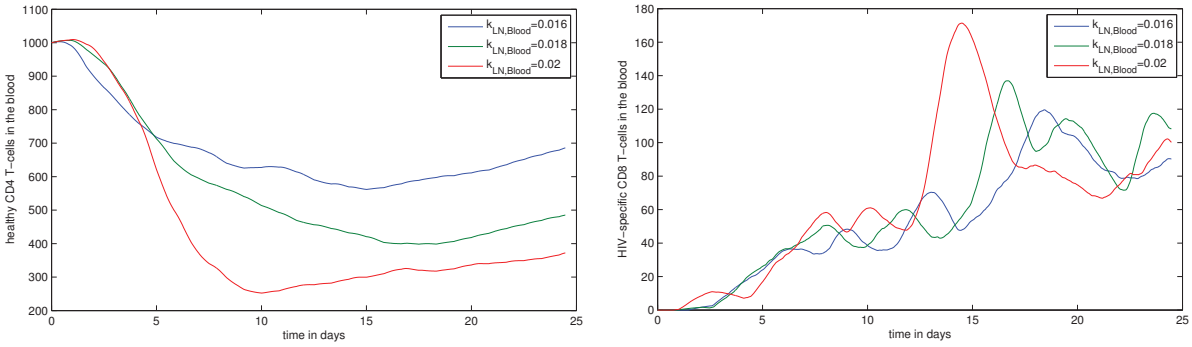

Figure 7.23: Sensitivity analysis for blood. The effect of the variation of the rate of CD8+ T cell migration from lymph node to blood ($k_{LN,Blood}$) by $\pm$ 11%. (**left**) Uninfected CD4$^+$ T cells (cell/μL); (**right**) HIV-specific CD8$^+$ T cells (cell/μL).

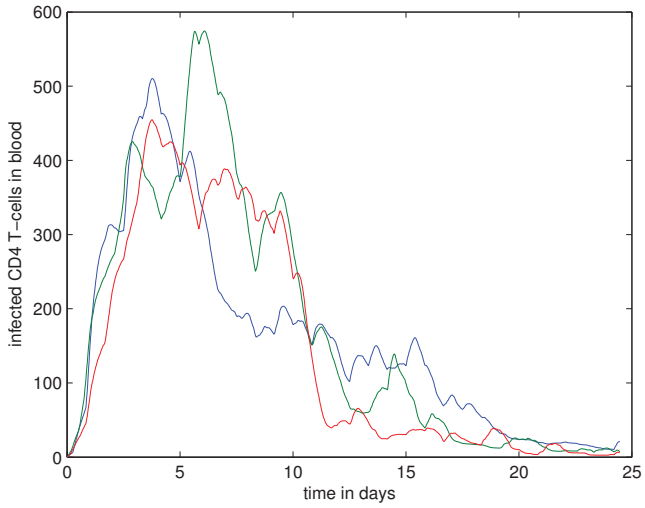

Figure 7.24: Three single runs of the model from the same starting conditions showing the effect of randomness on the dynamics of infected CD4$^+$ T cells in blood (cell/μL).

7.2.5 Discussion

In this study, we formulated a multiscale model of an acute HIV infection, which integrates the processes of infection spread and immune responses in lymph nodes and links to HIV dynamics observed in blood.

The spatio-temporal population dynamics of T lymphocytes in LN is governed by equations linking an intracellular regulation of the T lymphocyte fate by intercellular cytokine fields. We describe the balance of proliferation, differentiation and death at a single-cell level as a consequence of gene activation via multiple signaling events activated by IL-2, IFNa and FasL. Distinct activation thresholds uncouple the different modes of cellular responses depending on the relative levels of the cytokines. This scheme is consistent with recent findings of the rules for signal discrimination between qualitatively similar microbial products yielding context-specific functional responses [264].

The calibration of the model in a way that links the observed kinetics in the blood compartment with that in LNs in a quantitatively consistent way is a non-trivial task. We managed to specify a reference set of model parameters that provides a reasonable agreement with viral load and $CD4^+$ T cell dynamics in blood [230, 275]. Further refinement of the model and parameter estimates requires data on virological and immunological characteristics of HIV-infected individuals at the earliest stage of infection similar to those that have started to be gathered recently [276, 275].

The virus growth in HIV infection is a result of multiple local bursts of the infection-production-elimination occurring randomly in the lymphoid tissue. Indeed, clinical and experimental studies of HIV and SIV infections indicate that the virus growth occurs in multiple local bursts reflecting local non-equilibrium interactions between HIV and immune-activated cells [277]. It was further discussed in [228] that in chronic HIV infection, the efficient transmission of the virus is limited to microscopic clusters of T cells in lymphoid tissues, suggesting that the continuity of virus production is a result of spatially-separated bursts. In view of the above paradigm, the patterns of the model solution seem to be more realistic than the deterministic curves with an exponential pattern.

The multiscale model of HIV infection formulated in our study is based on a number of simplifying assumptions of which the following have to be outlined:

1. the spatial dynamics of cells and cytokines in LNs is considered in a 2D regular domain;

2. the model is restricted to primary acute HIV infection and concomitant cytotoxic T cell responses;

3. intracellular regulation of cell fate by multiple cytokine signaling is described via a hierarchy of activation thresholds;

4. HIV infection is considered in LN and blood compartments.

Detailed sensitivity analysis is an important issue of the developed model to be used for examining the HIV pathogenesis mechanisms. However, it goes beyond the scope of this particular work and will be comprehensively examined in a follow up study.

The here formulated model can be extended along many lines, depending on the questions to be explored and the data available for that. For example, the model allows a straightforward incorporation of a more detailed description of the intracellular fate regulation by considering regulatory networks. The ontogeny of HIV in infected cells can be described in much greater detail [278]. Additional cell fate regulation factors, such as PD1, can be incorporated [279, 280]. Finally, elaborate mechanisms for dynamic tuning of lymphocytes [282, 281], genetic evolution of HIV [283], viral latency [232], chronic immune activation [284] and complementary arms of the immune system [285] need to be considered for extending this model to describe the long-term HIV infection dynamics. The development of respective fine resolution mechanistic “elementary” modules and their integration into the developed multiscale modeling framework will allow one to study via the sensitivity analysis the efficacy of multi-modal treatment approaches of HIV infection combining ART, anti-fibrotic and immuno-modulatory drugs. The insight should assist clinicians in progressing towards an ambitious aim of a perfect long-term control/cure of the infection with minimal side effects.

7.3 Thrombotic complications in HIV-infected patients

A number of studies suggested that HIV is associated with an elevated risk of venous thrombosis. While clinical trials reported the incidence of venous thrombotic events in HIV-infected patients [303, 304,

305], the experimental studies did not accurately determine the underlying physiological mechanisms. However, these studies clearly indicate a hypercoagulable in HIV-infected patients characterized by the upregulation of endothelial TF and the number of TF-bearing microparticles, as well as the decrease in the concentrations of the anticoagulant factors such as antithrombin, protein C, and protein S [35]. For all these reasons, HIV is considered as an important risk factor of venous thrombosis with an 24% increase in the incidence rate of thromboembolic events in HIV-infected patients, especially those with a low CD4* T-cells count (<200/μL) [306].

HIV is a virus that can activate endothelial cells either directly [307], or indirectly through the upregulation of the expression of procoagulant cytokines such as IL-6 and TNF-α, as well as P-selectin on the surface of platelets. That is why HIV and inflammation are considered to be intimately related. The percent of P-selectin positive platelets in blood was found to be inversely proportional to the CD4$^+$ T-cells count in blood [308]. In particular, when the CD4$^+$ T-cells count is below 480/μL. In the same study, a linear correlation was also observed between TNF-α and the number of P-selectin positive platelets suggesting that the TNF-α is behind the over expression of P-selectin and tissue factor on the surface of platelets and possibly endothelial cells too [309]. To quantify the risk of thrombosis during HIV infection, we consider that the concentration of TF inversely correlates with the CD4$^+$ T-cells count:

$$TF(t) = \begin{cases} TF_0 & \text{if } CD4^+ \geq 480 \\ TF_0 + \Omega_2(480 - CD4^+) & \text{if } CD4^+ < 480 \end{cases},$$

Then, we use the TF threshold of thrombosis previously obtained in Section 2.4.7 (Eq. 4.2.22) to determine the periods where the incidence of venous thrombosis is possible (Fig. 7.25).

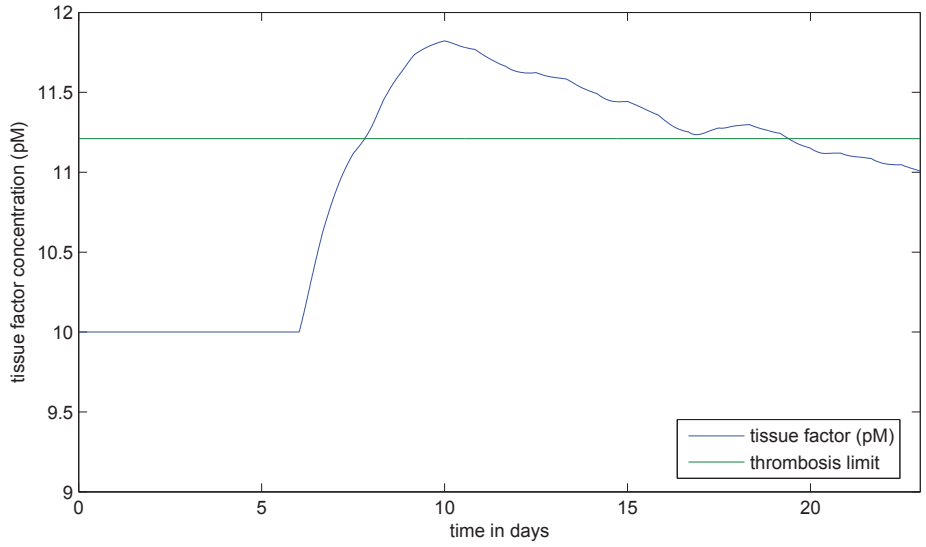

Figure 7.25: Tissue factor concentration during HIV infection vs. the threshold of thrombosis.

Chapter 8

Clinical and Pharmaceutical Applications of Blood Coagulation Modelling

8.1 Clinical background

If a blood vessel wall is damaged, hemostasis is preserved due to clot formation. Clot growth involves several mechanisms including blood coagulation and platelet aggregation. After some time, when the injury is healed, the clot is dissolved. In some pathological conditions, if the clot forms spontaneously or if it is not dissolved, then various physiological complications can emerge possibly demanding medical treatment. Deep venous thrombosis (DVT) is a blood clotting disorder that occurs when excessive blood clotting occurs inside deep veins. It can provoke embolisms where a part of the clot breaks off and subsequently blocks blood circulation in pulmonary vessels.

Under normal conditions, clot formation is initiated when tissue factor is exposed to bloodstream. It forms a complex with factor VIIa which activates the factors IX and X resulting in the generation of an initial concentration of thrombin. If the produced thrombin concentration in the initiation phase is sufficiently high, it activates other factors in the amplification phase leading to self-accelerating thrombin production through a positive feedback [311]. Other mechanisms act to stop clot growth. Activated protein C inhibits thrombin generation in the amplification phase, while antithrombin inactivates thrombin itself by binding to it. In addition, blood flow limits clot growth by transporting thrombin and other clotting factors away from the injury site.

The risk factors for developing deep venous thrombosis can be obesity, cancer, injury, slow blood flow due to the lack of physical activity, among the others. Recurrent thrombi can be prevented by controlling these risk factors (in the long term) or by anticoagulant drugs (in the short/medium term). There are several anticoagulant drugs that can have different mechanisms of action. They can inhibit the activation of the factor X or thrombin such as the new oral anticoagulants [312]. Others like heparin increase the activity of antithrombin [313]. Another important type of anticoagulant drugs is vitamin K antagonist (AVK) drugs such as warfarin. It acts by reducing vitamin K-dependent factors synthesis in the liver [314]. As a result, the concentrations of the key blood clotting factors such as prothrombin and FVII, FIX, FX are decreased.

One aspect of warfarin based treatments is that they can be monitored by blood testing for the International Normalized Ratio (INR). It is an *in vitro* assay based on the measurement of the prothrombin time (PT). The latter characterizes the time interval necessary to convert prothrombin into thrombin under specific experimental conditions. Depending on the measured value of INR, the administrated dose of warfarin is adjusted in order to reach a therapeutic range. In DVT, the targeted level of INR is between 2.0 and 3.0 [315]. A lower than 2.0 value of INR indicates the risk of the patient to develop recurrent thrombosis while a higher than 3.5 value signifies a high risk of bleeding. Furthermore, the difference between the experimental settings under which the INR is measured and *in vivo* physiological conditions can result in cardio-vascular events even for a normal INR level. In particular, these tests do not consider the effect of blood flow and the direct inhibition of thrombin by antithrombin.

The present study is devoted to the development of an individualized model describing blood clot-

ting dynamics during warfarin therapy. It consists of three components: clot formation at the injury site, vitamin-K dependent factors synthesis in the liver, blood testing for INR. We will be particularly interested by the effects of blood flow and direct thrombin inhibition by antithrombin on blood clotting during warfarin treatment. We will explore the patho-physiological conditions resulting in thromboembolic events in spite of the INR values corresponding to appropriate anticoagulant target values during warfarin treatment. Finally, we will suggest an *in silico* framework to accurately predict the appropriate therapeutic range for INR depending on the characteristics of the patient.

8.2 Individualized blood coagulation model to predict the action of anticoagulant drugs

To study the effect of anticoagulant drugs on the blood clotting system, we develop a blood coagulation model taking into account the main features of clot formation under warfarin treatment. The model consists of three sub-models. The first one is devoted to blood clotting at the injury site. The second one is a PK-PD model that describes synthesis of the vitamin K-dependent blood factors in the liver and the action of warfarin. The third model simulates *in vitro* blood testing for INR. These three components of the individualized model are connected with each other as shown in Fig. 8.1.

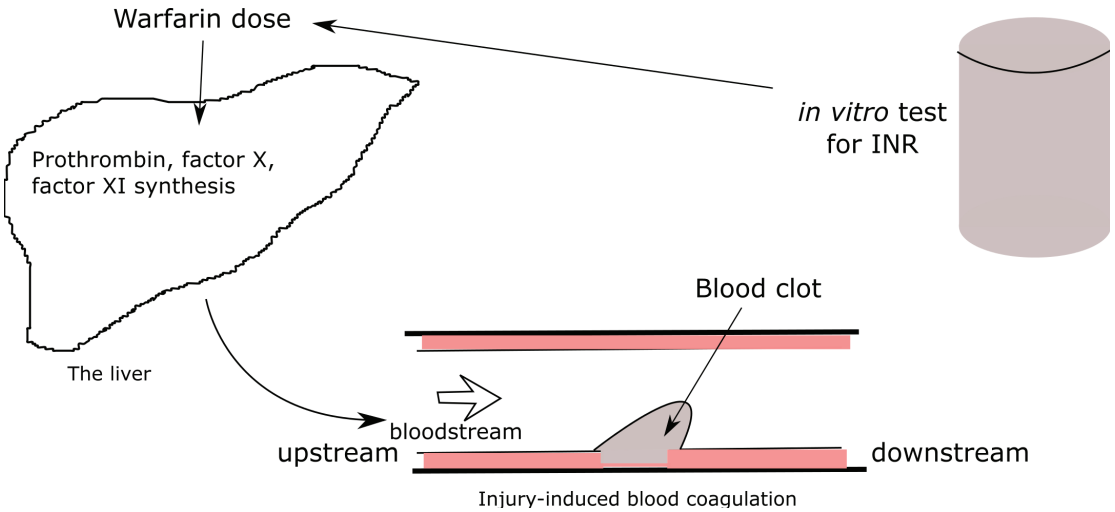

Figure 8.1: The structure of the model indicating the interaction between warfarin, vitamin-K dependent factors synthesis in the liver, INR tests and blood coagulation.

8.2.1 Blood clotting dynamics at the injury site

We use a previously developed model (Chapters 2 and 3) to describe clot formation initiated by a damage of the blood vessel wall. It consists of reaction-diffusion equations for the concentrations of clotting factors coupled with the Navier-Stokes equations for blood flow. Clot is considered as a partially penetrable medium where flow velocity decelerates. We represent the vein by a 2D rectangle where a part of the wall is damaged. Tissue factor is exposed to the bloodstream at the damaged part of the wall. The blood clotting pathway considered in the model is shown in Fig. 8.2 (left). We consider the following equations for the concentrations of prothrombin P, thrombin T, antithrombin A, factors IX and X with their total concentration denoted by B and their active form B_a, protein C denoted by C and its active form C_a, fibrinogen F_g, fibrin F and fibrin polymer F_p:
Prothrombin

$$\frac{\partial P}{\partial t} + \nabla.(vP) = D\Delta P - \left(k_1\phi_c + k_2 B_a + \frac{k_3 T^3}{1+k_8 C_a}\right) P, \tag{8.2.1}$$

thrombin

$$\frac{\partial T}{\partial t} + \nabla.(vT) = D\Delta T + \left(k_1\phi_c + k_2 B_a + \frac{k_3 T^3}{1+k_{10}C_a}\right)P - k_4 AT, \tag{8.2.2}$$

factors IXa, Xa

$$\frac{\partial B_a}{\partial t} + \nabla.(vB_a) = D\Delta B - k_5 AB_a, \tag{8.2.3}$$

APC

$$\frac{\partial C_a}{\partial t} + \nabla.(vC) = D\Delta C, \tag{8.2.4}$$

antithrombin

$$\frac{\partial A}{\partial t} + \nabla.(vA) = D\Delta A - k_4 AT - k_5 AB, \tag{8.2.5}$$

fibrinogen

$$\frac{\partial F_g}{\partial t} + \nabla.(vF_g) = D\Delta F_g - \frac{k_6 T F_g}{K_6 + F_g}, \tag{8.2.6}$$

fibrin

$$\frac{\partial F}{\partial t} + \nabla.(vF) = D\Delta F + \frac{k_6 T F_g}{K_6 + F_g} - k_7 F, \tag{8.2.7}$$

fibrin polymer

$$\frac{\partial F_p}{\partial t} = k_7 F. \tag{8.2.8}$$

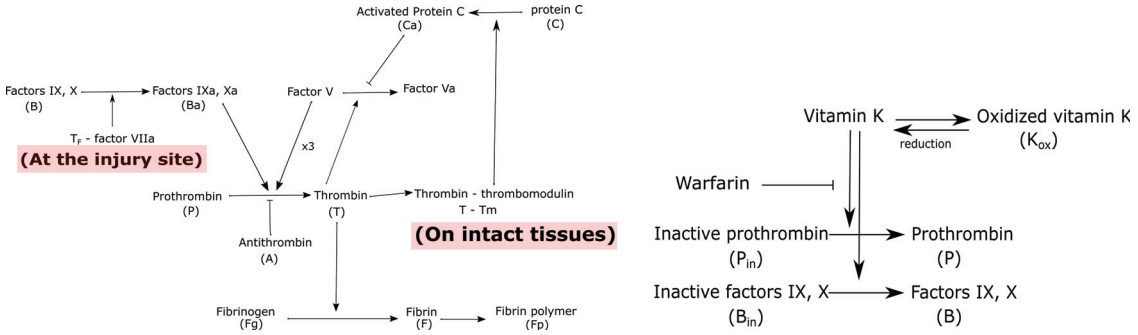

Figure 8.2: Blood clotting pathway (left) and synthesis of the vitamin-K dependent factors in the liver under warfarin therapy (right).

All these concentrations are normalized. Here v is the flow velocity, k_i denote reaction rate constants, D is the diffusion coefficient taken the same for all concentrations except for fibrin polymer. The latter forms a solid clot, it does not diffuse and it is not transported by flow. In equations (8.2.1) and (8.2.2), the reaction term $\Phi(T, B_a, C_a)$ is given by the function:

$$\Phi(T, B_a, C_a) = \underbrace{k_2 B_a}_{\text{initiation phase}} + \frac{\overbrace{k_3 T^3}^{\text{self-accelerated production}}}{\underbrace{1+k_8 C_a}_{\text{inhibition by APC}}}.$$

The boundary conditions for the activated factors IX and X depend on the amount of tissue factor at the damaged part of the wall:

$$\frac{\partial B_a}{\partial n}\Big|_{\Gamma_d} = \frac{\alpha_1(B^0 - B_a)}{1+\beta_1(B^0 - B_a)}, \tag{8.2.9}$$

where $K_6 = K_7^- K_7 T_F^*$. The activation of protein C depends on the complex of thrombin and thrombomodulin at the intact wall:

$$\frac{\partial C_a}{\partial n}\Big|_{\Gamma_u} = \frac{\alpha_2 (C^0 - C)[TT_m]}{1 + \beta_2 (C^0 - C_a)}, \tag{8.2.10}$$

$$[TT_m] = \frac{k_T^0 TT_m}{1 + k_T^0 TT_m}, \tag{8.2.11}$$

where $[TT_m]$ is the complex thrombin-thrombomodulin. The concentrations of prothrombin, fibrinogen and antithrombin are fixed at the inlet of the domain to P_0, A_0 and F_{g0}, respectively. No flux boundary conditions are prescribed at the other boundaries for these variables and at all boundaries for the other variables. We consider zero initial conditions for all variables except for prothrombin, fibrinogen and antithrombin for which the same initial values are prescribed as their values at the boundary.

Blood flow is modelled with the Navier-Stokes equations for the incompressible fluid. We describe the thrombus as a porous medium whose permeability depends on the concentration of fibrin polymer. To model the interplay between clot growth and venous hemodynamics, an additional term was added to the Navier-Stokes equations describing fluid deceleration by the porous medium

$$\rho \left(\frac{\partial v}{\partial t} + v \nabla v \right) = -\nabla p + \mu \Delta v - \frac{\mu}{K_f(\vec{x})} v, \tag{8.2.12}$$

$$\nabla v = 0.$$

Here v is the velocity vector, p is the pressure, ρ is the blood plasma density, μ is the blood viscosity, K_f is the permeability of fibrin polymer which depends on its concentration F_p [56]:

$$\frac{1}{K_f(\vec{x})} = \frac{16}{\alpha^2} F_p(\vec{x})^{1.5} (1 + 56 F_p(\vec{x})^3), \tag{8.2.13}$$

where α is the fiber radius. One of the advantages of this method is enabling the use of the same model in the entire computational domain. We prescribe the condition of constant pressure difference between the inlet and the outlet

$$p_{out} - p_{in} = \Delta p,$$

and we use the periodic boundary conditions for the velocity at the inlet and the outlet of the flow and the no-slip condition at the top and bottom walls.

Simplified model. Along with the complete model (8.2.1) - (8.2.12), we consider a simplified 1D model of thrombin production consisting of a single reaction-diffusion equation:

$$\frac{\partial T}{\partial t} = D \frac{\partial^2 T}{\partial y^2} + (k_2 B_a + k_3^+ T^3)(P_0 - T) - (k_4 A_0 + a v) T, \tag{8.2.14}$$

where D is the diffusion coefficient, P_0 is the prothrombin concentration initially present in blood flow, α_1 and α_2 are the coefficients representing thrombin inhibition by antithrombin and blood flow respectively, k_1 and k_2 are kinetic coefficients, $B_a(y)$ express the initiation of thrombin generation by factors IXa and Xa and is given as a function of y: $B_a(y) = Be^{-y/\sigma}$ where $\sigma = \sqrt{\frac{D}{k_5 A_0}}$. Blood flow velocity is introduced as a Poiseuille flow $v(y) = Ay(H - y)$, where H is the vessel diameter. We denote by $v(H/2) = v_m$ the maximal value of blood flow velocity in the middle of the vessel.

This equation describes thrombin distribution in the cross section of the vessel. In spite of the simplicity of the model, it gives a good approximation of the complete model. On the other hand, it will allow us to obtain analytical conditions of thrombosis and bleeding. We have represented the maximal height reached by the clot as we increase prothrombin concentration in plasma in Fig. 8.3. We compared the prothrombin effects on injury-induced clotting by using simulations of both the complete and 1D models. The similarity between the results obtained by the two models will allow us to use the simplified 1D model in what follows.

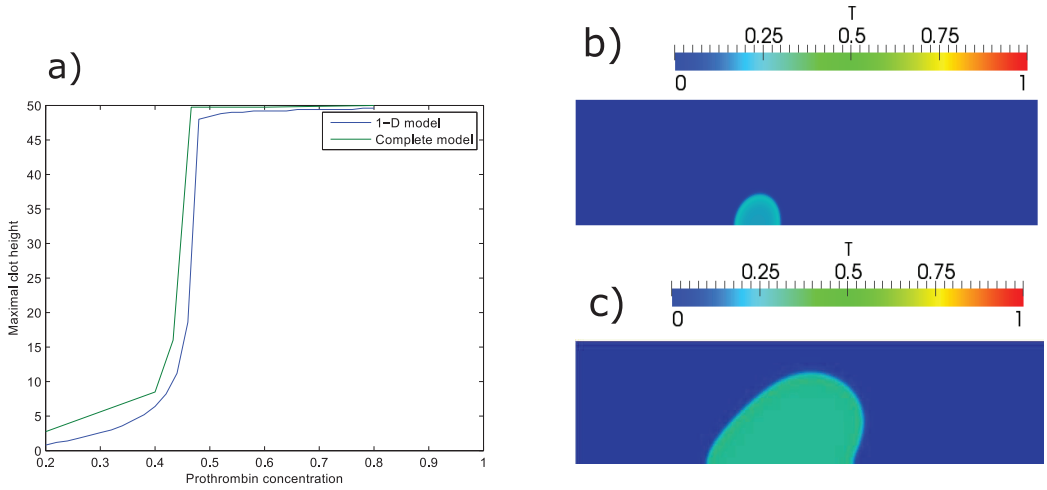

Figure 8.3: a) Comparison of the clot height in the simplified and complete models for an initial parabolic flow of $v_m = 200\ \mu m/s$. The maximal heights reached by the clot as a function of prothrombin concentration in plasma P_0; b) distribution of thrombin concentration obtained using the complete model for $P_0 = 0.4$; c) snapshot of thrombin distribution using the complete model for $P_0 = 0.6$.

Let us note that prothrombin is a zymogen that is converted to thrombin which plays an important role in the formation of blood clot. Prothrombin is activated by both factors IX, X (initiation phase) as well as factors that are subsequently activated by thrombin itself (amplification phase). When prothrombin concentration is low, it is insufficient to trigger clotting and thus bleeding is observed. As we increase prothrombin in the plasma, a small clot forms. The thrombin wave is not strong enough to withstand removal by blood flow and thus it stops propagating. This corresponds to normal blood clotting. As prothrombin concentration increases in blood plasma, thrombin generation becomes sufficiently high to resist to blood flow. Then partial or complete occlusions of the vein can occur. This corresponds to deep venous thrombosis.

8.2.2 PK-PD model of warfarin and rivaroxaban

Warfarin is one of the common anticoagulants whose mechanism of action implies the ihibition of synthesis of vitamin K in the liver. As a result, it downregulates the production of thrombin and factors IX and X. Below we develop a PK-PD model that reflects main features of warfarin treatment.

Warfarin and rivaroxaban pharmacokinetics

Warfarin. A knowledge of the pharmacokinetics of warfarin is helpful in understanding the initial response to therapy. Warfarin can be detected in the plasma one hour after oral administration, and peak concentrations occur in two to six hours [318].

Warfarin is a racemic mixture of stereo isomers, which are 99 percent bound to albumin. The drug is metabolized in the liver and kidneys, with the subsequent production of inactive metabolites that are excreted in the urine and stool [319]. It is almost completely absorbed, reaching a maximum plasma concentration between 2 and 6 hours after administration. It has a small volume of distribution (10 L/70kg) and it is eliminated by hepatic metabolism with a very small clearance (0.2 L/h/70kg). Its elimination half-life is about 35 hours [316]. We describe warfarin concentration in the body by the following equation:

$$\frac{dW}{dt} = m^1 W_{ex}(t) - n^1 W, \tag{8.2.15}$$

where W is warfarin concentration in plasma, $W_{ex}(t)$ equals some constant value during first 4 hours after administration and 0 after 4 hours because warfarin concentration in plasma reaches its maximal value after 2-6 hours of the administration time, m and n are two positive constants.

Rivaroxaban. Rivaroxaban is one of the novel anticoagulant drugs [312]. It downregulates the coagulation process by inhibiting the activity of factor Xa. While it cannot be monitored by *in vitro* tests like antivitamin-K drugs, it is also associated with both thrombosis and bleeding risks. In the present study, we use mathematical modelling tools to assess the efficacy and safety of rivaroxaban used numerical simulation and mathematical investigation of a simplified model. After onset of rivaroxaban, its concentration in plasma reaches a maximal value within 3 hours. The half-life time for rivaroxaban in plasma is 7 h- 13 h. We use the following equation for rivaroxaban concentration in plasma.

$$\frac{dR}{dt} = m^2 R_{ex}(t) - n^2 R, \tag{8.2.16}$$

where R is rivaroxaban concentration in plasma, $R_{ex}(t)$ equals some constant value during first 3 hours after administration and 0 after 3 hours. m and n are two positive constants.

Warfarin and rivaroxaban pharmacodynamics

Warfarin. Vitamin K is used for synthesis of some of the clotting factors in the liver such as factors II, IX and X [314]. It is formed in the reversible reaction of oxidized vitamin K reduction [321]. Warfarin inhibits vitamin K activity in the liver (Fig. 8.2, right). We consider the following reactions taking place in the liver:

$$K + P^{in} \to P,$$

$$K + B^{in} \to B.$$

Here P^{in} and B^{in} are the inactive forms of prothrombin and factors IX and X in the liver, P and B are their active forms and due to mass balance we have the relations:$P^{in} + P = P_0$ and $B^{in} + B = B_0$. Taking into account that $K^0 = K + K_{ox}$ where K_{ox} is the concentration of oxidized vitamin-K, we have the following equations for these concentrations:

$$\frac{dK}{dt} = \beta_1^0(K_0 - K) - (\beta_1^1(P_0 - P) + \beta_1^2(B_0 - B))K - \beta_2^0 WK, \tag{8.2.17}$$

$$\frac{dP}{dt} = \beta_1^1(P_0 - P)K - \beta_2^1 P, \quad \frac{dB}{dt} = \beta_1^2(B_0 - B)K - \beta_2^2 B, \tag{8.2.18}$$

Rivaroxaban. Rivaroxaban directly inhibits the factor Xa. Hence we following equation for factors IX, X concentration:

$$\frac{\partial B_a}{\partial t} + \nabla.(vB) = D\Delta B - k_7 AB - k_r RB, \tag{8.2.19}$$

8.2.3 INR and PT estimation

Prothrombin is converted into thrombin in the initiation and amplification phases of the coagulation cascade. In a quiescent platelet free plasma, this process can be approximated with:

$$P + B_a \to T, \quad P + 3T \to T.$$

We get the following equation for the concentration of prothrombin (P):

$$\frac{dP}{dt} = -k_2 B_a P - k_3^+ T^3 P. \tag{8.2.20}$$

Replacing T in the right-hand side by its maximal value P_0, we find:

$$P = P_0 e^{-(k_2 B_a + k_3^+ P_0^3)t}. \tag{8.2.21}$$

Prothrombin time (PT) characterizes plasma tendency to clotting. It shows how much time is necessary to reach some given concentration P_τ of prothrombin [320]. Set $P_0/P_\tau = \beta$. Then from (8.2.21) we find PT:

$$PT = \frac{ln(\beta)}{k_2 B_a + k_3^+ P_0^3}. \tag{8.2.22}$$

The International Normalized Ratio (INR) is given by the expression

$$INR = \left(\frac{PT}{PT_{ref}}\right)^{ISI},$$

where PT_{ref} is the reference prothrombin time and ISI indicates the increase in tissue factor in comparison with reference factor. We consider the prothrombin time at the beginning of treatment

$$PT_{ref} = \frac{\ln(\beta)}{k_2 B_a^* + k_3^+ P_*^3},$$

where B_a^* and P_* are the reference pre-treatment concentrations of activated factors IX and X and prothrombin, and set $ISI = 1$. Then

$$INR = \frac{k_2 B_a^* + k_3^+ P_*^3}{k_2 B_a + k_3^+ P_0^3}. \tag{8.2.23}$$

8.3 Results

In order to study the action of warfarin on blood clotting, we first determine the role of vitamin-K dependent coagulation factors on thrombosis and bleeding. We use numerical simulations and analytical estimates to derive the conditions on the existence of different regimes of blood clotting. We consider two main factors arresting clot growth: direct inhibition of blood factors by antithrombin and the role of blood flow. The latter is of particular interest since INR testing is measured in quiscent plasma while flow effect can have significant influence on the clotting dynamics. Then, we study the action of warfarin on blood coagulation combining three sub-models: *in situ* thrombus development submodel (Section 8.2.1), PK-PD submodel of warfarin action (Section 8.2.2), INR *in vitro* assay submodel (Section 8.2.3). We also address the problem of thrombosis persistence in patients with normal INR. We demonstrate the difference of PT measurement in artificial *in vitro* conditions as compared to the physiological conditions.

8.3.1 The levels of prothrombin and factors IX, X in plasma determine the regimes of blood coagulation

Using the simplified model given by equation (8.2.14), we will determine conditions on P and B which provide thrombosis or bleeding. Bleeding occurs if the initiation of blood clotting fails. This happens near the endothelial wall ($y = 0$), where $B_a(y) = B$ and $v(y) = 0$. Equation (8.2.14) in this case is written as follows:

$$\frac{\partial T}{\partial t} = D\frac{\partial^2 T}{\partial y^2} + (k_2 B + k_3^+ T^3)(P - T) - k_4 A_0 T. \tag{8.3.24}$$

This reaction-diffusion equation describes thrombin distribution. Set

$$\Phi(T) = (k_2 B + k_3^+ T^3)(P - T) - k_4 A_0 T.$$

This nonlinearity can have up to three zeros $0, T_1, T_2$ depending on the values of parameters. It can have travelling wave solutions corresponding to clot growth. The thrombin wave will either propagate and then will be followed by fibrinogen conversion into fibrin leading to clot formation. Otherwise, the wave does not propagate, thrombin will diffuse in the plasma without initiating self-sustained reaction and resulting in formation of a small clot or no clot formation at all (bleeding). In order to have a travelling wave solution with a positive speed, we impose the following condition [124]:

$$\int_0^{T_2} \Phi(T) > 0. \tag{8.3.25}$$

If this inequality is opposite, then the speed of the wave is negative, and thrombin wave does not propagate. In this case, the clot does not form even near the wall where the flow velocity is zero. This situation will result in complete clot absence and severe bleeding. In Section 3.3 below we will consider a more general case of insufficient clot formation where a small clot is formed near the wall but it cannot grow further.

Conditions of bleeding. If inequality (8.3.25) does not hold, then we obtain conditions on B or P when bleeding occurs:

$$B_a \le \frac{1}{4k_2 P - k_2 T_2^3}\left(\frac{4k_3^+ T_2^4}{5} - k_3^+ P T_2^3 + 2k_4 A_0 T_2\right) \tag{8.3.26}$$

or

$$P \le \frac{1}{4k_2 B + k_3^+ T_2^3}\left(k_2 B_a T_2^3 + \frac{4k_3^+}{5} T_2^4 + 2k_4 A_0 T_2\right). \tag{8.3.27}$$

Conditions of thrombosis. Deep venous thrombosis (DVT) occurs if clot fills the whole cross section of the vessel or its essential part. In the framework of the considered model, this situation corresponds to the travelling wave propagating across the vessel. Since the flow velocity depends on the distance from the vessel wall, conditions on thrombin wave propagation should also be given depending on this distance. We assume here that thrombin gradient is sufficiently large, and condition (8.3.25) can be considered for fixed values of y. Therefore we obtain the following conditions of thrombosis formulated either in terms of B_a or P:

$$B_a(y) > \frac{1}{4k_2 P - k_2 T_2^3}\left(\frac{4k_3^+ T_2^4}{5} - k_3^+ P T_2^3 + 2k_4 A_0 T_2 + 2av(y)\right), \tag{8.3.28}$$

$$P > \frac{1}{4k_2 B_a(y) + k_3^+ T^3}\left(2k_2 B_a(y) T^2 + \frac{4k_3+}{5} T^4 + 2k_4 A_0 + 2av(y)\right). \tag{8.3.29}$$

In order to have complete occlusion, conditions (8.3.28) or (8.3.29) should be verified for the maximal value of flow velocity in the middle of the vein $v(H/2) = v_{max}$. Otherwise, we obtain a partial

occlusion depending on the blood flow velocity. As we increase it, more prothrombin and factors IX, X concentrations are required for thrombosis to occur, and the regime of normal hemostasis is more likely to take place. Hence, blood flow plays a vital role in normal hemostasis providing an additional mechanism limiting clot growth. When blood flow is slower than normal, clot growth is not stopped and the thrombus completely occludes the vein. If flow velocity is sufficiently high, it limits clot growth at the middle of the vessel. We show the clot height for different prothrombin concentrations and flow velocities in Fig. 8.4.

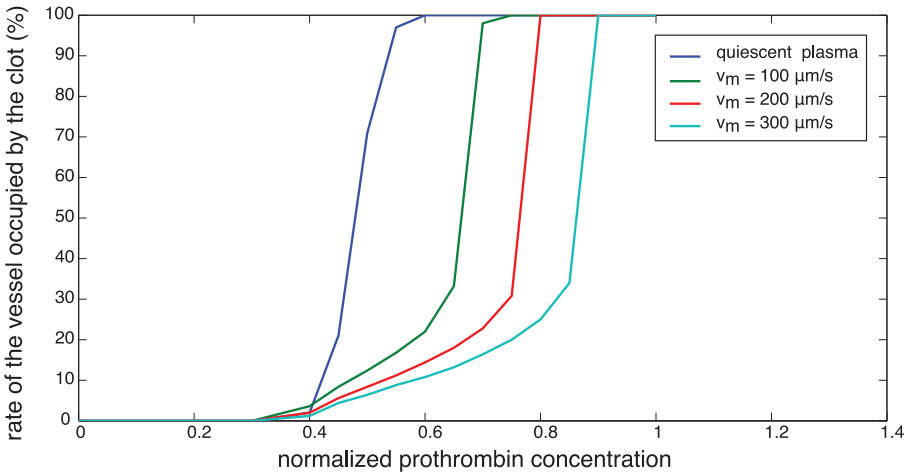

Figure 8.4: The final clot size (relative to the vein width) as a function of the concentration of prothrombin in blood plasma for different blood flow velocities.

8.3.2 Warfarin reduces synthesis of the vitamin-K dependent factors

Warfarin concentration is determined by equation (8.2.15). We simulate synthesis of the vitamin-K dependent factors with equations (8.2.17) and (8.2.18). The concentration of warfarin in bloodstream increases after each administration, and then decreases during the next several hours (Fig. 8.5, left). Its average value increases during the first 10 days and then oscillates around some constant value (0.8 mg/l) for a daily dose of 4 mg. The vitamin-K concentration in the liver is affected by warfarin, and it is reduced by half after the first ten days (Fig. 8.5, right). As a result, the amounts of factors IX, X and prothrombin released to bloodstream are reduced by 70% (Fig. 8.6).

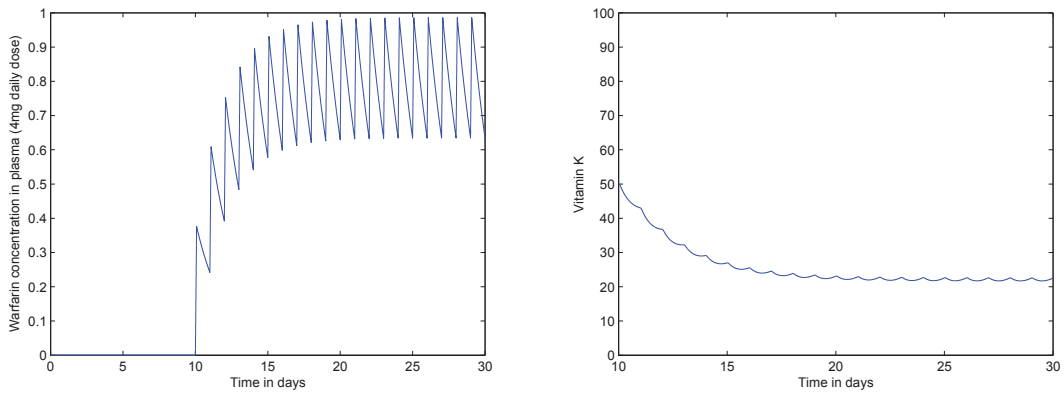

Figure 8.5: Prothrombin synthesis under warfarin treatment. Left: warfarin concentration in plasma (mg/l) during a protocol of daily administration of a 4mg dose starting from day 10; right: vitamin K concentration in the liver (% of the maximal value).

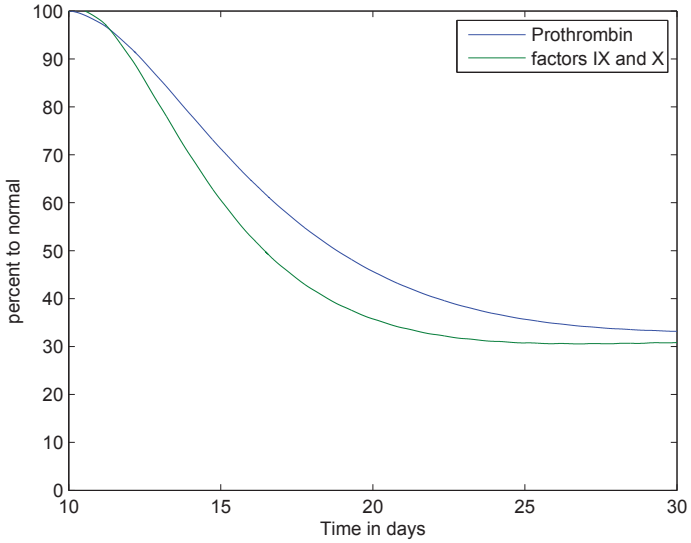

Figure 8.6: Prothrombin and factors IX and X percent of initial concentration during treatment.

INR measures the concentrations of vitamin-K dependent factors in bloodstream. When the concentrations of prothrombin and factors IX, X are below their reference value, INR increases. After 10 days of warfarin daily intake, INR reaches a stable value. In thrombosis prevention, warfarin daily dose is chosen in order to reach the required INR level (Fig. 8.7).

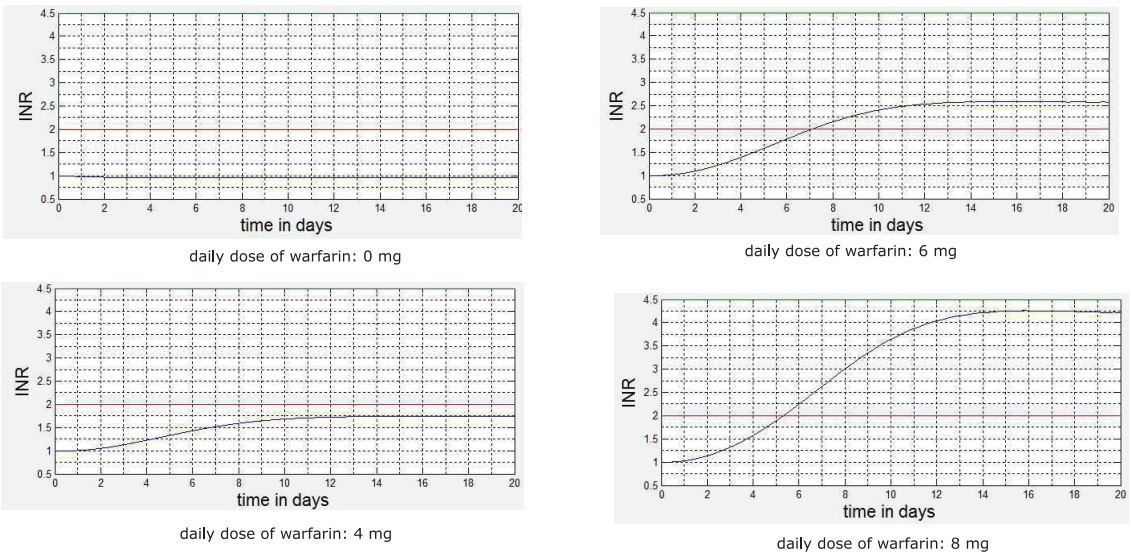

Figure 8.7: INR levels over time for different daily doses of warfarin.

8.3.3 Thrombosis and bleeding can persist even for the normal INR therapeutic range

Blood tests for INR are based on prothrombin time measurement. This time depends on the concentrations of vitamin-K dependent factors in blood. The model described in Section 3.2 provides the dynamics by which warfarin inhibits the production of prothrombin and factors IX and X. Using the conditions of bleeding and thrombosis on vitamin-K factors obtained in Section 3.1 and the INR formula, we derive conditions under which thromboembolic events can still occur even for the normal INR

level. From (8.2.23) and equality in (8.3.25), we get:

$$A = \frac{1}{2k_2k_4T_2}\left(\frac{k_2B_a^* + k_3^+P_*^3 - INRk_3^+P^3}{INR} - \frac{4k_3^+T_2^4}{5} + k_3^+T_0T_2^3 - 2avT_2\right). \tag{8.3.30}$$

To simplify its interpretation, we consider a constant blood flow velocity v.

We consider the antithrombin concentration A as a function of INR for different values of v. Set $v = v_m$, where v_m is the maximal flow velocity reached at the center of the vessel. The corresponding curve in Fig. 8.8 (dashed curve) separates the regions of parameters where the clot continues its growth (below the curve) and where it stops (above the curve) for this value of flow velocity. The first case corresponds to complete vessel occlusion where the clot fills the whole cross section of the vessel. In the second case the clot is stopped before it reaches the center of the vessel.

Next, we determine the region of insufficient clot formation. We set $v = v_m/8$ and draw the corresponding curve (solid curve in Fig. 8.8). In the region of parameters above this curve, clot growth is stopped near the vessel wall even though the flow velocity there is low. In particular this region includes the bleeding conditions suggested in Section 3.1 where clot does not form at all. The remaining region between the curves obtained for $v = v_m$ and $v = v_m/8$ we split by the curve for $v = v_m/4$ and consider that normal clot growth occurs above it and partial occlusion occurs below it. The choice of the values $v_m/8$ and $v_m/4$ is to some extent arbitrary with some low and intermediate flow velocities.

Thus, we identify four regions in the parameters plane: partial or complete occlusion, insufficient and normal clot growth. If $INR > 3$, then bleeding or insufficient clotting occurs for most values of antithrombin concentration. If $INR < 2$, then partial or complete occlusion occurs in the wide range of values of A. In the normal therapeutic range $2 < INR < 3$, insufficient, normal or excessive clotting can occur depending on the values of antithrombin concentration and flow velocity. This analysis confirms that low INR is specific for thrombosis and high INR to bleeding. However it also indicates that a more precise specification is required in the normal INR range.

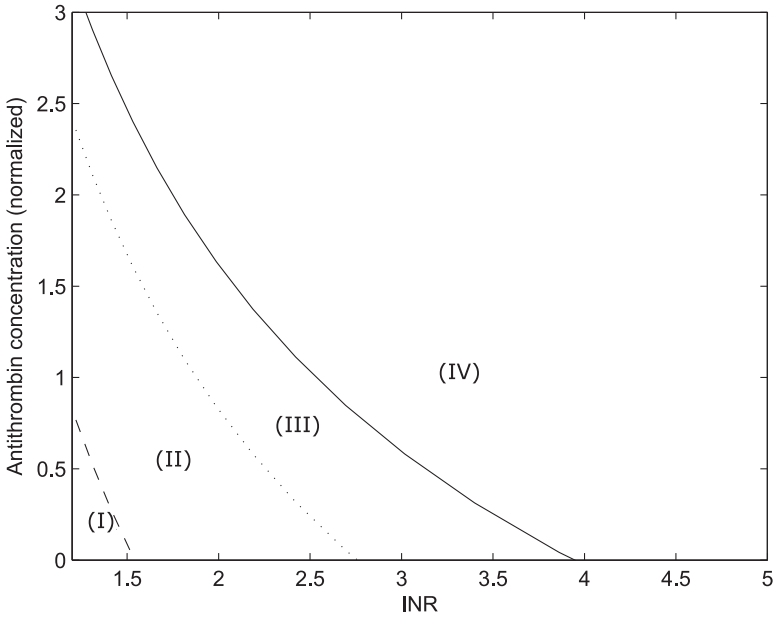

Figure 8.8: The regions with different regimes of blood clotting depending on INR and antithrombin concentration for a parabolic blood flow with a velocity $v_m = 400\ \mu m/s$. (I) Complete thrombosis, (II) partial thrombosis, (III) normal hemostasis, (IV) insufficient clotting. Solid line is obtained from 8.3.30 for $v = v_m/8$, dotted line for $v = v_m/4$, dashed line for $v = v_m$.

8.3.4 The therapeutic window of rivaroxaban therapy

The function $B_a(y)$ describes the distribution of factors IXa and Xa which initiats thrombin wave propagation. It corresponds to a stationary solution of the equation:

$$B_a'' - k_7 A_0 B_a - k_r R B_a = 0, \tag{8.3.31}$$

which is given in the form $B_a(y) = \lambda e^{-y/\sigma}$, where $\sigma = 1/\sqrt{k_7 A_0 + k_r R}$. We obtain the conditions of thrombin wave propagation on B_a, then σ and R.

The parameter k_r was fitted in both exhaustive and simplified model to obtain similar rivaroxaban effects on factor Xa activity than in experiments [323] (Fig. 8.9).

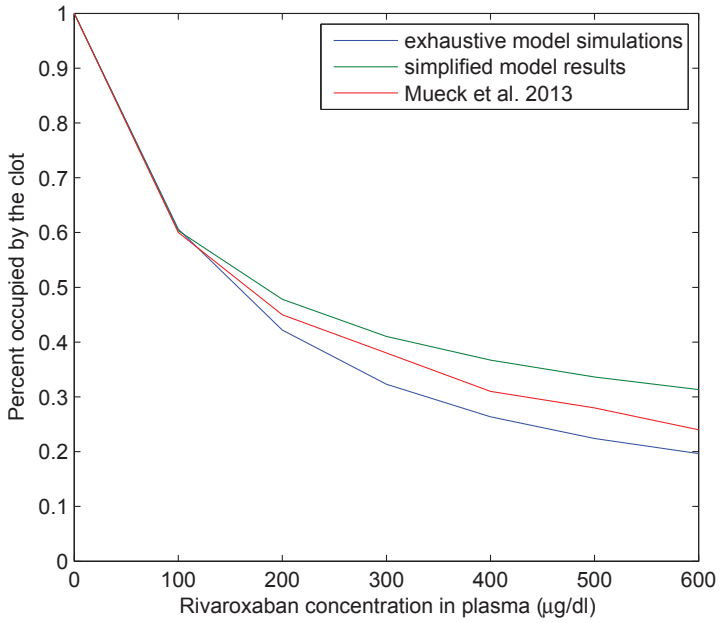

Figure 8.9: Factor Xa activity versus rivaroxaban concentration in experiments and modelling.

Using the the PK-PD results, we determine the patient-specific therapeutic window during rivaroxaban treatment (Fig. 8.10). The results show that the most efficient and safe treatment protocol for this individual patient is the 20 mg/day regimen. This coincides with the clinical indications that suggest to prescribe this regimen for patients exhibiting one or more of the thrombosis risk factors. Furthermore, the high variability of the rivaroxaban distribution in blood indicates that its concentration should remain within the individual therapeutic window during the entire period of treatment.

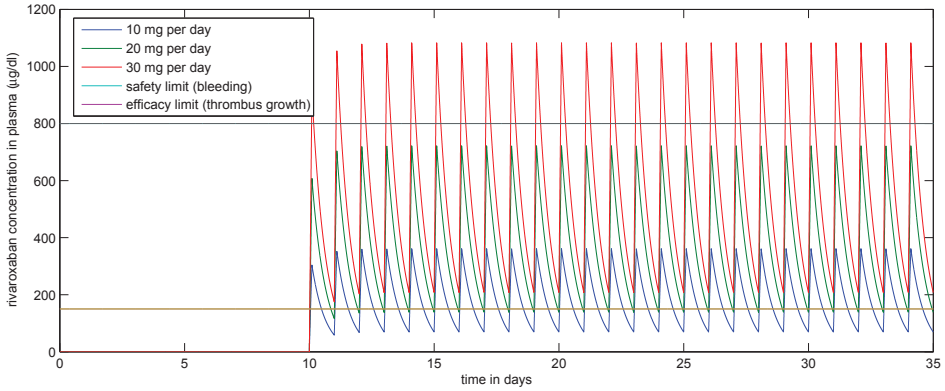

Figure 8.10: Therapeutic window (horizontal lines) vs. rivaroxaban plasma concentration under different protocols.

8.3.5 Patients response to warfarin treatment

We consider a cohort of $n = 200$ patients with random characteristics. These patients are exposed to the risk of thrombosis in deep vein (due to inflammation, cancer, chemotherapy or other thrombosis inducing disease). Physiological characteristics of these patients are chosen randomly with a normal distribution. The population is divided into four groups based on the daily intake dose of warfarin. The prescribed doses for each of the these groups are 0, 4, 6, 8 mg, respectively. The average values of the simulated variables for each group of patients are shown in Table 8.1.

Table 8.1: Baseline average characteristics of the virtual patients.

Characteristic	average ($\pm s.d.$)
Prothrombin (normalized)	0.69 ($\pm$0.09)
Factors IX and X (normalized)	0.69 ($\pm$0.09)
Antithrombin (normalized)	0.48 ($\pm$0.1)
Blood flow velocity ($\mu m/s$)	311 ($\pm$101)
Vessel diameter (mm)	7.47 ($\pm$0.39)

Depending on the part of the vessel cross section occupied by the clot (r), the patients are divided into four different categories depending on the observed regime of clot growth: (i) bleeding for $r < 0.5\%$, (ii) hemostasis for $0.5\% \leq r \leq 5\%$, (iii) partially occlusive thrombosis for $5\% < r < 100\%$, (iv) completely occlusive thrombosis for $r = 100\%$.

We compare the outputs of the two sub-models corresponding to the determination of the INR value and to the clot growth. For most patients, an INR value around 2.5 results in normal haemostatic response. Still, our modelling results suggest that blood flow velocity (related to venous pressure) should be considered in adjusting warfarin treatment as well as the level of antithrombin in plasma. Slow blood flow or low antithrombin concentration characterized the five patients that developed thrombosis among the fifty patients that presented an INR value targeted at 2.5. By contrast, nine of them developed bleeding. These patients all showed high blood flow velocities or high antithrombin levels. Interestingly, few normal hemostatic responses were observed for an INR below 2.0 or above 3.0. Overall, the majority of patients with an INR higher than 4.0 developed bleeding. This confirms the validity of our model as well as clinical indications for predicting the therapeutic range of INR. These clinical indications were adjusted for normal blood circulation and average antithrombin concentration in plasma.

Table 8.2: Average INR and clot vein percent occupied by the clot for the different groups of patients.

Population	INR	Percent of vessel occupied by the clot
Total ($n = 200$)	$2.36(\pm 1.16)$	$4\%(\pm 4\%)$
Group 1 ($n = 50$)	$1(\pm 0)$	$13.7\%(\pm 2.3\%)$
Group 2 ($n = 50$)	$1.72(\pm 0.009)$	$4.2\%(\pm 2.1\%))$
Group 3 ($n = 50$)	$2.54(\pm 0.03)$	$1.5\%(\pm 1.4\%)$
Group 4 ($n = 50$)	$4.14(\pm 0.09)$	$0.2\%(\pm 0.2\%)$

8.4 Discussion

The model developed in this work provides two ways of assessing warfarin action on blood clotting. In the injury-induced blood clotting model, we evaluated the patient response by simulating the percent of the vessel occupied by the clot after a potential vein injury. In the INR test model, we measured the INR level targeted by different treatment protocols. These two sub-models are connected by a PK-PD model describing vitamin-K dependent factors synthesis in the liver during warfarin treatment. Using mathematical investigation of simplified models, we obtained the exact patho-pysiological conditions of thrombosis and bleeding on vitamin-K dependent factors, blood flow and antithrombin. Then, we have described the dynamics of blood clotting during warfarin treatment. As a result, we have explained why bleeding and thrombosis persist even for appropriate INR values. In this context, there is a major distinction between the INR measurement model and the injury-induced blood clotting model. It is the absence of the effects of blood flow and direct thrombin inhibition by antithrombin in the first case. During *in vivo* blood clotting, blood flow plays an important role removing blood factors away from the injured zone and thus limiting clot growth. As a result, normal hemostasis is observed. The medical indications on the *in vitro* INR test were adjusted to correspond to normal levels of blood flow. Furthermore, antithrombin also plays an important role inactivating some of the coagulation factors. In this regard, the direct inhibition of thrombin by antithrombin is not considered in the prothrombin time measurements. Our results suggest that higher INR should be counterbalanced by low antithrombin levels or slow blood flow and vice versa.

The role of blood flow in thrombosis development is well known. It is mainly linked to haemostasis pathophysiology [317]. The clinical indications are only valid for average blood flow velocities as it was shown in our simulations. However, in case where blood flow is slow (usually $v_m < 100\mu m/s$), partially occlusive thrombosis was developed in some patients showing an INR close to 2.5. On the other hand, bleeding was also observed in patients with high blood flow or high antithrombin concentrations for the same INR range. This suggests that blood flow velocity should be considered in targeting the appropriate INR therapeutic range. We indicated the regions where each of the different regimes of clot growth will supposedly take place for individual patients in order to help choosing the appropriate INR value. We concluded that the clinical indications correspond exlusively to patients with normal blood circulation and antithrombin levels. Similar conclusions were highlighted in another work [74] using different models especially regarding the effect of blood flow: in both studies, we recommended that targeting an INR above 3.0 should be considered in case of slow blood circulation. The results presented in another comprehensive model [76] are in good agreement with our modelling especially those regarding the action warfarin on vitamin-K dependent synthesis.

Several assumptions were made when developing the model in order to be able study a complex system such as blood coagulation. While blood is known for its Non-Newtonian rheological properties, it was considered to be Newtonian flow in our model. This is a valid hypothesis because we do not consider blood cells. Next, the *in vivo* clot growth model is exclusively devoted to thrombus formation upon the rupture of endothelial tissues (extrinsic pathway). Other mechanisms of blood clotting initiation such as thrombin activation by contact with artificial surfaces or by ADP are not taken into consideration. To further simplify the study, we restrict the studied coagulation cascade to the most important proteins. This allowed us to interpret the obtained numerical results and to derive the simplified model. Finally,

venous walls were considered to be rigid and not deformable by the flow.

Although our model encompasses the main features of injury-induced blood clotting, it does not include platelets and their role in the coagulation process. Platelets increase the strength of the clot by aggregating and forming a plug [69, 70]. They detach when exposed to high shear stress and migrate with blood flow leading to embolisms. They may stimulate clot growth to a certain level. Still, they are affected by blood flow similarly to thrombin and the other factors. Hence, considering blood clotting without platelets is still valid for an initial approach. We will include the effect of platelets aggregation in a more complete model of coagulation in a forthcoming work and the study the action of combined anticoagulant and antiplatelet treatments. Another limitation of our model is the considered vitamin-K dependent factors. In order to use mathematical investigations, we assumed that warfarin only reduces the concentrations of factors IX, X and prothrombin. In reality, warfarin treatment down-regulates the synthesis of other factors such as protein C and S as well as factor VII. The reduction of the anti-coagulant proteins C and S in bloodstream is observed only the first three days of the treatment (hypercoagulation phase) [310]. Then, the reduction of procoagulant factors IX, X and prothrombin overshadows the decrease in the anticoagulant proteins. Lastly, in our model, the role of antithrombin was reduced to the direct inhibition of thrombin. In reality, antithrombin also inhibits factors of the initiation phase such as factors IX, X and XI [324]. We have studied the direct inhibition of thrombin by antithrombin since it is exclusively present in the real *in vivo* blood clotting and not considered in INR tests.

Our results not only explain the persistence of reccurent thrombosis and bleeding during warfarin treatment, but can also serve as a basis for individualized INR prediction. This methodology can be used by clinicians to adjust the administrated warfarin dose, especially for those with an embolic risk higher than 3. We suggest that the current test for INR should be accompagned with venous pressure as well as antithrombin measurements. Our computational models can be used then to predict the appropriate INR that should be targeted during warfarin therapy.

Chapter 9

Conclusions and Perspectives

9.1 Conclusions

This thesis is devoted to the mathematical modelling of blood coagulation and clot formation in normal and pathological conditions. The main results of this dissertation are as follows:

- We developed a novel mathematical model of blood coagulation encompassing the major components of this complex system. Then, we used this model in order to show the existence of different regimes of blood coagulation depending on the values of physical and physiological parameters. The complex model was reduced to an approximate one equation simplified sustaining mathematical investigation. The conditions of the regimes of blood coagulation were determined using numerical simulations and mathematical analysis. An approximate formula of the thrombin wave propagation speed was suggested based on purely analytical methods.

- A Navier-Stokes based model of blood flow was introduced to the previous model in order to capture the dynamics of clot growth in blood. The blood flow model incorporates a resistance term to the Navier-Stokes equation which describes the deceleration of flow as it goes through the thrombus. This term depends on the concentration of fibrin polymer and platelets in blood which represents the correlation between the clot permeability and these two parameters as observed in the experimental studies. The model was used to realistically simulate the dynamics of clot growth under blood flow with different shear rates. It was also used to determine the conditions of microvessel occlusion. The procoagulant effect of platelets in venous thrombosis was quantified by adding two equations for platelets in the flow and in thrombus to the previous model.

- The study of the regimes of blood coagulation and vessel occlusion has different applications particularly in the understanding of blood clotting disorders. Using the same models, it was possible to describe various clotting pathologies such as thrombosis incidence due to antithrombin deficiency and inflammation. The exact conditions where these disorders are observed were determined using numerical simulations and mathematical investigation of reduced models. The modelling was also used to quantify the action of blood coagulation factors (FII and ATIII) and inflammatory cytokines (IL-17 and TNF-α) on the formation of the clot.

- Bleeding is another disorder of the blood clotting system. Insufficient clot formation can lead to acute blood loss which provokes anemia. A previously developed multiscale model of erythropoiesis was extended to include the production of hemolgobin production by late erythroblasts. The model was used to simulate the recovery of the normal level of hemoglobin concentration and RBC count following the loss of 20% of blood. The model was able to reproduce the medical data and predict the recovery of the normal levels of hemoglobin within 10-14 days.

- A hybrid multiscale model of multiple myeloma and its treatment was proposed. The model describes the progression of MM and its intraclonal heterogeneity. The tumor growth dynamics

were simulated during chemotherapy to quantify the prothrombotic effects of MM treatment. Another proposed hybrid model focuses on the dynamics of HIV infection in the lymph node. The output of this model was used to predict the risk of thrombosis in HIV-infected patients.

- The action of anticoagulant drugs was quantified by incorporating PK-PD models of these treatments into the model of blood coagulation. The resulting model was used in order to determine the therapeutic window that should be targeted for individual patients. The model also explains the persistence of thrombi and bleedings in patients whose INR is within the therapeutic range. In the future, it can be used as a basis to develop more complicated software tools that predict the individual blood clotting responses.

9.2 Perspectives

The diversity of blood coagulation models developed in this thesis offers the opportunity to investigate other areas of research in the complex blood clotting system:

- The extension of the model of blood coagulation in order to include other key proteins such as TFPI and protein S, as well as other coagulation cascade activation mechanisms such as the contact pathway.
- The study of other important blood clotting abnormalities such as sepsis-associated thrombosis with more complex models in order to predict the risk of thrombosis during the progression of the disease.
- The association between thrombosis and cancer will be further investigated by quantifying the various effects of cancer on the coagulation process.
- Further advances in the systems pharmacology modelling of anticoagulant drugs. This time, clinical data will be used to develop realistic PK-PD models and to calibrate the existing ones. Ultimately, these models will help the clinicians to efficiently design clinical trials.
- The use of realistic patients characteristics such as the plasma composition as an input for the developed model. The models can be further calibrated and validated by comparing the predicted and the measured hemostatic responses.

We intend to study these questions in the forthcoming works.

9.2.1 coagIcoFoam: a three-dimensional numerical solver of thrombus formation in flow

In order to study the dynamics of clot formation in three dimensions, we develop a numerical solver of the exhaustive blood coagulation model in blood flow with the help of the OpenFOAM [325] open-source libraries. To obtain accurate results, we generate a fine structured mesh of a cylindrical domain using the open-source software SALOME [326] (Fig. 9.1). The outer layer of the mesh contains a rectangular zone where TF is exposed to bloodstream.

The program code solves the blood coagulation model presented in Chapter 3 using the finite volume method. An upwind difference scheme is used to discretize the convection terms. The laplacian terms were discretized using a linear scheme. The Navier-Stokes equations were solved using the PISO algorithm and the resistance term that represents the deceleration of flow in the porous clot is treated implicitly. Screenshots of the numerical simulations are shown in Fig. 9.2. The program code of the solver as well as a test case can be downloaded from the link: `https://github.com/MPS7/coagIcoFoam`. In the future, we will use the coagIcoFoam solver to investigate the genesis of blood clots in patient-specific domains such as aneurysms, chronic ischemic heart disease, and venous bifurcations.

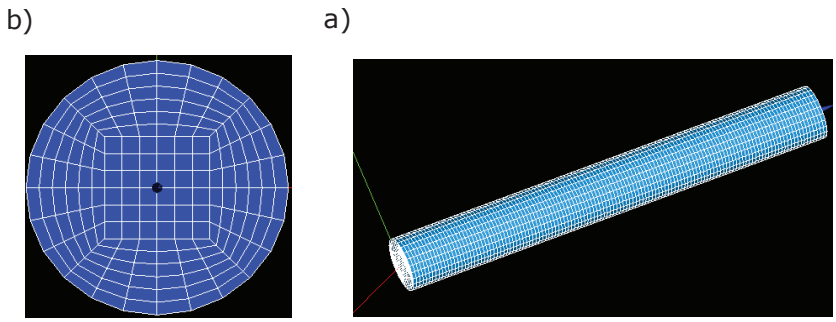

Figure 9.1: The computational mesh used to solve the coagIcoFoam numerical solver. a) A cross section view of the mesh, b) isometric view of the 3D mesh.

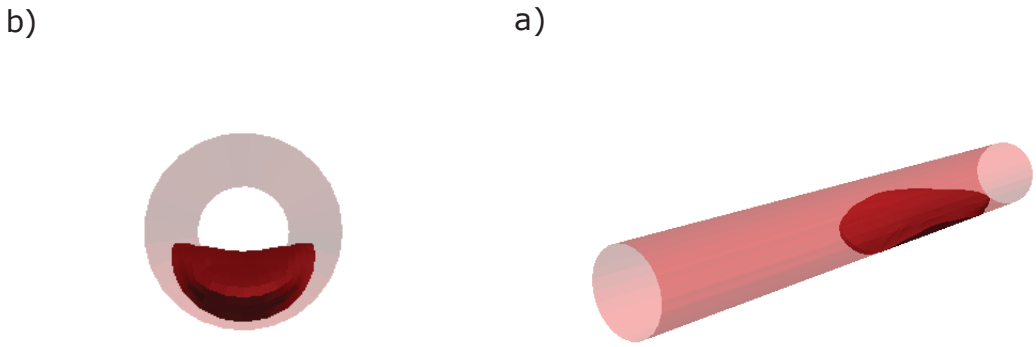

Figure 9.2: Screenshots of numerical simulations of clot formation under flow using coagIcoFoam. The clot is represented by an isovolume of fibrin polymer shown in red. a) A cross section view, b) an isometric view.

Bibliography

[1] Davie, E. W., & Ratnoff, O. D. (1964). Waterfall sequence for intrinsic blood clotting. Science, 145(3638), 1310-1312.

[2] Davie, E. W., Fujikawa, K., & Kisiel, W. (1991). The coagulation cascade: initiation, maintenance, and regulation. Biochemistry, 30(43), 10363-10370.

[3] Jesty, J., & Beltrami, E. (2005). Positive feedbacks of coagulation. Arteriosclerosis, thrombosis, and vascular biology, 25(12), 2463-2469.

[4] Hockin, M. F., Jones, K. C., Everse, S. J., & Mann, K. G. (2002). A model for the stoichiometric regulation of blood coagulation. Journal of Biological Chemistry, 277(21), 18322-18333.

[5] Luan, D., Zai, M., & Varner, J. D. (2007). Computationally derived points of fragility of a human cascade are consistent with current therapeutic strategies. PLoS Comput Biol, 3(7), e142.

[6] Bungay, S. D., Gentry, P. A., & Gentry, R. D. (2003). A mathematical model of lipid-mediated thrombin generation. Mathematical Medicine and Biology: A Journal of the IMA, 20(1).

[7] Brummel-Ziedins, K. E., Orfeo, T., Callas, P. W., Gissel, M., Mann, K. G., & Bovill, E. G. (2012). The prothrombotic phenotypes in familial protein C deficiency are differentiated by computational modeling of thrombin generation. PloS one, 7(9), e44378.

[8] Makin, J., Narayanan, S., & Ramamoorthi, R. (2008). Hybrid System Modeling of Human Blood Clotting. International Computer Science Institute Berkeley.

[9] Mitrophanov, A. Y., & Reifman, J. (2011). Kinetic modeling sheds light on the mode of action of recombinant factor VIIa on thrombin generation. Thrombosis research, 128(4), 381-390.

[10] Sagar, A., & Varner, J. D. (2015). Dynamic modeling of the human coagulation cascade using reduced order effective kinetic models. Processes, 3(1), 178-203.

[11] Sequeira, A., Santos, R. F., & Bodnár, T. (2011). Blood coagulation dynamics: mathematical modeling and stability results. Mathematical biosciences and engineering: MBE, 8(2), 425-443.

[12] Susree, A. M., & Anand, B. M. (2016). Reaction mechanisms and kinetic constants used in mechanistic models of coagulation and fibrinolysis. Mathematical Modelling of Natural Phenomena, 11(6), 71-90.

[13] Danforth, C. M., Orfeo, T., Everse, S. J., Mann, K. G., & Brummel-Ziedins, K. E. (2012). Defining the boundaries of normal thrombin generation: investigations into hemostasis. PloS one, 7(2), e30385.

[14] Lo, K., Denney, W. S., & Diamond, S. L. (2005). Stochastic modeling of blood coagulation initiation. Pathophysiology of haemostasis and thrombosis, 34(2-3), 80-90.

[15] Brotman, D. J., Deitcher, S. R., Lip, G. Y., & Matzdorff, A. C. (2004). Virchow's triad revisited. Southern medical journal, 97(2), 213-215.

[16] Brummel-Ziedins, K. E., Orfeo, T., Gissel, M., Mann, K. G., & Rosendaal, F. R. (2012). Factor Xa generation by computational modeling: an additional discriminator to thrombin generation evaluation. PloS one, 7(1), e29178.

[17] Bick, R. L. (2003). Cancer-associated thrombosis. New England Journal of Medicine, 349(2), 109-110.

[18] Rickles, F. R., & Falanga, A. (2001). Molecular basis for the relationship between thrombosis and cancer. Thrombosis research, 102(6), V215-V224.

[19] Lòpez, J. A., & Chen, J. (2009). Pathophysiology of venous thrombosis. Thrombosis research, 123, S30-S34.

[20] Haddad, T. C., & Greeno, E. W. (2006). Chemotherapy-induced thrombosis. Thrombosis research, 118(5), 555-568.

[21] Otten, H. M. M., Mathijssen, J., ten Cate, H., Soesan, M., Inghels, M., Richel, D. J., & Prins, M. H. (2004). Symptomatic venous thromboembolism in cancer patients treated with chemotherapy: an underestimated phenomenon. Archives of Internal Medicine, 164(2), 190-194.

[22] Clegg, L. E., & Mac Gabhann, F. (2015). Systems biology of the microvasculature. Integrative Biology, 7(5), 498-512.

[23] Lee, A., Tormoen, G. W., Kanso, E., McCarty, O., & Newton, P. K. (2012). Modeling and simulation of procoagulant circulating tumor cells in flow. Frontiers in oncology, 2, 108.

[24] Aksu, K., Donmez, A., & Keser, G. (2012). Inflammation-induced thrombosis: mechanisms, disease associations and management. Current pharmaceutical design, 18(11), 1478-1493.

[25] El Khatib, N., Génieys, S., Kazmierczak, B., & Volpert, V. (2012). Reaction–diffusion model of atherosclerosis development. Journal of mathematical biology, 65(2), 349-374.

[26] El Khatib, N., Genieys, S., & Volpert, V. (2007). Atherosclerosis initiation modeled as an inflammatory process. Mathematical Modelling of Natural Phenomena, 2(2), 126-141.

[27] Boujena, S., Kafi, O., & El Khatib, N. (2014). A 2D mathematical model of blood flow and its interactions in an atherosclerotic artery. Mathematical Modelling of Natural Phenomena, 9(6), 46-68.

[28] El Khatib, N., Génieys, S., Zine, A. M., & Volpert, V. (2009). Non-Newtonian effects in a fluid-structure interaction model for atherosclerosis. J. Tech. Phys, 1(50), 55-64.

[29] El Khatib, N., Génieys, S., Kazmierczak, B., & Volpert, V. (2009). Mathematical modelling of atherosclerosis as an inflammatory disease. Philosophical Transactions of the Royal Society of London A: Mathematical, Physical and Engineering Sciences, 367(1908), 4877-4886.

[30] Undas, A., Gissel, M., Kwasny-Krochin, B., Gluszko, P., Mann, K. G., & Brummel-Ziedins, K. E. (2010). Thrombin generation in rheumatoid arthritis: dependence on plasma factor composition. Thrombosis and haemostasis, 104(2), 224.

[31] Vodovotz, Y., Chow, C., Bartels, J., Lagoa, C., Kumar, R., Day, J., ... & Constantine, G. (2005, January). Mathematical simulations of sepsis and trauma. In Proceedings of the 11th Congress of the European Shock Society (pp. 151-159).

[32] Zuev, S. M., Kingsmore, S. F., & Gessler, D. D. (2006). Sepsis progression and outcome: a dynamical model. Theoretical Biology and Medical Modelling, 3(1), 8.

[33] Anand, M., Rajagopal, K., & Rajagopal, K. R. (2008). A model for the formation, growth, and lysis of clots in quiescent plasma. A comparison between the effects of antithrombin III deficiency and protein C deficiency. Journal of theoretical biology, 253(4), 725-738.

[34] Morel, O., Toti, F., Hugel, B., Bakouboula, B., Camoin-Jau, L., Dignat-George, F., & Freyssinet, J. M. (2006). Procoagulant microparticles. Arteriosclerosis, thrombosis, and vascular biology, 26(12), 2594-2604.

[35] Klein, S. K., Slim, E. J., De Kruif, M. D., Keller, T. T., Ten Cate, H., van Gorp, E. C., & Brandjes, D. P. (2005). Is chronic HIV infection associated with venous thrombotic disease? A systematic review. Neth J Med, 63(4), 129-136.

[36] A.A. Tokarev, Yu.V. Krasotkina, M.V. Ovanesov, M.A. Panteleev, M.A. Azhigirova, V.A. Volpert, F.I. Ataullakhanov, A.A. Butilin. Spatial dynamics of contact-activated fibrin clot formation in vitro and in silico in haemophilia B: effects of severity and Ahemphil B treatment. Math. Model. Nat. Phenom., 1 (2006), No. 2, 124-137.

[37] Baskurt, O. K., & Meiselman, H. J. (2003). Blood rheology and hemodynamics. In Seminars in thrombosis and hemostasis (Vol. 29, No. 05, pp. 435-450).

[38] Peyrou, V., Lormeau, J. C., Herault, J. P., Gaich, C., Pfliegger, A. M., & Herbert, J. M. (1999). Contribution of erythrocytes to thrombin generation in whole blood. Thrombosis and haemostasis, 81(3), 400-406.

[39] Macey, M. G., Wolf, S. I., Wheeler-Jones, C. P., & Lawson, C. (2009). Expression of blood coagulation factors on monocytes after exposure to TNF-treated endothelium in a novel whole blood model of arterial flow. Journal of immunological methods, 350(1), 133-141.

[40] Ku, D. N. (1997). Blood flow in arteries. Annual Review of Fluid Mechanics, 29(1), 399-434.

[41] Wootton, D. M., & Ku, D. N. (1999). Fluid mechanics of vascular systems, diseases, and thrombosis. Annual review of biomedical engineering, 1(1), 299-329.

[42] Bessonov, N., Sequeira, A., Simakov, S., Vassilevskii, Y., & Volpert, V. (2016). Methods of blood flow modelling. Mathematical Modelling of Natural Phenomena, 11(1), 1-25.

[43] Crowley, T. A., & Pizziconi, V. (2005). Isolation of plasma from whole blood using planar microfilters for lab-on-a-chip applications. Lab on a Chip, 5(9), 922-929.

[44] Einstein, A. (1911). Berichtigung zu meiner Arbeit:„Eine neue Bestimmung der Molek´uldimensionen". Annalen der Physik, 339(3), 591-592.

[45] Lee, S. W., & Steinman, D. A. (2007). On the relative importance of rheology for image-based CFD models of the carotid bifurcation. Journal of biomechanical engineering, 129(2), 273-278.

[46] Phillips, R. J., Armstrong, R. C., Brown, R. A., Graham, A. L., & Abbott, J. R. (1992). A constitutive equation for concentrated suspensions that accounts for shear-induced particle migration. Physics of Fluids A: Fluid Dynamics, 4(1), 30-40.

[47] Johnston, B. M., Johnston, P. R., Corney, S., & Kilpatrick, D. (2004). Non-Newtonian blood flow in human right coronary arteries: steady state simulations. Journal of biomechanics, 37(5), 709-720.

[48] Malkin, A. I. (1994). Rheology fundamentals. ChemTec Publishing.

[49] Rao, A. (2010). Rheology of fluid and semisolid foods: principles and applications. Springer Science & Business Media.

[50] Liu, Y. (2012). A lattice Boltzmann model for blood flows. Applied Mathematical Modelling, 36(7), 2890-2899.

[51] Qin, Y., Wu, J., Hu, Q., Ghista, D. N., & Wong, K. K. (2017). Computational evaluation of smoothed particle hydrodynamics for implementing blood flow modelling through CT reconstructed arteries. Journal of X-ray Science and Technology, (Preprint), 1-20.

[52] Bessonov, N., Babushkina, E., Golovashchenko, S. F., Tosenberger, A., Ataullakhanov, F., Panteleev, M., ... & Volpert, V. (2014). Numerical modelling of cell distribution in blood flow. Mathematical Modelling of Natural Phenomena, 9(6), 69-84.nt.

[53] Begent, N., & Born, G. V. R. (1970). Growth rate in vivo of platelet thrombi, produced by iontophoresis of ADP, as a function of mean blood flow velocity. Nature, 227(5261), 926-930.

[54] Brotman, D. J., Deitcher, S. R., Lip, G. Y., & Matzdorff, A. C. (2004). Virchow's triad revisited. Southern medical journal, 97(2), 213-215.

[55] Closse, C., Seigneur, M., Renard, M., Pruvost, A., Dumain, P., Belloc, F., & Boisseau, M. R. (1996). Influence of hypoxia and hypoxia-reoxygenation on endothelial P-selectin expression. Pathophysiology of Haemostasis and Thrombosis, 26(Suppl. 4), 177-181.

[56] Wufsus, A. R., Macera, N. E., & Neeves, K. B. (2013). The hydraulic permeability of blood clots as a function of fibrin and platelet density. Biophysical journal, 104(8), 1812-1823.

[57] Kuharsky, A. L., & Fogelson, A. L. (2001). Surface-mediated control of blood coagulation: the role of binding site densities and platelet deposition. Biophysical journal, 80(3), 1050-1074.

[58] Fogelson, A. L., Hussain, Y. H., & Leiderman, K. (2012). Blood clot formation under flow: the importance of factor XI depends strongly on platelet count. Biophysical journal, 102(1), 10-18.

[59] Haynes, L. M., Dubief, Y. C., & Mann, K. G. (2012). Membrane binding events in the initiation and propagation phases of tissue factor-initiated zymogen activation under flow. Journal of Biological Chemistry, 287(8), 5225-5234.

[60] Jordan, S. W., & Chaikof, E. L. (2011). Simulated surface-induced thrombin generation in a flow field. Biophysical journal, 101(2), 276-286.

[61] Bodnár, T., & Sequeira, A. (2008). Numerical simulation of the coagulation dynamics of blood. Computational and Mathematical Methods in Medicine, 9(2), 83-104.

[62] Sequeira, A., & Bodnár, T. (2014). Blood coagulation simulations using a viscoelastic model. Mathematical Modelling of Natural Phenomena, 9(6), 34-45.

[63] Storti, F., & Vosse, F. N. (2014). A continuum model for platelet plug formation, growth and deformation. International journal for numerical methods in biomedical engineering, 30(12), 1541-1557.

[64] Leiderman, K., & Fogelson, A. L. (2011). Grow with the flow: a spatial–temporal model of platelet deposition and blood coagulation under flow. Mathematical Medicine and Biology, 28(1), 47-84.

[65] Govindarajan, V., Rakesh, V., Reifman, J., & Mitrophanov, A. Y. (2016). Computational study of thrombus formation and clotting factor effects under venous flow conditions. Biophysical journal, 110(8), 1869-1885.

[66] Fogelson, A. L., & Guy, R. D. (2008). Immersed-boundary-type models of intravascular platelet aggregation. Computer methods in applied mechanics and engineering, 197(25), 2087-2104.

[67] Xu Z, Christley S, Lioi J, Kim O, Harvey C, Sun W, Alber M. Multiscale model of fibrin accumulation on the blood clot surface and platelet dynamics. *Methods Cell Biol* 2012; **110**:367-388.

[68] Yazdani, A., Li, H., Humphrey, J. D., & Karniadakis, G. E. (2017). A General Shear-Dependent Model for Thrombus Formation. PLoS computational biology, 13(1), e1005291.

[69] Tosenberger, A., Ataullakhanov, F., Bessonov, N., Panteleev, M., Tokarev, A., & Volpert, V. (2013). Modelling of thrombus growth in flow with a DPD-PDE method. Journal of theoretical biology, 337, 30-41.

[70] Tosenberger, A., Ataullakhanov, F., Bessonov, N., Panteleev, M., Tokarev, A., & Volpert, V. (2016). Modelling of platelet–fibrin clot formation in flow with a DPD–PDE method. Journal of mathematical biology, 72(3), 649-681.

[71] Brummel-Ziedins, K. (2013). Models for thrombin generation and risk of disease. Journal of Thrombosis and Haemostasis, 11(s1), 212-223.

[72] Brummel-Ziedins, K. E., Vossen, C. Y., Butenas, S., Mann, K. G., & Rosendaal, F. R. (2005). Thrombin generation profiles in deep venous thrombosis. Journal of Thrombosis and Haemostasis, 3(11), 2497-2505.

[73] Dahlbäck, B. (2000). Blood coagulation. The Lancet, 355(9215), 1627-1632.

[74] de Pillis, L., Graham, E. J., Hood, K., Ma, Y., Radunskaya, A., & Simons, J. (2015). Injury-initiated clot formation under flow: a mathematical model with warfarin treatment. Applications of Dynamical Systems in Biology and Medicine, 75-98.

[75] Dydek, E. V., & Chaikof, E. L. (2016). Simulated thrombin generation in the presence of surface-bound heparin and circulating tissue factor. Annals of biomedical engineering, 44(4), 1072-1084.

[76] Wajima, T., Isbister, G. K., & Duffull, S. B. (2009). A comprehensive model for the humoral coagulation network in humans. Clinical Pharmacology & Therapeutics, 86(3), 290-298.

[77] Burghaus, R., Coboeken, K., Gaub, T., Kuepfer, L., Sensse, A., Siegmund, H. U., ... & Lippert, J. (2011). Evaluation of the efficacy and safety of rivaroxaban using a computer model for blood coagulation. PLoS One, 6(4), e17626.

[78] Zhou, X., Huntjens, D. R. H., & Gilissen, R. A. H. J. (2015). A systems pharmacology model for predicting effects of factor Xa inhibitors in healthy subjects: assessment of pharmacokinetics and binding kinetics. CPT: pharmacometrics & systems pharmacology, 4(11), 650-659.

[79] Gribkova, I. V., Lipets, E. N., Rekhtina, I. G., Bernakevich, A. I., Ayusheev, D. B., Ovsepyan, R. A., ... & Sinauridze, E. I. (2016). The modification of the thrombin generation test for the clinical assessment of dabigatran etexilate efficiency. Scientific reports, 6.

[80] Cromme, L., Völler, H., Gäbler, F., Salzwedel, A., & Taborski, U. (2010). Computer-aided dosage in oral anticoagulation therapy using phenprocoumon. Hämostaseologie, 30(4), 183-189.

[81] Gulati, A., Isbister, G. K., & Duffull, S. B. (2014). Scale reduction of a systems coagulation model with an application to modeling pharmacokinetic–pharmacodynamic data. CPT: pharmacometrics & systems pharmacology, 3(1), 1-8.

[82] D. Luan. Computational modeling and simulation of thrombus formation. Doctoral dissertation, Cornell University, 2009.

[83] Lynd, L. D., & O'Brien, B. J. (2004). Advances in risk-benefit evaluation using probabilistic simulation methods: an application to the prophylaxis of deep vein thrombosis. Journal of clinical epidemiology, 57(8), 795-803.

[84] Parunov, L. A., Fadeeva, O. A., Balandina, A. N., Soshitova, N. P., Kopylov, K. G., Kumskova, M. A., ... & Panteleev, M. A. (2011). Improvement of spatial fibrin formation by the anti-TFPI aptamer BAX499: changing clot size by targeting extrinsic pathway initiation. Journal of Thrombosis and Haemostasis, 9(9), 1825-1834.

[85] Eymard, N., Bessonov, N., Gandrillon, O., Koury, M. J., & Volpert, V. (2015). The role of spatial organization of cells in erythropoiesis. Journal of mathematical biology, 70(1-2), 71-97.

[86] Hoffman, M. (2003). Remodeling the blood coagulation cascade. Journal of thrombosis and thrombolysis, 16(1), 17-20.

[87] Weitz, J. I., Hudoba, M., Massel, D., Maraganore, J., & Hirsh, J. (1990). Clot-bound thrombin is protected from inhibition by heparin-antithrombin III but is susceptible to inactivation by antithrombin III-independent inhibitors. Journal of Clinical Investigation, 86(2), 385.

[88] Mann, K. G., Van't Veer, C., Cawthern, K., & Butenas, S. (1998). The role of the tissue factor pathway in initiation of coagulation. Blood coagulation & fibrinolysis: an international journal in haemostasis and thrombosis, 9, S3-7.

[89] Esmon, C. T. (1989). The roles of protein C and thrombomodulin in the regulation of blood coagulation. J Biol Chem, 264(9), 4743-4746.

[90] Pogorelova, E. A., & Lobanov, A. I. (2014). Influence of enzymatic reactions on blood coagulation autowave. Biophysics, 59(1), 110.

[91] Butenas, S., & Mann, K. G. (2002). Blood coagulation. Biochemistry (Moscow), 67(1), 3-12.

[92] Orfeo, T., Butenas, S., Brummel-Ziedins, K. E., & Mann, K. G. (2005). The tissue factor requirement in blood coagulation. Journal of Biological Chemistry, 280(52), 42887-42896.

[93] Orfeo, T., Brummel-Ziedins, K. E., Gissel, M., Butenas, S., & Mann, K. G. (2008). The nature of the stable blood clot procoagulant activities. Journal of Biological Chemistry, 283(15), 9776-9786.

[94] Gailani, D., & Broze Jr, G. J. (1991). Factor XI activation in a revised model of blood coagulation. Science, 253(5022), 909-912.

[95] Panteleev, M. A., Ovanesov, M. V., Kireev, D. A., Shibeko, A. M., Sinauridze, E. I., Ananyeva, N. M., ... & Ataullakhanov, F. I. (2006). Spatial propagation and localization of blood coagulation are regulated by intrinsic and protein C pathways, respectively. Biophysical Journal, 90(5), 1489-1500.

[96] Monković, D. D., & Tracy, P. B. (1990). Functional characterization of human platelet-released factor V and its activation by factor Xa and thrombin. Journal of Biological Chemistry, 265(28), 17132-17140.

[97] Butenas, S., Orfeo, T., Gissel, M. T., Brummel, K. E., & Mann, K. G. (2004). The significance of circulating factor IXa in blood. Journal of Biological Chemistry, 279(22), 22875-22882.

[98] Baugh, R. J., & Krishnaswamy, S. (1996). Role of the activation peptide domain in human factor X activation by the extrinsic Xase complex. Journal of Biological Chemistry, 271(27), 16126-16134.

[99] Scandura, J. M., & Walsh, P. N. (1996). Factor X bound to the surface of activated human platelets is preferentially activated by platelet-bound factor IXa. Biochemistry, 35(27), 8903-8913.

[100] Zarnitsina, V. I., Pokhilko, A. V., & Ataullakhanov, F. I. (1996). A mathematical model for the spatio-temporal dynamics of intrinsic pathway of blood coagulation. II. Results. Thrombosis research, 84(5), 333-344.

[101] Lobanov, A. I., & Starozhilova, T. K. (2005). The effect of convective flows on blood coagulation processes. Pathophysiology of haemostasis and thrombosis, 34(2-3), 121-134.

[102] Pogorelova, E. A., & Lobanov, A. I. (2014). Influence of enzymatic reactions on blood coagulation autowave. Biophysics, 59(1), 110.

[103] Zarnitsina, V. I., Pokhilko, A. V., & Ataullakhanov, F. I. (1996). A mathematical model for the spatio-temporal dynamics of intrinsic pathway of blood coagulation. II. Results. Thrombosis research, 84(5), 333-344.

[104] Han, Q., & Lin, F. (2011). Elliptic partial differential equations (Vol. 1). American Mathematical Soc.

[105] Volpert, A. I., Volpert, V. A., & Volpert, V. A. (1994). Traveling wave solutions of parabolic systems (Vol. 140). American Mathematical Soc..

[106] Krishnaswamy, S. (2013). The transition of prothrombin to thrombin. Journal of Thrombosis and Haemostasis, 11(s1), 265-276.

[107] Zeldovich, Ya. B., & Frank-Kamenetskii, D. A. (1938). A theory of thermal propagation of flame. Acta Physicochim. USSR. 9, 341-350.

[108] Ovanesov, M V and Lopatina, E G and Saenko, E L and Ananyeva, N M and Ul'yanova, L I and Plyushch, O P and Butilin, A A, & Ataullakhanov, F I. (2003). Effect of factor VIII on tissue factor-initiated spatial clot growth. 2, 235-242.

[109] Ovanesov, M. V., Krasotkina, J. V., Ul'yanova, L. I., Abushinova, K. V., Plyushch, O. P., Domogatskii, S. P., ... & Ataullakhanov, F. I. (2002). Hemophilia A and B are associated with abnormal spatial dynamics of clot growth. Biochimica et Biophysica Acta (BBA)-General Subjects, 1572(1), 45-57.

[110] Dashkevich, N. M., Ovanesov, M. V., Balandina, A. N., Karamzin, S. S., Shestakov, P. I., Soshitova, N. P., ... & Ataullakhanov, F. I. (2012). Thrombin activity propagates in space during blood coagulation as an excitation wave. Biophysical journal, 103(10), 2233-2240.

[111] Ragni, M. V., Sinha, D., Seaman, F., Lewis, J. H., Spero, J. A., & Walsh, P. N. (1985). Comparison of bleeding tendency, factor XI coagulant activity, and factor XI antigen in 25 factor XI-deficient kindreds. Blood, 65(3), 719-724.

[112] Bolton-Maggs, P. H. B., Wan-Yin, B. Y., McCraw, A. H., Slack, J., & Kernoff, P. B. A. (1988). Inheritance and bleeding in factor XI deficiency. British journal of haematology, 69(4), 521-528.

[113] Berliner, J. I., Rybicki, A. C., Kaplan, R. C., Monrad, E. S., Freeman, R., & Billett, H. H. (2002). Elevated levels of Factor XI are associated with cardiovascular disease in women. Thrombosis research, 107(1), 55-60.

[114] Meijers, J. C., Tekelenburg, W. L., Bouma, B. N., Bertina, R. M., & Rosendaal, F. R. (2000). High levels of coagulation factor XI as a risk factor for venous thrombosis. New England Journal of Medicine, 342(10), 696-701.

[115] Volpert, V. (2014). Elliptic Partial Differential Equations: Volume 2: Reaction-Diffusion Equations (Vol. 104). Springer.

[116] Volpert, A. I., Volpert, V. A., & Volpert, V. A. (1994). Traveling wave solutions of parabolic systems (Vol. 140). American Mathematical Soc..

[117] Tokarev A, Sirakov I, Panasenko G, Volpert V, Shnol E, Butylin A, Ataullakhanov F. Continuous mathematical model of platelet thrombus formation in blood flow. *Russian Journal of Numerical Analysis and Mathematical Modelling* 2012; **27**(2),191-212.

[118] Bodnár T, Sequeira A, Prosi M. On the shear-thinning and viscoelastic effects of blood flow under various flow rates. *Applied Mathematics and Computation* 2011; **217**(11):5055-5067.

[119] Fogelson A L, Guy R D. Immersed-boundary-type models of intravascular platelet aggregation. *Computer methods in applied mechanics and engineering* 2008; **197**(25):2087-2104.

[120] Mehrabadi M. Effects of red blood cells and shear rate on thrombus growth (doctoral dissertation). 2014.

[121] Bouchnita A, Tosenberger A, Volpert V. On the regimes of blood coagulation. *Applied Mathematics Letters* 2016; **51**:74-79.

[122] Neeves K B, Onasoga A A, Wufsus A R. The use of microfluidics in hemostasis: clinical diagnostics and biomimetic models of vascular injury. *Current opinion in hematology 2013*; **20**(5): 417-423.

[123] Chorin A J. Numerical solution of the Navier-Stokes equations. *Mathematics of computation* 1968; **22**(104):745-762.

[124] Vol'pert A I, Volpert V A, Volpert V A. *Traveling wave solutions of parabolic systems* (Vol. 140). American Mathematical Soc. 1994.

[125] Beavers G S, Joseph D D. Boundary conditions at a naturally permeable wall. *Journal of fluid mechanics* 1967; **30**(01):197-207.

[126] Baumgartner H R (1973). The role of blood flow in platelet adhesion, fibrin deposition, and formation of mural thrombi. *Microvascular research* 1973; **5**(2):167-179.

[127] Falati S, Gross P, Merrill-Skoloff G, Furie B C, Furie B. Real-time in vivo imaging of platelets, tissue factor and fibrin during arterial thrombus formation in the mouse. *Nature medicine* 2002; **8**(10):1175-1180.

[128] Strang G. *Computational Science and Engineering, First Edition.* Wellesley Cambridge 2007. Press.

[129] Dashkevich N M, Ovanesov M V, Balandina A N, Karamzin S S, Shestakov P I, Soshitova N P, Tokarev A A, Panteleev M A, Ataullakhanov F I. Thrombin activity propagates in space during blood coagulation as an excitation wave. *Biophysical journal* 2012 **103**(10): 2233-2240.

[130] Gulati G, Hevelow M, George M, Behling E, Siegel J. International normalized ratio versus plasma levels of coagulation factors in patients on vitamin K antagonist therapy. *Archives of pathology & laboratory medicine* 2011 **135**(4) : 490-494.

[131] Rosenberg, R. D., & Damus, P. S. (1973). The purification and mechanism of action of human antithrombin-heparin cofactor. Journal of Biological Chemistry, 248(18), 6490-6505.

[132] Quinsey, N. S., Greedy, A. L., Bottomley, S. P., Whisstock, J. C., & Pike, R. N. (2004). Antithrombin: in control of coagulation. The international journal of biochemistry & cell biology, 36(3), 386-389.

[133] Pieters, J. and Willems, G. and Hemker, H. C. & Lindhout, T. (1988). Inhibition of Factor Xa and Factor X , by Antithrombin III / Heparin during Factor X Activation.The Journal of biological chemistry. 263(30). 15313-15318.

[134] Zarnitsina, V. I., Ataullakhanov, F. I., Lobanov, A. I., & Morozova, O. L. (2001). Dynamics of spatially nonuniform patterning in the model of blood coagulation. Chaos: An Interdisciplinary Journal of Nonlinear Science, 11(1), 57-70.

[135] Souter, P. J., Thomas, S., Hubbard, A. R., Poole, S., Römisch, J., & Gray, E. (2001). Antithrombin inhibits lipopolysaccharide-induced tissue factor and interleukin-6 production by mononuclear cells, human umbilical vein endothelial cells, and whole blood. Critical care medicine, 29(1), 134-139.

[136] Ilyashenko, V. M., Solovyov, S. E., & Pojman, J. A. (1995). Theoretical aspects of self-propagating reaction fronts in condensed medium. AIChE Journal, 41(12), 2631-2636.

[137] Aviña-Zubieta, J. A., Choi, H. K., Sadatsafavi, M., Etminan, M., Esdaile, J. M., & Lacaille, D. (2008). Risk of cardiovascular mortality in patients with rheumatoid arthritis: A meta-analysis of observational studies. Arthritis Care & Research, 59(12), 1690-1697.

[138] van Leuven, S. I., Franssen, R., Kastelein, J. J., Levi, M., Stroes, E. S., & Tak, P. P. (2007). Systemic inflammation as a risk factor for atherothrombosis. Rheumatology, 47(1), 3-7.

[139] Hannawi, S., Haluska, B., Marwick, T. H., & Thomas, R. (2007). Atherosclerotic disease is increased in recent-onset rheumatoid arthritis: a critical role for inflammation. Arthritis research & therapy, 9(6), R116.

[140] Ku, I.A, Imboden, J.B., Hsue, P.Y., & Ganz, P. (2009). Rheumatoid arthritis: model of systemic inflammation driving atherosclerosis. Circ J, 73, 977-985.

[141] Wolfe, F., Freundlich, B., & Straus, W. L. (2003). Increase in cardiovascular and cerebrovascular disease prevalence in rheumatoid arthritis. The Journal of rheumatology, 30(1), 36-40.

[142] Hot, A., Lavocat, F., Lenief, V., & Miossec, P. (2012). Simvastatin inhibits the pro-inflammatory and pro-thrombotic effects of IL-17 and TNF-α on endothelial cells. Annals of the rheumatic diseases, annrheumdis-2012.

[143] Hot, A., Lenief, V., & Miossec, P. (2012). Combination of IL-17 and TNFα induces a pro-inflammatory, pro-coagulant and pro- thrombotic phenotype in human endothelial cells. Annals of the rheumatic diseases, annrheumdis-2011.

[144] Marder, W., Khalatbari, S., Myles, J. D., Hench, R., Yalavarthi, S., Lustig, S., ... & Kaplan, M. J. (2011). Interleukin 17 as a novel predictor of vascular function in rheumatoid arthritis. Annals of the rheumatic diseases, 70(9), 1550-1555.

[145] Smith, E., Prasad, K. M. R., Butcher, M., Dobrian, A., Kolls, J. K., Ley, K., & Galkina, E. (2010). Blockade of interleukin-17A results in reduced atherosclerosis in apolipoprotein E–deficient mice. Circulation, 121(15), 1746-1755.

[146] Hashmi, S., & Zeng, Q. T. (2006). Role of interleukin-17 and interleukin-17-induced cytokines interleukin-6 and interleukin-8 in unstable coronary artery disease. Coronary artery disease, 17(8), 699-706.

[147] Anand, M., Rajagopal, K., & Rajagopal, K. R. (2005). A model for the formation and lysis of blood clots. Pathophysiology of haemostasis and thrombosis, 34(2-3), 109-120.

[148] Fogelson, A. L., & Tania, N. (2005). Coagulation under flow: the influence of flow-mediated transport on the initiation and inhibition of coagulation. Pathophysiology of haemostasis and thrombosis, 34(2-3), 91-108.

[149] Harrison, S. E., Bernsdorf, J., Hose, D. R., & Lawford, P. V. (2008). A lattice Boltzmann framework for simulation of thrombogenesis. Progress in Computational Fluid Dynamics, an International Journal, 8(1-4), 121-128.

[150] Stortelder, W., Hemker, P. W., & Hemker, H. C. (1997). Mathematical modelling in blood coagulation; simulation and parameter estimation. Report-Modelling, analysis and simulation, (20), 1-11.

[151] Filipovic, N., Kojic, M., & Tsuda, A. (2008). Modelling thrombosis using dissipative particle dynamics method. Philosophical Transactions of the Royal Society of London A: Mathematical, Physical and Engineering Sciences, 366(1879), 3265-3279.

[152] Galdi, G. P., Rannacher, R., Robertson, A. M., & Turek, S. (2008). Hemodynamical flows. Delhi Book Store.

[153] Shen, F., Kastrup, C. J., Liu, Y., & Ismagilov, R. F. (2008). Threshold response of initiation of blood coagulation by tissue factor in patterned microfluidic capillaries is controlled by shear rate. Arteriosclerosis, thrombosis, and vascular biology, 28(11), 2035-2041.

[154] Belyaev, A. V., Panteleev, M. A., & Ataullakhanov, F. I. (2015). Threshold of microvascular occlusion: injury size defines the thrombosis scenario. Biophysical journal, 109(2), 450-456.Threshold of microvascular occlusion: injury size defines

[155] A. Tosenberger, N. Bessonov, V. Volpert. Influence of fibrinogen deficiency on clot formation in flow by hybrid model. Mathematical Modelling of Natural Phenomena 10.1 (2015) 36-47.

[156] Papayannopoulou, T., Abkowitz, J., D'andrea, A., & Migliaccio, A. R. (2000). Biology of erythropoiesis, erythroid differentiation, and maturation. Hematology: Basic principles and practice, 5.

[157] Chasis, J. A., & Mohandas, N. (2008). Erythroblastic islands: niches for erythropoiesis. Blood, 112(3), 470-478.

[158] Eaves, C. J., Humphries, R. K., & Eaves, A. C. (1979). In vitro characterization of erythroid precursor cells and the erythropoietic differentiation process. Cellular and Molecular Regulation of Hemoglobin Switching, 251.

[159] Nijhof, W., & Wierenga, P. K. (1983). Isolation and characterization of the erythroid progenitor cell: CFU-E. The Journal of cell biology, 96(2), 386-392.

[160] Sawada, K., Krantz, S. B., Kans, J. S., Dessypris, E. N., Sawyer, S., Glick, A. D., & Civin, C. I. (1987). Purification of human erythroid colony-forming units and demonstration of specific binding of erythropoietin. Journal of Clinical Investigation, 80(2), 357.

[161] Socolovsky, M., Nam, H. S., Fleming, M. D., Haase, V. H., Brugnara, C., & Lodish, H. F. (2001). Ineffective erythropoiesis in Stat5a-/- 5b-/- mice due to decreased survival of early erythroblasts. Blood, 98(12), 3261-3273.

[162] Chen, K., Liu, J., Heck, S., Chasis, J. A., An, X., & Mohandas, N. (2009). Resolving the distinct stages in erythroid differentiation based on dynamic changes in membrane protein expression during erythropoiesis. Proceedings of the National Academy of Sciences, 106(41), 17413-17418.

[163] Hu, J., Liu, J., Xue, F., Halverson, G., Reid, M., Guo, A., ... & Lane, J. (2013). Isolation and functional characterization of human erythroblasts at distinct stages: implications for understanding of normal and disordered erythropoiesis in vivo. Blood, 121(16), 3246-3253.

[164] De Maria, R., Testa, U., Luchetti, L., Zeuner, A., Stassi, G., Pelosi, E., ... & Peschle, C. (1999). Apoptotic role of Fas/Fas ligand system in the regulation of erythropoiesis. Blood, 93(3), 796-803.

[165] Liu, Y., Pop, R., Sadegh, C., Brugnara, C., Haase, V. H., & Socolovsky, M. (2006). Suppression of Fas-FasL coexpression by erythropoietin mediates erythroblast expansion during the erythropoietic stress response in vivo. Blood, 108(1), 123-133.

[166] Dai, C. H., Krantz, S. B., & Zsebo, K. M. (1991). Human burst-forming units-erythroid need direct interaction with stem cell factor for further development. Blood, 78(10), 2493-2497.

[167] Koury, M. J., & Bondurant, M. C. (1990). Erythropoietin retards DNA breakdown and prevents programmed death in erythroid progenitor cells. Science, 248(4953), 378-382.

[168] Wu, H., Liu, X., Jaenisch, R., & Lodish, H. F. (1995). Generation of committed erythroid BFU-E and CFU-E progenitors does not require erythropoietin or the erythropoietin receptor. Cell, 83(1), 59-67.

[169] Koury, M. J. (2005). Erythropoietin: the story of hypoxia and a finely regulated hematopoietic hormone. Experimental hematology, 33(11), 1263-1270.

[170] Gregory, T., Yu, C., Ma, A., Orkin, S. H., Blobel, G. A., & Weiss, M. J. (1999). GATA-1 and erythropoietin cooperate to promote erythroid cell survival by regulating bcl-x L expression. Blood, 94(1), 87-96.

[171] Xiang, J., Wu, D. C., Chen, Y., & Paulson, R. F. (2015). In vitro culture of stress erythroid progenitors identifies distinct progenitor populations and analogous human progenitors. Blood, 125(11), 1803-1812.

[172] Cantor, A. B., & Orkin, S. H. (2002). Transcriptional regulation of erythropoiesis: an a air involving multiple partners. Oncogene, 21, 3368-3376.6.

[173] Koury, M. J., & Haase, V. H. (2015). Anaemia in kidney disease: harnessing hypoxia responses for therapy. Nature Reviews Nephrology, 11(7), 394-410.

[174] Ponka, P., Koury, M. J., & Sheftel, A. D. (2013). Erythropoiesis, hemoglobin synthesis, and erythroid mitochondrial iron homeostasis. Handbook of Porphyrin Science: erythropoiesis, Heme, and Applications to Biomedicine, 27, 41-84.

[175] Ghosh, M. C., Zhang, D. L., Jeong, S. Y., Kovtunovych, G., Ollivierre-Wilson, H., Noguchi, A., ... & Tong, W. H. (2013). Deletion of iron regulatory protein 1 causes polycythemia and pulmonary hypertension in mice through translational derepression of HIF2α. Cell metabolism, 17(2), 271-281.

[176] Anderson, S. A., Nizzi, C. P., Chang, Y. I., Deck, K. M., Schmidt, P. J., Galy, B., ... & Fleming, M. D. (2013). The IRP1-HIF-2α axis coordinates iron and oxygen sensing with erythropoiesis and iron absorption. Cell metabolism, 17(2), 282-290.

[177] Wilkinson, N., & Pantopoulos, K. (2013). IRP1 regulates erythropoiesis and systemic iron homeostasis by controlling HIF2α mRNA translation. Blood, 122(9), 1658-1668.

[178] Nai, A., Lidonnici, M. R., Rausa, M., Mandelli, G., Pagani, A., Silvestri, L., ... & Camaschella, C. (2015). The second transferrin receptor regulates red blood cell production in mice. Blood, 125(7), 1170-1179.

[179] Cianetti, L., Gabbianelli, M., & Sposi, N. M. (2010). Ferroportin and erythroid cells: an update. Advances in hematology, 2010.

[180] Sun, J., Brand, M., Zenke, Y., Tashiro, S., Groudine, M., & Igarashi, K. (2004). Heme regulates the dynamic exchange of Bach1 and NF-E2-related factors in the Maf transcription factor network. Proceedings of the National Academy of Sciences of the United States of America, 101(6), 1461-1466.

[181] Chen, J. J. (2007). Regulation of protein synthesis by the heme-regulated eIF2α kinase: relevance to anemias. Blood, 109(7), 2693-2699.

[182] Quigley, J. G., Yang, Z., Worthington, M. T., Phillips, J. D., Sabo, K. M., Sabath, D. E., ... & Abkowitz, J. L. (2004). Identification of a human heme exporter that is essential for erythropoiesis. Cell, 118(6), 757-766.

[183] Fleming, M. D., & Hamza, I. (2012). Mitochondrial heme: an exit strategy at last. The Journal of clinical investigation, 122(12), 4328.

[184] Mollan, T. L., Yu, X., Weiss, M. J., & Olson, J. S. (2010). The role of alpha-hemoglobin stabilizing protein in redox chemistry, denaturation, and hemoglobin assembly. Antioxidants & redox signaling, 12(2), 219-231.

[185] Vidal, M. (2010). Exosomes in erythropoiesis. Transfusion clinique et biologique, 17(3), 131-137.

[186] Willekens, F. L., Werre, J. M., Groenen-Döpp, Y. A., Roerdinkholder-Stoelwinder, B., De Pauw, B., & Bosman, G. J. (2008). Erythrocyte vesiculation: a self-protective mechanism?. British journal of haematology, 141(4), 549-556.

[187] Crauste, F., Demin, I., Gandrillon, O., & Volpert, V. (2010). Mathematical study of feedback control roles and relevance in stress erythropoiesis. Journal of theoretical biology, 263(3), 303-316.

[188] Demin, I., Crauste, F., Gandrillon, O., & Volpert, V. (2010). A multi-scale model of erythropoiesis. Journal of Biological Dynamics, 4(1), 59-70.

[189] Bessonov, N., Pujo-Menjouet, L., & Volpert, V. (2006). Cell modelling of hematopoiesis. Mathematical Modelling of Natural Phenomena, 1(2), 81-103.

[190] Bessonov, N., Crauste, F., Demin, I., & Volpert, V. (2009). Dynamics of erythroid progenitors and erythroleukemia. Mathematical Modelling of Natural Phenomena, 4(3), 210-232.

[191] Bessonov, N., Demin, I., Pujo-Menjouet, L., & Volpert, V. (2009). A multi-agent model describing self-renewal of differentiation effects on the blood cell population. Mathematical and computer modelling, 49(11), 2116-2127.

[192] Bessonov, N., Crauste, F., Fischer, S., Kurbatova, P., & Volpert, V. (2011). Application of hybrid models to blood cell production in the bone marrow. Mathematical Modelling of Natural Phenomena, 6(7), 2-12.

[193] Fischer, S., Kurbatova, P., Bessonov, N., Gandrillon, O., Volpert, V., & Crauste, F. (2012). Modeling erythroblastic islands: using a hybrid model to assess the function of central macrophage. Journal of theoretical biology, 298, 92-106.

[194] Hillman, R. S., & Giblett, E. R. (1965). Red cell membrane alteration associated with" marrow stress". Journal of Clinical Investigation, 44(10), 1730.

[195] Hillman, R. S. (1969). Characteristics of marrow production and reticulocyte maturation in normal man in response to anemia. Journal of Clinical Investigation, 48(3), 443.

[196] Koury, M. J., Sawyer, S. T., & Bondurant, M. C. (1984). Splenic erythroblasts in anemia-inducing Friend disease: a source of cells for studies of erythropoietin-mediated differentiation. Journal of cellular physiology, 121(3), 526-532.

[197] Sawyer, S. T., & Krantz, S. B. (1986). Transferrin receptor number, synthesis, and endocytosis during erythropoietin-induced maturation of Friend virus-infected erythroid cells. Journal of Biological Chemistry, 261(20), 9187-9195.

[198] Koury, M. J., & Bondurant, M. C. (1988). Maintenance by erythropoietin of viability and maturation of murine erythroid precursor cells. Journal of cellular physiology, 137(1), 65-74.

[199] Kim, H. D., Koury, M. J., Lee, S. J., Im, J. H., & Sawyer, S. T. (1991). Metabolic adaptation during erythropoietin-mediated terminal differentiation of mouse erythroid cells. Blood, 77(2), 387-392.

[200] Schranzhofer, M., Schifrer, M., Cabrera, J. A., Kopp, S., Chiba, P., Beug, H., & Müllner, E. W. (2006). Remodeling the regulation of iron metabolism during erythroid differentiation to ensure efficient heme biosynthesis. Blood, 107(10), 4159-4167.

[201] Niederreiter, H. (1992). Random number generation and quasi-Monte Carlo methods. Society for Industrial and Applied Mathematics.

[202] Palumbo, A., & Anderson, K. (2011). Multiple Myeloma. New England journal of medicine, 364(24), 2364-2364.

[203] Morgan, G. J., Walker, B. A., & Davies, F. E. (2012). The genetic architecture of multiple myeloma. Nature Reviews Cancer, 12(5), 335-348.

[204] Walker, B. A., Wardell, C. P., Melchor, L., Hulkki, S., Potter, N. E., Johnson, D. C., ... & Ashworth, A. (2012). Intraclonal heterogeneity and distinct molecular mechanisms characterize the development of t (4; 14) and t (11; 14) myeloma. Blood, 120(5), 1077-1086.

[205] Bouchnita, A., Belmaati, F. E., Aboulaich, R., Ellaia, R., & Volpert, V. (2016). Mathematical modelling of intra-clonal heterogeneity in multiple myeloma. Proceedings of the CARI.

[206] Brioli, A., Melchor, L., Cavo, M., & Morgan, G. J. (2014). The impact of intra-clonal heterogeneity on the treatment of multiple myeloma. British journal of haematology, 165(4), 441-454.

[207] Melchor, L., Brioli, A., Wardell, C. P., Murison, A., Potter, N. E., Kaiser, M. F., ... & Vijayaraghavan, G. (2014). Single-cell genetic analysis reveals the composition of initiating clones and phylogenetic patterns of branching and parallel evolution in myeloma. Leukemia, 28(8), 1705-1715.

[208] Chesi, M., Bergsagel, P. L., Brents, L. A., Smith, C. M., Gerhard, D. S., & Kuehl, W. M. (1996). Dysregulation of cyclin D1 by translocation into an IgH gamma switch region in two multiple myeloma cell lines [see comments]. Blood, 88(2), 674-681.

[209] Bouyssou, J. M., Ghobrial, I. M., & Roccaro, A. M. (2016). Targeting SDF-1 in multiple myeloma tumor microenvironment. Cancer letters, 380(1), 315-318.

[210] Vanderkerken, K., Van Camp, B., De Greef, C., Broek, I. V., Asosingh, K., & Van Riet, I. (2000). Homing of the myeloma cell clone. Acta Oncologica, 39(7), 771-776.

[211] Hideshima, T., Mitsiades, C., Tonon, G., Richardson, P. G., & Anderson, K. C. (2007). Understanding multiple myeloma pathogenesis in the bone marrow to identify new therapeutic targets. Nature Reviews Cancer, 7(8), 585-598.

[212] Rozemuller, H., van der Spek, E., Bogers-Boer, L. H., Zwart, M. C., Verweij, V., Emmelot, M., ... & Mutis, T. (2008). A bioluminescence imaging based in vivo model for preclinical testing of novel cellular immunotherapy strategies to improve the graft-versus-myeloma effect. haematologica, 93(7), 1049-1057.

[213] Manier, S., Sacco, A., Leleu, X., Ghobrial, I. M., & Roccaro, A. M. (2012). Bone marrow microenvironment in multiple myeloma progression. BioMed Research International, 2012.

[214] Kitano, H. (2002). Systems biology: a brief overview. Science, 295(5560), 1662-1664.

[215] Eymard, N., Bessonov, N., Gandrillon, O., Koury, M. J., & Volpert, V. (2015). The role of spatial organization of cells in erythropoiesis. Journal of mathematical biology, 70(1-2), 71-97.

[216] Mohandas, N., & Prenant, M. (1978). Three-dimensional model of bone marrow. Blood, 51(4), 633-643.

[217] Landgren, O., Kyle, R. A., Pfeiffer, R. M., Katzmann, J. A., Caporaso, N. E., Hayes, R. B., ... & Hoover, R. (2009). Monoclonal gammopathy of undetermined significance (MGUS) consistently precedes multiple myeloma: a prospective study. Blood, 113(22), 5412-5417.

[218] Weiss, B. M., Abadie, J., Verma, P., Howard, R. S., & Kuehl, W. M. (2009). A monoclonal gammopathy precedes multiple myeloma in most patients. Blood, 113(22), 5418-5422.

[219] Anderson, K. C., & Carrasco, R. D. (2011). Pathogenesis of myeloma. Annual Review of Pathology: Mechanisms of Disease, 6, 249-274.

[220] Kuehl, W. M., & Bergsagel, P. L. (2012). Molecular pathogenesis of multiple myeloma and its premalignant precursor. The Journal of clinical investigation, 122(10), 3456.

[221] Bianchi, G., & Munshi, N. C. (2015). Pathogenesis beyond the cancer clone (s) in multiple myeloma. Blood, 125(20), 3049-3058.

[222] Richardson, P. G., Weller, E., Lonial, S., Jakubowiak, A. J., Jagannath, S., Raje, N. S., ... & Mazumder, A. (2010). Lenalidomide, bortezomib, and dexamethasone combination therapy in patients with newly diagnosed multiple myeloma. Blood, 116(5), 679-686.

[223] Chen, N., Wen, L., Lau, H., Surapaneni, S., & Kumar, G. (2012). Pharmacokinetics, metabolism and excretion of [14C]-lenalidomide following oral administration in healthy male subjects. Cancer chemotherapy and pharmacology, 69(3), 789-797.

[224] Reddy, K. V., Bhattacharjee, G., Schabbauer, G., Hollis, A., Kempf, K., Tencati, M., ... & Mackman, N. (2004). Dexamethasone enhances LPS induction of tissue factor expression in human monocytic cells by increasing tissue factor mRNA stability. Journal of leukocyte biology, 76(1), 145-151.

[225] O'Sullivan, B. T., Cutler, D. J., Hunt, G. E., Walters, C., Johnson, G. F., & Caterson, I. D. (1997). Pharmacokinetics of dexamethasone and its relationship to dexamethasone suppression test outcome in depressed patients and healthy control subjects. Biological psychiatry, 41(5), 574-584.

[226] Isozumi, Y., Arai, R., Fujimoto, K., & Koyama, T. (2013). Activation of coagulation by lenalidomide-based regimens for the treatment of multiple myeloma. PloS one, 8(5), e64369.

[227] Levy, J. A. (1994). HIV and the Pathogenesis of AIDS. American Society for Microbiology.

[228] Grossman, Z., Meier-Schellersheim, M., Paul, W. E., & Picker, L. J. (2006). Pathogenesis of HIV infection: what the virus spares is as important as what it destroys. Nature medicine, 12(3), 289-295.

[229] Grossman, Z., Meier-Schellersheim, M., Sousa, A. E., Victorino, R. M., & Paul, W. E. (2002). CD4+ T-cell depletion in HIV infection: are we closer to understanding the cause?. Nature medicine, 8(4), 319-323.

[230] Chereshnev, V. A., Bocharov, G., Bazhan, S., Bachmetyev, B., Gainova, I., Likhoshvai, V., ... & Brander, C. (2013). Pathogenesis and treatment of HIV infection: the cellular, the immune system and the neuroendocrine systems perspective. International reviews of immunology, 32(3), 282-306.

[231] Kent, S. J., Reece, J. C., Petravic, J., Martyushev, A., Kramski, M., De Rose, R., ... & Lewin, S. R. (2013). The search for an HIV cure: tackling latent infection. The Lancet infectious diseases, 13(7), 614-621.

[232] Melkova, Z., Shankaran, P., Madlenakova, M., & Bodor, J. (2017). Current views on HIV-1 latency, persistence, and cure. Folia microbiologica, 62(1), 73-87.

[233] Kidd, B. A., Peters, L. A., Schadt, E. E., & Dudley, J. T. (2014). Unifying immunology with informatics and multiscale biology. Nature immunology, 15(2), 118-127.

[234] Carlson, J. M., Le, A. Q., Shahid, A., & Brumme, Z. L. (2015). HIV-1 adaptation to HLA: a window into virus–host immune interactions. Trends in microbiology, 23(4), 212-224.

[235] Banks, H. T., Davidian, M., Hu, S., Kepler, G. M., & Rosenberg, E. S. (2008). Modelling HIV immune response and validation with clinical data. Journal of biological dynamics, 2(4), 357-385.

[236] Ludewig, B., Stein, J. V., Sharpe, J., Cervantes-Barragan, L., Thiel, V., & Bocharov, G. (2012). A global "imaging"view on systems approaches in immunology. European journal of immunology, 42(12), 3116-3125.

[237] Bocharov, G., Chereshnev, V., Gainova, I., Bazhan, S., Bachmetyev, B., Argilaguet, J., ... & Meyerhans, A. (2012). Human immunodeficiency virus infection: from biological observations to mechanistic mathematical modelling. Mathematical Modelling of Natural Phenomena, 7(5), 78-104.

[238] Alizon, S., & Magnus, C. (2012). Modelling the course of an HIV infection: insights from ecology and evolution. Viruses, 4(10), 1984-2013.

[239] Canini, L., & Perelson, A. S. (2014). Viral kinetic modeling: state of the art. Journal of pharmacokinetics and pharmacodynamics, 41(5), 431-443.

[240] Weinan, E. (2011). Principles of multiscale modeling. Cambridge University Press.

[241] Fallahi-Sichani, M., El-Kebir, M., Marino, S., Kirschner, D. E., & Linderman, J. J. (2011). Multi-scale computational modeling reveals a critical role for TNF-α receptor 1 dynamics in tuberculosis granuloma formation. The Journal of Immunology, 186(6), 3472-3483.

[242] Cilfone, N. A., Kirschner, D. E., & Linderman, J. J. (2015). Strategies for efficient numerical implementation of hybrid multi-scale agent-based models to describe biological systems. Cellular and molecular bioengineering, 8(1), 119-136.

[243] Marino, S., & Kirschner, D. E. (2016). A multi-compartment hybrid computational model predicts key roles for dendritic cells in tuberculosis infection. Computation, 4(4), 39.

[244] Prokopiou, S. A., Barbarroux, L., Bernard, S., Mafille, J., Leverrier, Y., Arpin, C., ... & Crauste, F. (2014). Multiscale modeling of the early CD8 T-cell immune response in lymph nodes: an integrative study. Computation, 2(4), 159-181.

[245] Gao, X., Arpin, C., Marvel, J., Prokopiou, S. A., Gandrillon, O., & Crauste, F. (2016). IL-2 sensitivity and exogenous IL-2 concentration gradient tune the productive contact duration of CD8+ T cell-APC: a multiscale modeling study. BMC systems biology, 10(1), 77.

[246] Williams, R. A., Timmis, J., & Qwarnstrom, E. E. (2014). Computational models of the NF-KB signalling pathway. Computation, 2(4), 131-158.

[247] Baldazzi, V., Paci, P., Bernaschi, M., & Castiglione, F. (2009). Modeling lymphocyte homing and encounters in lymph nodes. BMC bioinformatics, 10(1), 387.

[248] Gong, C., Mattila, J. T., Miller, M., Flynn, J. L., Linderman, J. J., & Kirschner, D. (2013). Predicting lymph node output efficiency using systems biology. Journal of theoretical biology, 335, 169-184.

[249] Palsson, S., Hickling, T. P., Bradshaw-Pierce, E. L., Zager, M., Jooss, K., O'Brien, P. J., ... & Vicini, P. (2013). The development of a fully-integrated immune response model (FIRM) simulator of the immune response through integration of multiple subset models. BMC systems biology, 7(1), 95.

[250] Germain, R. N., Meier-Schellersheim, M., Nita-Lazar, A., & Fraser, I. D. (2011). Systems biology in immunology: a computational modeling perspective. Annual review of immunology, 29, 527-585.

[251] Cilfone, N. A., Kirschner, D. E., & Linderman, J. J. (2015). Strategies for efficient numerical implementation of hybrid multi-scale agent-based models to describe biological systems. Cellular and molecular bioengineering, 8(1), 119-136.

[252] Donovan, G. M., & Lythe, G. (2016). T cell and reticular network co-dependence in HIV infection. Journal of theoretical biology, 395, 211-220.

[253] Lackner, A. A., Lederman, M. M., & Rodriguez, B. (2012). HIV pathogenesis: the host. Cold Spring Harbor perspectives in medicine, 2(9), a007005.

[254] McMichael, A., Dorrell, L. (2009). The immune response to HIV. Medicine. 37, 321–325.

[255] Walker, B., & McMichael, A. (2012). The T-cell response to HIV. Cold Spring Harbor perspectives in medicine, 2(11), a007054.

[256] Ndhlovu, Z. M., Kamya, P., Mewalal, N., Kløverpris, H. N., Nkosi, T., Pretorius, K., ... & Ghebremichael, M. (2015). Magnitude and kinetics of CD8+ T cell activation during hyperacute HIV infection impact viral set point. Immunity, 43(3), 591-604.

[257] Petrovas, C., Mueller, Y. M., & Katsikis, P. D. (2005). Apoptosis of HIV-specific CD8+ T cells: an HIV evasion strategy. Cell Death & Differentiation, 12, 859-870.

[258] Bessonov, N., Eymard, N., Kurbatova, P., & Volpert, V. (2012). Mathematical modeling of erythropoiesis in vivo with multiple erythroblastic islands. Applied Mathematics Letters, 25(9), 1217-1221.

[259] Volpert, V., Bessonov, N., Eymard, N., & Tosenberger, A. (2013). Modèle multi-échelle de la dynamique cellulaire. Le vivant discret et continu. N. Glade, A. Stephanou, Editeurs, Editions Materiologiques, 91-111.

[260] Kurbatova, P., Eymard, N., & Volpert, V. (2013). Hybrid model of erythropoiesis. Acta biotheoretica, 61(3), 305-315.

[261] Eymard, N., Bessonov, N., Gandrillon, O., Koury, M. J., & Volpert, V. (2015). The role of spatial organization of cells in erythropoiesis. Journal of mathematical biology, 70(1-2), 71-97.

[262] Yeghiazarian, L., Cumberland, W. G., & Yang, O. O. (2013). A stochastic multi-scale model of HIV-1 transmission for decision-making: application to a MSM population. PloS one, 8(11), e70578.

[263] Stéphanou, A., & Volpert, V. (2016). Hybrid modelling in biology: a classification review. Mathematical Modelling of Natural Phenomena, 11(1), 37-48.

[264] Gottschalk, R. A., Martins, A. J., Angermann, B. R., Dutta, B., Ng, C. E., Uderhardt, S., ... & Germain, R. N. (2016). Distinct NF-κB and MAPK activation thresholds uncouple steady-state microbe sensing from anti-pathogen inflammatory responses. Cell systems, 2(6), 378-390.

[265] Nakaoka, S., Iwami, S., & Sato, K. (2016). Dynamics of HIV infection in lymphoid tissue network. Journal of mathematical biology, 72(4), 909-938.

[266] Stancevic, O., Angstmann, C. N., Murray, J. M., & Henry, B. I. (2013). Turing patterns from dynamics of early HIV infection. Bulletin of mathematical biology, 75(5), 774-795.

[267] Dunia, R., & Bonnecaze, R. (2013). Mathematical modeling of viral infection dynamics in spherical organs. Journal of mathematical biology, 67(6-7), 1425-1455.

[268] Strain, M. C., Richman, D. D., Wong, J. K., & Levine, H. (2002). Spatiotemporal dynamics of HIV propagation. Journal of theoretical biology, 218(1), 85-96.

[269] Zhang, C., Zhou, S., Groppelli, E., Pellegrino, P., Williams, I., Borrow, P., ... & Jolly, C. (2015). Hybrid spreading mechanisms and T cell activation shape the dynamics of HIV-1 infection. PLoS computational biology, 11(4), e1004179.

[270] Bocharov, G., Züst, R., Cervantes-Barragan, L., Luzyanina, T., Chiglintsev, E., Chereshnev, V. A., ... & Ludewig, B. (2010). A systems immunology approach to plasmacytoid dendritic cell function in cytopathic virus infections. PLoS pathogens, 6(7), e1001017.

[271] Webb, S. D., Sherratt, J. A., & Fish, R. G. (2002). Cells behaving badly: a theoretical model for the Fas/FasL system in tumour immunology. Mathematical biosciences, 179(2), 113-129.

[272] Baker, C. T. H., Bocharov, G. A., & Paul, C. A. H. (1997). Mathematical Modelling of the Interleukin-2 T-Cell System: A Comparative Study of Approaches Based on Ordinary and Delay Differential Equation. Computational and Mathematical Methods in Medicine, 1(2), 117-128.

[273] Grimm, V., Berger, U., Bastiansen, F., Eliassen, S., Ginot, V., Giske, J., ... & Huth, A. (2006). A standard protocol for describing individual-based and agent-based models. Ecological modelling, 198(1), 115-126.

[274] Grimm, V., Berger, U., DeAngelis, D. L., Polhill, J. G., Giske, J., & Railsback, S. F. (2010). The ODD protocol: a review and first update. Ecological modelling, 221(23), 2760-2768.

[275] Ananworanich, J., Chomont, N., Eller, L. A., Kroon, E., Tovanabutra, S., Bose, M., ... & O'Connell, R. J. (2016). HIV DNA set point is rapidly established in acute HIV infection and dramatically reduced by early ART. EBioMedicine, 11, 68-72.

[276] Ananworanich, J., Sacdalan, C. P., Pinyakorn, S., & Chomont, N. (2016). Virological and immunological characteristics of HIV-infected individuals at the earliest stage of infection. Journal of virus eradication, 2(1), 43.

[277] Grossman, Z., Polis, M., Feinberg, M. B., Grossman, Z., Levi, I., Jankelevich, S., ... & Goudsmit, J. (1999). Ongoing HIV dissemination during HAART. Nature medicine, 5(10), 1099-1104.

[278] Likhoshvai, V. A., Khlebodarova, T. M., Bazhan, S. I., Gainova, I. A., Chereshnev, V. A., & Bocharov, G. A. (2014). Mathematical model of the Tat-Rev regulation of HIV-1 replication in an activated cell predicts the existence of oscillatory dynamics in the synthesis of viral components. BMC genomics, 15(12), S1.

[279] Petrovas, C., Yamamoto, T., Price, D. A., Rao, S. S., Klatt, N. R., Brenchley, J. M., ... & Macallan, D. C. (2013). High production rates sustain in vivo levels of PD-1high simian immunodeficiency virus-specific CD8 T cells in the face of rapid clearance. Journal of virology, 87(17), 9836-9844.

[280] Peligero, C., Argilaguet, J., Güerri-Fernandez, R., Torres, B., Ligero, C., Colomer, P., ... & Meyerhans, A. (2015). PD-L1 blockade differentially impacts regulatory T cells from HIV-infected individuals depending on plasma viremia. PLoS pathogens, 11(12), e1005270.

[281] Grossman, Z., & Paul, W. E. (2015). Dynamic tuning of lymphocytes: physiological basis, mechanisms, and function. Annual Review of Immunology, 33, 677-713.

[282] Paul, W. E., & Grossman, Z. (2014). Pathogen-sensing and regulatory T cells: integrated regulators of immune responses. Cancer immunology research, 2(6), 503-509.

[283] Bocharov, G. A., Telatnikov, I. S., Chereshnev, V. A., Martinez, J., & Meyerhans, A. (2015). Mathematical modelling of the within-host HIV quasispecies dynamics in response to antiviral treatment. Russian Journal of Numerical Analysis and Mathematical Modelling, 30(3), 157-170.

[284] Okoye, A., Meier-Schellersheim, M., Brenchley, J. M., Hagen, S. I., Walker, J. M., Rohankhedkar, M., ... & Sylwester, A. W. (2007). Progressive CD4+ central–memory T cell decline results in CD4+ effector–memory insufficiency and overt disease in chronic SIV infection. Journal of Experimental Medicine, 204(9), 2171-2185.

[285] Paul, W. E., Milner, J. D., & Grossman, Z. (2013, January). Pathogen-sensing, regulatory T cells, and responsiveness-tuning collectively regulate foreign-and self-antigen mediated T-cell responses. In Cold Spring Harbor symposia on quantitative biology (Vol. 78, pp. 265-276). Cold Spring Harbor Laboratory Press.

[286] Khan, S. H., Martin, M. D., Starbeck-Miller, G. R., Xue, H. H., Harty, J. T., & Badovinac, V. P. (2015). The timing of stimulation and IL-2 signaling regulate secondary CD8 T cell responses. PLoS pathogens, 11(10), e1005199.

[287] Welsh, R. M., Bahl, K., Marshall, H. D., & Urban, S. L. (2012). Type 1 interferons and antiviral CD8 T-cell responses. PLoS pathogens, 8(1), e1002352.

[288] Hervas-Stubbs, S., Perez-Gracia, J. L., Rouzaut, A., Sanmamed, M. F., Le Bon, A., & Melero, I. (2011). Direct effects of type I interferons on cells of the immune system. Clinical Cancer Research, 17(9), 2619-2627.

[289] Mueller, S. N., & Germain, R. N. (2009). Stromal cell contributions to the homeostasis and functionality of the immune system. Nature Reviews Immunology, 9(9), 618-629.

[290] Girard, J. P., Moussion, C., & Förster, R. (2012). HEVs, lymphatics and homeostatic immune cell trafficking in lymph nodes. Nature Reviews Immunology, 12(11), 762-773.

[291] Junt, T., Scandella, E., & Ludewig, B. (2008). Form follows function: lymphoid tissue microarchitecture in antimicrobial immune defence. Nature Reviews Immunology, 8(10), 764-775.

[292] Förster, R., Braun, A., & Worbs, T. (2012). Lymph node homing of T cells and dendritic cells via afferent lymphatics. Trends in immunology, 33(6), 271-280.

[293] Fischer, S., Kurbatova, P., Bessonov, N., Gandrillon, O., Volpert, V., & Crauste, F. (2012). Modeling erythroblastic islands: using a hybrid model to assess the function of central macrophage. Journal of theoretical biology, 298, 92-106.

[294] Goldsby, R. A. A., Kuby, J., Kindt, Th. J. Immunology. W H Freeman & Co (Sd); Ch. 10: 222.

[295] Chang, J. T., & Reiner, S. L. (2008). Asymmetric division and stem cell renewal without a permanent niche: lessons from lymphocytes. In Cold Spring Harbor symposia on quantitative biology (Vol. 73, pp. 73-79). Cold Spring Harbor Laboratory Press.

[296] Broere, F., Apasov S. G., Sitkovsky, M. V., van Eden, W. (2011). T cell subsets and T cell-mediated immunity. In: Nijkamp FP, Parnham MJ, editors. Principles of Immunopharmacology: 3rd revised and extended edition. Basel: Springer AG.

[297] Nelson, B. H. (2004). IL-2, regulatory T cells, and tolerance. The Journal of Immunology, 172(7), 3983-3988.

[298] Cervantes-Barragan, L., Lewis, K. L., Firner, S., Thiel, V., Hugues, S., Reith, W., ... & Reizis, B. (2012). Plasmacytoid dendritic cells control T-cell response to chronic viral infection. Proceedings of the National Academy of Sciences, 109(8), 3012-3017.

[299] Kaech, S. M., & Wherry, E. J. (2007). Heterogeneity and cell-fate decisions in effector and memory CD8+ T cell differentiation during viral infection. Immunity, 27(3), 393-405.

[300] Fricke, G. M., Letendre, K. A., Moses, M. E., & Cannon, J. L. (2016). Persistence and adaptation in immunity: T cells balance the extent and thoroughness of search. PLoS computational biology, 12(3), e1004818.

[301] Cappuccio, A., Tieri, P., & Castiglione, F. (2015). Multiscale modelling in immunology: a review. Briefings in bioinformatics, 17(3), 408-418.

[302] Paul, W. E. (2012). The Immune System–Complexity Exemplified. Mathematical Modelling of Natural Phenomena, 7(5), 4-6. 7(5):4–6.

[303] Jenkins, R. E., Peters, B. S., & Pinching, A. J. (1991). Thromboembolic disease in AIDS is associated with cytomegalovirus disease. Aids, 5(12), 1540-1542.

[304] Hassell, K. L., Kressin, D. C., Neumann, A., Ellison, R., & Marlar, R. A. (1994). Correlation of antiphospholipid antibodies and protein S deficiency with thrombosis in HIV-infected men. Blood coagulation & fibrinolysis: an international journal in haemostasis and thrombosis, 5(4), 455-462.

[305] George, S. L., Swindells, S., Knudson, R., & Stapleton, J. T. (1999). Unexplained thrombosis in HIV-infected patients receiving protease inhibitors: report of seven cases. The American journal of medicine, 107(6), 624-626.

[306] Saif, M. W., Bona, R., & Greenberg, B. (2001). AIDS and thrombosis: retrospective study of 131 HIV-infected patients. AIDS patient care and STDS, 15(6), 311-320.

[307] Wiley, C. A., Schrier, R. D., Nelson, J. A., Lampert, P. W., & Oldstone, M. B. (1986). Cellular localization of human immunodeficiency virus infection within the brains of acquired immune deficiency syndrome patients. Proceedings of the National Academy of Sciences, 83(18), 7089-7093.

[308] Holme, P. A., Müller, F., Solum, N. O., Brosstad, F., Frøland, S. S., & Aukrust, P. (1998). Enhanced activation of platelets with abnormal release of RANTES in human immunodeficiency virus type 1 infection. The FASEB Journal, 12(1), 79-90.

[309] Mayne, E., Funderburg, N. T., Sieg, S. F., Asaad, R., Kalinowska, M., Rodriguez, B., ... & Lederman, M. M. (2012). Increased platelet and microparticle activation in HIV infection: upregulation of Pselectin and tissue factor expression. Journal of acquired immune deficiency syndromes (1999), 59(4), 340.

[310] Ansell, J., Hirsh, J., Hylek, E., Jacobson, A., Crowther, M., & Palareti, G. (2008). Pharmacology and management of the vitamin K antagonists: American College of Chest Physicians evidence-based clinical practice guidelines. Chest Journal, 133(6), 160S-198S.

[311] Antovic, J. P., & Blombäck, M. (Eds.). (2013). Essential guide to blood coagulation. John Wiley & Sons.

[312] J. Hirsh, J. E. Dalen, D. R. Anderson, L. Poller, H. Bussey, J. Ansell, J., D. Deykin. *Oral anticoagulants: mechanism of action, clinical effectiveness, and optimal therapeutic range*. Chest Journal, 119 (2001), 8S-21S.

[313] Hirsh, J., Warkentin, T. E., Shaughnessy, S. G., Anand, S. S., Halperin, J. L., Raschke, R., ... & Dalen, J. E. (2001). Heparin and low-molecular-weight heparin mechanisms of action, pharmacokinetics, dosing, monitoring, efficacy, and safety. Chest Journal, 119, 64S-94S.

[314] Fasco, M. J., Principe, L. M., Walsh, W. A., & Friedman, P. A. (1983). Warfarin inhibition of vitamin K 2, 3-epoxide reductase in rat liver microsomes. Biochemistry, 22(24), 5655-5660.

[315] Warfarin INR targets. `http://www.globalrph.com/warfarin_inr_targets.htm`. Accessed: 2016-02-22.

[316] Holford, N. H. (1986). Clinical pharmacokinetics and pharmacodynamics of warfarin. Clin. Pharmacokinet, 11, 483-504.

[317] Lowe, G. D. (2003). Virchow's triad revisited: abnormal flow. Pathophysiology of haemostasis and thrombosis, 33(5-6), 455-457.

[318] Majerus, P. W., Broze, G. J., Miletich, J. P., & Tollefsen, D. M. (1996). Anticoagulant, thrombolytic, and antiplatelet drugs. Pharmacologic Basis of Therapeutics, ed, 9, 1341-1359.

[319] Porter, R. S., Sawyer, W. T., & Lowenthal, D. T. (1992). Warfarin. Applied Pharmacokinetics Principles of Therapeutic Drug Monitoring, 3, 31-8.

[320] Prothrombin time. http://www.nlm.nih.gov/medlineplus/ency/article/003652.htm. Accessed: 2016-05-23

[321] Stenflo, J., & Suttie, J. W. (1977). Vitamin K-dependent formation of γ-carboxyglutamic acid. Annual review of biochemistry, 46(1), 157-172.

[322] Svec, J. M., Coleman, R. W., Mungall, D. R., & Ludden, T. M. (1985). Bayesian pharmacokinetic/pharmacodynamic forecasting of prothrombin response to warfarin therapy: preliminary evaluation. Therapeutic drug monitoring, 7(2), 174-180.

[323] Mueck, W., Stampfuss, J., Kubitza, D., & Becka, M. (2014). Clinical pharmacokinetic and pharmacodynamic profile of rivaroxaban. Clinical pharmacokinetics, 53(1), 1-16.

[324] Hensen, A., & Loeliger, E. A. (1962). ANTITHROMBIN III. ITS METABOLISM AND ITS FUNCTION IN BLOOD COAGULATION. Thrombosis et diathesis haemorrhagica, 83, SUPPL1-1.

[325] OpenFOAM. The Open Source CFD Toolbox. User Guide. OpenCFD Limited; 2009.

[326] http://www.salome-platform.org/.

[327] Wiebe, E. M., Stafford, A. R., Fredenburgh, J. C., & Weitz, J. I. (2003). Mechanism of catalysis of inhibition of factor IXa by antithrombin in the presence of heparin or pentasaccharide. Journal of Biological Chemistry, 278(37), 35767-35774.

[328] Tsiang, M., Paborsky, L. R., Li, W. X., Jain, A. K., Mao, C. T., Dunn, K. E., ... & Leung, L. L. K. (1996). Protein engineering thrombin for optimal specificity and potency of anticoagulant activity in vivo. Biochemistry, 35(51), 16449-16457.

[329] Solymoss, S., Tucker, M. M., & Tracy, P. B. (1988). Kinetics of inactivation of membrane-bound factor Va by activated protein C. Protein S modulates factor Xa protection. Journal of Biological Chemistry, 263(29), 14884-14890.

Chapter 10

Appendix A - Numerical implementation of continuous and hybrid models

10.1 Numerical methods for the implementation of the thrombus formation model

The computational domain was discretized into a regular 2000×400 mesh. We used the finite difference method to implement the advection-diffusion-reaction equations and the projection method was used to solve the Navier-Stokes equation. These methods are briefly presented below.

10.1.1 Advection-diffusion-reaction equations implementation

Reaction-diffusion equations (e.g., Equation (3.1.2)) are discretized as follows:

$$\begin{aligned}\frac{T_{i,j}^{n+1}-T_{i,j}^{n}}{dt}+v_{x\,i,j}^{n}(T_{i,j}^{n})_{x}^{+}+v_{y\,i,j}^{n}(T_{i,j}^{n})_{y}^{+}=D\frac{T_{i+1,j}^{n}+T_{i,j+1}^{n}-4T^{n+1}+T_{i-1,j}^{n}+T_{i,j-1}^{n}}{h^{2}}\\ +\left((k_{3}B_{a\,i,j}^{n})+\frac{k_{4}(T_{i,j}^{n})^{3}}{1+k_{5}C_{a\,i,j}^{n}}\right)P_{i,j}^{n}-k_{a}A_{i,j}^{n}T_{i,j}^{n}.\end{aligned} \tag{10.1.1}$$

Here dt the time step, h is the space step as, i and j are point numbers, n is the time step number. The terms $(T_{i,j}^{n})_{x}^{+}$ and $(T_{i,j}^{n})_{y}^{+}$ refers to an upwind scheme if the velocity is positive and to a downwind scheme otherwise. This scheme is conventionally introduced in order to treat numerical instabilities related to convection dominated problems. We have:

$$(T_{i,j}^{n})_{x}^{+}=\begin{cases}\frac{T_{i,j}^{n}-T_{i-1,j}^{n}}{h} & \text{if } v_{x\,i,j}^{n}\geq 0\\ \frac{T_{i+1,j}^{n}-T_{i,j}^{n}}{h} & \text{if } v_{x\,i,j}^{n}<0\end{cases}.$$

The term $(T_{i,j}^{n})_{y}^{+}$ is treated in a similar way.

10.1.2 Navier-Stokes equation implementation

We solve the Navier-Stokes equations for the incompressible fluid

$$\frac{\partial u_x}{\partial t}+u_x\nabla\frac{\partial u_x}{\partial x}+u_y\nabla\frac{\partial u_x}{\partial y}=-\frac{1}{\rho}\frac{\partial p}{\partial x}+\nu(\frac{\partial^2 u_x}{\partial x^2}+\frac{\partial^2 u_y}{\partial x^2})-\frac{\nu}{K_f}u_x,$$

$$\frac{\partial u_y}{\partial t}+u_x\nabla\frac{\partial u_y}{\partial x}+u_y\nabla\frac{\partial u_y}{\partial y}=-\frac{1}{\rho}\frac{\partial p}{\partial y}+\nu(\frac{\partial^2 u_x}{\partial y^2}+\frac{\partial^2 u_y}{\partial y^2})-\frac{\nu}{K_f}u_y,$$

$$\nabla \vec{u} = 0,$$

using the Chorin projection method presented in [123]. The general approach is described in [128] (section 6.7). We proceed in three steps:

(i) **Treat nonlinear terms**: We look for an intermediate velocity (u_x^*, u_y^*) verifying the equations:

$$\begin{aligned} \frac{u_x^* - u_x^n}{dt} &= -u_x^n (u_x^n)_x^+ - u_y^n (u_x^n)_y^+ - \frac{\nu}{K_f} u_x^n, \\ \frac{u_y^* - u_y^n}{dt} &= -u_x^n (u_y^n)_x^+ - u_y^n (u_y^n)_y^+ - \frac{\nu}{K_f} u_y^n. \end{aligned} \tag{10.1.2}$$

As above we use an upwind method to discretize the terms $(u_x^n)_x^+$, $(u_y^n)_x^+$, $(u_x^n)_y^+$, $(u_y^n)_y^+$ to avoid convection dominated problems.

(ii) **Implicit viscosity**: The viscosity terms are treated implicitly. We calculate a second intermediate velocity (u_x^{**}, u_y^{**}) by solving the equations:

$$\frac{u_x^{**} - u_x^*}{dt} = \nu((u_x^{**})_{xx} + (u_y^{**})_{xx}), \quad \frac{u_y^{**} - u_y^*}{dt} = \nu((u_x^{**})_{yy} + (u_y^{**})_{yy}). \tag{10.1.3}$$

(iii) **Pressure correction**: We correct the second intermediate velocity by the implicit pressure gradient $(\frac{\partial p^{n+1}}{\partial x}, \frac{\partial p^{n+1}}{\partial y})$:

$$\frac{u_x^{n+1} - u_x^{**}}{dt} = -\frac{1}{\rho} \frac{\partial p^{n+1}}{\partial x}, \quad \frac{u_y^{n+1} - u_y^{**}}{dt} = -\frac{1}{\rho} \frac{\partial p^{n+1}}{\partial y}. \tag{10.1.4}$$

The pressure gradient $(\frac{\partial p^{n+1}}{\partial x}, \frac{\partial p^{n+1}}{\partial y})$ is only given implicitly since it is obtained by solving a linear system. In order to compute it, we solve the Poisson equation:

$$-\frac{1}{\rho} \Delta p^{n+1} = -\frac{1}{dt} \nabla . u^n.$$

To solve the last equation, we use the successive over-relaxation method (SOR). It is an iterative method that converges faster than the Jacobi and Gauss-Seidel methods. In this method, we repeat the following iteration until the convergence of the solution:

$$p_{i,j}^{k+1} = (1-\omega) p_{i,j}^k + \frac{\omega}{4} (p_{i+1,j}^k + p_{i,j+1}^k + p_{i-1,j}^k + p_{i,j-1}^k) - \frac{\rho h^2}{2hdt} (u_{i+1,j}^n -$$

$$u_{i-1,j}^n + u_{i,j+1}^n - u_{i,j-1}^n),$$

where the constant ω is the relaxation factor. Let us denote the number of points in the computational mesh by $N_x \times N_y$. To ensure the fast convergence of the SOR algorithm, we set

$$\omega = 2 \left(1 + \sqrt{1 - \frac{(\cos(\pi/N_x) + \cos(\pi/N_y)^2}{2}} \right)^{-1}$$

10.1.3 Hybrid models implementation

10.1.4 Reaction-diffusion equations for extracellular cytokines concentration.

We consider a rectangular two-dimensional domain Ω and we denote its boundaries by Γ. We use the alternating direction implicit method to solve the following problem:

$$(P): \begin{cases} \frac{\partial S}{dt} = D\Delta S + W - \sigma I, & in\ \Omega \\ S(x,y,0) = \phi(x,y), & in\ \Omega \\ S = 0 & \text{on } \Gamma, \end{cases}$$

where D is the diffusion coefficient, W and σ are the production and degradation rates respectively, $\phi(x,y)$ represents the initial condition condition for I. We consider the two-dimensional grid $(x_i, y_j, t_n) = (ih, jh, n\delta t)$, where h and δt are the space and time steps respectively and we discretize it: $i = 1,2,...,N_x$ and $j = 1,2,...,N_y$. We first rewrite the problem (P) in the following form:

$$(P_1): \begin{cases} \frac{\partial S}{dt} = \frac{D}{2}(\frac{\partial^2 S}{\partial x^2} + \frac{\partial^2 S}{\partial y^2}) + \frac{D}{2}(\frac{\partial^2 S}{\partial x^2} + \frac{\partial^2 S}{\partial y^2}) + W - \sigma S, & \text{in } \Omega \\ S(x,y,0) = \phi(x,y), & \text{in } \Omega \\ S = 0 & \text{on } \Gamma, \end{cases}$$

We split the first equation of the problem (P_1) into two sub-steps as follows:

$$\begin{cases} \frac{S_{i,j}^{n+1/2} - S_{i,j}^n}{\delta t/2} = D\frac{S_{i-1,j}^{n+1/2} - 2S_{i,j}^{n+1/2} + S_{i+1,j}^{n+1/2}}{h^2} + D\frac{S_{i,j-1}^n - 2S_{i,j}^n + S_{i,j+1}^n}{h^2} + W - \sigma S_{i,j}^{n+1/2}, \\ \frac{S_{i,j}^{n+1} - S_{i+1/2,j}^n}{\delta t/2} = D\frac{S_{i-1,j}^{n+1} - 2S_{i,j}^{n/2} + S_{i+1,j}^{n+1}}{h^2} + D\frac{S_{i,j-1}^{n+1/2} - 2S_{i,j}^{n+1/2} + S_{i,j+1}^{n+1/2}}{h^2} + W - \sigma S_{i,j}^{n+1}. \end{cases} \tag{10.1.5}$$

We solve the first equation for each fixed j to obtain $S^{n+1/2}$. Next, we solve the second to obtain S^n. Let us consider the first equation:

$$\frac{S_{i,j}^{n+1/2} - S_{i,j}^n}{\delta t/2} = D\frac{S_{i-1,j}^{n+1/2} - 2S_{i,j}^{n+1/2} + S_{i+1,j}^{n+1/2}}{h^2} + D\frac{S_{i,j-1}^n - 2S_{i,j}^n + S_{i,j+1}^n}{h^2} + W - \sigma S_{i,j}^{n+1/2}.$$

Rearranging the terms we obtain:

$$\underbrace{\frac{D}{h^2}}_{a_{i,j}} S_{i-1,j}^{n+1/2} + \underbrace{\left(-\frac{2D}{h^2} - \frac{1}{\delta t/2} - \sigma\right)}_{b_{i,j}} S_{i,j}^{n+1/2} + \underbrace{\frac{D}{h^2}}_{c_{i,j}} S_{i+1,j}^{n+1/2} =$$

$$\underbrace{-\frac{S_{i,j}^n}{\delta t/2} - D\frac{S_{i,j-1}^n - 2S_{i,j}^n + S_{i,j+1}^n}{h^2} - W}_{f_{i,j}}.$$

Therefore, we can write the first equation of the system (10.1.5) in the form:

$$a_{i,j}S_{i-1,j}^{n+1/2} + b_{i,j}S_{i,j}^{n+1/2} + c_{i,j}S_{i+1,j}^{n+1/2} = f_{i,j},$$

for each fixed j, $j = 1,2,...,N_y - 1$, we solve numerically:

$$a_i S_{i-1}^{n+1/2} + b_i S_i^{n+1/2} + c_i S_{i+1}^{n+1/2} = f_i, \quad \forall i = 1,2,...,N_x - 1 \tag{10.1.6}$$

with the boundary conditions $S_{i=0}^n = 0$, $S_{i=Nx}^n = 0$. We solve the equation (10.1.6) using Thomas algorithm. For that, we write the left boundary condition $S_{i=0} = 0$ as follows:

$$0 = L_{1/2}S_1 + K_{1/2},$$

where $L_{1/2} = 0$ and $K_{1/2} = 0$. Then from the equation (10.1.6) for $i = 1$:

$$a_1 S_0^{n+1/2} + b_1 S_1^{n+1/2} + c_1 S_2^{n+1/2} = f_1,$$

we obtain $S_1^{n+1/2}$:

$$S_1^{n+1/2} = L_{3/2} S_{1,j} + K_{3/2},$$

where we denote $L_{3/2} = \frac{-c_1}{b_1}$, $K_{3/2} = \frac{a_1 S_{1,0} - f_1}{-b_1}$. We continue for $i = 2, 3, ..., N_x - 1$:

$$S_i = L_{i+1/2} S_{i+1} + K_{i+1/2}, \tag{10.1.7}$$

where $L_{i+1/2} = \frac{-c_i}{b_i + a_i L_{i-1/2}}$, $K_{i+1/2} = \frac{f_i + a_i K_{i-1/2}}{b_i + a_i L_{i-1/2}}$. We first obtain the coefficients $L_{i+1/2}$, $K_{i+1/2}$ using the formula (10.1.6). Next, we find the solution $S^{n+1/2}$ for the sub-step $n + 1/2$ by backward sweep using the equation (10.1.7). We apply the same procedure on the second equation of the system (10.1.5) to compute the next step solution S^n.

10.1.5 Equations for cell motion and intracellular regulation

We solve the following problem which describes the motion of each cell:

$$m\ddot{x}_i + m\mu\dot{x}_i - \sum_{j \neq i} f_{ij} - f_{ch} = 0, \tag{10.1.8}$$

First, we write the late equation as a system of displacement x_i and velocity v_i:

$$\begin{cases} m\dot{v}_i + m\mu v_i - \sum_{j \neq i} f_{ij} - f_{ch} = 0, \\ \dot{x}_i = v_i \end{cases}$$

We first determine the velocity using the first equation of the system, then we compute the displacement of the cell using the second equation. The forces term were introduced implicitly at each timestep. The equations for intracellular regulation are solved using the Euler explicit scheme.

Chapter 11

Appendix B - Parameter values

11.1 Parameter values of the blood coagulaton models

The values of parameters used in the both the exhaustive and simplified continuous models of blood coagulation are presented in the Table 11.1. The values of the model of the intrinsic pathway are provided in Table 11.2. The parameters of the warfarin PK-PD model are provided in Table 11.3.

Simulation	Numerical value	Description
dx	0.2	spatial step
dt	0.02	time step in haemostatis simulations
dt	0.00069	time step of PK-PD model
D	0.5	diffusion coefficient for all proteins
Reactions coefficients	Numerical value	Description
k_1	1	generation of thrombin in the initiation phase
k_2	22.5	generation of thrombin in the propagation phase
α_1	0.63	thrombin-antithrombin binding reaction rate
α_2	0.658	thrombin removal rate by blood flow
β_1^0	0.01	oxidized vitamin K reduction
β_2^0	0.3	oxidized vitamin K reduction inhibition by warfarin
β_1^1	0.0037	prothrombin activation by vitamin K
β_2^1	0.23	prothrombin inactivation
β_1^1	0.0056	factors IX and X activation by vitamin K
β_2^1	0.48	factors IX and X inactivation
Warfarin treatment	Numerical value	Description
m^1	1.15	warfarin distribution in blood rate
n^1	0.48	warfarin elimination by clearance rate
m^2	15	rivaroxaban distribution in blood rate
n^2	0.077	rivaroxaban elimination by clearance rate

Table 11.3: The values of parameters used for the 1D simplified model and the PK-PD model of warfarin and rivaroxaban.

11.2 Values of the parameters used in hybrid models

Unknown parameters were fitted to account for biologically acceptable results. The parameters of CFU-E/Pro-EBs regulation used in the model [85] were slightly changed in order to keep the same number of

SIMULATION	Value	Unit	Description
h	0.02	mm	space step
dt	0.005	s	time step
DIFFUSION COEFFICIENTS	Value	Unit	
D	510^{-5}	mm^2/s	Blood factors diffusion coefficient [64]
D_p	2.510^{-5}	mm^2/s	Platelets diffusion coefficient [64]
KINETIC RATES	Value	Unit	Reaction
k_1	5×10^{-7}	$nM^{-1}s^{-1}$	P activation by ϕ_c [64]
k_2	7.5×10^{-6}	$nM^{-1}s^{-1}$	P activation by B_a [4]
k_3	1.84×10^{-9}	$nM^{-3}s^{-1}$	P activation by T (fitted)
k_4	4.817×10^{-6}	$nM^{-1}s^{-1}$	T inactivation by A [327]
k_5	2.223×10^{-9}	$nM^{-1}s^{-1}$	B_a inactivation by A [327]
k_6	59	s^{-1}	F_g activation by T [328]
K_6	3160	nM	substrate fibrin concentration [328]
k_7	0.1	s^{-1}	$F \rightarrow F_p$ fibrin polymerization
k_8	0.17	nM^{-1}	factor V inactivation by C_a [329]
k_9	0.3	$nM^{-1}s^{-1}$	platelets activation by thrombin [57]
k_{10}	0.37	$nM^{-1}s^{-1}$	platelets activation by platelets [57]
k_3^+	1.57×10^{-9}	$nM^{-3}s^{-1}$	P activation by T in the simplified model (fitted)
k_T	1×10^5	nM^{-1}	T binding to TM
KINETIC CONSTANTS	Value	Unit	Description
α_1	0.0015	$nM^{-1}s^{-1}$	$\alpha_1 = k_f^- k_f[VII]$
β_1	0.225	nM^{-1}	$\beta_1 = k_f^+/k_f^-$
α_2	9.4	$nM^{-1}s^{-1}$	$\alpha_2 = k_c^- k_c$
β_2	100	nM^{-1}	$\alpha_2 = k_c$
ϕ_{max}	12	nM	maximal density of platelets
INITIAL CONCENTRATIONS	Value	Unit	Description
P_0	1400	nM	prothrombin concentration [4]
A_0	3400	nM	antithrombin concentration [4]
B^0	200	nM	sum of factors IX and X concentrations [4]
$[VII]$	10	nM	factor VII concentration [4]
C^0	60	nM	PC concentration [4]
Fg_0	7000	nM	fibrinogen concentration [4]
ϕ_f^0	10	nM	platelets density [4]
ϕ_c^0	0.001	nM	activated platelets bound to the inflamed tissues [4]
FLOW PROPERTIES	Value	Physical	Description
ρ	1.06×10^{-6}	$kgmm^{-3}$	blood density
ν	3	$mm^{-2}s^{-1}$	blood viscosity
α	100×10^{-6}	mm	fiber radius
a	5.6×10^{-4}	$s\ mm^{-1}$	thrombin removal rate by flow in the simplified model (fitted)

Table 11.1: Values of all parameters used in the numerical simulation of the clot formation continuous model.

cells per EBI although differentiated cells now remain for a longer period of time. The list of parameter values for the erythropoiesis and iron production model are given in Table 11.4, Table 11.5, and Table 11.6. The parameter values for the MM model are given in Table 11.7 and Table 11.8. The parameters for the release of immunoglobulins by MM cells and their treatment are given in Table 11.9 and Table 11.10.

Parameter	Value	Units	Description
dx	0.25	mm	spatial step
dt	0.005	min	time step
H	25	mm	diameter of the vessel
L	200	mm	length of the vessel
D	0.0037	mm^2min^{-1}	diffusion coefficient for all proteins
ρ	1023	kg/m^3	blood density
μ	3	$10^{-6}m^2/s$	blood viscosity
γ	60	nm	fibrin radius
Reactions rates	Value	Units	Description
k_1	0.0083	min^{-1}	conversion of fibrinogen into fibrin
k_2	2.45	min^{-1}	activation of thrombin by Xa
$\overline{k_2}$	2500	min^{-1}	activation of thrombin by [Va,Xa] complex
k_{11}	0.000002	min^{-1}	activation of XI by thrombin
h_{11}	0.7	min^{-1}	inhibition of XI
k_{10}	0.00033	min^{-1}	activation of X by IXa
$\overline{k_{10}}$	500	min^{-1}	activation of X by [VIIIa,IXa] complex
h_{10}	1	min^{-1}	inhibition of X
k_9	20	min^{-1}	activation of IX by XIa
h_9	0.2	min^{-1}	inhibition of IX
k_8	0.00001	min^{-1}	activation of VIII by thrombin
h_8	0.31	min^{-1}	inhibition of VIII
k_5	0.17	min^{-1}	activation of V by thrombin
h_5	0.31	min^{-1}	inhibition of V
k_{89}	5.36	$(\mu g/L)^{-1}min^{-1}$	activation of V by [VIIIa,IXa] complex
h_{89}	5.36	min^{-1}	inhibition of V
k_{510}	33	$(\mu g/L)^{-1}min^{-1}$	activation of V by [Va,Xa] complex
h_{510}	33	min^{-1}	inhibition of V
$\bar{k}$	0.11	min^{-1}	fibrin polymerization
α	0.0000401	$(\mu g/L)^{-1}min^{-1}$	inactivation of thrombin by antithrombin in the reduced models
α^*	0.0001575	$(\mu g/L)^{-1}min^{-1}$	inactivation of thrombin by antithrombin in the complete models
β	0.00005	$(\mu g/L)mm^{-1}$	rate of thrombin removal by blood flow
Concentration	Value	Units	Description
U_0	0.1	$\mu g/L$	The initial XI concentration on damaged wall
T_0	10	$\mu g/L$	Thrombin concentration on damaged wall
P_0	100	$\mu g/L$	prothrombin concentration in blood plasma
F_0	2600	$\mu g/L$	fibrinogen concentration in blood

Table 11.2: The values of the parameters of the intrinsic pathway model used in numerical simulations.

Parameter	Value	Unit
Differentiated Cells cycle length	52	h
Cells cycle variation	2	h
space variable x		NU
time variable		h
Blood reference volume V^*	3.75	nL

Table 11.4: Values of intracellular parameters for differentiated cell hemoglobin production in the multi-scale model.

Parameter	Value	Unit
Cells cycle length T	18	h
Cells cycle variation	3	h
space variable x		NU
time variable		h
a_0^0	0.001	h^{-1}
a_0^1	0	h^{-1}
a_1^1	0.00012	h^{-1}
a_1^0	0.0000005	h^{-1}
a_2^1	0	h^{-1}
a_2^0	0.00077	h^{-1}
a_3^1	0.00021	h^{-1}
a_3^0	0.000001	h^{-1}
b_1	0.0004	h^{-1}
b_2	0.0045	h^{-1}
b_3	0.43	h^{-1}
w_{cr}^0	0.06	NU

Table 11.5: Values of intracellular parameters used in CFU-E cells regulation. NU denotes nondimensional unit.

Parameter	Value	Unit
σ_1	0.01	h^{-1}
D_1	1e-5	$\delta^2.h^{-1}$
w_1	0.00005	$molecules.\delta^{-2}.h^{-1}$
σ_2	0.005	h^{-1}
D_2	0.05e-4	$\delta^2.h^{-1}$
w_2	0.0005	$molecules.\delta^{-2}.h^{-1}$

Table 11.6: Values of extracellular parameters. δ is an arbitrary length unit

Parameter	Value	Unit
Myeloma cells cycle length	26	h
Cells cycle variation	13	h
space variable and step x	1	δ
time variable	1	min
time step	0.01	min
β_1	0.001	min^{-1}
α_2	0.03	min^{-1}
β_2	0.002	min^{-1}
α_3	0.001	min^{-1}
β_3	0.01	min^{-1}
γ_3	0.00083	min^{-1}

Table 11.7: Values of intracellular regulation parameters for myeloma cells. δ is an arbitrary length unit.

Parameter	Value	Unit
D	0.5×10^{-5}	$\delta^2.min^{-1}$
W	0.0003	$molecules.\delta^{-2}.min^{-1}$
λ	0.1	NU
σ	1×10^{-7}	min^{-1}

Table 11.8: Values of extracellular parameters in the MM development model. δ is an arbitrary length unit.

Parameter	Value	Unit
ω	0.615 to 0.617	NU
p^*	0.712	NU
k_1	0.001	h^{-1}
k_2	0.0009	h^{-1}
k_1^1	0.00135	h^{-1}
k_2^1	160450736	h^{-1}
k_1^2	0.8	h^{-1}
k_2^2	0.037753114	h^{-1}
k_1^3	1.4	h^{-1}
k_2^3	0.035655719	h^{-1}
k_1^4	0.9	h^{-1}
k_2^4	0.113259343	h^{-1}
k_1^3	1.05	h^{-1}
k_2^3	0.096270442	h^{-1}
k_1^4	0.22	h^{-1}
k_2^4	0.160450736	h^{-1}

Table 11.9: Values of intracellular parameters used for MM cells intracellular regulation and immunoglobulins expression. NU denotes nondimensional unit

Parameter	Value	Unit
σ_1	0.01	h^{-1}
$D1$	0.25e-5	$L^2.h^{-1}$
W_1	0.00005	$molecules.L^{-2}.h^{-1}$
W_1^*	0.00009	$molecules.L^{-2}.h^{-1}$
σ_2	0.005	h^{-1}
D_2	0.05e-4	$L^2.h^{-1}$
W_2	0.0005	$molecules.L^{-2}.h^{-1}$

Table 11.10: Values of extracellular parameters. L is an arbitrary length unit